UNIVERSITY OF SOUTHAMPTON

Faculty of Engineering and Physical Sciences
School of Physics and Astronomy

An Investigation of Charged Higgs Phenomenology in 3HDM and its CP-violation Anomalies

by

Muyuan Song

ORCiD: 0000-0003-0446-5043

A thesis for the degree of
Doctor of Philosophy

July 2021

University of Southampton

Abstract

Faculty of Engineering and Physical Sciences
School of Physics and Astronomy

Doctor of Philosophy

An Investigation of Charged Higgs Phenomenology in 3HDM and its CP-violation Anomalies

by Muyuan Song

In this thesis, we focus on the 3-Higgs-Doublets-Model (3HDM) with 3 active Higgs doublets and study some of the features of its extended scalar structure. Specifically, we investigate the phenomenology of the charged Higgs boson sector at both lepton and hadron colliders as well as in low energy experiments. By using LHC and LEP2 data, we study the properties of a CP-conserving light charged Higgs boson in its $H_2^\pm \to cb$ decay channel. In order to detect this signature, we discuss the benefit of improved flavour tagging at both LEP2 and the LHC. In addition, we study three testable CP-violating asymmetry observables at the LHC and B factories, which could constrain the Yukawa couplings in the 3HDM when these are assumed complex only in the charged Higgs boson sector. Of particular interest is the untagged-asymmetry $\mathcal{A}_{\rm CP}(\bar{B} \to X_{s+d}\gamma)$, a measurement of which at 2.5% or more could produce 5σ evidence for new physics that can be accommodated in such a 3HDM. Moreover, we evaluate the constraints on the charged Higgs boson sector from both BR($\bar{B} \to X_s\gamma$) and electron/neutron electric dipole moments (e/nEDMs), again, by assuming only a single CP-violating phase in the charged Higgs boson sector. In such a context, we illustrate a special GIM-type cancellation mechanism entering the e/nEDMs, which is exact when the two physical charged Higgs bosons of the 3HDM ($H_2^\pm$ and $H_3^\pm$) are strictly degenerate in mass but still enables interesting and viable new phenomenology with a mass difference up to the Electroweak (EW) scale.

Contents

List of Figures

List of Tables

Declaration of Authorship

I declare that this thesis and the work presented in it is my own and has been generated by me as the result of my own original research.

I confirm that:

1. This work was done wholly or mainly while in candidature for a research degree at this University;
2. Where any part of this thesis has previously been submitted for a degree or any other qualification at this University or any other institution, this has been clearly stated;
3. Where I have consulted the published work of others, this is always clearly attributed;
4. Where I have quoted from the work of others, the source is always given. With the exception of such quotations, this thesis is entirely my own work;
5. I have acknowledged all main sources of help;
6. Where the thesis is based on work done by myself jointly with others, I have made clear exactly what was done by others and what I have contributed myself;
7. Parts of this work have been published as: [15; 16; 17; 18]

Signed:..... Date:.....

Acknowledgements

Firstly, I would like to thank my supervisors, Professor Stefano Moretti and Doctor Andrew Akeroyd who have been a constant source of support and guidance throughout the entirety of my PhD research. Both of them always asked to see how things were going both in social and research life in Southampton. They were keen to listen to the problems I encountered and enthusiastic to help out and find a solution.

Secondly, I would like to thank the members of High Energy Physics Theory group in the University of Southampton. Especially I would like to thank Ryan Hill, Kareem Farrag, Billy Ford, Henry Day-Hall, and Alex Mitchell. They have provided me with a variety of valuable suggestions and knowledge in my PhD life.

Thirdly, I would like to especially thank the former postdoc who worked in the University of Southampton, Diana Rojas-Ciofalo, who is now working in the University of Warsaw. She was one of our project collaborators. During the research time, she helped me to improve my understanding of particle physics and taught me how to use certain computation tools.

Furthermore, I would like to thank Professor Tetsuo Shindou and Professor Heather E. Logan. I was fortunate enough to meet both of them at conferences and workshops, and also the projects I have worked on with them gave me a broader view of B meson and Higgs physics research.

Also, for those who helped me but cannot be exhaustively listed since I met them in workshops all over the world, I look forward to the opportunity to meet them again, since I would like to thank them personally.

Finally, the most important people I should mention here are my parents. I am really grateful for their caring and dedication. Without their support, both mental and financial, I would not have the opportunity and courage to finish this PhD research. I am glad to have them in my life.

Definitions and Abbreviations

SM	The Standard Model
BSM	Beyond the Standard Model
EW scale	Electroweak scale
CERN	European Organization for Nuclear Research
LEP	Large Electron-Positron collider
LHC	Large Hadron Collider
ATLAS	A Toroidal LHC Apparatus
CMS	Compact Muon Solenoid
2HDM	2-Higgs-Doublets Model
3HDM	3-Higgs-Doublets Model
MHDM	Multi-Higgs-Doublets Model
CEPC	Cicular Electron Positron Collider
ILC	International Linear Collider
FCC-ee	Future Circular Collider- Electron Positron
$SU(3)$	Special Unitary group of degree 3
$SU(2)$	Special Unitary group of degree 2
$U(1)$	Unitary group of degree 1
QCD	Quantum Chromodynamics
SSB	Spontaneous Symmetry Breaking
VEV	Vacuum Expectation Value
UV	Ultra-Violent
CP	Charge conjugation-Parity
CKM matrix	Cabibbo–Kobayashi–Maskawa matrix
PMNS matrix	Pontecorvo-Maki-Nakagawa-Sakata matrix
SUSY	Supersymmetry
DM	Dark matter
EWPT	ElectroWeak Phase Transition
MSSM	Minimal Supersymmetry Standard model
NFC	Natural Flavour Conservation
FCNC	Flavour Changing Neutral Current
RH	Right-Handed
BR	Branching Ratio

SPYDER	Scientific PYthon Development EnviRonment
IDE	Integrated Development Environment
ALEPH	Apparatus for LEP physics at CERN
DELPHI	Detector with Lepton, Photon and Hadron Identification
OPAL	Omni-purpose apparatus for LEP
CL	Confidence Level
LHCb	Large Hadron Collider beauty
ALICE	Large Ion Collider Experiment
TOTEM	Total Elastic and diffractive cross section Measurement
LHCf	Large Hadron Collider forward
MoEDAL	Monopole and Exotics Detector at the LHC
FASER	ForwArd Search ExpeRiment
SLAC	Stanford Linear Accelerator Center
EDM	Electric Dipole Moment
eEDM	Elecron Electric Dipole Moment
nEDM	Neutron Electric Dipole Moment
LO	Leading Order
NLO	Next Leading Order
NNLO	Next-to-Next Leading Order
UCN	Ultra-Cold Neutrons
CEDM	Chromo-Electric Dipole Moments
GIM mechanism	Glashow–Iliopoulos–Maiani mechanism

Chapter 1

Introduction

1.1 Motivation

At the end of the 20th century, human research led to the achievement of the Standard Model (SM), which connects the electromagnetic, weak and strong interactions (three of the fundamental forces of the universe). The SM formed the latest understanding of physics based on relativity and quantum field theory and its predictions have been confirmed in many experiments since the 1970s. The searches for new particles in experimental colliders (such as CERN's LEP or later LHC) found particles, including fermions (new quarks and leptons) and bosons (W, Z). These are all part of the SM, which unifies Human's understanding of subatomic information in the Universe. The recent discovery of the Higgs boson in 2012 [19], which generates the masses of other fermions and bosons, is confirmation of the mechanism of electroweak symmetry breaking. Experimentalists at ATLAS and CMS have now moved their attention onto the precision measurements of the properties of the Higgs boson (which will also be an important part of the research programme at proposed Hadron or electron-positron colliders. One important measurement will be that of the Higgs self-interaction. The self-interaction parameter of Higgs boson will provide a hint to understand the structure of the scalar potential. The required phase transition in the early universe and the necessary Baryon asymmetry would both depend on the structure of the scalar potential [20]. On the other hand, the deficiencies of the SM such as not including gravity, the energy-scale dependency of the Higgs mass, the mass of neutrinos and the need of a dark matter candidate still motivates scientist to investigate the possibility of physics beyond the SM. There are a lot of theories that extend the SM. In particular the 2-Higgs-Doublet-Model (2HDM) and 3-Higgs-Doublet-Model (3HDM) have attracted more and more attention by scientists in recent years [21; 22]. In the 2HDM, the structure of the Higgs sector is no longer a single doublet as in SM. Instead, a spontaneous time violation theory is introduced, which consists of two independent complex spin-0 fields [23]. In the 3HDM, there are three $SU(2)$ doublets with more physical degrees of freedom. In the

rich scalar structure of the 2HDM and 3HDM, there are possible BSM candidates of a scalar nature. The discovered Higgs boson could be the solitary Higgs boson as originally proposed in the SM. However, a non-minimal scalar sector is also allowed by the precision measurements at LEP/LHC. (i.e. there could exist non-discovered neutral or even charged physical scalars). Thus, this thesis will focus on the 2HDM and specifically the 3HDM to order to investigate the phenomenology of such extension scalar structures.

1.2 Overview

In this thesis, we discuss the phenomenology of light charged Higgs bosons in the 3HDM and their potential detection at the colliders LEP2, LHC, KEK-B and at future colliders such as CEPC/FCC-ee. We first present the scalar sector of the 2HDM and the 3HDM because the Yukawa sector of the two models are similar. Within the 3HDM, we also investigate the effect of charged Higgs bosons on Charge conjugation Parity (CP)-asymmetry observables in the decay $\bar{B} \to X_s\gamma$ and the electron/neutron-EDMs (e/n-EDMs). The whole work contains and connects four papers [15; 16; 17; 18].

The structure of the thesis as follows. In chapter 2, a brief review of the standard model of particle physics is presented, and since the thesis is about the Higgs physics, the mechanism of electroweak symmetry breaking will be discussed. There will be a short introduction to the characteristics of the SM Higgs boson. In chapter 3, this thesis will illustrate a simple extension of SM, 2HDM. It then will cover the general structure of the 2HDM, in particular the scalar potential and the Yukawa sector. The connection between the 2HDM and 3HDM is close. To date, considerably more research has been done for the 2HDM and so this thesis focuses on the 3HDM. In particular, the phenomenology of the charged scalar sector in the 3HDM will be covered. We will show the structure and relevant parameters for the relationship between the charged Higgs and fermions in chapter 4. The work is based on the paper [17]. This chapter focuses on the charged Higgs boson and it will illustrate the decay products of the charged Higgs and the dependence on the parameter space of the Yukawa couplings. In chapter 5 the experimental production of charged Higgs at LEP2 will be discussed. It is shown that the implementation of $b-$tagging could improve the statistical significances and possibly lead to the detection of a charged scalar using LEP2 data, and an analysis is done for a future e^+e^- collider based on numerical extrapolations from LEP2 results (e.g. CEPC, ILC or FCC-ee). The chapter contains work from both [17] and [18]. In chapter 6, the constraints from CP-violating observables on the parameter space of charged Higgs Yukawa couplings will be shown. Moreover, several features of CP-asymmetry observables will be shown (e.g. $\bar{B} \to X_s\gamma$, direct asymmetry ($\mathcal{A}_{X_{s(d)}\gamma}$), CP-asymmetry difference ($\Delta\mathcal{A}_{X_{s(d)}\gamma}$), the inclusive or the untagged-asymmetry ($\mathcal{A}_{\rm CP}(\bar{B} \to X_{s+d}\gamma)$) and electric-dipole moment (EDM) of neutron and electron). It will be shown that the 3HDM can provide a stronger signal the the SM in some of these observables. The material is taken from both [15] and [16]. The final results of the whole postgraduate research which are described in detail in both chapter 5 and chapter 6 will then be summarised in the conclusions in chapter 7.

Chapter 2

The Standard Model (SM)

Here we give a brief discussion of the Standard Model (SM) [24; 25; 26]. The SM is an $SU(3) \times SU(2) \times U(1)$ gauge theory. The SM Lagrangian is invariant under a local $SU(3)_C \otimes SU(2)_L \otimes U(1)_Y$ gauge transformation. $SU(3)$ is quantum chromodynamics (QCD) which describes strong interactions. In $SU(3)$, a total of 8 massless gauge fields are present with the name "gluons" (g). For $SU(2) \times U(1)$, there are three massive gauge fields called $W^{\pm}$ and Z bosons. Together with a massless photon (γ), the electroweak interactions are described by these gauge bosons.

The first column of Tab. (2.1) shows the matter content of the SM, and consists of quarks and leptons, with a total of 15 numbers of Weyl fermions. The notation of q_L and l_L are for the left-handed Weyl fermions and $(u, c, t, d, s, b, e, \mu, \tau)_R$ are the right-handed Weyl fermions. The second column is the representation of $SU(3)$ with number 3, the fundamental, and number 1 as singlet. The third column is the representation of $SU(2)$ with number 2 as fundamental and 1 as singlet. The last column is the generator of $U(1)$, Hypercharge (Y). A detailed review of the structure of the SM structure can be found in [27; 28].

	$SU(3)_C$	$SU(2)_L$	$U(1)_Y$
$q_L = \begin{pmatrix} u_L \\ d_L \end{pmatrix}, \begin{pmatrix} c_L \\ s_L \end{pmatrix}, \begin{pmatrix} t_L \\ b_L \end{pmatrix}$	3	2	$\frac{1}{6}$
u_R, c_R, t_R	3	1	$\frac{2}{3}$
d_R, s_R, b_R	3	1	$-\frac{1}{3}$
$l_L = \begin{pmatrix} \nu_{eL} \\ e_L \end{pmatrix}, \begin{pmatrix} \nu_{\mu L} \\ \mu_L \end{pmatrix}, \begin{pmatrix} \nu_{\tau L} \\ \tau_L \end{pmatrix}$	1	2	$-\frac{1}{2}$
e_R, μ_R, τ_R	1	1	-1

TABLE 2.1: The three Families of SM particles with the quantum number representations of the subgroups of $SU(3)_C$, $SU(2)_L$, and $U(1)_Y$.

2.1 Standard Model Lagrangian

The kinetic term of the SM Lagrangian can be written as :

$$\mathcal{L}_{\text{kin}} = -\frac{1}{4}G^a_{\mu\nu}G^{a\mu\nu} - \frac{1}{4}W^i_{\mu\nu}W^{i\mu\nu} - \frac{1}{4}B_{\mu\nu}B^{\mu\nu} + i\bar{\psi}_L \not{D}\psi_L + i\bar{\psi}_R \not{D}\psi_R \tag{2.1}$$

Here $\bar{\psi}$ or ψ are the SM fermions taken from Tab. (2.1). The subscripts L and R on the bottom-right corner of $\bar{\psi}$ or ψ represent left-handed and right-handed chiralities. The $\not{D}$ is a short-hand of notation $\not{D} = \gamma_\mu D^\mu$ for the covariant derivative and the notation γ_μ is represented as four Gamma matrices (or Dirac matrices) of the Clifford algebra under Dirac representation which is defined below:

$$\begin{aligned}
\gamma^0 &= \begin{pmatrix} 1 & 0 & 0 & 0 \\ 0 & 1 & 0 & 0 \\ 0 & 0 & -1 & 0 \\ 0 & 0 & 0 & -1 \end{pmatrix}, \gamma^1 = \begin{pmatrix} 0 & 0 & 0 & 1 \\ 0 & 0 & 1 & 0 \\ 0 & -1 & 0 & 0 \\ -1 & 0 & 0 & 0 \end{pmatrix} \\
\gamma^2 &= \begin{pmatrix} 0 & 0 & 0 & -i \\ 0 & 0 & i & 0 \\ 0 & i & 0 & 0 \\ -i & 0 & 0 & 0 \end{pmatrix}, \gamma^3 = \begin{pmatrix} 0 & 0 & 1 & 0 \\ 0 & 0 & 0 & -1 \\ -1 & 0 & 0 & 0 \\ 0 & 1 & 0 & 0 \end{pmatrix}.
\end{aligned} \tag{2.2}$$

For covariant derivative D_μ, it is expressed as below:

$$D_\mu = \partial_\mu - i[g_s T^a G^a_\mu + g\tau^i W^i_\mu + g^{'}\frac{Y}{2}B_\mu] \tag{2.3}$$

In the above, T^a and τ^i are the $SU(3)_C$ and $SU(2)_L$ group generators. In the colour triplet representation, T^a can be written as $T^a = \frac{\lambda^a}{2}$ where λ^a are Gell-mann matrices with a total number of 8 linear independent 3×3 matrices. The formulas are below:

$$\begin{aligned}
\lambda_1 &= \begin{pmatrix} 0 & 1 & 0 \\ 1 & 0 & 0 \\ 0 & 0 & 0 \end{pmatrix}, \lambda_2 = \begin{pmatrix} 0 & -i & 0 \\ i & 0 & 0 \\ 0 & 0 & 0 \end{pmatrix}, \lambda_3 = \begin{pmatrix} 1 & 0 & 0 \\ 0 & -1 & 0 \\ 0 & 0 & 0 \end{pmatrix} \\
\lambda_4 &= \begin{pmatrix} 0 & 0 & 1 \\ 0 & 0 & 0 \\ 1 & 0 & 0 \end{pmatrix}, \lambda_5 = \begin{pmatrix} 0 & 0 & -i \\ 0 & 0 & 0 \\ i & 0 & 0 \end{pmatrix}, \lambda_6 = \begin{pmatrix} 0 & 0 & 0 \\ 0 & 0 & 1 \\ 0 & 1 & 0 \end{pmatrix} \\
\lambda_7 &= \begin{pmatrix} 0 & 0 & 0 \\ 0 & 0 & -i \\ 0 & i & 0 \end{pmatrix}, \lambda_8 = \frac{1}{\sqrt{3}}\begin{pmatrix} 1 & 0 & 0 \\ 0 & 1 & 0 \\ 0 & 0 & -2 \end{pmatrix}
\end{aligned} \tag{2.4}$$

For τ^i, it is equal to $\tau^i = \frac{\sigma^i}{2}$ under weak doublet where σ^i are the Pauli matrices containing a total number of three 2×2 matrices. The formulas are below:

$$\sigma^1 = \begin{pmatrix} 0 & 1 \\ 1 & 0 \end{pmatrix}, \sigma^2 = \begin{pmatrix} 0 & -i \\ i & 0 \end{pmatrix}, \sigma^3 = \begin{pmatrix} 1 & 0 \\ 0 & -1 \end{pmatrix} \tag{2.5}$$

Y in Eq. (2.3) is the weak hypercharge or the generator of $U(1)_Y$ group which is defined from:

$$\frac{Y}{2} = Q - T_3. \tag{2.6}$$

Q is the electric charge and T_3 is the third component of the weak isospin.

In Eq. (2.1), terms like $G^a_{\mu\nu}, W^i_{\mu\nu}$ and $B_{\mu\nu}$ are the 8 gluon fields ($a = 1, 2, 3...8$), three ($i = 1, 2, 3$) SU(2) gauge fields and one U(1) gauge field representations respectively based on below transformation:

$$\begin{aligned} G^a_{\mu\nu} &= \partial_\mu G^a_\nu - \partial_\nu G^a_\mu + g_s f^{abc} G^b_\mu G^c_\nu \\ W^i_{\mu\nu} &= \partial_\mu W^i_\nu - \partial_\nu W^i_\mu + g\epsilon^{ijk} W^j_\mu W^k_\nu \\ B_{\mu\nu} &= \partial_\mu B_\nu - \partial_\nu B_\mu \end{aligned} \tag{2.7}$$

These are the field strength tensors of gauge fields.

The interaction of quarks with the gauge fields can be written as:

$$\mathcal{L}_{\text{Quark}} = \bar{Q}_L \not{D}_\mu Q_L + \bar{u}_R \not{D}_\mu u_R + \bar{d}_R \not{D}_\mu u_R + h.c \tag{2.8}$$

where $Q_L = \begin{pmatrix} u_L \\ d_L \end{pmatrix}$ and $\bar{Q}_L = (\bar{u}_L, \bar{d}_L)$. We simply write all up-type quark fields as u and all down-type quark fields as d, and so any left-handed down-type quark is written as d_L. The covariant derivatives D_μ determine reveal the coupling between the quarks and the gauge fields:

$$\begin{aligned} D_\mu \begin{pmatrix} u_L \\ d_L \end{pmatrix} &= (\partial_\mu + ig_s \frac{\lambda_a}{2} G^a_\mu + i\frac{g}{2}\sigma^i W^i_\mu + ig' \frac{Y}{2} B_\mu) \begin{pmatrix} u_L \\ d_L \end{pmatrix} \\ D_\mu u_R &= (\partial_\mu + ig_s \frac{\lambda_a}{2} G^a_\mu + ig' \frac{Y}{2} B_\mu) u_R \\ D_\mu d_R &= (\partial_\mu + ig_s \frac{\lambda_a}{2} G^a_\mu + ig' \frac{Y}{2} B_\mu) d_R \end{aligned} \tag{2.9}$$

All quarks couple to G^a_μ and B_μ. These two fields correspond to strong and electromagnetic interactions respectively. The difference for left-handed and right-handed quarks

comes from coupling to W^i_μ. Only left-handed quarks couple to W^i_μ which leads no weak interaction for right-handed quarks. Similarly, the lepton part can be written as:

$$\mathcal{L}_{\text{Lepton}} = (\bar{\nu}_{\ell,L}, \bar{\ell}_L) \not{D}_\mu \begin{pmatrix} \nu_{\ell,L} \\ \ell_L \end{pmatrix} + \bar{\ell}_R \not{D}_\mu \ell_R + h.c \tag{2.10}$$

where ℓ represents all three leptons (e, μ, τ). In the SM, neutrinos are left-handed particles only and thus, no terms like ν_R appear. The interaction between leptons and gauge fields are:

$$\begin{aligned} D_\mu \begin{pmatrix} \nu_{\ell,L} \\ \ell_L \end{pmatrix} &= (\partial_\mu + i\frac{g}{2}\sigma^i W^i_\mu + ig'\frac{Y}{2}B_\mu) \begin{pmatrix} \nu_{\ell,L} \\ \ell_L \end{pmatrix} \\ D_\mu \ell_R &= (\partial_\mu + ig'\frac{Y}{2}B_\mu)\ell_R \end{aligned} \tag{2.11}$$

Leptons are $SU(3)$ singlets and so do not couple G^a_μ (therefore they do not experience the strong interaction). Moreover, only left-handed leptons experience weak interactions.

2.2 Spontaneous Symmetry Breaking (SSB) and Higgs

Spontaneous Symmetry Breaking (SSB) is a mechanism of introducing mass (for the massive fermions and the massive gauge bosons $W^{\pm}, Z$) into a gauge theory while preserving gauge invariance, the latter being essential in order to ensure that the predictions of theory are finite. Introducing explicit mass terms that break the gauge symmetry would lead to unphysical predictions for experimental observables. We first take the case of a complex field case (ϕ) with the scalar potential ($V(\phi^+\phi)$):

$$\begin{aligned} \mathcal{L} &= \partial_\mu \phi^+ \partial^\mu \phi - V(\phi^+\phi) \\ V(\phi^+\phi) &= -\mu^2 \phi^+\phi + \lambda(\phi^+\phi)^2 \end{aligned} \tag{2.12}$$

In the case of the sign of μ^2 in Eq. (2.12) being positive, the Vacuum Expectation Value (VEV), which is the value of the scalar field at the minimum of the scalar potential becomes zero and the minimum of the potential is also zero. If $\mu^2 < 0$, the VEV is no longer zero, as shown the right hand side of Fig. (2.1):

The minimum or the vacuum expectation value will be the minimum point of $V(\phi^+\phi)$:

$$\begin{aligned} \phi_0 &= \sqrt{\frac{\mu^2}{2\lambda}} e^{i\alpha} \\ &= \frac{v}{\sqrt{2}} e^{i\alpha} \end{aligned} \tag{2.13}$$

The phase α is not physical because even defining $\phi_0 = \frac{v}{\sqrt{2}}$, the phase α can be recovered from the $U(1)_Y$ transformation by:

$$\phi \to e^{i\alpha}\phi \tag{2.14}$$

Thus, the $U(1)_Y$ symmetry invariance will disappear if the phase of angle α in the vacuum state is fixed. The physical vacuum state of the system causes "the vacuum spontaneous symmetry breaking".

Spontaneous symmetry breaking occurs if the Lagrangian or a system is invariant under several symmetries but the ground state (minimum) is not. In that case the ground state does not hold the same gauge symmetry as the Lagrangian. In particular, the mechanism supplies the weak gauge boson masses and predicts the existence of a new scalar physical particle, the "Higgs boson". It was introduced by F. Englert, R. Brout, and P. W. Higgs in Refs. [29; 30; 31].

One introduces a new definition of the complex scalar field:

$$\phi(x) = \frac{1}{\sqrt{2}}[v + \chi(x) + i\theta(x)] \tag{2.15}$$

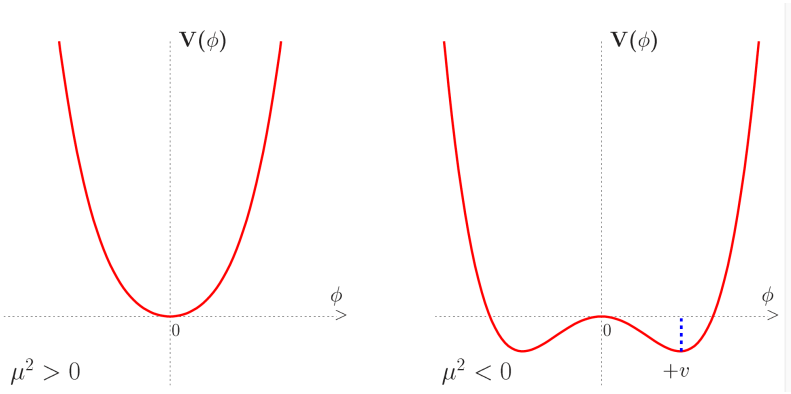

FIGURE 2.1: The potential of ϕ, $V(\phi)$, in two cases of μ. Left-handed side: $\mu^2 > 0$. Right-handed side: $\mu^2 < 0$. This figure is taken from Fig. (1.1) of [1].

$$\begin{aligned} Re\,\phi &= v + \chi \\ Im\,\phi &= \theta \end{aligned} \tag{2.16}$$

This expression for $\phi(x)$ is then substituted into the expression for $V(\phi^+\phi)$ of Eq. (2.12) and the potential is then given by:

$$\begin{aligned} V(\phi^+\phi) &= -\mu^2\phi^+\phi + \lambda(\phi^+\phi)^2 \\ &= -\frac{1}{2}\mu^2|v+\chi(x)+i\theta(x)|^2 + \frac{1}{4}\lambda|v+\chi(x)+i\theta(x)|^4 \\ &= -\frac{1}{2}\mu^2[(v+\chi)^2+\theta^2] + \frac{1}{4}\lambda[(v+\chi)^2+\theta^2]^2 \\ &= -\frac{1}{2}\mu^2[v^2+2v\chi+\chi^2+\theta^2] + \frac{1}{4}\lambda\,[v^2+2v\chi+\chi^2+\theta^2]^2 \\ &= \left(\frac{1}{4}\lambda\,v^4 - \frac{1}{2}\mu^2v^2\right) + \frac{1}{2}(l\lambda v^2-\mu^2)(2v\chi+\chi^2+\theta^2) + \lambda\,v^2\chi^2 \\ &+ \lambda\,v\chi(\chi^2+\theta^2) + \frac{1}{4}\lambda(\chi^2+\theta^2)^2 \\ &= -\frac{1}{4}v^2\mu^2 + \lambda v^2\chi^2 + \lambda\,v\chi(\chi^2+\theta^2) + \frac{1}{4}\lambda(\chi^2+\theta^2)^2 \end{aligned} \tag{2.17}$$

Eq. (2.17) uses Eq. (2.13) with $v = \sqrt{\frac{\mu^2}{\lambda}}$.

The Lagrangian of this complex scalar field is now:

$$\begin{aligned} \mathcal{L} &= \frac{1}{2}\partial_\mu\chi\partial^\mu\chi + \frac{1}{2}\partial_\mu\theta\partial^\mu\theta - \lambda\,v^2\,\chi^2 - \lambda\,v\,\chi(\chi^2+\theta^2) - \frac{1}{4}\lambda\,(\chi^2+\theta^2)^2 \\ &= \frac{1}{2}\partial_\mu\chi\partial^\mu\chi - \frac{1}{2}(2\lambda\,v^2)\chi^2 + \frac{1}{2}\partial_\mu\theta\partial^\mu\theta - \lambda\,v\,\chi(\chi^2+\theta^2) \\ &+ \frac{1}{4}v^2\mu^2 - \frac{1}{4}(\chi^2+\theta^2)^2 \end{aligned} \tag{2.18}$$

Eq. (2.18) shows the field χ gains a mass but θ does not due to the second χ^2 term and no alone θ^2 term in the Lagrangian:

$$M_\chi^2 = 2\lambda\, v^2, \;\; M_\theta^2 = 0. \tag{2.19}$$

After spontaneous symmetry breaking, the masses of the two fields are:

$$M_\chi^2 = \frac{\partial^2 V}{\partial \chi^2}\Big|_{\chi,\theta=0}, \; M_\theta^2 = \frac{\partial^2 V}{\partial \theta^2}\Big|_{\chi,\theta=0}. \tag{2.20}$$

The second derivative in the direction of χ is not zero and this leads to a mass for χ. The second derivative in the direction of θ is zero, which means the scalar field is still massless as in Fig. (2.2). Thus, the symmetry breaking provides the field χ with mass. Meanwhile, the zero mass particle is in the direction which is tangent to the symmetry breaking. The zero-mass particle is called the Goldstone particle. The Goldstone theorem states the existence of massless particles which arise from spontaneous symmetry breaking.

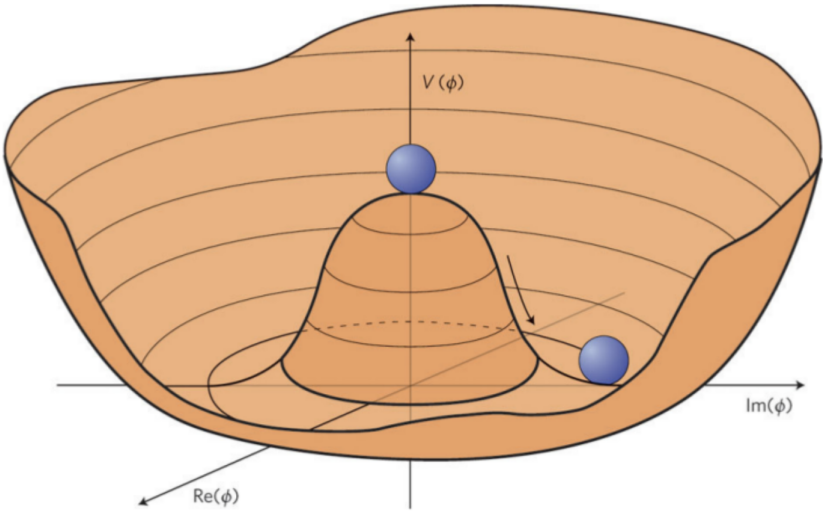

FIGURE 2.2: The potential of $V(\phi^+\phi)$ with $\mu^2 < 0$. This figure is taken from Ref. [2].

2.2.1 Higgs sector in SM

In the SM, the SSB is implemented from one complex $SU(2)$ Higgs field with four degrees of freedom. The complex Higgs field has hypercharge $Y = \frac{1}{2}$ with the third component of weak isospin $T_3 = \frac{1}{2}, -\frac{1}{2}$ (an isodoublet).

$$\begin{aligned} \Phi &= \begin{pmatrix} \phi^+ \\ \phi^0 \end{pmatrix} \\ &= \begin{pmatrix} \phi^+ \\ \frac{[v+h+i\eta]}{\sqrt{2}} \end{pmatrix} \end{aligned} \tag{2.21}$$

The vacuum expectation value of real scalar field breaks the gauge symmetry, which means the SM gauge group $SU(3)_C \otimes SU(2)_L \otimes U(1)_Y$ breaks down to the subgroup $SU(3)_C \otimes U(1)_{\rm EM}$ through Spontaneous Symmetry Breaking (SSB). The Lagrangian of the Higgs sector can be written simply as:

$$\begin{aligned} \mathcal{L}_\Phi &= |D_\mu \Phi|^2 - V(\Phi), \quad V(\Phi) = \mu^2(\Phi^\dagger\Phi) + \lambda(\Phi^\dagger\Phi)^2 \\ V(\Phi) &= \mu^2|\Phi^2 + \lambda|\Phi|^4 \end{aligned} \tag{2.22}$$

Under $SU(2)_L \times U(1)_Y$, Φ transforms as follows:

$$\begin{aligned} \Phi(x) \to \Phi'(x) &= U_2\Phi(x) = e^{igT^i\alpha^i x}\Phi(x) \\ \Phi(x) \to \Phi'(x) &= U_1\Phi(x) = e^{i\frac{g'}{2}Y\beta(x)}\Phi(x) \end{aligned} \tag{2.23}$$

while $\Phi^+\Phi$ is not invariant under the transformation below:

$$\begin{pmatrix} \phi^+ \\ \frac{[h+i\eta]}{\sqrt{2}} \end{pmatrix} \to U_1\, U_2 \begin{pmatrix} \phi^+ \\ \frac{[h+i\eta]}{\sqrt{2}} \end{pmatrix} \tag{2.24}$$

The symmetry of $SU(2)_L \times U(1)_Y$ is broken but the transformation of $U(1)_{\rm EM}$ is invariant for $\Phi^+\Phi$ by:

$$\begin{aligned} \phi^+ \to e^{ie\hat{Q}\alpha(x)}\phi^+ &= e^{ie\alpha(x)}\phi^+ \\ \phi^- \to e^{ie\hat{Q}\alpha(x)}\phi^- &= e^{-ie\alpha(x)}\phi^- \\ h \to e^{ie\hat{Q}\alpha(x)}h &= h \\ \eta \to e^{ie\hat{Q}\alpha(x)}\eta &= \eta \end{aligned} \tag{2.25}$$

where $\hat{Q}$ is the electric charge operator of electric charge Q where the relationship with the isospin and the hypercharge can be found in Eq. (2.6). Thus, $\hat{Q}$ acts on field h and η will give $\hat{Q}h = 0, \hat{Q}\eta = 0$, as the two scalar fields are neutral. The electric charge operator $\hat{Q}$ is the $U(1)_{\rm EM}$ generator which commutes with Hamiltonian H. Thus, the

symmetry of $SU(2)_L \times U(1)_Y$ is broken down to $U(1)_{\text{EM}}$, and $U(1)_{\text{EM}}$ is a good symmetry of the Lagrangian (as in Quantum Electrodynamics).

2.2.2 Gauge boson masses from Higgs

The masses of gauge bosons originate from the interaction of the scalar Higgs field and the gauge fields from the second and third terms of the covariant derivatives of Eq. (2.3):

$$\begin{aligned} D_\mu &= \partial_\mu - ig\frac{\sigma^i}{2}W_\mu^i - ig'\frac{Y}{2}\mathbb{1}B_\mu \\ &= \partial_\mu - \frac{i}{2}\begin{pmatrix} gW_\mu^3 + g^{'}YB_\mu & gW_\mu^1 - igW_\mu^2 \\ gW_\mu^1 + gW_\mu^2 & -gW_\mu^3 + g^{'}YB_\mu \end{pmatrix} \end{aligned} \tag{2.26}$$

$\mathbb{1} = \begin{pmatrix} 1 & 0 \\ 0 & 1 \end{pmatrix}$ and σ^i are defined from Eq. (2.5). We can then define the mass eigenstates of two gauge eigenstates (W_μ^1 and W_μ^2):

$$W_\mu^- = \frac{W_\mu^1 + i\,W_\mu^2}{\sqrt{2}}, W_\mu^+ = \frac{W_\mu^1 - i\,W_\mu^2}{\sqrt{2}} \tag{2.27}$$

Eq. (2.26) is then rewritten as:

$$D_\mu = \partial_\mu - \frac{i}{2}\begin{pmatrix} gW_\mu^3 + g'YB_\mu & g\sqrt{2}W_\mu^+ \\ g\sqrt{2}W_\mu^- & -gW_\mu^3 + g'YB_\mu \end{pmatrix} \tag{2.28}$$

The term $|D_\mu\Phi|^2$ becomes:

$$\begin{aligned} |D_\mu\Phi|^2 &= \left|\left(\partial_\mu - \frac{i}{2}\begin{pmatrix} gW_\mu^3 + g'YB_\mu & g\sqrt{2}W_\mu^+ \\ g\sqrt{2}W_\mu^- & -gW_\mu^3 + g'YB_\mu \end{pmatrix}\right)\frac{1}{\sqrt{2}}\begin{pmatrix} 0 \\ v+h+i\eta \end{pmatrix}\right|^2 \\ &= \left| -\frac{i}{2\sqrt{2}}\begin{pmatrix} gW_\mu^3 + g'YB_\mu & g\sqrt{2}W_\mu^+ \\ g\sqrt{2}W_\mu^- & -gW_\mu^3 + g'YB_\mu \end{pmatrix}\begin{pmatrix} 0 \\ v \end{pmatrix}\right|^2 \\ &= |\frac{i}{2\sqrt{2}}v\begin{pmatrix} g\sqrt{2}W_\mu^+ \\ -gW_\mu^3 + g'YB_\mu \end{pmatrix}|^2 \\ &= |\left(-\frac{1}{4}g^2v^2W_\mu^+W^{-\mu} - \frac{1}{8}v^2(g^2W_\mu^3W^{3\mu} + g'^2B_\mu B^\mu - 2gg'W_\mu^3B^\mu)\right)| \\ &= \frac{1}{4}g^2v^2W_\mu^+W^{-\mu} + \frac{1}{8}v^2g^2W_\mu^3W^{3\mu} + \frac{1}{8}v^2g'^2B_\mu B^\mu - \frac{1}{4}v^2gg'W_\mu^3B^\mu \\ &= \frac{1}{4}g^2v^2W_\mu^+W^{-\mu} + \frac{1}{8}v^2(W_\mu^3\ B_\mu)\begin{pmatrix} g^2 & -gg' \\ -gg' & g'^2 \end{pmatrix}\begin{pmatrix} W^{3\mu} \\ B^\mu \end{pmatrix} \end{aligned} \tag{2.29}$$

Here we took only VEV (v) in the Φ and neglected the ∂_μ terms to obtain the gauge boson masses. From the above, $\frac{1}{4}g^2\,v^2$ corresponds to the mass term of $W^\pm$.

$$M_W = \frac{1}{2}g\,v \tag{2.30}$$

Since the matrix $\begin{pmatrix} g^2 & -gg' \\ -gg' & g'^2 \end{pmatrix}$ is not diagonalised, the W^3_μ, B^μ do not represent mass eigenstates. We then obtain the mass eigenstate of W^3_μ, B_μ from the normalised eigenvector of $\begin{pmatrix} g^2 & -gg' \\ -gg' & g'^2 \end{pmatrix}$:

$$\begin{aligned} A_\mu &= \frac{1}{\sqrt{g^2+g'^2}}(g'W^3_\mu + gB_\mu) \\ Z_\mu &= \frac{1}{\sqrt{g^2+g'^2}}(gW^3_\mu - g'B_\mu) \end{aligned} \tag{2.31}$$

Defining the relation below:

$$\sin\theta_W = \frac{g'}{\sqrt{g^2+g'^2}},\ \cos\theta_W = \frac{g}{\sqrt{g^2+g'^2}} \tag{2.32}$$

Where θ_W is the weak mixing Weinberg angle, $g\sin\theta_W = g'\cos\theta_W = e$. e is the electric charge. g is the coupling constant of $SU(2)_L$ local gauge transformation and g' is the coupling constant of $U(1)_Y$ local gauge transformation. Then one can write:

$$\begin{aligned} A_\mu &= \sin\theta_W W^3_\mu + \cos\theta_W B_\mu \\ Z_\mu &= \cos\theta_W W^3_\mu - \sin\theta_W B_\mu \end{aligned} \tag{2.33}$$

Thus, the mass eigenstates (A_μ, Z_μ) in terms of the two gauge eigenstates (W^3_μ and B_μ) is:

$$W^3_\mu = \sin\theta_W A_\mu + \cos\theta_W Z_\mu \tag{2.34}$$

$$B_\mu = \cos\theta_W A_\mu - \sin\theta_W Z_\mu \tag{2.35}$$

Substituting Eqs. (2.34 and 2.35) into Eq. (2.29) gives the following expressions for M^2_γ and M^2_Z:

$$\begin{aligned} M^2_\gamma = 0,\ \ M^2_Z &= \frac{1}{4}v^2(g^2+g'^2) \\ M_\gamma = 0,\ \ M_Z &= \frac{1}{2}v\sqrt{g^2+g'^2} \end{aligned} \tag{2.36}$$

Thus, Three of the Goldstone bosons from the Higgs field are eaten by $W^\pm$ and Z and obtain longitudinal components (and masses). On the other hand, the photon (γ) is still massless, which means that the $U(1)$ symmetry is unbroken. Three gauge bosons $W^\pm, Z$ receive the mass by absorbing three degrees of freedom, and the one remaining scalar degree of freedom is the physical Higgs boson.

If we look at the Eqs. (2.30 and 2.36), and the relationship of g, g', and θ_W (which is $\tan\theta_W = \frac{g'}{g}$ from relation Eq. (2.32)), one could have below relationship:

$$\frac{M_W}{M_Z} = \cos\theta_W \tag{2.37}$$

This relationship is a reason that the mass of Z boson is different than the mass of $W^{\pm}$ boson. In the scenario which $\cos\theta_W = 1$ (i.e. no weak mixing angle or θ_W), $M_Z = M_W$. The Higgs model holds the parameter ρ at tree level to be:

$$\rho = \frac{M_W^2}{M_Z^2\cos^2\theta_W} = 1. \tag{2.38}$$

In the case of $\theta_W \to 0, h_{\rm SM} \to 0$, there is a special $SU(2)_L \times SU(2)_R$ custodial symmetry in scalar potential before SSB. After the SSB, the custodial symmetry breaks to $SU(2)_{L+R}$ symmetry and will be a subgroup of the custodial symmetry of the SM [32].

2.2.3 Fermion mass generation from Higgs

The same scalar field is also needed to generate the masses of the fermions. A filed $\tilde{\Phi}$ is obtained from Φ (with hypercharge $Y = -\frac{1}{2}$) as follows:

$$\begin{aligned}\tilde{\Phi} &= i\sigma_2\Phi^* = i\begin{pmatrix} 0 & -i \\ i & 0 \end{pmatrix}\begin{pmatrix} \phi^+ \\ \phi^0 \end{pmatrix}^* \\ &= \begin{pmatrix} 0 & 1 \\ -1 & 0 \end{pmatrix}\begin{pmatrix} \phi^- \\ \phi^{0*} \end{pmatrix} = \begin{pmatrix} \phi^{0*} \\ -\phi^- \end{pmatrix},\ (\phi^+)^* = \phi^-\end{aligned} \tag{2.39}$$

This field will generate the mass generation for the up-type quarks after SSB. The transformation of $\tilde{\Phi}$ under $SU(2)$ is the same as Φ. In this way, the sector which generates the mass for the fermions (also called the "Yukawa sector"), and is also invariant under $SU(2) \times U(1)$ is given by:

$$\mathcal{L}_Y = -\lambda_\ell \bar{L}\Phi\ell_R - \lambda_d\bar{Q}\Phi d_R - \lambda_u\bar{Q}\tilde{\Phi}u_R + h.c \tag{2.40}$$

Taking the same procedure as Eq. (2.29), which only used $\Phi = \frac{1}{\sqrt{2}}\begin{pmatrix} 0 \\ v+h \end{pmatrix}$, and focussing on the first generation leptons ($-\lambda_\ell\bar{L}\Phi\ell_R$) only, one has:

$$\begin{aligned}\mathcal{L}_{\rm Yukawa} &= -\frac{1}{\sqrt{2}}\lambda_\ell(\bar{v}_\ell, \bar{\ell}_L)\begin{pmatrix} 0 \\ v+h \end{pmatrix}\ell_R + ... \\ &= -\frac{1}{\sqrt{2}}\lambda_\ell(\bar{\ell}_L v\ell_R + \bar{\ell}_L h\ell_R) + ...\end{aligned} \tag{2.41}$$

The term $\frac{\lambda_\ell v}{\sqrt{2}}$ is the mass of lepton (i.e. $m_\ell = \frac{\lambda_\ell v}{\sqrt{2}}$) and the term $\frac{\lambda_\ell}{\sqrt{2}}$ is the Yukawa coupling between Higgs h and fermion pairs $\bar{\ell}_L, \ell_R$ or $(\bar{\ell}, \ell)$.

In the unitary gauge, the Yukawa interaction is written as:

$$\mathcal{L} = -\sum_f m_f \bar{\psi}_f \psi_f - \sum_f \frac{m_f}{v} \bar{\psi}_f \psi_f \, h + ... \tag{2.42}$$

where ψ are the fermion fields.

2.3 Higgs hierarchy problem and its proposed solution

In this section we present the meaning of fine tuning problem of the Higgs mass and discuss its possible solution. The discovery of the Higgs boson confirms the origin of the mass of fermions and bosons from the Higgs mechanism. In fact, scientists have moved their attention from the origin of electroweak symmetry breaking to the origin of the Higgs mass. Corrections to the Higgs mass from loops of virtual particles (quantum correction) are very large, and a Higgs boson of the mass of 125 GeV would be very unnatural. This is illustrated below, the correction of Higgs mass from Ref. [33]:

$$\delta M_h^2 = -\frac{\lambda_f^2}{8\pi^2}\Lambda_{\mathbf{UV}}^2 + ... \tag{2.43}$$

$\Lambda_{\mathbf{UV}}$ is the Ultra-violent (UV) momentum cut-off which regulates the loop integral. Eq. (2.43) shows that the correction increases quadratically with the value of the cut off. In the other words, the bare mass of Higgs has to be of the order of the cut off in order to cancel such values to reproduce the discovery of 125 GeV Higgs boson as ($M_{h_{\text{bare}}}^2 + \delta M_h^2 \approx 100$ GeV) - this is called the "hierarchy problem". On the other hand, fermion masses do not have such quadratic corrections to their bare masses. A non-zero fermion mass breaks the chiral symmetry transformation of fermion fields. A broken chiral symmetry generates a fermion mass which is proportional to quantum correction, preserves naturalness [34]. One of possible solutions for the hierarchy problem is from Supersymmetry (SUSY) [33; 35]. In SUSY models, the SUSY partners of the SM particles introduce cancellations of the quadratic terms from quantum loops, and the corrections are of the order of the mass the SUSY particles. SUSY models require at least two scalar doublets, thus leading to more physical Higgs bosons.

2.4 Electroweak interaction

The electromagnetic and weak interaction are unified by Glashow, Salam and Weinberg into the GSW model [36; 37; 38]. Low energy processes are good enough for describing the modern electroweak theory [39; 40]. The experimental facts (i.e. $\mu^- \to e^- \bar{\nu}_e \nu_\mu$, β decay, $\pi^- \to \ell^- \bar{\nu}$, $\Delta S = 1$ transitions, etc.) could be described by an effective Hamiltonian:

$$\mathcal{H}_{\text{effective}} = \frac{G_f}{2} J^\mu J_\mu \tag{2.44}$$

where G_f is the Fermi constant.

The charged weak currents can be written (for example, lepton generations, $\psi_L = \begin{pmatrix} \nu \\ \ell \end{pmatrix}_L$):

$$J_\mu^+ = \bar{\psi}_L \gamma_\mu \tau_+ \psi_L \tag{2.45}$$

$$J_\mu^- = \bar{\psi}_L \gamma_\mu \tau_- \psi_L \text{ with } \tau_\pm = \frac{\sigma_1 \pm i\sigma_2}{2}. \tag{2.46}$$

where $\tau_+ = \begin{pmatrix} 0 & 1 \\ 0 & 0 \end{pmatrix}$, $\tau_- = \begin{pmatrix} 0 & 0 \\ 1 & 0 \end{pmatrix}$ and determined from Pauli matrices σ_1 and σ_2.

A $SU(2)$ neutral current for weak current will be:

$$J_\mu^3 = \bar{\psi}_L \gamma_\mu \frac{1}{2} \sigma_3 \psi_L. \quad (= \frac{1}{2} \bar{\nu} L \gamma_\mu \nu_L - \frac{1}{2} \bar{\ell} L \gamma_\mu \ell_L) \tag{2.47}$$

In addition, the neutral electromagnetic current is included which is extended with a neutral $U(1)_Y$ singlet J_μ^Y that acts on both LH and RH singlet fermions:

$$J_\mu^Y = \bar{\psi} \gamma_\mu Y \psi \text{ with } J_\mu^{\text{EM}} = J_\mu^3 + \frac{1}{2} J_\mu^Y \tag{2.48}$$

where Y is the hypercharge operator which generates the $U(1)_Y$ symmetry. J_μ^{EM} is the electromagnetic current in Quantum Electric Dynamics (QED).

The electroweak interaction currents couple to vector bosons as electromagnetic interaction couples to photon. The full form will be:

$$J_{\text{EW}}^{\text{GSW}} = -ig(J^i)^\mu W_\mu^i - ig'(J^Y)^\mu B_\mu \tag{2.49}$$

where W_μ^i, $i = 1, 2, 3$ are the $SU(2)_L$ isotriplet vector fields with coupling g to the weak isospin current J_μ^i and B_μ is the $U(1)_Y$ single vector field with the coupling $\frac{g'}{2}$ to the hypercharge current J_μ^Y. The mixing of them will give the physical charged and neutral gauge fields where charged bosons are from $W_\mu^\pm = \frac{W_\mu^1 \mp W_\mu^2}{\sqrt{2}}$ and neutral bosons from

$A_\mu = B_\mu \cos\theta_W + W^3_\mu \sin\theta_W$, $Z_\mu = -B_\mu \sin\theta_W + W^3_\mu \cos\theta_W$ as Eq. (2.27,2.33). θ_W is the Weinberg angle.

Using the above neutral formulas, one can write neutral electroweak current:

$$\begin{aligned} J^{\mathrm{NC}} &= -ig(J^3)^\mu W_\mu - i\frac{g'}{2}(J^Y)^\mu B_\mu \\ &= -i\left(g\sin\theta_W (J^3)^\mu + g'\cos\theta_W \frac{(J^Y)^\mu}{2}\right) A_\mu \\ &\quad -i\left(g\cos\theta_W (J^3)^\mu - g'\sin\theta_W \frac{(J^Y)^\mu}{2}\right) Z_\mu \end{aligned} \tag{2.50}$$

The first section with A_μ will be the electromagnetic interaction, so that section could match to electromagnetic current, $-i\,e\,(J^{\mathrm{EM}})^\mu A_\mu$:

$$\begin{aligned} e(J^{\mathrm{EM}})^\mu A_\mu &= e\left((J^3)^\mu + \frac{(J^Y)^\mu}{2}\right) A_\mu \\ e &= g\sin\theta_W = g'\cos\theta_W \end{aligned} \tag{2.51}$$

That is why $\tan\theta_W = \frac{g'}{g}$. The second section of Eq. (2.50) with Z_μ will be the neutral current interaction which can be rewritten as (without $-i$):

$$\frac{g}{\cos\theta_W}\left((J^3)^\mu - \sin^2\theta_W (J^{\mathrm{EM}})^\mu\right) \tag{2.52}$$

Thus, for charge electroweak current (CEC), $W^\pm$ with fermions ψ_f, we will have :

$$\mathcal{L}^{\mathrm{Interaction}}_{\mathrm{CEC}} = -\frac{g}{\sqrt{2}}(J^\pm)^\mu W^\pm_\mu = -\frac{g}{\sqrt{2}}\bar{\psi}_f\left[\gamma^\mu \frac{1}{2}(1-\gamma^5)\right]\psi_f W^\pm \tag{2.53}$$

where $\frac{1}{2}(1-\gamma^5)$ is the LH projection operator. γ^5 equals to $i\gamma^0\gamma^1\gamma^2\gamma^3$ which are from Eq. (2.2).

The neutral electroweak current (NEC), Z with fermions ψ_f will be:

$$\begin{aligned} \mathcal{L}^{\mathrm{Interaction}}_{\mathrm{NEC}} &= -\frac{g}{\cos\theta_W}(J^{\mathrm{NC}})^\mu Z_\mu \\ &= -\frac{g}{\cos\theta_W}\gamma^\mu\bar{\psi}_f\left[\frac{1}{2}(1-\gamma^5)T^3 - \sin^2\theta_W Q\right]\psi_f Z \end{aligned} \tag{2.54}$$

where T^3 is the third component of weak isospin and the Q is the electric charge.

2.5 CP-violation in the SM

CP transformation is a transformation of both charge-conjugation (C) and parity (P). Charge-conjugation (C) is a flip transformation between particle and anti-particle (it changes particle to anti-particle, and vice versa). The parity transformation acts as a mirror on an object, and multiplies the position coordinates by minus one. "CP-symmetry" means the combined transformation of C and P leaves the Lagrangian invariant. On the other hand, "CP-violation" means that the Lagrangian is not invariant under the CP transformation. C and P are separately conserved in strong and electromagnetic interactions, but are not preserved individually in weak interactions. However, the combined CP transformation is very nearly conserved in weak interactions, and its violation in nature (in Kaon decays) was observed for the first time in 1964. CP violation is a necessary ingredient for a matter-antimatter asymmetry in the universe. For exact CP-symmetry, matter and antimatter would be produced in the same amounts in the early universe, but there must have been more slightly more matter produced than antimatter [41; 42; 43]. In fact, the observation of matter more than anti-matter means that CP is not a good symmetry of the Lagrangian, and thus CP violation is a necessary ingredient for a matter-antimatter asymmetry in the universe. CP-violation in SM arises from the intergenerational mixing among the quarks and among the neutrinos.

Firstly, we recall the Yukawa interactions between quarks and Higgs in Eq. (2.40). The mass terms can be written as:[1]

$$\mathcal{L}_{\text{Yukawa}} = -m_{u_{ij}} \bar{u}_{i,L} u_{j,R} - m_{d_{ij}} \bar{d}_{i,L} d_{j,R} + h.c \tag{2.55}$$

The mass matrices $(m_{u_{ij}}, m_{d_{ij}})$ are diagonalised by the transformation of left-handed and right-handed quark fields through the unitary matrices:

$$u_{i,L} = P^u_L u^{'}_L \quad u_{i,R} = P^u_R u^{'}_{i,R} \tag{2.56}$$

$$d_{i,L} = P^d_L d^{'}_L \quad d_{i,R} = P^d_R d^{'}_{i,R} \tag{2.57}$$

where $u_{i,L/R}, d_{i,L/R}$ are representations in the weak basis and $u^{'}_{i,L/R}, d^{'}_{i,L/R}$ are mass eigenstates. The matrices of $P^u_{L/R}, P^d_{L/R}$ are used to diagonalise the mass matrices of

[1] Here u and d terms represent up-type and down-type quarks rather than up and down quarks alone for simplicity.

the quarks by below [44]:

$$m_{u_{ij}} \rightarrow (P_L^u)^\dagger m_{u_{ij}} P_R^u = \begin{pmatrix} m_u & 0 & 0 \\ 0 & m_c & 0 \\ 0 & 0 & m_t \end{pmatrix} \tag{2.58}$$

$$m_{d_{ij}} \rightarrow (P_L^d)^\dagger m_{d_{ij}} P_R^d = \begin{pmatrix} m_d & 0 & 0 \\ 0 & m_s & 0 \\ 0 & 0 & m_b \end{pmatrix} \tag{2.59}$$

Now we take the quark-charged current processes which are an interaction between the left-handed quark fields and the gauge boson $W^\pm$. These can be written as below:

$$\mathcal{L}_{\text{CC}} = -\frac{G_f}{\sqrt{2}}[\bar{u}_{i,L}\gamma^\mu d_{i,L} W_\mu^+ + \bar{d}_{i,L}\gamma^\mu u_{i,L} W_\mu^-] + h.c \tag{2.60}$$

and mass eigenstates can be written as:

$$\mathcal{L}_{\text{CC}} = -\frac{G_f}{\sqrt{2}}[\bar{u}'_{i,L}\gamma^\mu (P_L^u)^\dagger P_L^d d'_{i,L} W_\mu^+ + \bar{d}'_{i,L}\gamma^\mu (P_L^d)^\dagger P_L^u u'_{i,L} W_\mu^-] + h.c \tag{2.61}$$

The terms $(P_L^u)^\dagger P_L^d$ and $(P_L^d)^\dagger P_L^u$ are defined as Cabibbo-Kobayshi-Maskawa matrix (V_{CKM}) and its conjugate (V_{CKM}^*) respectively. For three family of quarks, the matrix is defined by a unitary 3×3 representation form as:[2]

$$V_{\text{CKM}} = \begin{pmatrix} |V_{ud}| \approx 0.97 & |V_{us}| \approx 0.22 & |V_{ub}| \approx 0.0038 \\ |V_{cd}| \approx 0.22 & |V_{cs}| \approx 0.98 & |V_{cb}| \approx 0.041 \\ |V_{td}| \approx 0.008 & |V_{ts}| \approx 0.038 & |V_{tb}| \approx 1.00 \end{pmatrix} \tag{2.62}$$

This unitary 3×3 CKM matrix (V_{CKM}) is parametrised by three mixing angles $\theta_{12,13,23}$ and one CP-violation phase δ_{13} (which are responsible for quark flavour changing processes) from Ref. [45]:

$$V_{\text{CKM}} = \begin{pmatrix} c_{12}c_{13} & s_{12}s_{13} & s_{13}e^{-i\delta_{13}} \\ -s_{12}s_{23} - c_{12}s_{23}s_{13}e^{i\delta_{13}} & c_{12}c_{23} - s_{12}s_{23}s_{13}e^{i\delta_{13}} & s_{23}s_{13} \\ s_{12}s_{23} - c_{12}c_{23}s_{13}e^{i\delta_{13}} & -c_{12}s_{23} - s_{12}c_{23}s_{13}e^{i\delta_{13}} & c_{23}c_{13} \end{pmatrix} \tag{2.63}$$

where s_{ij}, c_{ij} represent the sine and cosine of the three mixing angles of $\theta_{12,13,23}$. The above CKM matrix using Wolfstein parameterization could show the famous unitarity triangle as Fig. 2.3 from unitarity relationship: $V_{ud}V_{ub}^* + V_{cd}V_{cb}^* + V_{td}V_{tb}^* = 0$. In Wolfstein parameterization, $S_{12} = \lambda$, $s_{13}e^{i\delta} = A\lambda^3(\rho + i\eta)$, $S_{23} = A\lambda^2$ ensure phase independent convention of $\bar{\rho} + i\bar{\eta}$ to be $-\frac{V_{ud}V_{ub}^*}{V_{cd}V_{cb}^*}$ (the left side of the unitarity triangle).

The CP-violation from these quarks was first observed in the decays of neutral Kaon [46]. CP-violation has also been observed in the B mesons and D mesons [47; 48; 49].

[2] Values of V_{ij} in Eq. (2.62) are taken from [3].

Additionally, CP violation could also manifest itself in the oscillations of neutrinos, which was first pointed out by Pontecorvo-Maki-Nakagawa-Sakata (PMNS) matrix [50]. Leptogenesis [51] would require CP-violation in the lepton sector [52].

However, the observed matter-antimatter asymmetry cannot be explained from the sources of CP-violation in the SM [53], and thus additional sources of CP violation are needed (and are often provided in models beyond the SM).

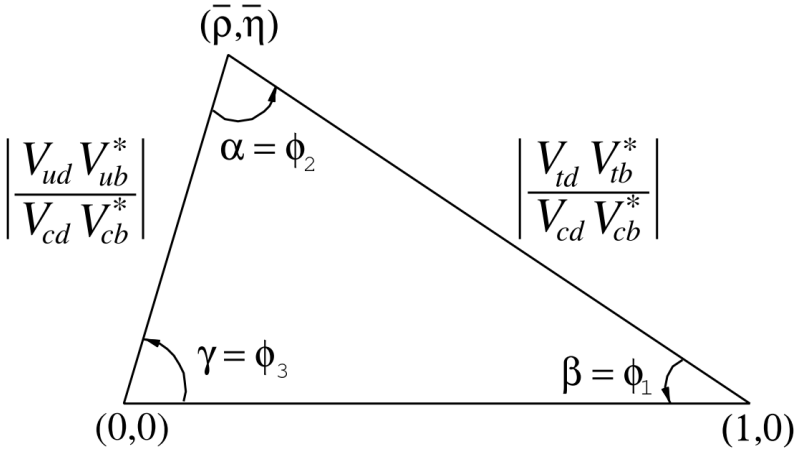

FIGURE 2.3: The sketch of the unitarity triangle based on CKM matrix elements. $\bar{\rho}, \bar{\eta}$ are defined related to Wolfstein parameters A, ρ, η, λ. This figure is taken from Fig. 12.1 of [3].

2.6 Motivation of BSM physics and MHDM

Although the SM is a theory with a very good precision agreement with experimental data, there are still several unsolved problems that cannot be explained in the SM. The gravitational force is not included due to the difficulty of the renormalisability of gravitation [54]. Others include: Neutrino oscillations (the evidence of neutrinos being massive) [55; 56], Dark Matter (DM) (the observation that galaxy rotation velocities are inconsistent with its distance from the centre) [57; 58], CP violation (the discovery of the electroweak interaction violating the CP-symmetry.) [59; 60], baryon-asymmetry (the discrepancy of number of particles and anti-particles in the Universe) [41; 61; 62], the fine-tuning problem (unnaturalness of Higgs mass) [63] and more. Hence the SM requires needs to be extended to accommodate and explain these experimental observations, in other words, theories of "beyond the Standard Model" (BSM).

One possibility is to extend the scalar sector. In the SM it is assumed that there is only a single Higgs doublet, but it is possible that this minimal structure is not realised in nature. The existence of a nonminimal Higgs sector is still an open question. In a Multi-Higgs Doublet Model (MHDM) such as the 2HDM and 3HDM, the explanation of several unsolved problems could be possible. For example, there could be a relationship between the SM fermion flavour mixing and 2HDM structure [64] which could explain the observed pattern of the flavour mixing. In addition, a particular 3HDM called the 'Inert 3HDM' could give rise to a large First-Order electroweak phase transition (EWPT) [65], which is not possible in the SM with one Higgs doublet. The reason is that the Higgs mass would be much lighter than the recent data within the SM EWPT. The contribution of Higgs trilinear self-coupling from extra Higgs bosons would allow electroweak baryogenesis occur to understand the asymmetry of the Universe [66]. Moreover, a scalar DM candidate could be provided in the 'Inert 3HDM' [67; 68; 69]. Furthermore, since the sources of CP-violation in SM are not large enough for a baryon asymmetry in the universe it is expected that any model of BSM will provide additional sources of CP violation. For a general MHDM, the scalar doublets could supply CP phases in the scalar potential, which will contain more free (complex) parameters. In a general 3HDM scenario, the CP-violation could manifest itself in the neutral and charged scalar sectors. In this thesis, we will mainly focus on these two extended scalar models, 2HDM and 3HDM.

Chapter 3

2-Higgs-doublets model (2HDM)

3.1 Overview

A simplified model which extends the particle content beyond the SM is called the 2HDM. In this model an additional SU(2) scalar doublet is added to the Lagrangian of the SM. One of the motivations for such a model comes from the particle content. In the SM there are three generations of fermions (which appear in the model as left-handed isospin doublets and right-handed isospin singlets) but only one scalar isospin doublet is assumed. In fact, it is not necessary that there is only one scalar sector in nature since SSB can be implemented with two or more scalar doublets. In addition to the above there is other motivations for 2HDM. Perhaps the best motivation comes from SUSY. In the Minimal Supersymmetric Standard Model (MSSM) [33], the fermions reside in chiral multiplets and a single Higgs scalar cannot possibly couple to opposite chirality multiplets in the Lagrangian. In order to give masses for seperate flavours spontaneously, two scalar fields are required. Hence at least two scalar doublets are necessary in order to give mass to different flavour fermions.

Another motivation is from gauge anomaly. In SM, the accidental chiral symmetry of certain loop diagrams (e.g. one-loop triangle Feynman diagrams with three fermions in the loop) prevents a complete cancellation of quarks and leptons contributions. For SUSY/MSSM, the same chiral mechanism affects the extra particles (e.g Higgsino), which generate terms that break the gauge symmetry. Thus, an extension of single scalar doublet to a pair of scalar doublets solves the problem and removes the anomaly [33]. One more motivation comes from the baryon-asymmetry of the Universe. The SM does not provide a sufficient amount of CP-violating phases, and additional sources of CP-violation could arise from the scalar potential (which will have many more parameters than the scalar potential for one scalar doublet). Baryogenesis at electroweak scale could possibly be testable (e.g flavour changing of Higgs couplings [70]) .

In this chapter we will describe the model structure of four 2HDMs. We will list the Yukawa structures of each model because this will become the basis of the 3HDM when we investigate the phenomenology of light charged Higgs in chapter 4.

3.2 Scalar potential of 2HDM

At tree level, the constraining effect of one parameter, (ρ) is important to investigate [71] and is described by below:

$$\rho = \frac{\sum_{i=1}^{n}[I_i(I_i+1) - \frac{1}{4}Y_i^2]v_i}{\sum_{i=1}^{n}\frac{1}{2}Y_i^2 v_i} \tag{3.1}$$

In Eq. (3.1), number of n scalar multiplets ϕ_i, each has weak isospin I_i, vacuum expectation values v_i and Y_i is the specific Hypercharge number. Measurements of the parameter ρ are very close, and any scalar sector that is composed of Higgs doublets and singlets will have $\rho = 1$ at tree level [72]. Other representations will cause deviation from $\rho = 1$, e.g. a single $I = 1$ triplet of $SU(2)$ scalar with $Y = \pm 2$ is satisfied while an additional $I = 1$ triplet of $SU(2)$ scalar with $Y = \pm 2$ will drops the parameter ρ below 1.

Another constraint on any extension of the scalar sector comes from flavour mixing. In the SM, the Higgs fermion couplings and fermion matrices are automatically diagonalised [73] and this property eliminates flavour changing neutral currents (FCNC) at tree level. Without such suppression, tree level FCNC currents would be present, and have not been observed in nature. If such FCNCs are present then they must be either absent or suppressed below experimental sensitivity. Several ways have been introduced to explain the absence of FCNCs. One way is to require an alignment in flavour space of the Yukawa couplings of the two scalar doublet e.g. the Aligned 2HDM [74]. Another interesting way was introduced by Sheldon L. Glashow and Steven Weinberg [75] and is called "Natural Flavour Conservation" (NFC). In this case, a discrete Z_2 symmetry is imposed such that only one field of Higgs doublet couples to a single type of fermion, and leads to four distinct versions of the 2HDM (which differ only in the Yukawa interactions).

The most general form of the gauge invariant scalar potential for the 2HDM can be taken from [21; 22; 76], which contains two complex $Y = 1, SU(2)_L$ doublet scalar fields:

$$\begin{aligned} V &= m_{11}^2\Phi_1^2 + m_{22}^2\Phi_2^2 - m_{12}^2\Phi_1^\dagger\Phi_2 - m_{12}^2\Phi_2^\dagger\Phi_1 \\ &+ \frac{1}{2}\lambda_1(\Phi_1^\dagger\Phi_1)^2 + \frac{1}{2}\lambda_2(\Phi_2^\dagger\Phi_2)^2 + \lambda_3(\Phi_1^\dagger\Phi_1)(\Phi_2^\dagger\Phi_2) \\ &+ \lambda_4(\Phi_1^\dagger\Phi_2)(\Phi_2^\dagger\Phi_1) + \frac{1}{2}\lambda_5(\Phi_1^\dagger\Phi_2)^2 + \frac{1}{2}\lambda_5(\Phi_2^\dagger\Phi_1)^2 \\ &+ \lambda_6(\Phi_1^\dagger\Phi_1)(\Phi_1^\dagger\Phi_2) + \lambda_6(\Phi_1^\dagger\Phi_1)(\Phi_2^\dagger\Phi_1) \\ &+ \lambda_7(\Phi_2^\dagger\Phi_2)(\Phi_1^\dagger\Phi_2) + \lambda_7(\Phi_2^\dagger\Phi_2)(\Phi_2^\dagger\Phi_1) \end{aligned} \tag{3.2}$$

The two Higgs doublets are defined as below ($i = 1, 2$) where $\tilde{\Phi}_i$ are the isospin conjugates of Φ_i:

$$\Phi_i = \begin{pmatrix} \phi_i^+ \\ (v_i + \phi_i^0 + i\eta_i)/\sqrt{2} \end{pmatrix}, \tilde{\Phi}_i = i\sigma_2\phi_i^* = \begin{pmatrix} (v_i + \phi_i^0 - i\eta_i)/\sqrt{2} \\ -\phi_i^- \end{pmatrix} \tag{3.3}$$

The 2HDM Lagrangian contains eight real scalar fields. After SSB, three of the Goldstone states will be eaten and become the longitudinal modes of the $W^\pm$ and Z bosons. That leaves five physical states: $H^\pm$ (the charged Higgs pair), and the three neutral Higgs bosons.

For general 2HDMs without tree-level FCNC, there are four possibilities. The different quark and lepton types couple with Φ_1, Φ_2 lead the natural flavour conservation has shown in Tab. (3.1). In type-I 2HDM, all right-handed (RH) quarks (up-,down-types) and RH lepton couple to only one doublet Φ_2. Only RH up-type quark (charge, $Q = \frac{2}{3}$) couples to Φ_2 while others couple to Φ_1 in type-II. Type-I can be enforced with $\Phi_1 \to -\Phi_1$ discrete symmetry, whereas type-II can be enforced with $\Phi_1 \to -\Phi_1$, d-quark $\to -d$-quark discrete symmetry. Type-lepton specific requires all RH quark couple to Φ_2 while RH lepton couples to Φ_1. The last possibility of 2HDM is then called type-flipped and have the condition which RH up-type quark and leptons couple to Φ_2, and RH down-type quark (charge, $Q = -\frac{1}{3}$) couples to Φ_1.

It is convenient to define VEVs:

$$v_1 = v\cos\beta, v_2 = v\sin\beta \tag{3.4}$$

with the relation $v^2 = v_1^2 + v_2^2 = (\sqrt{2}G_f)^{-1/2} = 246^2\,\mathrm{GeV}^2$. By taking the VEV to be real, the minimisation conditions for the potential are:

$$\begin{aligned}
\frac{\partial V}{\partial \Phi_1} &= 0, \frac{\partial V}{\partial \Phi_2} = 0, \quad \text{take} \quad \Phi_1 = <\Phi_1>, \Phi_2 = <\Phi_2> \\
m_{11}^2 &= Re(m_{12}^2)\tan\beta - \frac{\lambda_1}{2}v_1^2 - \frac{\lambda_{345}}{2}v_2^2 - \frac{1}{2}[3Re(\lambda_6)v_1v_2 + Re(\lambda_7)v_2^2\tan\beta] \\
m_{22}^2 &= Re(m_{12}^2)\cot\beta - \frac{\lambda_2}{2}v_2^2 - \frac{\lambda_{345}}{2}v_1^2 - \frac{1}{2}[Re(\lambda_6)\cot\beta v_1^2 + 3Re(\lambda_7)v_1^2] \qquad (3.5)
\end{aligned}$$

Here $\lambda_{345} = \lambda_3 + \lambda_4 + Re(\lambda_5)$. The above equations yield the VEVs of the doublets $\Phi_{1,2}$, which can then be taken as input parameters instead of m_{11} and m_{22}. The CP-even, CP-odd and charged Higgs mass squared matrix with corresponding $m_{ii}^2, m_{ij}^2, \lambda_i$ can be obtained as follows:

$$[M^2_{H_{\text{CP-even}}}] = \begin{pmatrix} \frac{\partial^2 V_0}{\partial\phi_1^0\partial\phi_1^0} & \frac{\partial^2 V_0}{\partial\phi_1^0\partial\phi_2^0} \\ \frac{\partial^2 V_0}{\partial\phi_2^0\partial\phi_1^0} & \frac{\partial^2 V_0}{\partial\phi_2^0\partial\phi_2^0} \end{pmatrix} \qquad (3.6)$$

$$[M^2_{H_{\text{CP-odd}}}] = \begin{pmatrix} \frac{\partial^2 V_0}{\partial\eta_1\partial\eta_1} & \frac{\partial^2 V_0}{\partial\eta_1\partial\eta_2} \\ \frac{\partial^2 V_0}{\partial\eta_2\partial\eta_1} & \frac{\partial^2 V_0}{\partial\eta_2\partial\eta_2} \end{pmatrix} \qquad (3.7)$$

$$[M^2_{H^\pm}] = \begin{pmatrix} \frac{\partial^2 V_0}{\partial\phi_1^+\partial\phi_1^-} & \frac{\partial^2 V_0}{\partial\phi_1^+\partial\phi_2^-} \\ \frac{\partial^2 V_0}{\partial\phi_2^+\partial\phi_1^-} & \frac{\partial^2 V_0}{\partial\phi_2^+\partial\phi_2^-} \end{pmatrix} \qquad (3.8)$$

The potential V_0 is taken by inserting Eq. (3.5) into Eq. (3.2) and the squared mass of CP-even/odd and the charged Higgs can be calculated by finding the eigenvalues of each mass squared matrix.

$$\begin{aligned}
M_A^2 &= -v^2\lambda_5 + (m_{12}^2 - \frac{v^2\lambda_6}{2})\cot\beta + (m_{12}^2 - \frac{v^2\lambda_7}{2})\tan\beta \qquad (3.9) \\
M_{H^\pm}^2 &= M_A^2 + \frac{1}{2}v^2(-\lambda_4 + \lambda_5) \qquad (3.10)
\end{aligned}$$

The two CP-even Higgs states mix via the following squared-mass matrix:[1]

$$\mathcal{M}^2 = m_A^2 \begin{pmatrix} s_\beta^2 & -s_\beta c_\beta \\ -s_\beta c_\beta & c_\beta^2 \end{pmatrix} + \mathcal{B}^2 \qquad (3.11)$$

where

$$\mathcal{B}^2 = v^2 \begin{pmatrix} \lambda_1 c_\beta^2 + 2\lambda_6 s_\beta c_\beta + \lambda_5 s_\beta^2 & (\lambda_3+\lambda_4)s_\beta c_\beta + \lambda_6 c_\beta^2 + \lambda_7 s_\beta^2 \\ (\lambda_3+\lambda_4)s_\beta c_\beta + \lambda_6 c_\beta^2 + \lambda_7 s_\beta^2 & \lambda_2 s_\beta^2 + 2\lambda_7 s\beta c_\beta + \lambda_5 c_\beta^2 \end{pmatrix} \qquad (3.12)$$

[1] Here, we used the short form, $s_\beta = \sin\beta, c_\beta = \cos\beta$.

Model	$u-$quark	$d-$quark	charged-lepton
Type-I	Φ_2	Φ_2	Φ_2
Type-II	Φ_2	Φ_1	Φ_1
Type-Lepton specific	Φ_2	Φ_2	Φ_1
Type-Flipped	Φ_2	Φ_1	Φ_2

TABLE 3.1: Four NFC 2HDM models. By convention, up-type quark always couple to Φ_2.

Thus, the physical mass eigenstates can be defined as:

$$\begin{aligned} H &= \sqrt{2}[(\mathrm{Re}\Phi_1^0 - v_1)c_\alpha + (\mathrm{Re}\Phi_2^0 - v_2)s_\alpha] \\ h &= \sqrt{2}[-(\mathrm{Re}\Phi_1^0 - v_1)s_\alpha + (\mathrm{Re}\Phi_2^0 - v_2)c_\alpha] \end{aligned} \tag{3.13}$$

One can diagonalise the neutral states by introducing a mixing angle α: [2]:

$$\begin{pmatrix} M_H^2 & 0 \\ 0 & M_h^2 \end{pmatrix} = \begin{pmatrix} c_\alpha & s_\alpha \\ -s_\alpha & c_\alpha \end{pmatrix} \begin{pmatrix} M^2_{11_{\mathrm{even}}} & M^2_{12_{\mathrm{even}}} \\ M^2_{12_{\mathrm{even}}} & M^2_{22_{\mathrm{even}}} \end{pmatrix} \begin{pmatrix} c_\alpha & -s_\alpha \\ s_\alpha & c_\alpha \end{pmatrix}$$

$$= \begin{pmatrix} M_{11}^2 c_\alpha^2 + 2M_{12}^2 c_\alpha s_\alpha + M_{22}^2 s_\alpha^2 & M_{12}^2(c_\alpha^2 - s_\alpha^2) + (M_{22}^2 - M_{11}^2)s_\alpha c_\alpha \\ M_{12}^2(c_\alpha^2 - s_\alpha^2) + (M_{22}^2 - M_{11}^2)s_\alpha c_\alpha & M_{11}^2 s_\alpha^2 - 2M_{12}^2 c_\alpha s_\alpha + M_{22}^2 c_\alpha^2 \end{pmatrix} \tag{3.14}$$

With the choice of $M_H >> M_h$, the mass eigenstates will be equal to:

$$M_{h,H}^2 = \frac{1}{2}\left[M_{11}^2 + M_{22}^2 \mp \sqrt{(M_{11}^2 - M_{22}^2)^2 + 4(M_{12}^2)^2}\right] \tag{3.15}$$

The mixing angle (α) between two CP-even physical states h, H will be:

$$\begin{aligned} \sin 2\alpha &= \frac{2(M_{12}^2)^2}{(M_{11}^2 - M_{22}^2)^2 + 4(M_{12}^2)^2} \\ \cos 2\alpha &= \frac{M_{11}^2 - M_{22}^2}{(M_{22}^2 - M_{11}^2)^2 + 4(M_{12}^2)^2} \end{aligned} \tag{3.16}$$

with $-\pi/2 \leq \alpha \leq \pi/2$.

[2]Here, $M^2_{11,12,22} = M^2_{11_{\mathrm{even}},12_{\mathrm{even}},22_{\mathrm{even}}}$.

	Type-I	Type-II	X (Lepton-specific)	Y (Flipped)
g_h^u	$\cos\alpha / \sin\beta$	$\cos\alpha / \sin\beta$	$\cos\alpha / \sin\beta$	$\cos\alpha / \sin\beta$
g_h^d	$\cos\alpha / \sin\beta$	$-\sin\alpha / \cos\beta$	$\cos\alpha / \sin\beta$	$-\sin\alpha / \cos\beta$
g_h^ℓ	$\cos\alpha / \sin\beta$	$-\sin\alpha / \cos\beta$	$-\sin\alpha / \cos\beta$	$\cos\alpha / \sin\beta$
g_H^u	$\sin\alpha / \sin\beta$	$\sin\alpha / \sin\beta$	$\sin\alpha / \sin\beta$	$\sin\alpha / \sin\beta$
g_H^d	$\sin\alpha / \sin\beta$	$\cos\alpha / \sin\beta$	$\sin\alpha / \sin\beta$	$\cos\alpha / \sin\beta$
g_H^ℓ	$\sin\alpha / \sin\beta$	$\cos\alpha / \sin\beta$	$\cos\alpha / \sin\beta$	$\sin\alpha / \sin\beta$
g_A^u	$\cot\beta$	$\cot\beta$	$\cot\beta$	$\cot\beta$
g_A^d	$-\cot\beta$	$\tan\beta$	$-\cot\beta$	$\tan\beta$
g_A^ℓ	$-\cot\beta$	$\tan\beta$	$\tan\beta$	$-\cot\beta$
$g_{H^\pm}^u$	$\cot\beta$	$\cot\beta$	$\cot\beta$	$\cot\beta$
$g_{H^\pm}^d$	$-\cot\beta$	$\tan\beta$	$-\cot\beta$	$\tan\beta$
$g_{H^\pm}^\ell$	$-\cot\beta$	$\tan\beta$	$\tan\beta$	$-\cot\beta$

TABLE 3.2: Yukawa couplings with fermion types (u, d, ℓ) and Higgs bosons $(h, H, A, H^\pm)$ in the four types of 2HDM with NFC

3.3 Alignment limit of 2HDM

The scenario of which one of the neutral Higgs mass eigenstates aligns to the vacuum expectation value will be an important limit [77; 78]. The observed Higgs boson reduced coupling to gauge boson approximates to 1 at the LHC tends to be a special condition for 2HDM [79]. Thus, the participation of increased accuracy of the LHC data will constrain the 2HDM which can provide SM-like Higgs particles within specific condition. The condition will be called the *"alignment limit"* for 2HDM. The characteristic of lightest Higgs in 2HDM couples to gauge boson like SM Higgs can be easily achieved from the decoupling limit in most of the 2HDM scenarios.[3] Alternatively, this *"alignment limit"* condition of 2HDM can provide additional mass spectrum spaces which one or more non-SM like Higgs to be light (or even lighter than the SM like Higgs).

From the kinetic term of the Higgs in SM, we recall the gauge boson and Higgs coupling relation [80]:

$$\mathcal{L}_{\text{Kinetic}} = \sum_{k=1}^{2} |D_\mu \Phi_k|^2 \ni \frac{g^2}{2} W_\mu^+ W^{\mu-} (v\, h_{\text{SM}}) = \frac{g^2 v}{2} W_\mu^+ W^{\mu-} (\frac{1}{v} \sum_{k=1}^{2} v_k h_k) \tag{3.17}$$

Here $(\frac{1}{v}\sum_{k=1}^{2} v_k h_k) = H_0$ will be compatible with the SM Higgs tree-level coupling. Again, g is the $SU(2)_L$ coupling constant. However, H_0 is not guaranteed to be a physical mass eigenstate. Thus, the alignment will be occur when this H_0 state aligns with the CP-even h_1 state. The relationship between H_0 and its orthogonal combination $\mathcal{R}$

[3] Decoupling limit is the scenario where all non-SM like neutral Higgs particles in the 2HDM mass spectrum are much heavier than the lightest SM-like Higgs. See in Ref. [76] for more details.

can be obtained from CP-even scalar states, h_1 and h_2:

$$\begin{pmatrix} H_0 \\ \mathcal{R} \end{pmatrix} = \mathcal{O}_\beta \begin{pmatrix} h_1 \\ h_2 \end{pmatrix} = \begin{pmatrix} \cos\beta & \sin\beta \\ -\sin\beta & \cos\beta \end{pmatrix} \begin{pmatrix} h_1 \\ h_2 \end{pmatrix} \tag{3.18}$$

Where β is the parameter which mentioned in Eq. (3.4). On the other hand, the physical mass eigenstates, h and H are obtained from another rotation matrix which is relate to the mixing angle α as Eq. (3.14):

$$\begin{pmatrix} h \\ H \end{pmatrix} = \begin{pmatrix} \cos\alpha & \sin\alpha \\ -\sin\alpha & \cos\alpha \end{pmatrix} \begin{pmatrix} h_1 \\ h_2 \end{pmatrix} \tag{3.19}$$

Then, plug the Eq. (3.18) into above:

$$\begin{pmatrix} h \\ H \end{pmatrix} = \mathcal{O}_\beta \mathcal{O}_\alpha^T \begin{pmatrix} H_0 \\ \mathcal{R} \end{pmatrix} = \begin{pmatrix} \cos(\alpha-\beta) & \sin(\alpha-\beta) \\ -\sin(\alpha-\beta) & \cos(\alpha-\beta) \end{pmatrix} \begin{pmatrix} H_0 \\ \mathcal{R} \end{pmatrix} \tag{3.20}$$

In the case of the lightest CP-even physical h state matches H_0, one would have $\sin(\alpha-\beta) = 0$ in the relation of $h = \cos(\alpha-\beta)H_0 + \sin(\alpha-\beta)\mathcal{R}$. Thus, $\cos(\alpha-\beta) = 1$ and which gives $\alpha = \beta$. This scenario makes sure that the lightest CP-even Higgs in 2HDM matches to the SM-like Higgs and is the alignment limit for 2HDMs. On the hand, the heavier CP-even Higgs align to the SM-like Higgs requires the condition $\cos(\alpha-\beta) = 0$ (from the relationship $H = -\sin(\alpha-\beta)H_0 + \cos(\alpha-\beta)\mathcal{R}$). In this case, $\alpha - \beta = \frac{\pi}{2}$.[4]

[4] An important feature is required to be mentioned here. This second relation which the heavier CP-even Higgs aligns to the SM Higgs is only satisfied from Type-I and Type-X in 2HDM while Type-II and -Y (Flipped) is not allowed due to current exclusion limit in 2HDM [81].

3.4 Yukawa sector of 2HDM

The charged scalar Yukawa sector of the 2HDM can be taken from the general Yukawa sector in SM:

$$\mathcal{L}_{Y_{\rm SM}} = -g_i^L \bar{l}_{iR}\Phi^\dagger l_L^i - g_{ij}^d \bar{d'}_{iR}\Phi^\dagger u_L^j - g_{ij}^u \bar{u}_{iR}\tilde{\Phi}^\dagger u_L^i + \text{h.c} \tag{3.21}$$

where i and j are the flavour indices.

In the 2HDM with NFC there are four distinct models: type-I, type-II, X (Lepton specific), and Y (Flipped). The names for the latter two models are from after the year 2009, with different names (II′ and III for Y; I′ and IV for X) being used before then. The corresponding Yukawa couplings and mass eigenstates of the physical states from the two doublets are covered in Tab. (3.2). Taking the type-II 2HDM, the charged Higgs Yukawa sector is as follows:

$$\mathcal{L}_{Y_{\rm 2hdm}} = -g_i^L \bar{l}_{iR}\Phi_1^\dagger l_L^i - g_{ij}^d \bar{d'}_{iR}\Phi_1^\dagger u_L^j - g_{ij}^u \bar{u}_{iR}\tilde{\Phi}_2^\dagger u_L^i + \text{h.c} \tag{3.22}$$

The mass eigenstates are defined by:

$$\begin{aligned}
\begin{pmatrix} \phi_1^0 \\ \phi_2^0 \end{pmatrix} &= \begin{pmatrix} \cos\alpha & -\sin\alpha \\ \sin\alpha & \cos\alpha \end{pmatrix} \begin{pmatrix} h \\ H \end{pmatrix}, \\
\begin{pmatrix} \eta_1 \\ \eta_2 \end{pmatrix} &= \begin{pmatrix} \cos\beta & -\sin\beta \\ \sin\beta & \cos\beta \end{pmatrix} \begin{pmatrix} G^0 \\ A \end{pmatrix}, \\
\begin{pmatrix} \phi_1^+ \\ \phi_2^+ \end{pmatrix} &= \begin{pmatrix} \cos\beta & -\sin\beta \\ \sin\beta & \cos\beta \end{pmatrix} \begin{pmatrix} G^+ \\ H^+ \end{pmatrix}
\end{aligned} \tag{3.23}$$

We can also write the mass eigenstate in terms of each weak interaction state:

$$\begin{aligned}
\begin{pmatrix} G^0 \\ A \end{pmatrix} = \begin{pmatrix} \cos\beta & \sin\beta \\ -\sin\beta & \cos\beta \end{pmatrix} \begin{pmatrix} \eta_1 \\ \eta_2 \end{pmatrix} \rightarrow \\
G^0 = \cos\beta\eta_1 + \sin\beta\eta_2, A = \cos\beta\eta_2 - \sin\beta\eta_1
\end{aligned} \tag{3.24}$$

Then the Yukawa interaction of type-II Eq. (3.22) will be:

$$\begin{aligned}
\mathcal{L}_Y = -g_i^L \bar{l}_{iR} \left(\phi_1^-, (v_1 + \phi_1^0 - i\eta_1)/\sqrt{2} \right) \begin{pmatrix} v_{iL} \\ l_{iL} \end{pmatrix} \\
-g_{ij}^d \bar{d'}_{iR} \left(\phi_1^-, (v_1 + \phi_1^0 - i\eta_1)/\sqrt{2} \right) \begin{pmatrix} u_{jL} \\ d'_{jL} \end{pmatrix} \\
-g_{ij}^u \bar{u}_{iR} \left((v_2 + \phi_2^0 + i\eta_2)/\sqrt{2}, -\phi_2^+ \right) \begin{pmatrix} u_{iL} \\ d'_{iL} \end{pmatrix} + \text{h.c}
\end{aligned} \tag{3.25}$$

$$\begin{aligned}\mathcal{L}_Y = &-g_i^L \bar{l}_{iR} v_{iL} \phi_1^- - v_1/\sqrt{2} g_i^L \bar{l}_{iR} l_{iL} - \phi_1^0/\sqrt{2} g_i^L \bar{l}_{iR} l_{iL} + i\eta_1/\sqrt{2} g_i^L \bar{l}_{iR} l_{iL} \\ &-g_{ij}^d \bar{d'}_{iR} u_{jL} \phi_1^- - v_1/\sqrt{2} g_{ij}^d \bar{d'}_{iR} d'_{jL} - \phi_1^0/\sqrt{2} g_{ij}^d \bar{d'}_{iR} d'_{jL} + i\eta_1/\sqrt{2} g_{ij}^d \bar{d'}_{iR} d'_{jL} \\ &-v_2/\sqrt{2} g_i^u \bar{u}_{iR} u_{iL} - \phi_2^0/\sqrt{2} g_i^u \bar{u}_{iR} u_{iL} - i\eta_2/\sqrt{2} g_i^u \bar{u}_{iR} u_{iL} + g_i^u \bar{u}_{iR} d'_{iL} \phi_2^+ + \text{h.c}\end{aligned} \tag{3.26}$$

In Eq. (3.26), g_{ij}^d is not a diagonal matrix because d' is not a mass eigenstate. By introducing two unitary matrices P_R^d and P_L^d, we can diagonalise g_{ij}^d:

$$(P_L^d)_{ki}^\dagger g_{ij}^d P_{Rjl}^d = g_k^d \delta_{kl} \tag{3.27}$$

Then d'_{iR} and d'_{iL} will be transformed to:

$$d'_{iR} = (P_R^d)_{ik} d_{kR}, d'_{jL} = (P_L^d)_{jl} d_{lL} \tag{3.28}$$

Terms like $g_{ij}^d \bar{d'}_{iR} d'_{jL}$ will be equal to:

$$g_{ij}^d \bar{d'}_{iR} d'_{jL} = g_{ij}^d (P_R^d)_{ki}^\dagger \bar{d}_{kR} (P_L^d)_{jl} d_{lL} = (P_R^d)_{ki}^\dagger g_{ij}^d (P_L^d)_{jl} \bar{d}_{kR} d_{lL} = g_i^d \bar{d}_{iR} d_{iL} \tag{3.29}$$

Then using the definition of VEVs in Eq. (3.4) and one obtains

$$\begin{aligned} m_{li} &= \frac{g_i^L v_1}{\sqrt{2}} = \frac{g_i^L v \cos\beta}{\sqrt{2}}, g_i^L = \frac{\sqrt{2} m_{li}}{v \cos\beta}; \\ m_{di} &= \frac{g_i^d v_1}{\sqrt{2}} = \frac{g_i^d v \cos\beta}{\sqrt{2}}, g_i^d = \frac{\sqrt{2} m_{di}}{v \cos\beta}; \\ m_{ui} &= \frac{g_i^u v_2}{\sqrt{2}} = \frac{g_i^u v \sin\beta}{\sqrt{2}}, g_i^u = \frac{\sqrt{2} m_{ui}}{v \sin\beta} \end{aligned} \tag{3.30}$$

We plug Eq. (3.30) into Eq. (3.26) :

$$\begin{aligned} \mathcal{L}_Y = &- g_i^L \bar{l}_{iR} v_{iL} \phi_1^- - v_1/\sqrt{2} g_i^L \bar{l}_{iR} l_{iL} - \phi_1^0/\sqrt{2} g_i^L \bar{l}_{iR} l_{iL} + i\eta_1/\sqrt{2} g_i^L \bar{l}_{iR} l_{iL} \\ &- g_{ij}^d \bar{d'}_{iR} u_{jL} \phi_1^- - v_1/\sqrt{2} g_{ij}^d \bar{d'}_{iR} d'_{jL} - \phi_1^0/\sqrt{2} g_{ij}^d \bar{d'}_{iR} d'_{jL} + i\eta_1/\sqrt{2} g_{ij}^d \bar{d'}_{iR} d'_{jL} \\ &- v_2/\sqrt{2} g_i^u \bar{u}_{iR} u_{iL} - \phi_2^0/\sqrt{2} g_i^u \bar{u}_{iR} u_{iL} - i\eta_2/\sqrt{2} g_i^u \bar{u}_{iR} u_{iL} + g_i^u \bar{u}_{iR} d'_{iL} \phi_2^+ \\ &+ \text{h.c} \end{aligned} \tag{3.31}$$

$$\begin{aligned} = &- \frac{\sqrt{2} m_{li}}{v \cos\beta} \bar{l}_i \frac{1-\gamma_5}{2} v_{iL} \phi_1^- - m_{li} \bar{l}_{iR} l_{iL} - \frac{\phi_1^0 m_{li}}{v \cos\beta} \bar{l}_{iR} l_{iL} + i \frac{\eta_1 m_{li}}{v \cos\beta} \bar{l}_{iR} l_{iL} \\ &- \frac{\sqrt{2} m_{dj}}{v \cos\beta} V_{ij}^* \bar{d}_j \frac{1-\gamma_5}{2} u_i \phi_1^- - m_{di} \bar{d}_{iR} d_{iL} - \frac{\phi_1^0 m_{di}}{v \cos\beta} \bar{d}_{iR} d_{iL} + i \frac{\eta_1 m_{di}}{v \cos\beta} \bar{d}_{iR} d_{iL} \\ &+ \frac{\sqrt{2} m_{ui}}{v \sin\beta} V_{ij} \bar{u}_i \frac{1-\gamma_5}{2} d_j \phi_2^+ - m_{ui} \bar{u}_{iR} u_{iL} - \frac{\phi_2^0 m_{ui}}{v \sin\beta} \bar{u}_{iR} u_{iL} - i \frac{\eta_2 m_{ui}}{v \sin\beta} \bar{u}_{iR} u_{iL} \\ &+ \text{h.c} \end{aligned} \tag{3.32}$$

Here we define $V_{ij} = P_L^d$ and $V_{ij}^* = (P_L^d)^\dagger$ for the CKM matrix. $\frac{1-\gamma_5}{2}$ and $\frac{1+\gamma_5}{2}$ are the RH and LH projection operators which act on the spinor fields as RH and LH states respectively. To display the full expression of Yukawa Lagrangian we include the Hermitian conjugate terms:

$$\begin{aligned}
\mathcal{L}_Y = & - m_{li}\bar{l}_i l_i - m_{di}\bar{d}_i d_i - m_{ui}\bar{u}_i u_i \\
& - \frac{\phi_1^0 m_{li}}{v\cos\beta}\bar{l}_i l_i - \frac{\phi_1^0 m_{di}}{v\cos\beta}\bar{d}_i d_i + \frac{\phi_2^0 m_{di}}{v\cos\beta}\bar{u}_i u_i \\
& + i\frac{\eta_1 m_{di}}{v\cos\beta}\bar{d}_i\gamma_5 d_i + \frac{\eta_1 m_{li}}{v\cos\beta}\bar{l}_i\gamma_5 l_i - i\frac{\eta_2 m_{ui}}{v\cos\beta}\bar{u}_i\gamma_5 u_i \\
& - \frac{m_{li}}{\sqrt{2}v\cos\beta}\bar{l}_i(1-\gamma_5)v_i\phi_1^- - \frac{m_{li}}{\sqrt{2}v\cos\beta}\bar{v}_i(1+\gamma_5)l_i\phi_1^+ \\
& - \frac{\sqrt{2}m_{dj}}{v\cos\beta}V_{ij}^*\bar{d}_j\frac{1-\gamma_5}{2}u_i\phi_1^- - \frac{\sqrt{2}m_{dj}}{v\cos\beta}V_{ji}\bar{u}_i\frac{1+\gamma_5}{2}d_j\phi_1^+ \\
& + \frac{\sqrt{2}m_{ui}}{v\sin\beta}V_{ij}\bar{u}_i\frac{1-\gamma_5}{2}d_j\phi_2^+ + \frac{\sqrt{2}m_{ui}}{v\sin\beta}V_{ji}^*\bar{d}_j\frac{1+\gamma_5}{2}u_i\phi_2^- \qquad (3.33)
\end{aligned}$$

The Yukawa couplings for the pseudoscalar state (A) are obtained by inersting the relationship between η_1, η_2 and G^0, A into the above equation:

$$\begin{aligned}
\mathcal{L}_{Y_{\eta_{1,2}}} = & \frac{i(\cos\beta G^0 - \sin\beta A)m_{di}}{vcos\beta}\bar{d}_i\gamma_5 d_i + \frac{i(\cos\beta G^0 - \sin\beta A)m_{li}}{v\cos\beta}\bar{l}_i\gamma_5 l_i \\
& - \frac{i(\sin\beta G^0 + \cos\beta A)m_{ui}}{v\cos\beta}\bar{u}_i\gamma_5 u_i + ... \qquad (3.34)
\end{aligned}$$

If we isolate the pseudoscalar state (A) only, then Eq. (3.34) becomes:

$$\begin{aligned}
\mathcal{L}_Y &= -i\frac{\sin\beta A m_{di}}{v\cos\beta}\bar{d}_i\gamma_5 d_i - i\frac{\sin\beta A m_{li}}{v\cos\beta}\bar{l}_i\gamma_5 l_i - i\frac{\cos\beta A m_{ui}}{v\sin\beta}\bar{u}_i\gamma_5 u_i \\
&= -i\frac{\tan\beta A m_{di}}{v}\bar{d}_i\gamma_5 d_i - i\frac{\tan\beta A m_{li}}{v}\bar{l}_i\gamma_5 l_i - i\frac{\cot\beta A m_{ui}}{v}\bar{u}_i\gamma_5 u_i \qquad (3.35)
\end{aligned}$$

We know $\frac{gv}{2} = M_W$, and so $v = \frac{2M_W}{g}$ or $\frac{1}{v} = \frac{g}{2M_W}$. Hence Eq. (3.35) will be equal to:

$$= -i\frac{g\tan\beta}{2M_W}A m_{di}\bar{d}_i\gamma_5 d_i - i\frac{g\tan\beta}{2M_W}A m_{li}\bar{l}_i\gamma_5 l_i - i\frac{g\cot\beta}{2M_W}A m_{ui}\bar{u}_i\gamma_5 u_i \qquad (3.36)$$

If we ignore the factor $i\frac{m_{fi}}{v}\gamma_5$, $f = d, \ell, u$, the Yukawa coupling between pseudoscalar A and fermions in type-II 2HDM will depend on whether $\tan\beta$ or $\cot\beta$. This is how the Yukawa couplings determined through the Yukawa sector as in Tab. (3.2). Similarly, Yukawa couplings between charged Higgs and fermions are also determined in the same way.

3.5 Conclusion

In this chapter we introduced the general 2HDM, which is an extension of the SM with an additional Higgs doublet. The motivation for such a model was discussed. In total there are four 2HDMs with NFC presented (i.e. a Z_2 symmetry is imposed on the Lagrangian). In a 2HDM there are five additional physical scalars. There are total two neutral scalars, one pseudoscalar and one charged scalar pair. The mass matrices of charged scalar, pseudoscalar, and two CP-even neutral scalars are determined by the differentiation of the Higgs potential with corresponding VEVs ($v^2 = v_1^2 + v_2^2 = 246\text{GeV}^2$) and the mixing angle between two CP-even Higgs states. We also showed the explicit form of the Yukawa interactions in a specific 2HDM (type-II) to illustrate how such a result will be generalised in a 3HDM. In next chapter, we will focus on the 3HDM and which will use the results from this chapter.

Chapter 4

3-Higgs-doublets model (3HDM)

4.1 Overview

The 2HDM has been studied in many papers and has attracted a lot of attention. However, as mentioned in the previous chapter it is possible that more than two Higgs doublets exist. Several works have studied the imposition of various symmetries on the 3HDM scalar potential [82; 83; 84; 85; 86; 87].

There are several motivations for a 3HDM. The first one comes from the flavour problem. The quark sector and also the lepton sector have three generations, and so it is natural to consider the possibility of three generations of scalar doublets. In addition, the ρ parameter in Eq. (3.1) is predicted to be equal to one at tree-level for $I = \frac{1}{2}, Y = 1$ scalar doublets which leaves unforbidden opportunity for three $I = \frac{1}{2}, Y = 1$ scalar doublets.

Another important motivation is from the CP-violation in scalar sector. It is known that the 2HDM could have rich CP-violating effects in the CP-even sector [88; 89]. However, the charged sector in a general 2HDM does not have a source of CP-violation. On the other hand, three active Higgs doublets contain two physical charged scalars (and one charged Goldstone boson), and there is a CP-violating phase (analogous to the CKM phase) in the 3×3 unitary matrix that diagonalises the charged scalar mass matrix.

In this chapter, the phenomenology of light charged Higgs bosons in 3HDMs is studied. Firstly, we describe the Higgs potential and the Yukawa sector in the 3HDM. Two softly-broken Z_2 symmetries are imposed to prevent FCNC at tree-level. Based on the two symmetries, five independent types of model for a 3HDM are realised. Four of these structures are similar to those in the 2HDM, with an extra structure that is called 'Democratic' 3HDM (which is not possible in 2HDM). In particular which a different scalar doublet couples to up-type quarks, down-type quarks, and leptons. Since our

goal is to study the charged scalar sector, the dominant decay modes are studied, and their searches at collider experiment is considered.

4.2 Structure of 3HDM

In a MHDM, there will be n number of scalar doublets. Before SSB, there will be total number of $2 \times n$ charged and neutral fields. After SSB, three fields will be eaten (2 charged fields and 1 neutral field which are the Goldstone bosons) and absorbed by $W^{\pm}$ boson and Z boson to give them masses. The result leaves only $2(n-1)$ charged physical fields and $2n-1$ neutral physical fields left. For a general 3HDM, the number $n = 3$ [73]. This will cause the 3HDM contains four charged and five neutral physical fields in the end.

In the general 3HDM, the $SU(2) \times U(1)$ invariant part of the Higgs potential is:

$$V_0 = \sum_{i}^{3}[-|\mu_i^2|(\phi_i^\dagger\phi_i) + \lambda_{ii}(\phi_i^\dagger\phi_i)^2] + \sum_{ij}^{3}[\lambda_{ij}(\phi_i^\dagger\phi_i)(\phi_j^\dagger\phi_j) + \lambda_{ij}^{'}(\phi_i^\dagger\phi_j)(\phi_j^\dagger\phi_i)] \tag{4.1}$$

In Tab. (4.1), all possible NFC Three Higgs-Doublets Models (3HDM) are shown. The first four types model are similar to those in the 2HDM. However, the 3HDM has a fifth structure, because three different Higgs doublets could actually couple to different fermions separately. In Tab. (4.1), this structure is called as the "Democratic". The $SU(2)_L \times U(1)_Y$ invariant potential is as follows:

$$\begin{aligned}
V &= m_{11}^2\Phi_1^\dagger\Phi_1 + m_{22}^2\Phi_2^\dagger\Phi_2 + m_{33}^2\Phi_3^\dagger\Phi_3 \\
&- [m_{12}^2\Phi_1^\dagger\Phi_2 + m_{13}^2\Phi_1^\dagger\Phi_3 + m_{23}^2\Phi_2^\dagger\Phi_3 + \text{h.c.}] \\
&+ \frac{1}{2}\lambda_1(\Phi_1^\dagger\Phi_1)^2 + \frac{1}{2}\lambda_2(\Phi_2^\dagger\Phi_2)^2 + \frac{1}{2}\lambda_3(\Phi_3^\dagger\Phi_3)^2 \\
&+ \lambda_{12}(\Phi_1^\dagger\Phi_1)(\Phi_2^\dagger\Phi_2) + \lambda_{13}(\Phi_1^\dagger\Phi_1)(\Phi_3^\dagger\Phi_3) + \lambda_{23}(\Phi_2^\dagger\Phi_2)(\Phi_3^\dagger\Phi_3) \\
&+ \lambda_{12}'(\Phi_1^\dagger\Phi_2)(\Phi_2^\dagger\Phi_1) + \lambda_{13}'(\Phi_1^\dagger\Phi_3)(\Phi_3^\dagger\Phi_1) + \lambda_{23}'(\Phi_2^\dagger\Phi_3)(\Phi_3^\dagger\Phi_2) \\
&+ \frac{1}{2}[\lambda_{12}''(\Phi_1^\dagger\Phi_2)^2 + \lambda_{13}''(\Phi_1^\dagger\Phi_3)^2 + \lambda_{23}''(\Phi_2^\dagger\Phi_3)^2 + \text{h.c.}],
\end{aligned} \tag{4.2}$$

The terms like m_{ij}^2 break the Z_2 symmetry softly.

In general, there are six complex parameters in the potential, namely: three soft-breaking mass terms m_{12}^2, m_{13}^2 and m_{23}^2; three quartic coupling terms $\lambda_{12}'', \lambda_{13}''$ and λ_{23}''. Two of these six complex parameters are actually non-physical. Since the potential is invariant under a phase rotation of three fields Φ_1, Φ_2, and Φ_3, one could set the VEV of Φ_3 to be real. With another phase rotation of Φ_1 and Φ_2, two VEVs could be set as real as well.

The condition is required by the two formulae below:

$$\begin{aligned}
\mathrm{Im}(m_{13}^2) &= -\frac{v_2}{v_3}\mathrm{Im}(m_{12}^2) + \frac{v_1 v_2^2}{2v_3}\mathrm{Im}(\lambda_{12}'') + \frac{v_1 v_3}{2}\mathrm{Im}(\lambda_{13}''), \\
\mathrm{Im}(m_{23}^2) &= \frac{v_1}{v_3}\mathrm{Im}(m_{12}^2) - \frac{v_1^2 v_2}{2v_3}\mathrm{Im}(\lambda_{12}'') + \frac{v_2 v_3}{2}\mathrm{Im}(\lambda_{23}''). \qquad (4.3)
\end{aligned}$$

These two equations fix the two imaginary parameters $\mathrm{Im}(m_{13}^2), \mathrm{Im}(m_{23}^2)$. Thus, the condition above leaves the other four imaginary parameters as physical. These remaining four will be have complex phases which are responsible for CP-violation in the three neutral CP-even, two neutral CP-odd Higgs states, and two physical charged Higgs states. The result is that there are the CP-violation phases in the Yukawa couplings of the physical Higgs eigenstates. In this thesis, CP-violation will be discussed only in the context of the charged Higgs sector.

The CP-violating in the neutral Higgs sector can be removed by using the following relations:

$$\begin{aligned}
\mathrm{Im}(\lambda_{13}'') &= -\frac{v_2^2}{v_3^2}\,\mathrm{Im}(\lambda_{12}'') \\
\mathrm{Im}(\lambda_{23}'') &= \frac{v_1^2}{v_3^2}\,\mathrm{Im}(\lambda_{12}'') \\
\mathrm{Im}(m_{12}^2) &= v_1\, v_2\, \mathrm{Im}(\lambda_{12}'') \qquad (4.4)
\end{aligned}$$

This causes all CP-violation to reside in the parameter $\mathrm{Im}(\lambda_{12}'')$. This will be the remaining CP-violation phase that appear in the charged Higgs Yukawa coupling.

The mass eigenstate charged scalars are related to the gauge eigenstates ϕ_i^+ $(i = 1, 2, 3)$ by a mixing matrix U as follows [90]:

$$\begin{pmatrix} G^+ \\ H_2^+ \\ H_3^+ \end{pmatrix} = U \begin{pmatrix} \phi_1^+ \\ \phi_2^+ \\ \phi_3^+ \end{pmatrix}, \qquad (4.5)$$

Here G^+ is the charged Goldstone boson, and H_2^+ and H_3^+ are the physical charged Higgs mass eigenstates. Here, U is obtained by diagonalising the charged Higgs mass-squared matrix, $V \supset \phi_i^- (\mathcal{M}_{H^\pm}^2)_{ij} \phi_j^+$, which is taken from Ref. [90]:

$$\mathcal{M}_{H^\pm}^2 = \begin{pmatrix} \frac{v_2}{v_1}A_{12} + \frac{v_3}{v_1}A_{13} & -A_{12} + iB & -A_{13} - i\frac{v_2}{v_3}B \\ -A_{12} - iB & \frac{v_1}{v_2}A_{12} + \frac{v_3}{v_2}A_{23} & -A_{23} + i\frac{v_1}{v_3}B \\ -A_{13} + i\frac{v_2}{v_3}B & -A_{23} - i\frac{v_1}{v_3}B & \frac{v_1}{v_3}A_{13} + \frac{v_2}{v_3}A_{23} \end{pmatrix}, \qquad (4.6)$$

where $A_{12}A_{13}, A_{23}, B$ are combinations of the original parameters in the scalar potential as follows:

$$\begin{aligned} A_{12} &= \mathrm{Re}(m_{12}^2) - \frac{v_1 v_2}{2}[\lambda'_{12} + \mathrm{Re}(\lambda''_{12})], \\ A_{23} &= \mathrm{Re}(m_{23}^2) - \frac{v_2 v_3}{2}[\lambda'_{23} + \mathrm{Re}(\lambda''_{23})], \\ A_{13} &= \mathrm{Re}(m_{13}^2) - \frac{v_1 v_3}{2}[\lambda'_{13} + \mathrm{Re}(\lambda''_{13})], \\ B &= -\mathrm{Im}(m_{12}^2) + \frac{v_1 v_2}{2}\mathrm{Im}(\lambda''_{12}). \end{aligned} \tag{4.7}$$

Notice here that the CP violation enters only via B. In the case that CP violation in the neutral Higgs sector is turned off by imposing Eqs. (4.4), B becomes:

$$B = -\frac{v_1 v_2}{2}\mathrm{Im}(\lambda''_{12}). \tag{4.8}$$

We now diagonalise the charged Higgs mass matrix. A rotation in two stages is performed, starting with rotating to the Higgs basis using the matrix:

$$U_1 = \begin{pmatrix} \sin\gamma & 0 & \cos\gamma \\ 0 & 1 & 0 \\ -\cos\gamma & 0 & \sin\gamma \end{pmatrix} \begin{pmatrix} \cos\beta & \sin\beta & 0 \\ -\sin\beta & \cos\beta & 0 \\ 0 & 0 & 1 \end{pmatrix}, \tag{4.9}$$

where we define the angles β and γ in terms of the VEVs:

$$\tan\beta = \frac{v_2}{v_1}, \ \tan\gamma = \frac{\sqrt{v_1^2 + v_2^2}}{v_3}. \tag{4.10}$$

This rotation isolates the charged goldstone boson, yielding the following mass matrix:

$$\mathcal{M}'^2_{H^\pm} = U_1 \mathcal{M}^2_{H^\pm} U_1^\dagger = \begin{pmatrix} 0 & 0 & 0 \\ 0 & \mathcal{M}'^2_{22} & \mathcal{M}'^2_{23} \\ 0 & \mathcal{M}'^{2*}_{23} & \mathcal{M}'^2_{33} \end{pmatrix}, \tag{4.11}$$

where in Ref. [90]:[1]

$$\mathcal{M}'^2_{22} = \frac{v_{12}^2}{v_1 v_2} A_{12} + \frac{v_2^2 v_3}{v_1 v_{12}^2} A_{13} + \frac{v_1^2 v_3}{v_2 v_{12}^2} A_{23}, \tag{4.12}$$

$$\mathcal{M}'^2_{33} = \frac{v_1 v^2}{v_3 v_{12}^2} A_{13} + \frac{v_2 v^2}{v_3 v_{12}^2} A_{23}, \tag{4.13}$$

$$\mathcal{M}'^2_{23} = \frac{v_2 v}{v_{12}^2} A_{13} - \frac{v_1 v}{v_{12}^2} A_{23} + i\frac{v}{v_3} B, \tag{4.14}$$

[1] We correct two typos in the expression for $\mathcal{M}^2_{22}$ in Eq. (A8) of Ref. [90].

and $v_{12}^2 = v_1^2 + v_2^2$. The next step is to diagonalize the matrix in Eq. (4.11). This is done with the matrix U_2,

$$U_2 = \begin{pmatrix} 1 & 0 & 0 \\ 0 & e^{-i\delta} & 0 \\ 0 & 0 & 1 \end{pmatrix} \begin{pmatrix} 1 & 0 & 0 \\ 0 & \cos\theta & \sin\theta e^{i\delta} \\ 0 & -\sin\theta e^{-i\delta} & \cos\theta \end{pmatrix}, \tag{4.15}$$

Since only the term B contains the imaginary part, the imaginary component of $(\mathcal{M}_{23}'^2)$ will be the only source of CP-violation, where the CP-violating phase δ is given by

$$\delta = \text{phase}(\mathcal{M}_{23}'^2), \tag{4.16}$$

with $0 \leq \delta < 2\pi$.

By choosing the state H_2^+ to be lighter than H_3^+, the masses of the two charged Higgs mass eigenstates are as follows:

$$M^2_{H^\pm_{2,3}} = \frac{1}{2}\left[\mathcal{M}_{22}'^2 + \mathcal{M}_{33}'^2 \mp \sqrt{(\mathcal{M}_{22}'^2 - \mathcal{M}_{33}'^2)^2 + 4|\mathcal{M}_{23}'^2|^2}\right] \tag{4.17}$$

The mixing angle (θ) between two physical states $H^\pm_{2,3}$ is:

$$\begin{aligned} \sin 2\theta &= \frac{-2|\mathcal{M}_{23}'^2|^2}{(\mathcal{M}_{22}'^2 - \mathcal{M}_{33}'^2)^2 + 4|\mathcal{M}_{23}'^2|^2} \\ \cos 2\theta &= \frac{-\mathcal{M}_{22}'^2 + \mathcal{M}_{33}'^2}{(\mathcal{M}_{22}'^2 - \mathcal{M}_{33}'^2)^2 + 4|\mathcal{M}_{23}'^2|^2} \end{aligned} \tag{4.18}$$

with $-\pi/2 \leq \theta \leq 0$.[2]

Together with the mixing angle θ (of $H_2^\pm$ and $H_3^\pm$) ,$\tan\beta$, and $\tan\gamma$, the CP-violation phase (δ) can also be written explicitly as a function of several parameters in the scalar

[2] In the Democratic (or type-Z) 3HDM, the coupling of H_2^+ to leptons goes to zero when $\theta = 0$, likewise the coupling of H_3^+ to leptons goes to zero when $\theta = -\pi/2$.

potential. The explicit form of U is given in the paper [90] as:

$$\begin{aligned} U &= \begin{pmatrix} 1 & 0 & 0 \\ 0 & e^{-i\delta} & 0 \\ 0 & 0 & 1 \end{pmatrix} \begin{pmatrix} 1 & 0 & 0 \\ 0 & c_\theta & s_\theta e^{i\delta} \\ 0 & -s_\theta e^{-i\delta} & c_\theta \end{pmatrix} \begin{pmatrix} s_\gamma & 0 & c_\gamma \\ 0 & 1 & 0 \\ -c_\gamma & 0 & s_\gamma \end{pmatrix} \begin{pmatrix} c_\beta & s_\beta & 0 \\ -s_\beta & c_\beta & 0 \\ 0 & 0 & 1 \end{pmatrix} \\ &= \begin{pmatrix} 1 & 0 & 0 \\ 0 & c_\theta e^{-i\delta} & s_\theta \\ 0 & -s_\theta e^{-i\delta} & c_\theta \end{pmatrix} \begin{pmatrix} s_\gamma c_\beta & s_\gamma s_\beta & c_\gamma \\ -s_\beta & c_\beta & 0 \\ -c_\gamma c_\beta & -c_\gamma s_\beta & s_\gamma \end{pmatrix} \\ &= \begin{pmatrix} s_\gamma c_\beta & s_\gamma s_\beta & c_\gamma \\ -c_\theta s_\beta e^{-i\delta} - s_\theta c_\gamma c_\beta & c_\theta c_\beta e^{-i\delta} - s_\theta c_\gamma s_\beta & s_\theta s_\gamma \\ s_\theta s_\beta e^{-i\delta} - c_\theta c_\gamma c_\beta & -s_\theta c_\beta e^{-i\delta} - c_\theta c_\gamma s_\beta & c_\theta s_\gamma \end{pmatrix}. \end{aligned} \tag{4.19}$$

Here s, c denote the sine or cosine of the respective angle. The connection between the gauge eigenstates and the mass eigenstates can now be written as (using $U^\dagger U = I$):

$$\begin{aligned} \begin{pmatrix} G_1^+ \\ H_2^+ \\ H_3^+ \end{pmatrix} &= U \begin{pmatrix} \phi_d^+ \\ \phi_u^+ \\ \phi_\ell^+ \end{pmatrix}, \; U^\dagger \begin{pmatrix} G_1^+ \\ H_2^+ \\ H_3^+ \end{pmatrix} = U^\dagger U \begin{pmatrix} \phi_d^+ \\ \phi_u^+ \\ \phi_\ell^+ \end{pmatrix} \\ \begin{pmatrix} \phi_d^+ \\ \phi_u^+ \\ \phi_\ell^+ \end{pmatrix} &= U^\dagger \begin{pmatrix} G_1^+ \\ H_2^+ \\ H_3^+ \end{pmatrix} \end{aligned} \tag{4.20}$$

The full rotation matrix in Eq. (4.19) is then Hermitian conjugated to give:

$$U^\dagger = (U_2 U_1)^\dagger = \begin{pmatrix} s_\gamma c_\beta & -c_\theta s_\beta e^{i\delta} - s_\theta c_\gamma c_\beta & s_\theta s_\beta e^{i\delta} - c_\theta c_\gamma c_\beta \\ s_\gamma s_\beta & c_\theta c_\beta e^{i\delta} - s_\theta c_\gamma s_\beta & -s_\theta c_\beta e^{i\delta} - c_\theta c_\gamma s_\beta \\ c_\gamma & s_\theta s_\gamma & c_\theta s_\gamma \end{pmatrix}, \tag{4.21}$$

where $s_\beta = \sin\beta$, $c_\beta = \cos\beta$ and similarly for the other mixing angles. The above explicit form of $U^\dagger$ (rather than U) will be useful later when the phenomenology of charged Higgs is discussed.

4.3 Charged Higgs Yukawa sector in 3HDM

For a Multi-Higgs-Doublet Model (MHDM) with n-1 doublets the charged Higgs Yukawa interaction can be written as:

$$\mathcal{L}_{Y^\pm} = (2\sqrt{2}G_F)^{\frac{1}{2}} \sum_{i=2}^{n} H_i^+ \{ X_i \bar{u}_L V M_d d_R + Y_i \bar{u}_R M_u V u_L + Z_i \bar{e}_L M_e e_R \} + \text{h.c} \tag{4.22}$$

Here M_d, M_u, M_e are diagonal mass matrices of specific types of fermions. V is the CKM matrix which was introduced by [91] and [92] and also mentioned in chapter 2. As

	$d-quark$	$u-quark$	$charged-leptons$
Type I	2	2	2
Type II	1	2	1
Type X (Lepton-specific)	2	2	1
Type Y (Flipped)	1	2	2
Type Z (Democratic)	1	2	3

TABLE 4.1: Total possibilities of 3HDM structures. Number represents which type of Higgs doublet couples to which fermion type.

mentioned earlier, the gauge eigenstates of the charged Higgs bosons and the physical mass eigenstates have relation as below [90]:

$$\begin{pmatrix} G_1^+ \\ H_2^+ \\ H_3^+ \end{pmatrix} = U \begin{pmatrix} \phi_d^+ \\ \phi_u^+ \\ \phi_\ell^+ \end{pmatrix} \tag{4.23}$$

This matrix U connects the charged scalar fields in the weak eigenbasis $(\phi_d^+, \phi_u^+, \phi_l^+)$ with the physical scalar fields $(H_2^+,\ H_3^+)$ and the charged goldstone boson G^+. The matrix U is a 3×3 unitary matrix and rotates the interaction basis to the mass eigenstates. G_1^+ is a charged goldstone boson and $H_i^+ (i = 2,3)$ are the physical charged scalars. Here, U is an $n \times n$ unitary matrix that can be parameterized as the generalized CKM matrix with $n(n-1)/2$ angles and $(n-1)(n-2)/2$ phases [93]. Thus, we will have 3 angles and 1 phase parameters for the 3×3 matrix and this is why we have $\tan\beta, \tan\gamma, \theta$ and δ in last section.

X_i,Y_i,Z_i are the complex Yukawa couplings. We now compare these couplings with those in the type-II 2HDM:

$$\frac{v_2}{v_1} = \tan\beta = X = Z, \quad \cot\beta = Y \tag{4.24}$$

In a 2HDM the Yukawa couplings depend on one free parameter, $\tan\beta$. In the 3HDM the Yukawa couplings are functions of the four parameters in the unitary 3×3 matrix of Eq. (4.21). In this model, it is assumed that $H_2^\pm$ is the lighter of the two charged Higgs bosons with couplings X_2, Y_2, Z_2:

$$X_2 = \frac{U_{d2}^\dagger}{U_{d1}^\dagger}, \qquad Y_2 = -\frac{U_{u2}^\dagger}{U_{u1}^\dagger}, \qquad Z_2 = \frac{U_{\ell 2}^\dagger}{U_{\ell 1}^\dagger}\,. \tag{4.25}$$

and the Yukawa couplings X_3, Y_3, Z_2 corresponding to $H_3^\pm$ are:

$$X_3 = \frac{U_{d3}^\dagger}{U_{d1}^\dagger}, \qquad Y_3 = -\frac{U_{u3}^\dagger}{U_{u1}^\dagger}, \qquad Z_3 = \frac{U_{\ell 3}^\dagger}{U_{\ell 1}^\dagger}\,. \tag{4.26}$$

Model	X_i	Y_i	Z_i
Type I	$\frac{U^\dagger_{2i}}{U^\dagger_{21}}$	- $\frac{U^\dagger_{2i}}{U^\dagger_{21}}$	$\frac{U^\dagger_{2i}}{U^\dagger_{21}}$
Type II	$\frac{U^\dagger_{1i}}{U^\dagger_{11}}$	- $\frac{U^\dagger_{2i}}{U^\dagger_{21}}$	$\frac{U^\dagger_{1i}}{U^\dagger_{11}}$
Type X (Lepton-specific)	$\frac{U^\dagger_{2i}}{U^\dagger_{21}}$	- $\frac{U^\dagger_{2i}}{U^\dagger_{21}}$	$\frac{U^\dagger_{1i}}{U^\dagger_{11}}$
Type Y (Flipped)	$\frac{U^\dagger_{1i}}{U^\dagger_{11}}$	- $\frac{U^\dagger_{2i}}{U^\dagger_{21}}$	$\frac{U^\dagger_{2i}}{U^\dagger_{21}}$
Type Z (Democratic)	$\frac{U^\dagger_{1i}}{U^\dagger_{11}}$	- $\frac{U^\dagger_{2i}}{U^\dagger_{21}}$	$\frac{U^\dagger_{3i}}{U^\dagger_{31}}$

TABLE 4.2: Yukawa couplings X_i, Y_i, Z_i in the charged Higgs Lagrangian of Eq. (4.22) to down-type quarks, up-type quarks, and (charged) leptons, respectively, with $i = 2, 3$. The matrices $U^\dagger$ are taken from Eq. (4.21).

In above Eqs. (4.25) and (4.26), matrix $U^\dagger_{ij}$ is taken from Eq. (4.21). For example, type Flipped model 3HDM gives $d = 1$, so X_2 will be given from the first row and the second column matrix element of Eq. (4.21) over the first row and the first column matrix element of Eq. (4.21):

$$X_2 = \frac{U^\dagger_{12}}{U^\dagger_{11}} = \frac{-c_\theta s_\beta (c_\delta + i s_\delta) - s_\theta c_\gamma c_\beta}{c_\beta s_\gamma}. \tag{4.27}$$

Where s and c are sine and cosine of relevant mixing parameters θ, β, γ and δ. All other Yukawa formulas (i.e.Y_2, Z_2, X_3, Y_3, Z_3) can be seen in Appendix C. Also, that Appendix gives the Yukawa formulas of Democratic 3HDM.

The Yukawa interaction of a charged Higgs boson in the 3HDM is shown in detail below. First, we give the relationship between the three different VEVs (v_1, v_2, v_3) and the SM VEV (v):

$$v_1 = v \cos\beta \sin\gamma, v_2 = v \sin\beta \sin\gamma, v_3 = v \cos\gamma \tag{4.28}$$

Taking the Democratic 3HDM as an example one has:

$$\mathcal{L}_Y = -g^L_i \bar{l}_{iR} \Phi^\dagger_3 l^i_L - g^d_{ij} \bar{d'}_{iR} \Phi^\dagger_1 u^j_L - g^u_{ij} \bar{u}_{iR} \tilde{\Phi}^\dagger_2 u^i_L + \text{H.c} \tag{4.29}$$

Here Φ_1, Φ_2 and Φ_3 are given by:

$$\Phi_i = \begin{pmatrix} \phi^+_i \\ (v_i + h_i + i\eta_i)/\sqrt{2} \end{pmatrix}, \tilde{\Phi}_i = \begin{pmatrix} (v_i + h_i - i\eta_i)/\sqrt{2} \\ -\phi^-_i \end{pmatrix} \tag{4.30}$$
$$\text{where } i = 1, 2, 3$$

Thus the Yukawa sector, Eq. (4.29) can be written as:

$$\begin{aligned}\mathcal{L}_Y = &- g_i^L \bar{l}_{iR}\left(\phi_3^-, (v_3+h_3-i\eta_3)/\sqrt{2}\right)\begin{pmatrix} v_{iL} \\ l_{iL}\end{pmatrix} \\ &- g_{ij}^d \bar{d'}_{iR}\left(\phi_1^-, (v_1+h_1-i\eta_1)/\sqrt{2}\right)\begin{pmatrix} u_{jL} \\ d'_{jL}\end{pmatrix} \\ &- g_{ij}^u \bar{u}_{iR}\left((v_2+h_2+i\eta_2)/\sqrt{2}, -\phi_2^+\right)\begin{pmatrix} u_{iL} \\ d'_{iL}\end{pmatrix} + \text{H.c} \end{aligned} \tag{4.31}$$

On multiplying out one has

$$\begin{aligned}\mathcal{L}_Y = &- g_i^L \bar{l}_{iR} v_{iL}\phi_3^- - v_3/\sqrt{2} g_i^L \bar{l}_{iR} l_{iL} - h_3/\sqrt{2} g_i^L \bar{l}_{iR} l_{iL} + i\eta_3/\sqrt{2} g_i^L \bar{l}_{iR} l_{iL} \\ &- g_{ij}^d \bar{d'}_{iR} u_{jL}\phi_1^- - v_1/\sqrt{2} g_{ij}^d \bar{d'}_{iR} d'_{jL} - h_1/\sqrt{2} g_{ij}^d \bar{d'}_{iR} d'_{jL} + i\eta_1/\sqrt{2} g_{ij}^d \bar{d'}_{iR} d'_{jL} \\ &- v_2/\sqrt{2} g_i^u \bar{u}_{iR} u_{iL} - h_2/\sqrt{2} g_i^u \bar{u}_{iR} u_{iL} - i\eta_2/\sqrt{2} g_i^u \bar{u}_{iR} u_{iL} + g_i^u \bar{u}_{iR} d'_{iL}\phi_2^+ \\ &+ \text{h.c} \end{aligned} \tag{4.32}$$

$$\begin{aligned} = &- \frac{\sqrt{2}m_{li}}{v\cos\gamma}\bar{l}_i \frac{1-\gamma_5}{2} v_{iL}\phi_3^- - m_{li}\bar{l}_{iR} l_{iL} - \frac{h_3 m_{li}}{v\cos\gamma}\bar{l}_{iR} l_{iL} + i\frac{\eta_3 m_{li}}{v\cos\gamma}\bar{l}_{iR} l_{iL} \\ &- \frac{\sqrt{2}m_{dj}}{v\cos\beta\sin\gamma} V_{ij}^* \bar{d}_j \frac{1-\gamma_5}{2} u_i \phi_1^- - m_{di}\bar{d}_{iR} d_{iL} \\ &- \frac{h_1 m_{di}}{v\cos\beta\sin\gamma}\bar{d}_{iR} d_{iL} + i\frac{\eta_1 m_{di}}{v\cos\beta\sin\gamma}\bar{d}_{iR} d_{iL} \\ &+ \frac{\sqrt{2}m_{ui}}{v\sin\beta\sin\gamma} V_{ij}\bar{u}_i \frac{1-\gamma_5}{2} d_j \phi_2^+ - m_{ui}\bar{u}_{iR} u_{iL} \\ &- \frac{h_2 m_{ui}}{v\sin\beta\sin\gamma}\bar{u}_{iR} u_{iL} - i\frac{\eta_2 m_{ui}}{v\sin\beta\sin\gamma}\bar{u}_{iR} u_{iL} \\ &+ \text{h.c} \end{aligned} \tag{4.33}$$

where we define:

$$\begin{aligned} m_{li} &= \frac{g_i^L v_3}{\sqrt{2}} = \frac{g_i^L v\cos\gamma}{\sqrt{2}}, g_i^L = \frac{\sqrt{2}m_{li}}{v\cos\gamma}; \\ m_{di} &= \frac{g_i^d v_1}{\sqrt{2}} = \frac{g_i^d v\cos\beta\sin\gamma}{\sqrt{2}}, g_i^d = \frac{\sqrt{2}m_{di}}{v\cos\beta\sin\gamma}; \\ m_{ui} &= \frac{g_i^u v_2}{\sqrt{2}} = \frac{g_i^u v\sin\beta\sin\gamma}{\sqrt{2}}, g_i^u = \frac{\sqrt{2}m_{ui}}{v\sin\beta\sin\gamma} \end{aligned} \tag{4.34}$$

One could convert $\frac{1}{v}$ to $\frac{g}{2M_W}$,

$$\begin{aligned}
\mathcal{L}_Y = & - m_{li}\bar{l}_i l_i - m_{di}\bar{d}_i d_i - m_{ui}\bar{u}_i u_i \\
& - \frac{g h_3 m_{li}}{2M_W \cos\gamma}\bar{l}_i l_i - \frac{g h_1 m_{di}}{2M_W \cos\beta \sin\gamma}\bar{d}_i d_i + \frac{g h_2 m_{di}}{2M_W \sin\beta \sin\gamma}\bar{u}_i u_i \\
& + i\frac{g \eta_3 m_{li}}{2M_W \cos\gamma}\bar{l}_i \gamma_5 l_i + i\frac{g \eta_1 m_{di}}{2M_W \cos\beta \sin\gamma}\bar{d}_i \gamma_5 d_i - i\frac{g \eta_2 m_{ui}}{2M_W \sin\beta \sin\gamma}\bar{u}_i \gamma_5 u_i \\
& - \frac{m_{li}}{2\sqrt{2} m_W \cos\gamma}\bar{l}_i (1-\gamma_5) v_i \phi_3^- - \frac{m_{li}}{2\sqrt{2} M_W \cos\gamma}\bar{v}_i (1+\gamma_5) l_i \phi_3^+ \\
& - \frac{m_{dj}}{2\sqrt{2}\cos\beta\sin\gamma} V_{ij}^* \bar{d}_j \frac{1-\gamma_5}{2} u_i \phi_1^- - \frac{m_{dj}}{2\sqrt{2}\cos\beta\sin\gamma} V_{ji} \bar{u}_i \frac{1+\gamma_5}{2} d_j \phi_1^+ \\
& + \frac{m_{ui}}{2\sqrt{2}\sin\beta\sin\gamma} V_{ij} \bar{u}_i \frac{1-\gamma_5}{2} d_j \phi_2^+ + \frac{m_{ui}}{2\sqrt{2}\sin\beta\sin\gamma} V_{ji}^* \bar{d}_j \frac{1+\gamma_5}{2} u_i \phi_2^- \quad (4.35)
\end{aligned}$$

Using the rotation matrix Eq. (4.21), the equation of gauge states and mass states can be written as:

$$\begin{aligned}
s_\gamma c_\beta G^\pm + (-c_\theta s_\beta e^{+i\delta} - s_\theta c_\gamma c_\beta) H_2^\pm + (s_\theta s_\beta e^{+i\delta} - c_\theta c_\gamma c_\beta) H_3^\pm &= \phi_1^\pm \\
s_\gamma s_\beta G^\pm + (c_\theta c_\beta e^{+i\delta} - s_\theta c_\gamma s_\beta) H_2^\pm + (-s_\theta c_\beta e^{-i\delta} - c_\theta c_\gamma s_\beta) H_3^\pm &= \phi_2^\pm \\
c_\gamma G^\pm + s_\theta s_\gamma H_2^\pm + c_\theta s_\gamma H_3^\pm &= \phi_3^\pm \quad (4.36)
\end{aligned}$$

Taking $-\frac{m_{li}}{2\sqrt{2}M_W \cos\gamma}\bar{l}_i(1-\gamma_5)v_i\phi_3^-$ as an example to isolate the interaction between the physical H_2^-, H_3^- and $\bar{l}_i, v_i$ by Eq. (4.36), we obtain:

$$\begin{aligned}
& -\frac{m_{li}}{2\sqrt{2}M_W \cos\gamma}\bar{l}_i(1-\gamma_5)v_i\phi_3^- \\
= \; & \frac{m_{li}}{2\sqrt{2}M_W \cos\gamma}\bar{l}_i(1-\gamma_5)v_i(c_\gamma G^- + s_\theta s_\gamma H_2^- + c_\theta s_\gamma H_3^-) \\
(H_2^-, H_3^-) \text{ terms} = \; & \frac{m_{li}}{2\sqrt{2}M_W \cos\gamma}\bar{l}_i(1-\gamma_5)v_i(s_\theta s_\gamma H_2^- + c_\theta s_\gamma H_3^-) \quad (4.37)
\end{aligned}$$

Thus, the Yukawa couplings between H_2^-, H_3^- and $\bar{l}_i, v_i$ are:

$$H_2^- \text{ term} : \frac{s_\theta s_\gamma}{c_\gamma}; H_3^- \text{ term} : \frac{c_\theta s_\gamma}{c_\gamma} \quad (4.38)$$

Here the labels of s and c represent sine and cosine respectively.

4.4 Decay Modes of Charged Higgs

The search for a charged Higgs particle depends on its decay products. Specifically, the decay of charged Higgs to fermions depends on the Yukawa couplings. In this section, we investigate the fermionic decays of charged Higgs particle, specifically for the case of charged Higgs mass $M_{H^\pm} < m_t$. Any decay to a neutral Higgs state is assumed to be absent and this scenario corresponds to the case of the two-body decay channels $H_2^\pm \to (h_{\rm SM}, H^0, A)\, W^\pm$ not being kinematically open. In order to do that, the scalar masses that correlate to couplings ($\lambda_{12}, \lambda_{12}^{'}$, etc.) in the scalar potential would be varied for a limit which the discrepancy of these scalar masses should be less than W boson mass.

4.4.1 Fermionic decay of charged Higgs

The decay modes of charged Higgs are depend on the Yukawa couplings $g_{H^\pm}$. In the case of the 2HDM case, the couplings depend on $\tan\beta$ alone while in the 3HDM scenario the couplings are X_i, Y_i, Z_i (and are different in general for $H_2^\pm$ and $H_3^\pm$). For fermionic decay modes, the partial widths are as follows:

Two-body decay of $H_i^\pm$ [94]:

$$\Gamma(H_i^\pm \to \ell^\pm \nu) = \frac{G_f M_{H_i^\pm} m_\ell^2 |Z_i|^2}{4\pi\sqrt{2}}\,, \tag{4.39}$$

$$\Gamma(H_i^\pm \to ud) = \frac{3 G_f V_{ud} M_{H_i^\pm} (m_d^2 |X_i|^2 + m_u^2 |Y_i|^2)}{4\pi\sqrt{2}}\,. \tag{4.40}$$

Here m_u and m_d the up-type and down-type quark masses respectively. G_f is the Fermi constant. In the 3HDM, there are two physical charged Higgs state $H_2^\pm$ and $H_3^\pm$, so $i = 2, 3$ for $H_i^\pm$. The corresponding Yukawa couplings X_i, Y_i, and Z_i are given in Eqs. (4.25, 4.26). V_{ud} is the CKM matrix element for the final state fermions in the decay. For example, charged Higgs to $c\,b$ will use V_{cb}, charged Higgs to $t\,b$ will use V_{tb} etc. In Eq. (4.40), the quark masses need to be evaluate at the scale of $M_{H_i^\pm}$, and QCD vertex corrections (from virtual gluons) multiplies the partial width by a factor of $(1 + 17\frac{\alpha}{3\pi})$ [1].

In 1994 in Ref. [95] by A.G Akeroyd and W.J.Stirling the branching ratios in a 3HDM were studied, the possible dominance of the decay $H_2^\pm \to cb$ was emphasised. Further studies of the fermionic decays of a light charged Higgs were carried out in [96; 97]. In Ref. [96],[3] the paper chose the light charged Higgs state $H_2^\pm$ and set the value of $|Z|$ to

[3] In this reference, the authors took the light charged Higgs and they used the symbol $H^\pm$ for later study. Furthermore, the corresponding Yukawa coupling of $H^\pm$ are set as X, Y, Z. In this thesis, the light charged Higgs state has set to $H_2^\pm$ and corresponding Yukawa couplings X_2, Y_2, Z_2.

be 0.1 and 0.05 separately. The magnitudes of the branching ratios (BR) of $H^\pm \to cb$, $H^\pm \to cs$ and $H^\pm \to \tau\nu_\tau$ (the three dominant fermionic channels) were studied in the plane of $|X|$ and $|Y|$. Specifically, they showed that BR$(H^\pm \to cb)$ can be large as 80%. Branching ratio of specific decay channel is determined by the partial width of the specific decay channel over all possible decays. e.g. BR$(H^\pm \to cb) = \frac{\Gamma(H^\pm \to cb)}{\text{All } \Gamma(H^\pm)\text{s}}$. The dependence of the BRs on the four mixing parameters in Eq. (4.19) was not studied in those works, and will be investigated in this section. It is assumed that only $H_2^\pm$ can be lighter than the top quark,[4] and so $M_{H_3^\pm} > m_t$. We then study fermion the three dominant channels cs, cb and $\tau\nu_\tau$.

4.4.2 Branching ratios of $H_2^\pm$ as a function of the Yukawa couplings X_2,Y_2,Z_2

In this section the branching ratios of $H_2^\pm$ as a function of X_2, Y_2 and Z_2 will be presented. In the scenario of a light charged Higgs boson the Yukawa couplings (X_i, Y_i, Z_i are constrained by several low-energy processes. The constraints below are taken from Refs. [98; 99].

For the charged Higgs state in the 2HDM,[5] one constraint comes from $Z \to b\bar{b}$ which limits the coupling Y. With a charged Higgs mass of around 100 GeV, the value of $|Y|$ has to lower than 1. Another constraint comes from the rare decay $\bar{B} \to X_s\gamma$, which limits combination of Re$(X_2 Y_2^*)$ as follows:

$$-1.1 \;\leq\; \mathrm{Re\,XY^*} \;\leq 0.7\,, \mathrm{M_{H^\pm}} = 100\,\mathrm{GeV}. \tag{4.41}$$

In this case the contribution of $|Y^2|$ is neglected. Details of this constraint can be found from [98].

The electric-dipole moment (EDM) of the electron limits the combination Im(XY^*) [99]:

$$|\mathrm{Im\,XY^*}| \;\leq 0.1\,, \mathrm{M_{H^\pm}} = 100\,\mathrm{GeV}. \tag{4.42}$$

These last two constraints will be studied in more detail in chapter 6. In this section, the above two approximate bounds will be used when studying the branching ratios of $H_2^\pm$. In 3HDM, the constraints are applied $\mathrm{Re\,X_2Y_2^*}$ and $\mathrm{Im\,X_2Y_2^*}$, and the contribution of $H_3^\pm$ (which is taken to be much heavier) is assumed to be negligible.

Before going to the detail of BR physics results, we first state what scientific tool we used for our analysis. The computation tool we used is programme Python [100] and the figures we produced are based on Matplotlib [101]. All formulas are plugged into

[4] For the rest of our discussion and analysis, we use symbol $H_2^\pm$ for the physical light charged Higgs state. When discussing the collider searches the symbols $H^\pm$ or H^+ are used, especially in chapter 5.

[5] A 2HDM contains only one charged Higgs state, so there is only one coupling X, Y, Z.

SPYDER (Scientific PYthon Development EnviRonment) integrated development environment (IDE) [102].[6] The mixing matrix parameterization has done by the Mathematica [103] in order to check the consistency with Reference [90]. We took a separate check by taking the minimum condition of three Higgs doublets scalar potential in 3HDM, charged Higgs mass-squared matrix are diagonalised by dividing two unitary mixing matrices with four mixing parameters which are mentioned in section 4.2.

With the assumption of the mass of the CP-odd scalar A being heavier than $H_2^\pm$, we plot BR($H_2^\pm \to cb, cs, \tau\nu_\tau$) with corresponding Yukawa couplings $|X_2|, |Y_2|, |Z_2|$ in Fig. (4.1) and (4.2). The running masses are evaluated at the scale $M_{H_2^\pm} = 100$ GeV and take the values $tm_s(Q = M_{H_2^\pm}) = 0.0583$ GeV, $m_b(Q = M_{H_2^\pm}) = 3.058$ GeV, and $m_c(Q = M_{H_2^\pm}) = 0.686$ GeV. We take $Z_2 = 0.1$. From these two figures, it can be seen that a large BR($H_2^\pm \to cb$) is predicted in the region of $|X_2| > 4$ and $|Y_2| < 0.5$. The red and blue dashed lines of the figures show the approximate constraint from $b \to s\gamma$ in Eq. (4.41). The red dashed line is the bound for $|X_2 Y_2^*|$ =1.1, and the blue dashed line is for $|X_2 Y_2^*|$ =0.7, with the allowed region being below these lines. In Fig. (4.3) and (4.4) the value of Z_2 is changed to $|Z_2| = 0.8$.[7] For this value of $|Z_2|$ there is a reduction of BR($H_2^\pm \to cs$) with a maximum 0.15% in the bottom left corner of the right panel of Fig. (4.3). In the scenario of $|X_2| >> |Y_2|, |Z_2|$ with $|Z_2| < |Y_2|$, cb can be the dominant decay channel.

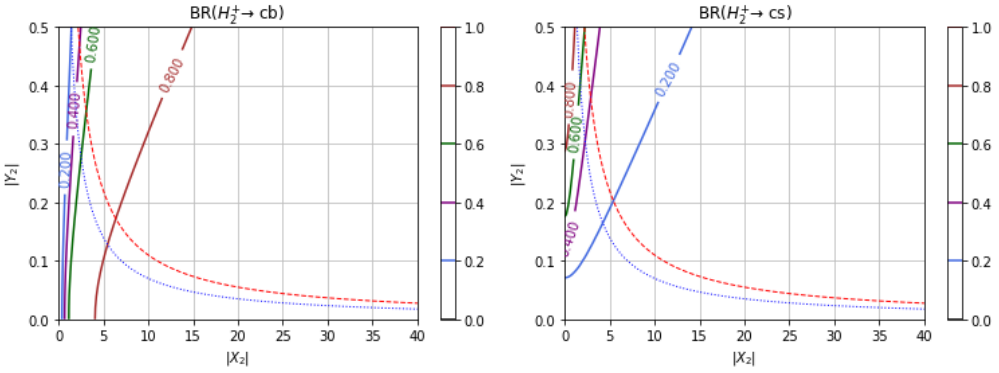

FIGURE 4.1: Top Left panel: Contours of BR($H_2^\pm \to cb$) in the plane [$|X_2|$, $|Y_2|$] with $|Z_2| = 0.1$. Top Right panel: Contours of BR($H_2^\pm \to cs$) in the plane [$|X_2|$, $|Y_2|$] with value of $|Z_2| = 0.1$. The mass of the light charged Higgs boson is $M_{H_2^\pm} = 100$ GeV. The region below the red and blue dashed lines are allowed by the (approximate) bounds in Eq. (4.41). The red line is $|XY^*|$ =1.1, and the blue line is $|XY^*|$ =0.7.

[6] All formula calculations are included that means even the ones from chapter 5 and chapter 6 are also calculated through SPYDER IDE.

[7] The label H_2^+ in all figure titles later on is actually $H_2^\pm$. i.e. All our results are ranging from H_2^+ and its conjugate state H_2^-.

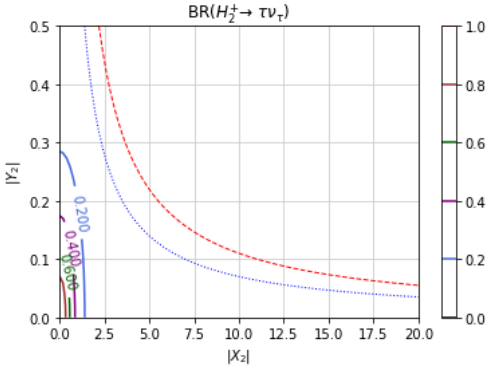

FIGURE 4.2: Contours of BR($H_2^\pm \to \tau\nu_\tau$) in the plane [$|X_2|$, $|Y_2|$] $|Z_2| = 0.1$. The mass of the light charged Higgs boson is $M_{H_2^\pm} = 100$ GeV. The red and blue dashed lines are same limits as Fig. (4.1).

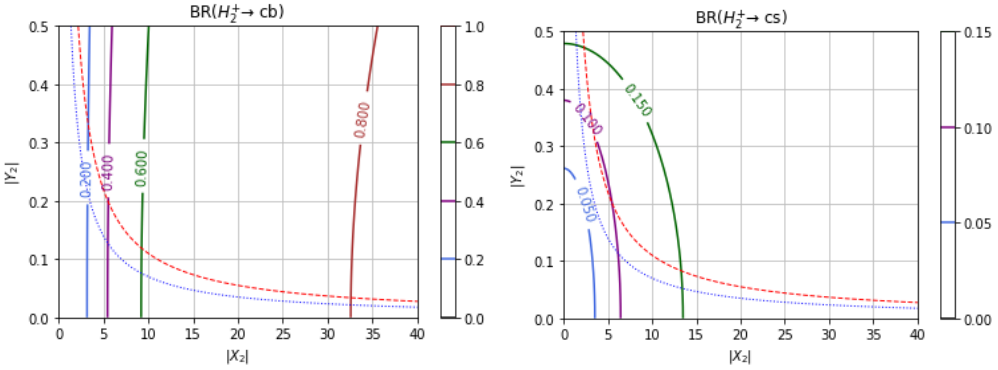

FIGURE 4.3: Top Left panel: Contour of BR($H_2^\pm \to cb$) in the plane [$|X_2|$, $|Y_2|$] with $|Z_2| = 0.8$. Top Right panel: Contours of BR($H_2^\pm \to cs$) in the plane [$|X_2|$, $|Y_2|$] with value of $|Z_2| = 0.8$. The mass of the light charged Higgs boson is $M_{H_2^\pm} = 100$ GeV. The red and blue dashed lines are the same limits as Fig. (4.1).

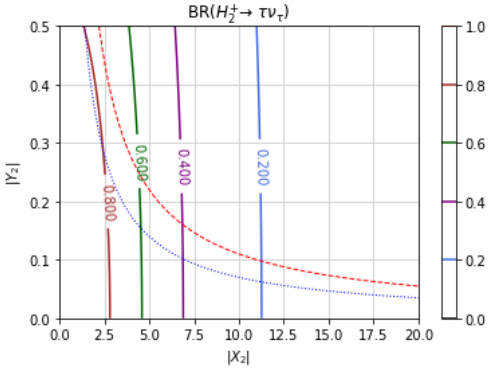

FIGURE 4.4: Contours of BR($H_2^\pm \to \tau\nu_\tau$) in the plane [$|X_2|$, $|Y_2|$] with $|Z_2| = 0.8$. The mass of the light charged Higgs boson is $M_{H_2^\pm} = 100$ GeV. The red and blue dashed lines are the same limits as Fig. (4.1).

4.4.3 Branching ratios of $H_2^\pm$ as a function of the parameters of the scalar potential

In this section the branching ratios of $H_2^\pm$ as a function of $\tan\beta, \tan\gamma, \theta, \delta$ (which are all functions of the parameters of the scalar potential) will be presented. We focus on specific type-Y (Flipped) and type-Z (Democratic) 3HDM, the Yukawa couplings for these two models differing in the coupling to the leptons. In type-I,-II, and X (lepton-specific) it is not possible to obtain a large BR of charged Higgs to cb. Tab. (4.2) list X_i,Y_i and Z_i in terms of the matrix elements of $U^\dagger$. In Fig. (4.5) to (4.8) the BRs in the type-Y (Flipped) 3HDM plots are shown, while in Fig. (4.9) the BRs in the type-Z (Democratic) 3HDM are shown.

The four mixing parameters are varied in the folllowing ranges (See Ref. [104]):

$$\begin{aligned} 0.1 < \tan\beta < 60 \qquad & 0.1 < \tan\gamma < 60, \\ -\frac{\pi}{2} < \theta < 0 \qquad & 0 < \delta < 2\pi \end{aligned} \tag{4.43}$$

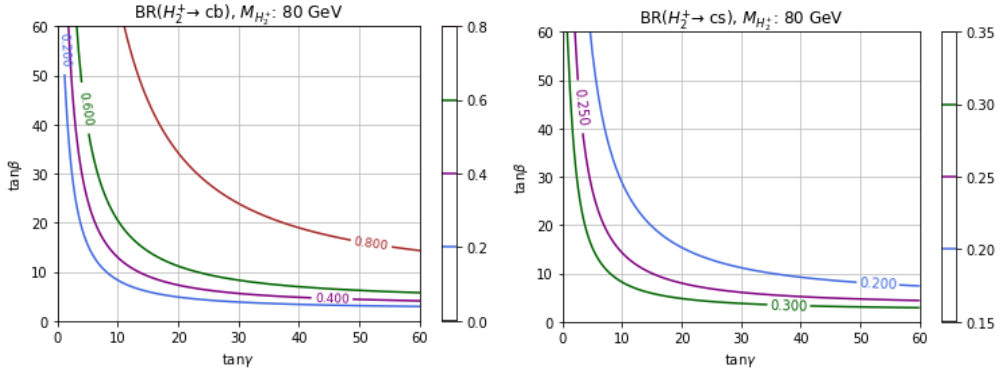

FIGURE 4.5: BRs in the plane $[\tan\gamma, \tan\beta]$ with value of $\theta = -\frac{\pi}{2.1}, \delta = 0.0$ in type-Y (Flipped) 3HDM. Left Panel: The contour of BR($H_2^\pm \to cb$). Right panel: The contour of BR($H_2^\pm \to cs$). The mass of the light charged Higgs mass is $M_{H_2^\pm} = 80$ GeV.

Firstly, we show the BRs of $(cb, cs, \tau\nu_\tau)$ in the plane $[\tan\beta, \tan\gamma]$ with the choice of $\theta = -\frac{\pi}{2.1}, \delta = 0.0$ in Fig. (4.5 and 4.6). The mass of the charged Higgs is $M_2^\pm = 80$ GeV. It can be seen that BR($H_2^\pm \to cb$) is large when $\tan\gamma$ and $\tan\beta$ are large, for this specific choice of parameters. BR($H_2^\pm \to cb$) of 60% can be achieved for $\tan\gamma$ and $\tan\beta > 10$, and could reach 80% with values of both larger than 20. For the approximate constraint of $\bar{B} \to X_s\gamma$, we used the Eq. (4.41) and plot in the same parameter plane as the right panel of Fig. (4.6). The coloured area is allowed by such a constraint, and would grow in size if $M_2^\pm$ GeV were increased. The CP-violation phase has been fixed to zero, leading to $\mathrm{Im}(X_2 Y_2^* = 0)$, and the above constraint on $\mathrm{Im}(X_2 Y_2^*)$ is automatically satisfied. These two figures will be referred to when we evaluate the charged Higgs significances based on LEP2 OPAL results in chapter 5.

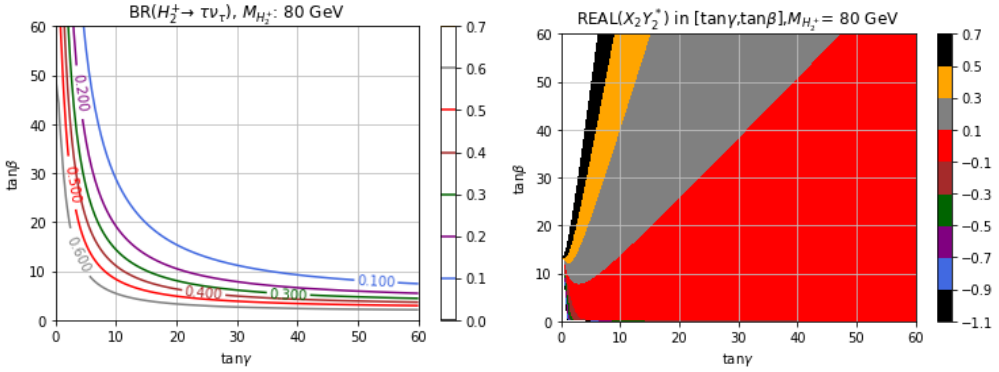

FIGURE 4.6: BR and Re($X_2Y_2^*$) in the plane [tan γ, tan β] with $\theta = -\frac{\pi}{2.1}, \delta = 0.0$ in type-Y (Flipped) 3HDM. Left panel: The contour of BR($H_2^\pm \to \tau\nu_\tau$). Right panel: Re($X_2Y_2^*$) in the range of (-1.1,0.7) which is the constraint of Eq. (4.41). All colour filled region is allowed. The mass of the light charged Higgs is $M_{H_2^\pm} = 80$ GeV.

In our paper Ref. [17], a figure the same as Fig. (4.5) was shown but with a different choice of $\theta(= -\frac{\pi}{3})$. Also, in that paper the light charged Higgs mass $M_{H_2^\pm}$ was set to 85 GeV. The figure can be seen as Fig. (4.7). The allowed parameter space for BR($H_2^\pm \to cb$) lies under the contour of Re($X_2Y_2^*$) = 0.7 in the right panel of the figure.

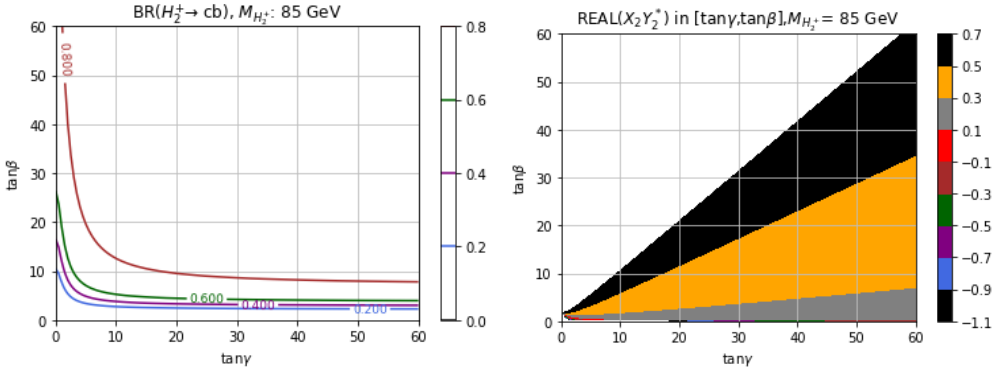

FIGURE 4.7: BR($H_2^\pm \to cb$) and Re($X_2Y_2^*$) constraint in plane [tan γ, tan β] with value of $\theta = -\frac{\pi}{3}, \delta = 0.0$ in type-Y (Flipped) 3HDM. Left panel: The contour of BR($H_2^\pm \to cb$). Right panel: The allowed area from the constraint Re($X_2Y_2^*$) as Eq. (4.41). All colour filled region is allowed. The mass of the light charged Higgs mass is $M_{H_2^\pm} = 85$ GeV.

In order to find parameter space for large BR($H_2^\pm \to cb$), we fix the value of tan β to be 10 to see the dependence on the value of θ. Here, the left panel of Fig. (4.8) displays the same charged Higgs mass as in plane [tan γ, θ] but with the choice of tan $\beta = 10, \delta = 0.0$ as Fig. (4.7). A large BR($H_2^\pm \to cb$) requires θ to be close to zero. In the right panel of Fig. (4.8), the constraint from Re($X_2Y_2^*$) is presented. For this choice of parameters, the constraint of Re($X_2Y_2^*$) limits the allowed area to be below 0.7. Thus, a large BR($H_2^\pm \to cb$) can be obtained while satisfying the approximate constraint on Re($X_2Y_2^*$).

Finally, in Fig. (4.9) we study the influence of CP-violation phase on BR($H_2^\pm \to cb$) in the parameter plane of $[\theta, \delta]$ with the choice of tan $\beta = 40$, tan $\gamma = 10$. We present

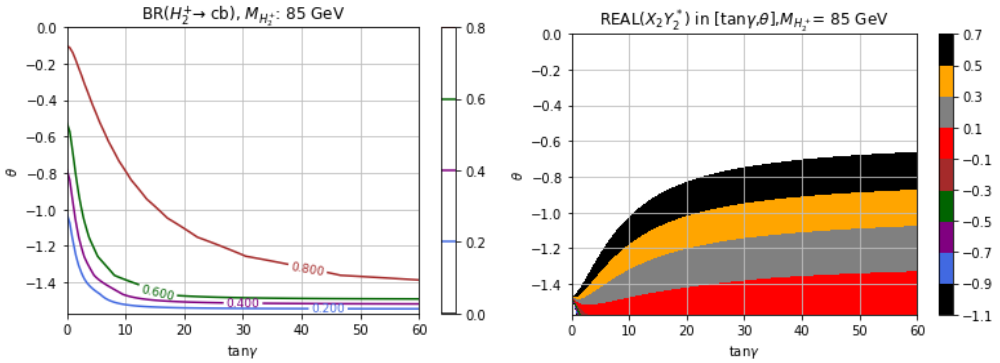

FIGURE 4.8: BR($H_2^\pm \to cb$) and Re($X_2Y_2^*$) constraint in the plane [tan γ, θ] with values tan $\beta = 10, \delta = 0$ in type-Y (Flipped) 3HDM. Left Panel: The contour of BR($H_2^\pm \to cb$). Right panel: The allowed area from the constraint Re($X_2Y_2^*$) as Eq. (4.41). All colour filled region is allowed. The mass of the light charged Higgs mass is $M_{H_2^\pm} = 85$ GeV.

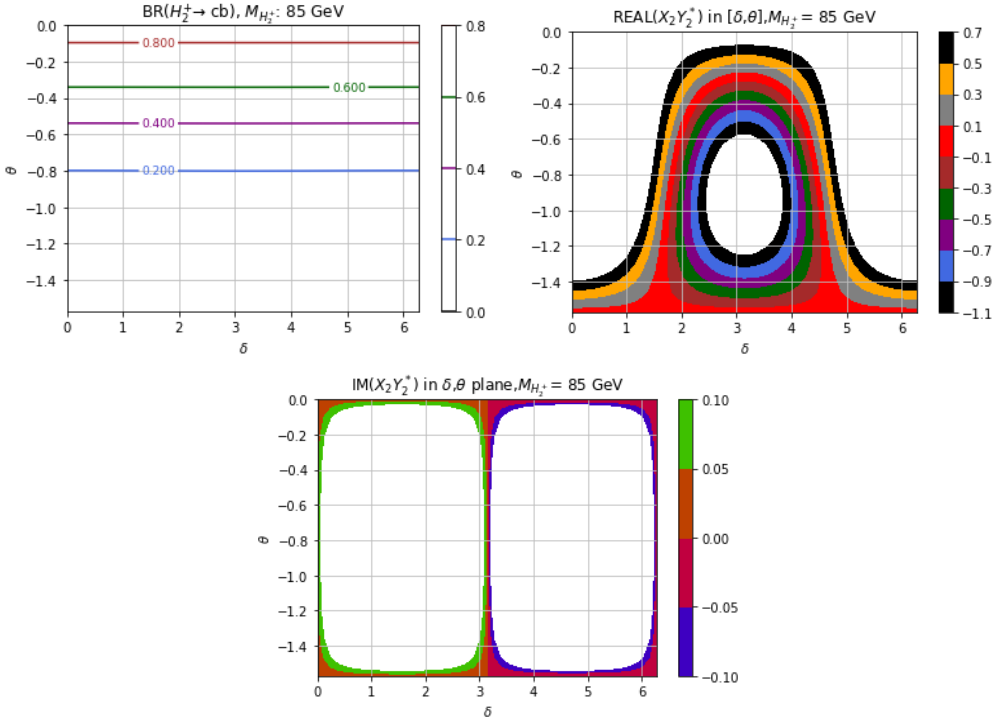

FIGURE 4.9: The type-Z (Democratic) 3HDM with tan $\beta = 40$, tan $\gamma = 10$ and $M_{H_2^\pm} =$ 85 GeV. Top left Panel: The contour of BR($H_2^\pm \to cb$) in $[\theta, \delta]$ plane. Top right panel: The contour of allowed Re($X_2Y_2^*$) as Eq. (4.41) constraint in $[\theta, \delta]$. Bottom panel: The contour of allowed Im($X_2Y_2^*$) as Eq. (4.42) constraint in plane $[\theta, \delta]$. All colour filled region is allowed.

the results in the model type-Z (Democratic) 3HDM. In the left panel, the CP-violation phase δ does not have any effect and BR($H_2^\pm \to cb$). In the right panel of Fig. (4.9), Re($X_2Y_2^*$) constrains the allowed parameter space to be in the area between - 1.1 and 0.7. The case of a large BR for cb channel satisfies the constraint from Re($X_2Y_2^*$). However, this region is also constrained by the electric-dipole moment (EDM) limit in the bottom panel figure. This constraint restricts Im($X_2Y_2^*$) and the allowed area is outside of the

two white colour ellipses in the bottom panel of Fig. (4.9). The allowed strip is close to π and gives the final allowed region for large BR($H_2^{\pm} \to cb$). Comparing two constraints, the EDM constraint restricts more parameter space and is the strongest bound for a light charged Higgs if the CP-violation phase δ is non-zero.

4.5 Conclusion

In this chapter, we mainly focused on 3HDM with two additional active Higgs doublets. Several motivations for the model were presented. Firstly we presented the potential of the 3HDM, which is a $SU(2) \times U(1)$ invariant scalar potential with two imposed Z_2 symmetries. In the 3HDM, three active Higgs doublets are introduced and each contains a VEV which obeys the SM sum rule. The minimisation conditions of the potential were discussed. We obtained the physical charged scalars $H_2^\pm, H_3^\pm$ by diagonalising the charged Higgs mass matrix. A unitary 3×3 matrix, which is similar to the CKM matrix, rotates the charged Higgs gauge eigenstates to the physical states. This unitary mixing matrix is parametrised by four mixing parameters (θ, the mixing angle between the two physical charged Higgs states; $\tan\beta$ and $\tan\gamma$, which involve the VEVs of the three doublets; δ, the CP-violating phase). The BRs of $H_2^\pm$ to fermions (the three dominant channels being $cs, cb, \tau\nu$) were studied with X_2,Y_2 and Z_2 as the input parameters. It was shown that BR($H_2^\pm \to cb$) could be large for $|X_2| >> |Y_2|, |Z_2|$, condition that can be satisfied in the type-Y (Flipped) and type-Z (Democratic) 3HDMs. Then we studied the fermionic BRs with the input parameters being $\tan\beta, \tan\gamma, \theta, \delta$ (and so X_2,Y_2 and Z_2 as output parameters). A sizeable parameter space for BR($H_2^\pm \to cb$) that satisfies the approximate limits of $\bar{B} \to X_s\gamma$ and the electron EDM was found in the above two types of 3HDM. In the next chapter we will discuss the search for the light charged Higgs to cb at colliders.

Chapter 5

Production of light charged Higgs in LEP and LHC with its search

5.1 Overview

In this chapter, we study the phenomenology of the production of the lightest charged Higgs boson $H_2^\pm$ in the 3HDM at the LEP collider. In the 3HDM, there exist two physical charged Higgs bosons ($H_2^\pm$,$H_3^\pm$). In the 2HDM, the mass of the charged Higgs boson in type-II and type-Y has to be larger than 400 GeV due to the constraint BR($\bar{B} \to X_s\gamma$) limit. Although the Flipped-type (type-Y) 2HDM could also have in principle a large BR in the cb channel [105], the fact that $M_{H^\pm} > 400$ GeV means that the decay channel $H^\pm \to tb$ would always be open and thus dominates due to the large top Yukawa coupling and $V_{tb} \approx 1$. In one of our papers [17], the charged Higgs boson with a mass lighter than top quark has been studied, and the BR of the charged Higgs boson to cb could be as large as 80% in a 3HDM. This was also discussed in the previous chapter. Such a scenario is of interest for colliders as the majority of searches for a light charged Higgs boson search focus on the decay modes cs and $\tau\nu_\tau$ [5; 7; 8; 10; 12; 106; 107; 108; 109; 110; 111; 112; 113; 114; 115; 116]. We first present the production of a light charged Higgs boson at both LEP and LHC. In both cases, we discuss the current experiment limits on the scenario of $M_{H^\pm} \leq m_t$ at each collider. We pay particular attention to the charged Higgs mass region 80 GeV $\leq M_{H^\pm} \leq$ 90 GeV, and we show that data taken at LEP2 when supplemented by $b-$tagging could discover or exclude a light $H^\pm$ state decaying to cb pairs more efficiently than LHC searches in the region 80 GeV $\leq M_{H^\pm} \leq$ 90 GeV. Furthermore, we consider the search for a charged Higgs boson at a proposed future circular e^+e^- collider with $\sqrt{s} = 240$ GeV.

5.2 LEP

5.2.1 Experiment groups of LEP

After the successful discovery of three massive vector gauge bosons ($W^{\pm}$, Z^0) from the proton-antiproton collider in 1983 [117; 118], the LEP (Large Electron Positron) collider was designed to study the Z boson in more detail. It was built on the border between France and Switzerland with a tunnel of circumference 26.65 km underground, with a depth of 50 to 175m [4]. The first collision of LEP was on August 13th 1989 and the last collision was on November 2rd 2000. In its period of operation a total number of four million pairs of Z bosons and 10000 $W^{\pm}$ pairs events were collected. The performance of LEP from 1989 to 2000 is given in Tab. (5.1).

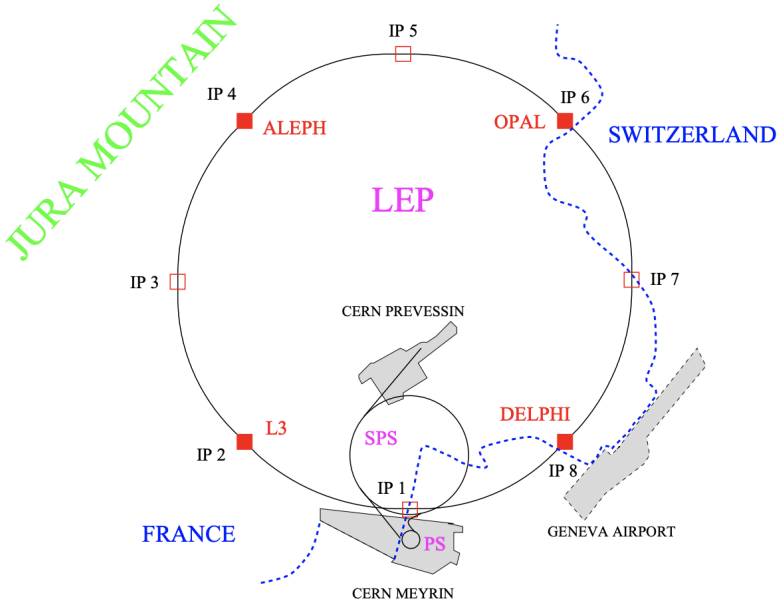

FIGURE 5.1: The LEP ring at CERN. In total there are 8 access points labelled as IP1 to IP8. At each red point there is a LEP experiment group. The two injectors, the SPS (Super Proton Synchroton) and PS (Proton Synchroton) are near the access point of IP1. The positrons are injected clockwise and the electrons are injected in the oppostie direction. This figure is taken from Fig. 1 in [4].

The experimental groups are at IP2 (Interaction Point 2), IP4 (Interaction Point 4), IP6 (Interaction Point 6), and IP8 (Interaction Point 8) and can be seen in Fig. (5.1) :

- Apparatus for LEP physics at CERN (ALEPH) [119].
- Detector with Lepton, Photon and hadron identification (DELPHI).
- Omni-purpose apparatus for LEP (OPAL).

YEAR	$\int \mathcal{L}dt$ (pb^{-1})	E_{beam} (GeV/c^2)	k_b	I_{tot}	$\mathcal{L}$
1989	1.74	45.6	4	2.6	4.3
1990	8.6	45.6	4	3.6	7
1991	18.9	45.6	4	3.7	10
1992	28.6	45.6	4/8	5.0	11.5
1993	40.0	45.6	8	5.5	19
1994	64.5	45.6	8	5.5	23.1
1995	46.1	45.6	8/12	8.4	34.1
1996	24.7	80.5-86	4	4.2	35.6
1997	73.4	90-92	4	5.2	47.0
1998	199.7	94.5	4	6.1	100
1999	253	98-101	4	6.2	100
2000	233.4	102-104	4	5.2	60

TABLE 5.1: Overview of LEP performance from 1989 to 2000. $\int \mathcal{L}dt$ is the luminosity integrated per experiment over each year and I_{tot} is the total beam current $k_b I_{\text{beam}}$. The luminosity $\mathcal{L}$ is given in units of (10^{30}cm^{-2}s^{-1}). The table is taken from Tab.2 of Ref. [11]

- L3 detector. The ALICE detector in CERN nowadays use the cavern which L3 used, and ALICE detector reuses the L3's magnet.

A much more detailed information of LEP can be found in [11].

5.2.2 LEP search for a charged Higgs boson

Searches for a charged Higgs boson in LEP were carried out in the context of the MSSM, for which the branching ratios to $H^{\pm} \to cs$ and $\tau\nu$ are dominant [107]. The LEP working group combined the separate searches from the four LEP experiments described above. These searches were carried out at energies in the range $\sqrt{s} = 183$ GeV and $\sqrt{s} = 209$ GeV with a total combined integrated luminosity of 2.6 fb^{-1} [5].

The production mechanism of a charged Higgs pair at LEP is shown in Fig. (5.2). The analytical expression is given by [95]:

$$\sigma_{e^+e^-\to H^+H^-} = \frac{\pi\alpha^2}{3s}\left(\sqrt{1-\frac{4M_{H^\pm}^2}{s}}\right)^3 F(s, M_Z, \Gamma_Z, \theta_W) \tag{5.1}$$

$$\begin{aligned}\text{Where } F(s, M_Z, \Gamma_Z, \theta_W) &= 1 - 2C_V C'_V \frac{s(s-M_Z^2)}{(s-M_Z^2)^2 + M_Z^2\Gamma_Z^2} \\ &+ C'^2_V(C_V^2 + C_A^2)\frac{s^2}{(s-M_Z^2)^2 + M_Z^2\Gamma_Z^2}\end{aligned} \tag{5.2}$$

The factors C_A,C_V, and C'_V in Eq. (5.2) are correlated to Weinberg angle (θ_W):

$$C_A = \frac{-1}{4\sin\theta_W\cos\theta_W},\ C_V = \frac{1-4\sin\theta_W^2}{4\sin\theta_W\cos\theta_W},\ C'_V = \frac{-1+2\sin\theta_W^2}{2\sin\theta_W\cos\theta_W} \tag{5.3}$$

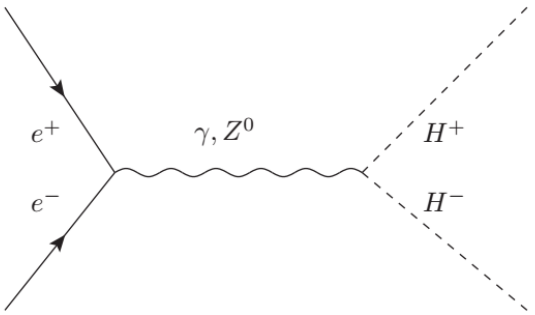

FIGURE 5.2: The possible Feynman diagram to produce charged Higgs pair H^+, H^- from electron and positron at LEP.

Here M_Z is the Z boson mass, Γ_Z is the width of Z boson and $\sqrt{s}$ is the total centre of mass energy from e^+e^-. Due to the term $(\sqrt{1-\frac{4M^2_{H^\pm}}{s}})^3$ in Eq. (5.1), cross section decreases when the mass of the charged Higgs boson increases. According to the above formulae, it is easily observed that the charged Higgs production through this mechanism depends on only one unknown parameter, and that is the charged Higgs boson mass ($M_{H^\pm}$).

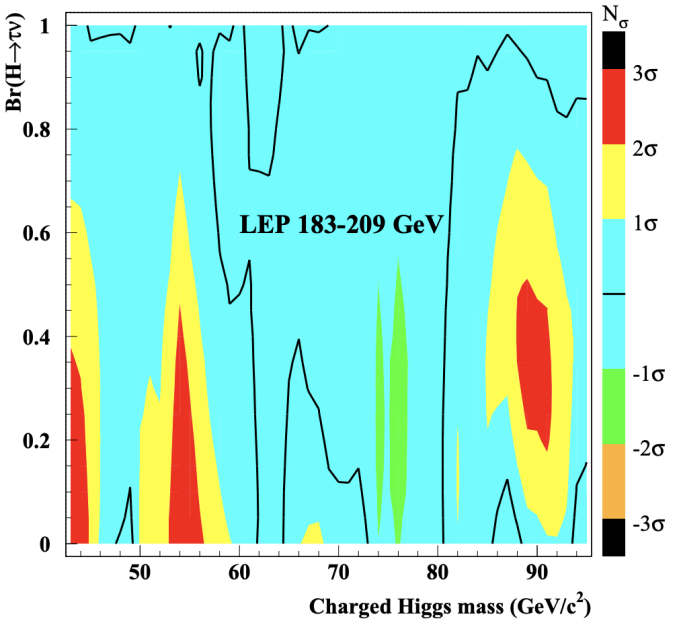

FIGURE 5.3: Result of search for the charged Higgs at LEP. Charged Higgs boson mass between 42 GeV and 96 GeV (x-axis) against the BR to $\tau\nu_\tau$ (y-axis). The colour bands indicate the statistical significance N_σ which shows from an excess of events (near read colour band) and a deficit of events (near orange colour band). The figure is from Ref. [5].

The decay of $H^\pm \to cb$ was not explicitly searched for at LEP2 [108; 109; 110; 111]. In the searches for the fermionic decay modes of $H^\pm$ it is assumed that BR($H^\pm \to cs$) + BR($H^\pm \to cb$) = 1, but the actual experimental search for $H^\pm \to cs$ would be also be sensitive to $H^\pm \to cb$ and other light favours of quark. The bosonic search for the decay mode $H^\pm \to AW^*$ is carried out in Ref. [5]. In our later data analysis of LEP2 search, however, we do not include the bosonic channel by taking the mass of A to be sufficiently heavy. From the search for fermionic decays the excluded region at 95% confidence level (CL) in the plane $[M_{H^\pm}, BR(H^\pm \to \tau\nu_\tau)]$ is shown in Fig. (5.3) which is taken from Ref. [5]. For the mass region of $H^\pm \leq 80$ GeV, the whole region of $0 \leq BR(H^\pm \to \tau\nu_\tau) \leq 100\%$ is already excluded. On the other side, the mass region between 80 GeV $\leq M_{H^\pm} \leq$ 90 GeV, most of the region is not excluded with $BR(H^\pm \to \tau\nu_\tau) \leq 80\%$ (i.e $BR(H^\pm \to cs) \geq 20\%$). Notably, there is an excess of events of greater than 2σ significances around the point $M_{H^\pm} = 90$ GeV. In a later discussion, we will show this scenario of BR($H^\pm \to cs$) = 65% and BR($H^\pm \to \tau\nu_\tau$) = 35% could readily accommodated in a 3HDM with appropriate choices of Yukawa couplings. In Ref. [97], it is mentioned that an excess like this is an example of a possible signal for $H^\pm$ that was just out of the range of LEP2. Such an excess, if genuine, could be observed at the LHC provided that the values of $|X|$ and $|Y|$ are large enough to ensure enough events of $t \to H^\pm b$ at a given integrated luminosity. If $|X|$ and $|Y|$ are sufficiently small then such an $H^\pm$ signal would escape the detection at the LHC, but could be observed at future e^+e^- colliders.

In Ref. [108], the ALEPH collaboration performed a search for a charged Higgs pair in three final decay states $cscs$, $cs\tau\nu_\tau$ and $\tau\nu_\tau\tau\nu_\tau$ with a centre of mass energy from 189 to 209 GeV and with a total 629 pb^{-1}. Within the framework of the 2HDM, the search assumed BR($H^\pm \to \tau\nu_\tau$) + BR($H^\pm \to c\bar{s}/\bar{c}s$) = 1. The DELPHI collaboration [109] took the framework of the 2HDM to search charged Higgs pairs in five final states W^*AW^*A, $\tau\nu_\tau W^*A$, $cscs$, $cs\tau\nu_\tau$ and $\tau\nu_\tau\tau\nu_\tau$. The L3 collaboration [110] took the same final states as in the ALEPH search and presented a lower limit on charged Higgs boson of 76.5 GeV at 95% Confidence level (CL). In the latest OPAL paper [111], the search was carried out for $\sqrt{s} = 189 - 209$ GeV and with 600 pb^{-1} integrated luminosity. A lower limit of 75.6 GeV was obtained under the assumption of BR($H^\pm \to \tau\nu_\tau$) + BR($H^\pm \to q\bar{q}$) = 1.

5.3 LHC

5.3.1 Experiment groups at LHC

The large hadron collider (LHC) is the world's largest and the most powerful particle acceleration collider. It uses the tunnel of the LEP collider (27km circumstances) and is a proton-proton collider at the CERN laboratory near Geneva, Switzerland [120]. Its

design centre of mass energy is $\sqrt{s}$ = 14 TeV, and in the completed Run II data was taken at $\sqrt{s}$ = 13 TeV.

There are eight experimental groups:

- A Toroidal LHC Apparatus (ATLAS): The purpose of this group mainly focus on discovery and precision measurement experiments.
- Compact Muon Solenoid (CMS): Same purpose as ATLAS. There are several differences between the two experiments. The major difference is from the solenoidal fields that are used. For ATLAS, the solenoid field is 2 Tesla while for CMS it is 4 Tesla.
- Large Hadron Collider beauty (LHCb): The purpose to study composite particles with b-quarks in order to study the decay $b-$quarks (i.e. rare b decays), including possible CP-violation.
- A Large Ion Collider Experiment (ALICE): This experiment group focuses on heavy-ion physics. The designing purpose is to study quark-gluon plasma. It is designed to understand the phenomenon of confinement which is described by QCD.
- Total Elastic and diffractive cross section Measurement (TOTEM experiment): The detector shares the interaction point with CMS. The aim for this experiment is to understand elastic scattering and diffraction processes.
- Large Hadron Collider forward (LHCf): The detector analyses neutral pion-particles produced from ATLAS in order to contribute to the understanding of cosmic astroparticles.
- Monopole and Exotics Detector at the LHC (MoEDAL): The main purpose is to search for magnetic monopole [121].
- ForwArd Search ExpeRiment (FASER) : The primary purpose of the FASER experiment is to search for new light and weakly interacting particles, that have not been discovered yet, such as dark photons, axion-like particles and sterile neutrinos [122; 123; 124].

The most significant achievement of the ATLAS and CMS experiments is the discovery of the Higgs boson in 2012 [125; 126]. The discovery completes the puzzle of mass generation of fermions and bosons mass from the breaking the electroweak symmetry. A much more detailed description of these two groups with their detectors can be found in refs. [127] and [128] respectively. For BSM charged Higgs searches, these two are the main experiments.

5.3.2 LHC search for charged Higgs

The search channel for a charged Higgs boson with a mass heavier than the top quark $M_{H^\pm} > m_t$ is the following:

$$pp \to tbH^\pm \to tbtb \tag{5.4}$$

The search channel for a charged Higgs with a mass lower than then top quark $M_{H^\pm} < m_t$ is the following channel:

$$pp \to \bar{t}t \to H^\pm b, W^\pm b \tag{5.5}$$

where p, p are the protons.

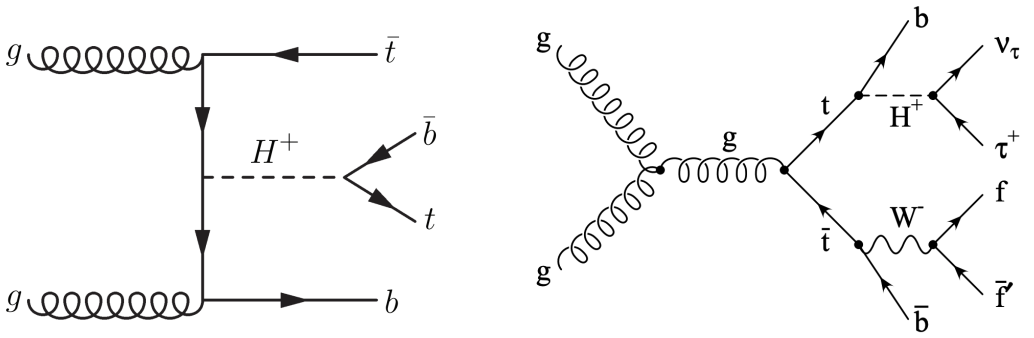

FIGURE 5.4: Left panel: One example of a LO Feynman diagram for the production of a charged Higgs boson which is heavier than m_t, in association with a t and a b quark from gluon-gluon fusion at the LHC. This figure is taken from Fig.1 of Ref. [6]. Right panel: One example of a LO Feynman diagram for the production of a charged Higgs boson which is lighter than the top quark mass m_t follows, which then decays to τ and ν_τ. This figure is taken from Ref. [7].

The Feynman diagrams for two search scenarios ($M_{H^\pm} > m_t$ [left panel of the Fig. (5.4)], $M_{H^\pm} < m_t$ [right panel of the Fig. (5.4)]) are shown. The number of expected Higgs events $R_{H^\pm}$ produced at a proton-proton collider is defined as the production cross-section multiplied by the integrated (accumulated) luminosity of the collider:

$$\begin{aligned} R_{H^\pm} &= \mathcal{L}_{\text{integrated}} \times \sigma(pp \to \bar{t}t \to H^\pm b, W^\pm b), \text{ or} \\ &= \mathcal{L}_{\text{integrated}} \times \sigma(pp \to \bar{t}t \to tbH^\pm \to tbtb) \end{aligned} \tag{5.6}$$

For charged Higgs lighter than the top quark at the LHC the main search channel is (5.5 and right panel of Fig. (5.4), and the expression for the partial width of ($t \to H^\pm b$) is:

$$\Gamma_{t\to H^\pm b} = \frac{G_f m_t}{8\sqrt{2}\pi}[m_t^2|Y|^2 + m_b^2|X|^2][1 - \frac{M_{H^\pm}^2}{m_t^2}]^2 \tag{5.7}$$

	ATLAS	CMS
7 TeV (5 fb^{-1})	cs [10] , $\tau\nu_\tau$ [7; 112],	$\tau\nu_\tau$ [12]
8 TeV (20 fb^{-1})	$\tau\nu_\tau$ [116]	cs [113], $\tau\nu_\tau$ [114], cb[9]
13 TeV (36 fb^{-1})	$\tau\nu_\tau$ [115]	$\tau\nu_\tau$ [8; 106]

TABLE 5.2: Searches for $H^\pm$ at the LHC, using $pp \to t\bar{t}$ and $t \to H^\pm b$. The given integrated luminosities are approximate. The search in [12] used 2 fb^{-1}.

The other top quark decays to $W^\pm$ and b with a partial width given by:

$$\Gamma_{t\to W^\pm b} = \frac{G_f m_t}{8\sqrt{2}\pi}[m_t^2 + 2M_W^2][1 - \frac{M_{W^\pm}^2}{m_t^2}]^2 \tag{5.8}$$

5.3.3 LHC limit on light charged Higgs

The LHC accumulated around 150 fb^{-1} of integrated luminosity at $\sqrt{s}$ = 13 TeV by the end of the year 2018, at which point long shut down 2 commenced. So far, the LHC has carried out a search for $H^\pm$ via three channels from top decay, $H^\pm \to cs, cb, \tau\nu_\tau$. These are summarised below.(see Tab (5.2)).

5.3.3.1 $H^\pm \to \tau\nu_\tau$

The searches for $H^\pm \to \tau\nu_\tau$ constrain the product of BR($t \to H^\pm b$) $\times$ BR($H^\pm \to \tau\nu_\tau$) in the mass region of 80 GeV $< M_{H^\pm} <$160 GeV, with the upper limit ranging from $<$ 0.36% for $M_{H^\pm}$ = 80 GeV to $<$ 0.08% for $M_{H^\pm}$ = 160 GeV. In the search for the decay of $H^\pm \to \tau\nu_\tau$ there are four basic signatures, which arise from the leptonic and hadronic decays of $H^\pm$ and $W^\pm$. Note that ATLAS used two different search strategies [7; 112] that give comparable sensitivity. In [7], the signatures that were searched for are lepton + jets, τ_{hadron}+ lepton, and τ_{hadron}+ jets while only τ_{hadron}+ jets is searched for in [112]. Only the CMS search [12] presented limits ($\geq$ 4%) for the mass range 80 GeV $\leq M_{H^\pm} \leq$ 90 GeV.[1]

In the searches for ($H^\pm \to \tau\nu_\tau$) with the 8 TeV data [116; 114] both the τ and the W boson from $t \to W^\pm b$ decay were taken to decay hadronically. This signature (of the four) offers the greatest sensitivity at present. The transverse mass of $H^\pm$ is calculated from its decay products of hadrons and missing energy.[2] Both the ATLAS and CMS searches presented limits for the mass range 80 GeV $\leq M_{H^\pm} \leq$ 90 GeV. Limits on the

[1]The label $\geq$ means the exclusion limit has set to this bound. For example, $\geq$ 4% means that above 4% is excluded. Similarly, $\geq$ 1% means that above 1% is excluded. On the other hand, label $<$ or $\leq$ means the allowed limit should be smaller then certain value. i.e. $<$ 0.36% means the upper limit sensitivity is 0.36% which below 0.36% is allowed.

[2]Transverse mass relates to the invariant mass m and the x and y direction momentum of the moving particle (these two direction are perpendicular to the z-direction, the particle collider beam-axis direction). It is defined as $M_T^2 = m^2 + p_x^2 + p_y^2$. Please see the section 48.5.2 in Ref. [129] for more details.

product BR($t \to H^\pm b$) $\times$ BR($H^\pm \to \tau\nu_\tau$) were obtained, being around $\geq 1\%$ for $M_{H^\pm}$ = 80 GeV and strengthening with increasing $M_{H^\pm}$ to $\geq 0.2\%$ for $M_{H^\pm}$ = 160 GeV.

The CMS search [106] with 13 TeV data and 13 fb^{-1} also used the hadronic decay of the τ from $H^\pm \to \tau\nu_\tau$, and selected the hadronic decay of the $W^\pm$. Similar limits to those in [116] and [114] were obtained, but are slightly weaker for the region 80 GeV $\leq M_{H^\pm} \leq$ 90 GeV. Recently a CMS search was carried out with 13 TeV data and 36 fb^{-1} [8], which combined separate searches for three of the four basic signatures (the case where both the $W^\pm$ and τ decay leptonically was not searched for). Significantly improved limits on BR($t \to H^\pm b$) $\times$ BR($H^\pm \to \tau\nu_\tau$) were obtained, ranging is given from the beginning as $\geq 0.36\%$ for $M_{H^\pm}$ = 80 GeV to $\geq 0.08\%$ for $M_{H^\pm}$ = 160 GeV.

There has been a search with the 13 TeV data [115] from the ATLAS collaboration using 36 fb^{-1}, with limits similar to those in [8] . In contrast to the ATLAS search with 8 TeV data [116], both the leptonic and hadronic decays of the $W^\pm$ boson were considered (the τ is still taken to decay hadronically). No limits are presented for the region 80 GeV $\leq M_{H^\pm} \leq$ 90 GeV but the sensitivity to $M_{H^\pm} >$ 90 GeV has improved e.g. for $M_{H^\pm}$ = 90 GeV the limit on BR($t \to H^\pm b$) $\times$ BR($H^\pm \to \tau\nu_\tau$) is $\geq 0.3\%$, and with the 8 TeV data it is $\geq 1.2\%$.

5.3.3.2 $H^\pm \to cs$

For the hadronic channel, the searches for $H^\pm$ via $H^\pm \to cs$ decay have constrained the product BR($t \to H^\pm b$) $\times$ BR($H^\pm \to cs$) in the mass region of 90 GeV $< M_{H^\pm} <$ 160 GeV. The upper limit is from $< 5\%$ for 90 GeV and $< 2\%$ for $M_{H^\pm}$ = 160 GeV. Note that this search would be sensitive to any flavour of quark (q, q') in the decay $H^\pm qq'$ (except the tb channel, which would not be open as a 2-body decay).

ATLAS carried out a search for $H^\pm \to cs$ [10] with 5 fb^{-1} of data at 7 TeV, while CMS [113] carried out a search for $H^\pm \to cs$ using 20 fb^{-1} of data at 8 TeV. The $W^\pm$ boson is taken to decay leptonically. Two tagged b quarks are required (which arise from the decay of the t quarks), and the invariant mass distribution of the two quarks that are not b-tagged (i.e. the c and s quarks that originate from $H^\pm$) is plotted. The signature of $H^\pm$ would be a peak at $M_{H^\pm}$ in this invariant mass distribution. Limits on the product of BR($t \to H^\pm b$) $\times$ BR($H^\pm \to cs$) are obtained, which range from around $\geq 5\%$ for $M_{H^\pm}$ = 90 GeV to 2% for $M_{H^\pm}$ = 160 GeV. Note that these limits are weaker than those for $H^\pm \to \tau\nu_\tau$ decay for a given $M_{H^\pm}$. In the invariant mass distribution the dominant background from $W^\pm \to qq$ decays gives rise to a peak around 80 GeV. Hence the expected sensitivity starts to weaken significantly with decreasing $M_{H^\pm}$ in the region 90 GeV $\leq M_{H^\pm} \leq$ 100 GeV, and there are no limits for the region 80 GeV $\leq M_{H^\pm} \leq$ 90 GeV.

5.3.3.3 $H^{\pm} \to cb$

The search for the channel $H^{\pm} \to cb$ constrains the product of BR($t \to H^{\pm}b$) $\times$ BR($H^{\pm} \to cb$) with the upper limit ranging from $\leq$ 1.4% for $M_{H^{\pm}}$ = 90 GeV to $\leq$ 0.5% for $M_{H^{\pm}}$ = 150 GeV. CMS carried out a search [9] for $H^{\pm} \to cb$ decay (assuming a branching ratio of 100%) with the leptonic decay of $W^{\pm}$. Signal events will have three b quarks, although one (or more) might not be tagged as a b quark. Two event categories were defined:

i) $3b + e^{\pm}$ and ii) $3b + \mu^{\pm}$.

A fitting procedure was carried out in order to correctly identify the tagged b quark that arises from $H^{\pm} \to cb$ which is then used (together with the non $b-$tagged c quark) in the invariant mass distribution of $M_{H^{\pm}}$. Due to BR($W^{\pm} \to cb$) being very small, the background to $H^{\pm} \to cb$ decays is much smaller than that for $H^{\pm} \to cs$. Combining both event categories results in limits on BR($t \to H^{\pm}b$) $\times$ BR($H^{\pm} \to cb$) of around $\geq$ 1.4% for $M_{H^{\pm}}$ = 90 GeV,which strengthens with increasing $M_{H^{\pm}}$ to $\geq$ 0.5% for $M_{H^{\pm}}$ = 150 GeV. These limits are stronger than those for $H^{\pm} \to cs$ decays for a given $M_{H^{\pm}}$. Although (unlike the case for $H^{\pm} \to cs$) the sensitivity does not diminish considerably in the range 90 GeV $\leq M_{H^{\pm}} \leq$ 100 GeV. Given the significantly lower backgrounds for the $3b$ signature arising from $H^{\pm} \to cb$ decays it is hoped that future searches (e.g. with 150 fb^{-1} and $\sqrt{s} = 13$ TeV) will be able to set limits on BR($t \to H^{\pm}b$) $\times$ BR($H^{\pm} \to cb$) in the region 80 GeV $\leq M_{H^{\pm}} \leq$ 90 GeV. Eventually, one would also expect some sensitivity in this region for the search with the $2b$ signature (which is sensitive to both $H^{\pm} \to cb$ and $H^{\pm} \to cs$ decays) with 150 fb^{-1} and above. However, the limits would (most likely) be inferior to those in the $3b$ channel for a given luminosity.

A search for $t \to H^{\pm}b$ via a different strategy (a "disappearance search", in contrast to the "appearance searches" above) was carried out at the Fermilab Tevatron. This would be sensitive to both $H^{\pm} \to cb$ and $H^{\pm} \to cs$. Such a search strategy has not yet been attempted at the LHC [130; 131]. A dedicated disappearance search at the LHC would be likely to improve on the Tevatron limit on BR($t \to H^{\pm}b$) $\times$ BR($H^{\pm} \to cs/cb$) of 20% [131] for 80 GeV $\leq M_{H^{\pm}} \leq$ 90 GeV. However, we are not aware of any LHC simulations, and so at present it is not clear whether or not this strategy could give a sensitivity that is competitive with that for the (ongoing) appearance searches at the LHC.

5.4 Numerical analysis at LHC, LEP2 and prospects at CEPC

We now present our results for the possible signal for $H_2^{\pm} \to cb$ in the 3HDM at the LHC, LEP2 and CEPC. We only consider the scenario of $M_{H_2^{\pm}} \leq m_t$ and assume only fermionic decay channels (i.e. masses of additional neutral Higgs, whether CP-even

or CP-odd, are chosen so that the decays $H_2^\pm \to hW^\pm$ (CP-even neutral Higgs and W boson) or $H_2^\pm \to AW^\pm$ (CP-odd neutral Higgs and W boson) are forbidden).

We show the parameter space in the 3HDM that is ruled out by the current LHC searches and discuss the prospects in future searches with increased integrated luminosity. The production mechanism relies on the Yukawa couplings and thus such a charged Higgs boson could escape detection at the LHC if these couplings are sufficiently small. It is of interest to study in more detail the LEP2 searches for a hadronically decaying charged Higgs (in which $H^\pm$ is produced in pairs via fixed gauge couplings rather than via Yukawa couplings). We study the effect of using $b-$quark tagging in the LEP2 search and show that the implementation of such tagging would increases the sensitivity to the decay $H_2^\pm \to cb$.

5.4.1 Analysis of LHC search region

In chapter 4, we displayed the BRs of three fermion decay modes of light charged Higgs $H_2^\pm$. We now study the magnitude of the product BR($t \to H^\pm b$) $\times$ BR($H^\pm \to cb$) [9] in the same plane of [$\tan\gamma, \tan\beta$] as the Figs. (4.5 and 4.6). The LHC searches are constraining the magnitude of this product of BRs. In our analysis, we used Eqs. (4.40 and 5.5) to obtain the product of BR($t \to H_2^\pm b$) $\times$ BR($H_2^\pm \to cb$) which can be compared with the CMS search [9] with three $b-$jet tags. In Ref. [9], the CMS search used $\sqrt{s} = 8$ TeV with $\mathcal{L} = 19.7$ fb^{-1} and showed the upper limit of the BR of top decays to charged Higgs with bottom quark via assumption of top decays to W and b equals to one with the masses of charged Higgs range between 90 and 150 GeV. We then study this BR under the mixing parameter plane of our Flipped 3HDM.

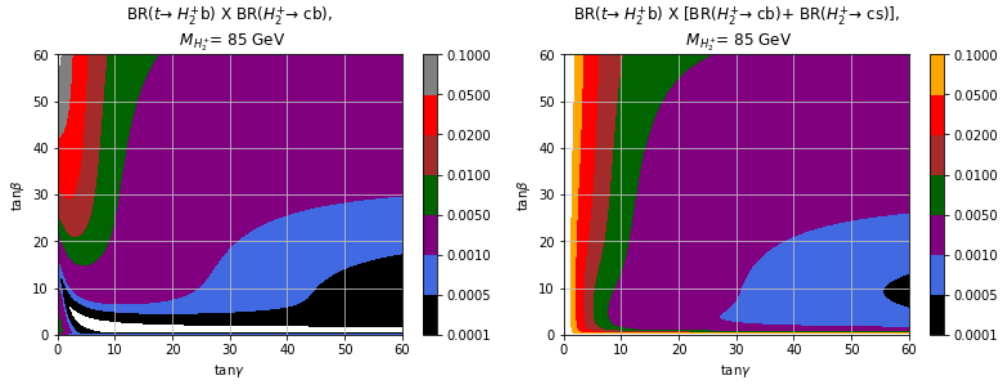

FIGURE 5.5: The type - Y (Flipped) 3HDM contour plots in the plane [$\tan\gamma, \tan\beta$] with the mass of $H_2^\pm = 85$ GeV, using the same θ, δ as Fig. (4.5). Left panel: BR($t \to H_2^\pm b$)$\times$ BR($H_2^\pm \to cb$). Right panel: BR($t \to H_2^\pm b$)$\times$ [BR($H_2^\pm \to cb$) + BR($H_2^\pm \to cs$)].

Figs. (5.5) and (5.6) are contour plots in the plane [$\tan\gamma, \tan\beta$] with $\theta = -\frac{\pi}{2.1}, \delta = 0$ for the product of BR($t \to H_2^\pm b$)$\times$ BR($H_2^\pm \to cb$) and BR($t \to H_2^\pm b$)$\times$ [BR($H_2^\pm \to cb$) + BR($H_2^\pm \to cs$)] with $M_{H_2^\pm} = 85$ and 130 GeV respectively. The left panel of Fig. (5.5)

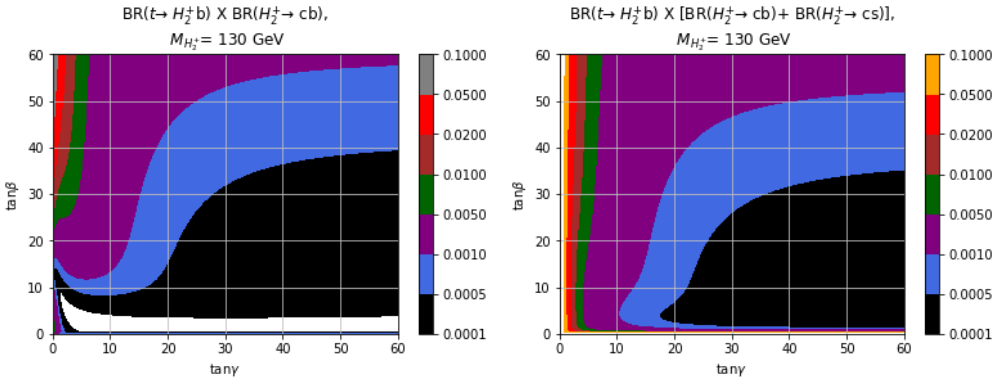

FIGURE 5.6: The type - Y (Flipped) 3HDM contour plots under mixing parameter plane [$\tan\gamma, \tan\beta$] with the mass of $H_2^\pm = 130$ GeV which used same θ, δ as Fig. (4.5). Left panel: BR($t \to H_2^\pm b$)$\times$ BR($H_2^\pm \to cb$). Right panel: BR($t \to H_2^\pm b$)$\times$ [BR($H_2^\pm \to cb$) + BR($H_2^\pm \to cs$)].

shows the product of BR($t \to H_2^\pm b$)$\times$ BR($H_2^\pm \to cb$) which is being constrained by the CMS search at the LHC using three $b-$tags as Ref. [9]. In comparison with [9] paper, there is no exclusion limit with the choice of charged Higgs mass at 85 GeV. The only limit in this mass region comes from the Tevatron search which gives $\leq 20\%$ in Ref. [131]. The search applies to any quark decay of the charged Higgs boson. In the figure the white region has a product of BRs much smaller than 0.0001 (0.01%). We expect that future searches at LHC with a centre of mass energy $\sqrt{s} = 13$ TeV with 150 fb^{-1} or more will obtain a lower limit less than 0.2. The right panel is the product BR($t \to H_2^\pm b$)$\times$ [BR($H_2^\pm \to cb$) + BR($H_2^\pm \to cs$)] which is the observable that is being constrained by the searches that use $2b-$tags as cs channel in Tab. (5.2). Using this $2b-$tags search, we expect the sensitivity should be less than the left panel since three $b-$tags has less backgrounds.

On the other hand, with the light charged Higgs mass $M_2^\pm = 130$ GeV, the same product is displayed in Fig. (5.6). In this scenario, the exclusion region is already known to be above 0.02 (which is 10 times stronger than the case with 85 GeV). Further details can be found in the references for LHC searches [9; 10; 113]. Thus, the allowed region is below the brown region in these two contour plots. The left panel of Fig. (5.6) rules out the top left corner above the brown area which constrains $\tan\beta$ to be less than roughly 35 and $\tan\gamma$ to be above roughly 2 or 3. Again, the white region of the left panel has a value smaller than 0.0001 (0.01%) for the product of BRs. On the right panel, the value of $\tan\gamma$ need to be larger than roughly 2 or 3. We expect future sensitivity to be 0.005 or less in the charged Higgs mass region between 90 and 160 GeV as the search from Tab. (5.2).

For the case of $\theta = -\frac{\pi}{3}$ and $\delta = 0$ as Fig. (4.7), we show four additional plots in Fig. (5.7) and (5.8). These two figures are from our work in Ref. [17]. The left panel of Fig. (5.7) shows the product of BR($t \to H_2^\pm b$)$\times$ BR($H_2^\pm \to cb$) as contours in the plane [$\tan\gamma, \tan\beta$] while the right panel shows the product of BR($t \to H_2^\pm b$)$\times$ [BR($H_2^\pm \to cb$)

+ BR($H_2^\pm \to cs$)]. The charged Higgs mass ($M_{H_2^\pm}$) has been set to 85 GeV. For the LHC search channel with 3 b-tags all colour filled areas below the grey band are allowed since almost all of the area of this parameter space is below 0.2. The white strip in the figure is ruled out since that area is above 0.2. Again, the right panel of Fig. (5.7) is the $2b$ LHC search, for which we expect more luminosity to obtain a given sensitivity.

In Fig. (5.8) the exclusion limit of value 0.02 actually rules out part of left panel BR($t \to H_2^\pm b$)$\times$ BR($H_2^\pm \to cb$) product. The allowed parameter space for this plot is only the region under the brown shaded area. In the coloured region of green, purple, blue and black, a potential signal for charged Higgs could exist.

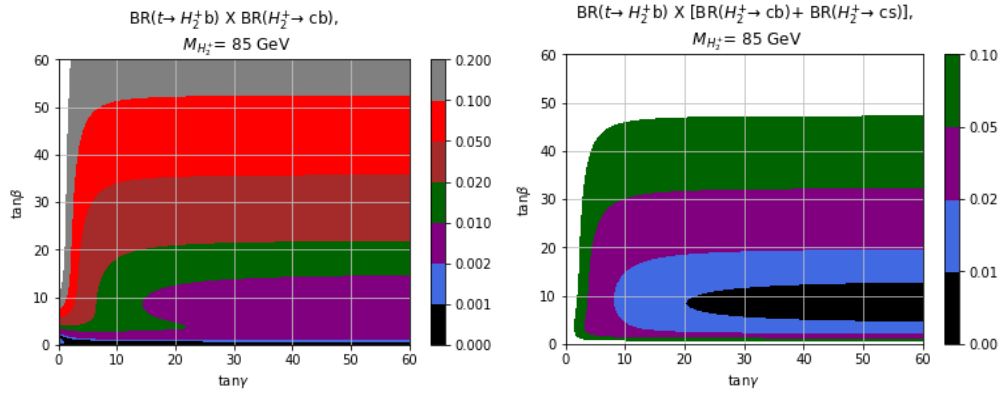

FIGURE 5.7: The type - Y (Flipped) 3HDM contour plots in the plane [$\tan\gamma, \tan\beta$] with the mass of $H_2^\pm = 85$ GeV using the same θ, δ as Fig. (4.7). Left panel: BR($t \to H_2^\pm b$)$\times$ BR($H_2^\pm \to cb$). Right panel: BR($t \to H_2^\pm b$)$\times$ [BR($H_2^\pm \to cb$) + BR($H_2^\pm \to cs$)].

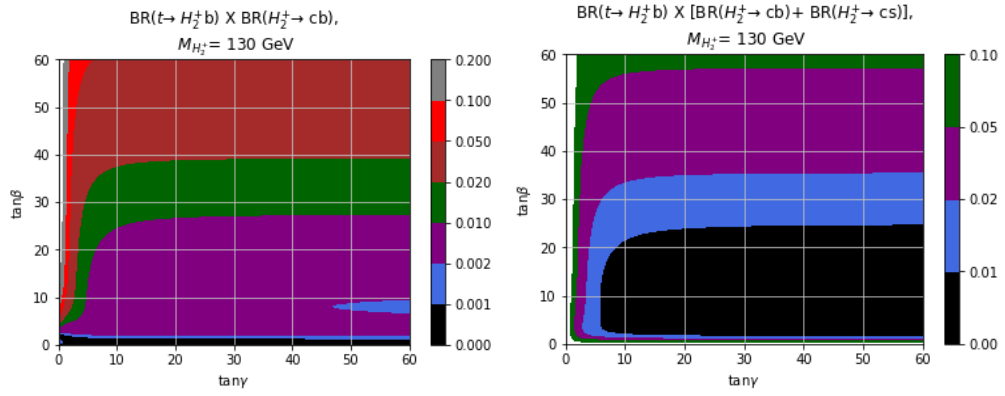

FIGURE 5.8: The type - Y (Flipped) 3HDM contour plots under mixing parameter plane [$\tan\gamma, \tan\beta$] with the mass of $H_2^\pm = 130$ GeV which used same θ, δ as Fig. (4.7). Left panel: BR($t \to H_2^\pm b$)$\times$ BR($H_2^\pm \to cb$). Right panel: BR($t \to H_2^\pm b$)$\times$ [BR($H_2^\pm \to cb$) + BR($H_2^\pm \to cs$)].

5.4.2 LEP2 data and future electron-positron collider analysis strategy

At the LEP collider, an important difference with the searches for $H^{\pm}$ at hadron colliders is that the couplings X, Y, Z do not appear in the production cross-section for $e^+e^- \to H^+H^-$, which can be seen from the cross section in Eq. (5.1). Instead, the cross section depends on only one unknown parameter, the mass of the charged Higgs boosn ($M_{H^{\pm}}$). Hence this production mechanism at e^+e^- colliders can produce $H^{\pm}$ even with very small values of X, Y, Z provided that $2M_{H^{\pm}} \leq \sqrt{s}$. At LEP2, the charged Higgs search from fermion decay modes considers two channels, $H^{\pm} \to cs$ and $H^{\pm} \to \tau\nu_{\tau}$. From these two decay channels the pair production of charged Higgs leads to three signature possibilities, $cscs$, $\tau\nu_{\tau}\tau\nu_{\tau}$, and $cs\tau\nu_{\tau}$. There was no dedicated search for $H^{\pm} \to cb$ at any of the LEP2 experiments [108; 109; 110; 111]. A search in the cb channel would make used of the experimental search strategy for $cs\tau\nu_{\tau}$ and $cscs$. The quarks hadronise and so the latter two channels give the following signatures: i) 4-jets channel. ii) 2-jets (with $\tau\nu_{\tau}$) channel.

In the 4-jets channel for light charged Higgs boson at LEP, the dominant hadronic decay mode was assumed to be cs, and this is the case within 2HDMs. The DELPHI collaboration [109] used c-tagging of the c quarks in $H^{\pm} \to cs$ in order to reduce backgrounds while the other three collaborations did not [108; 110; 111]. In the 2-jets (with $\tau\nu_{\tau}$) channel, the signature is from one charged Higgs decay to $\tau\nu_{\tau}$ and the other decaying to a quark pair.

In this section, we recast the LEP2 OPAL analysis [132] background events and use the Eq. (5.1) to simulate the charged Higgs signals with the centre of mass energies $\sqrt{s} = 189 \to 209$GeV and the luminosity $\mathcal{L} = 0.6$ fb^{-1} at LEP2. By using the quark tagging efficiencies $\epsilon_{b,c,j}$, we calculated the statistical signficances ($S/\sqrt{B}$) based on the background of OPAL paper and our signal results. We studied the two charged Higgs search channels (i) 4-jets channel. ii) 2-jets (with $\tau\nu_{\tau}$ channel.). We also studied the effect of applying a b quark tag to increase the sensitivity from the decay of charged Higgs to cb, which could have a large BR in type-Y (Flipped) 3HDM. A $b-$tag is a cut on the impact parameter (defined below) of a jet, and such a cut can remove light quark events (which would have a smaller impact parameter). The lifetime of B meson is normally considerably longer than that of lighter quarks, and the impact parameter is proportional to the lifetime of the quark. The 4-jets channel can be separated into two separate cases: the first one is the requirement of exactly two $b-$tagged jets, and the second one is requiring exactly one $b-$tagged jet. In the 2-jets with $\tau\nu_{\tau}$ channel there is just one case in which exactly one jet is tagged as a $b-$quark. Using the selection cuts for the LEP 4-jets and 2-jets (with $\tau\nu_{\tau}$) channels, we study the effect of adding the the b-tag requirement to improve the sensitivity to a light charged Higgs decay that decays to cb in. In our numerical values of the statistical significances of a signal for $H_2^{\pm} \to cb$, LEP2 operated at a centre of mass energy between $189 \to 209$ GeV while

CEPC/FCC-ee case would operate at a centre of mass energy of $\sqrt{s} = 240$ GeV. In the numerical analysis at LEP2 the b-tag efficiency (ϵ_b) is taken to be $\epsilon_b = 0.7$, while the fake b-tag efficiencies for charm quarks (ϵ_c) and u; d; s quarks (ϵ_j) are $\epsilon_c = 0.06$ and $\epsilon_j = 0.01$ respectively. These numbers are roughly similar (although slightly optimistic for ϵ_b) to those in the OPAL measurement of R_b in Ref. [133] for $\sqrt{s} = 189 \rightarrow 209$ GeV. Due to ϵ_c and ϵ_j being small we will not consider the signatures of three or four tagged b-jets, in which one or two non-b quarks have been mistagged as b quarks. In our numerical analysis at CEPC/FCC-ee, ϵ_c is arised in the range $0.01 \leq \epsilon_c \leq 0.06$, while ϵ_b and ϵ_j are conservatively taken to have the same values as at LEP2. Each LEP2 experiment accumulated around 0.6 fb^{-1} of integrated luminosity (L), while at CEPC/FCC-ee at least 1000 fb^{-1} is expected. These input parameters are summarised in Tab 5.3.

	$\sqrt{s}$ (GeV)	$\mathcal{L}$(fb^{-1})	ϵ_b	ϵ_c	ϵ_j	$M_{H^\pm}$ (GeV)
LEP2	$189 \rightarrow 209$	0.6	0.7	0.06	0.01	$80 \rightarrow 90$
CEPC/FCC-ee	240	1000	0.7	$0.01 \rightarrow 0.06$	0.01	$80 \rightarrow 120$

TABLE 5.3: Input parameters used in the numerical analysis at LEP2 and at CEPC/FCC-ee.

In what follows below the three dominant decay channels are denoted as BR_{cb}, BR_{cs}, and $BR_{\tau\nu_\tau}$ respectively. In next section, we will firstly show the selection strategy from the LEP searches without b tagging.

5.4.2.1 LEP2 signal for charged Higgs to c and b quark pair.

The number of events of pair-produced charged Higgs bosons from e^+e^- collisons (with no $b-$tagging applied) in the search of 4-jets and 2-jets channels are denoted as $S_{4\text{jnobtag}}$ and $S_{2\text{j}\tau\text{nobtag}}$ respectively in the expressions below:

4-jets without $b-$tag:

$$S_{4\text{jnobtag}} = \sigma \times \mathcal{L} \times \epsilon_{4\text{jnobtag}} \times (BR_{cb} + BR_{cs})^2 \tag{5.9}$$

BR_{cb} and BR_{cs} are summed since no $b-$tag is applied in this search channel.

2-jets (with $\tau\nu_\tau$) without $b-$tag:

$$S_{2\text{j}\tau\text{nobtag}} = \sigma \times \mathcal{L} \times \epsilon_{2\text{j}\tau\text{nobtag}} \times 2(BR_{cb} + BR_{cs}) \times BR_{\tau\nu_\tau}. \tag{5.10}$$

BR_{cb} and BR_{cs} are summed again for total hadronic channel without $b-$tag. The factor of 2 is present there are two distinct combinations (from $c\bar{s}\tau^-\bar{\nu_\tau}$ and $\bar{c}s\tau^+\nu_\tau$) that contribute to the signal.

In the above equations σ denotes the cross section for charged Higgs pair production at LEP, and for this we use Eq. (5.1); $\mathcal{L}$ is the integrated luminosity at the centre-of-mass energy $\sqrt{s}$. At LEP2, charged Higgs searches were carried out at eight different values of $\sqrt{s}$, each with a unique integrated luminosity. The eight individual $\mathcal{L}$ are summed to obtain the total $\sigma\mathcal{L}$. The parameters $\epsilon_{4\text{jnobtag}}$ and $\epsilon_{2\text{j}\tau\text{nobtag}}$ are the efficiency of the selection cuts for the 4-jets and 2-jets searches at LEP. For their magnitudes we take the numerical values in the search of the OPAL collaboration. Now that we have discussed the selection efficiencies of the 4-jets and 2-jets searches without b tagging, we now move to the case of applying b tagging. As mentioned previously, the two search channels will be separated into three cases (4-jets with exactly two $b-$tags, 4-jets with exactly one $b-$tag, and the 2-jets with exact one $b-$tag.).

5.4.2.2 Signal in 4-jets with exact 2 $b-$jets

$$\begin{aligned} S_{4\text{j2btag}} &= \sigma \times \mathcal{L} \times \epsilon_{4\text{jnobtag}} \\ &\times \left(BR_{cb}BR_{cb}\epsilon^{cbcb}_{4\text{j2btag}} + 2BR_{cb}BR_{cs}\epsilon^{cbcs}_{4\text{j2btag}} + BR_{cs}BR_{cs}\epsilon^{cscs}_{4\text{j2btag}}\right) \end{aligned} \tag{5.11}$$

The number 2 in the second term of above expression denotes the two possibilities signatures of $c\bar{b}\bar{c}s$ and $\bar{c}bc\bar{s}$.

$$\epsilon^{cbcb}_{4\text{j2btag}} = \epsilon_b^2\,(1-\epsilon_c^2) + 4\,\epsilon_b\,\epsilon_c\,(1-\epsilon_b)\,(1-\epsilon_c) + \epsilon_c^2\,(1-\epsilon_b)^2 \tag{5.12}$$

$$\epsilon^{cscs}_{4\text{j2btag}} = 4\,\epsilon_c\,\epsilon_j\,(1-\epsilon_c)\,(1-\epsilon_j) + \epsilon_c^2\,(1-\epsilon_j)^2 + \epsilon_j^2\,(1-\epsilon_c)^2 \tag{5.13}$$

$$\begin{aligned} \epsilon^{cbcs}_{4\text{j2btag}} &= 2\epsilon_b\,\epsilon_c\,(1-\epsilon_c)\,(1-\epsilon_j) + \epsilon_b\,\epsilon_j(1-\epsilon_c)^2 \\ &+ 2\,\epsilon_c\,\epsilon_j\,(1-\epsilon_b)\,(1-\epsilon_c) + \epsilon_c^2\,(1-\epsilon_b)\,(1-\epsilon_j) \end{aligned} \tag{5.14}$$

Using values of ϵ_b, ϵ_c, and ϵ_j in Tab. (5.3), the three expressions would give roughly values of 0.048, 0.005, and 0.086 for $\epsilon^{cbcb}_{4\text{j2btag}}, \epsilon^{cscs}_{4\text{j2btag}}, \epsilon^{cbcs}_{4\text{j2btag}}$ respectively.[3] In the term $\epsilon^{cbcb}_{4\text{j2btag}}$, the three expressions denote the cases of two tagged $b-$jets from i) two real b quarks, ii) one real b and one fake b quark (e.g. a mistagged c quark as a b quark.), iii) two fake b quarks. In $\epsilon^{cscs}_{4\text{j2btag}}$, the terms are expressed as three parts which are from two fake b quarks. $\epsilon^{cbcs}_{4\text{j2btag}}$ has four parts, in which the first two are from the case of one real and one fake b quark, and the last two terms are the cases for two fake b quarks. In each expression, the factor of 2 or 4 represents the various combinations (e.g. $c\bar{s}$ and $\bar{c}s$ are two signatures which contribute to the fake b quark tags in the expression of $\epsilon^{cbcs}_{4\text{j2btag}}$ and this leads to a factor of 2 in front).

[3] ϵ_b means real b quark tagged, $(1-\epsilon_b)$ means not tag as b quark. ϵ_c means fake c quark as b quark and $(1-\epsilon_c)$ means not fake c quark as b quark. For other light quarks, we denote as j and ϵ_j means mistagged a light quark as b quark. Similarly, $(1-\epsilon_j)$ will be not mistagged a light quark as b quark.

5.4.2.3 Signal in 4-jets with exact 1 $b-$jet

$$\begin{aligned} S_{\text{4j1btag}} &= \sigma \times \mathcal{L} \times \epsilon_{\text{4jnobtag}} \\ &\times \ (BR_{cb}BR_{cb}\epsilon^{cbcb}_{\text{4j21btag}} + 2BR_{cb}BR_{cs}\epsilon^{cbcs}_{\text{4j1btag}} + BR_{cs}BR_{cs}\epsilon^{cscs}_{\text{4j1btag}}) \end{aligned} \tag{5.15}$$

The explicit expressions for $\epsilon^{cbcb}_{\text{4j1btag}}$, $\epsilon^{cscs}_{\text{4j1btag}}$, and $\epsilon^{cbcs}_{\text{4j1btag}}$ are as follows:

$$\epsilon^{cbcb}_{\text{4j1btag}} = 2\,\epsilon_b\,(1-\epsilon_b)\,(1-\epsilon_c)^2 + 2\,(1-\epsilon_b)^2\,\epsilon_c\,(1-\epsilon_c) \tag{5.16}$$

$$\epsilon^{cscs}_{\text{4j1btag}} = 2\,\epsilon_j\,(1-\epsilon_c)^2\,(1-\epsilon_j) + 2\,\epsilon_c\,(1-\epsilon_c)\,(1-\epsilon_j)^2 \tag{5.17}$$

$$\begin{aligned} \epsilon^{cbcs}_{\text{4j1btag}} &= \epsilon_b\,(1-\epsilon_c)^2\,(1-\epsilon_j) \\ &+ \ 2\,(1-\epsilon_b)\,\epsilon_c\,(1-\epsilon_c)\,(1-\epsilon_j) + \epsilon_j\,(1-\epsilon_b)\,(1-\epsilon_c)^2 \end{aligned} \tag{5.18}$$

The values are roughly 0.38, 0.13, and 0.65 for $\epsilon^{cbcb}_{\text{4j1btag}}$, $\epsilon^{cscs}_{\text{4j1btag}}$, and $\epsilon^{cbcs}_{\text{4j1btag}}$ respectively by inserting the values of ϵ_b, ϵ_c, and ϵ_j. In the expression of $\epsilon^{cbcb}_{\text{4j1btag}}$, the first term has the one real b quark, and the second term has one fake b quark case. The first term of expression $\epsilon^{cscs}_{\text{4j1btag}}$ shows the fake b quark comes from s quark and in the second term the fake b quark comes from the c quark. In the expression of $\epsilon^{cbcs}_{\text{4j1btag}}$, the first term gives one real b quark case. The second term gives one fake b comes from the c quark and the last one is one fake b coming from an s quark. Here, again, the number 2 in front of some terms represents the variation combinations (e.g. $2\,\epsilon_b\,(1-\epsilon_b)\,(1-\epsilon_c)^2$ means one of the b quark can be tagged and there are two possibilities since $cbcb$ have two b quarks so first b can be selected one possibility and the other b can also be selected for the second possibility. This affects a factor 2 in front of the term $\epsilon_b\,(1-\epsilon_b)\,(1-\epsilon_c)^2$. Similarly, other terms in $\epsilon^{cscs}_{\text{4j1btag}}$ and $\epsilon^{cbcs}_{\text{4j1btag}}$ have the same situation.)

5.4.2.4 Signal in 2-jets with exact 1 $b-$jet

$$\begin{aligned} S_{\text{2j1btag}} &= \sigma \times \mathcal{L} \times \epsilon_{\text{2jnobtag}} \\ &\times \ 2(BR_{cb}BR_{\tau\nu_\tau}\epsilon^{cb\tau\nu_\tau}_{\text{2j1btag}} + BR_{cs}BR_{\tau\nu_\tau}\epsilon^{cs\tau\nu_\tau}_{\text{2j1btag}}) \end{aligned} \tag{5.19}$$

The explicit expressions for $\epsilon^{cb\tau\nu_\tau}_{\text{2j1btag}}$ and $\epsilon^{cs\tau\nu_\tau}_{\text{2j1btag}}$ are as follows:

$$\epsilon^{cb\tau\nu_\tau}_{\text{2j1btag}} = \epsilon_b\,(1-\epsilon_c) + \epsilon_c\,(1-\epsilon_b) \tag{5.20}$$

$$\epsilon^{cs\tau\nu_\tau}_{\text{2j1btag}} = \epsilon_c\,(1-\epsilon_j) + \epsilon_j\,(1-\epsilon_c) \tag{5.21}$$

The numerical values are roughly 0.68 and 0.07 for $\epsilon^{cb\tau\nu_\tau}_{\text{2j1btag}}$ and $\epsilon^{cs\tau\nu_\tau}_{\text{2j1btag}}$ respectively. The first term of expression $\epsilon^{cb\tau\nu_\tau}_{\text{2j1btag}}$ gives one real b quark and the second term gives one

fake b quark that comes from a c quark. $\epsilon^{cs\tau\nu_\tau}_{\text{2j1btag}}$ shows that the b tagged quark is a fake b, coming from either the c quark and or the s quark.

5.4.2.5 Background to light charged Higgs to cb decay

The background to the above three signal selections are denoted by B_{4j2btag}, $B_{4j1b\text{tag}}$, and $B_{2j+\tau 1b\text{tag}}$ respectively. The main contributions for B_{4j2btag} $B_{4j1b\text{tag}}$ are from 4-fermion production in electron-positron collisions. The main contribution is from W^+W^- pairs with a small amount contribution from ZZ. Another contribution is from 2-fermion production (e.g. $e^+e^- \to \gamma^*, Z^* \to q\bar{q}gg$), which can give four jets. The main contribution for $B_{2j+\tau 1b\text{tag}}$ is coming from W^+W^- production.

In order to evaluate the background before imposing $b-$tagging we use the numbers from the OPAL search paper. For simplicity we assume a diagonal CKM matrix, which takes BR($W^\pm \to cs$) = BR($W^\pm \to ud$) = 35%. OPAL had around 1100 4-jet events after all cuts, of which 90% are expected to be from 4-fermion events. With the assumption of a diagonal CKM matrix this background would be composed of 250 *cscs* events, 250 *udud* events and 500 *csud* events. Given these numbers, it turns out that the contributions to the background from $W^\pm \to cb$ decays can be neglected because its branching ratio is about 600 times smaller than that of $W^\pm \to cs$. The contribution of $W^+W^- \to cbcb$ to the background would be much less than one event (= $\frac{250}{600^2}$), and the contributions from $W^+W^- \to cbcs$ and $W^+W^- \to cbud$ would each be less than one event (= $\frac{500}{600}$), before b-tagging is imposed.

5.4.2.6 Background to 4-jets channel with exactly two $b-$tagged jets

The 4-fermion background to the 4-jet signal with two tagged b quarks is given by:

$$B^{4fermion}_{\text{4j2btag}} = 1000 \times (0.25 \times \epsilon^{W_{cscs}}_{\text{4j2btag}} + 0.5 \times \epsilon^{W_{csud}}_{\text{4j2btag}} + 0.25 \times \epsilon^{W_{udud}}_{\text{4j2btag}}). \tag{5.22}$$

$$\begin{aligned}
\epsilon^{W_{cscs}}_{\text{4j2btag}} &= 4\,\epsilon_c\,\epsilon_j\,(1-\epsilon_c)\,(1-\epsilon_j) + \epsilon_c^2\,(1-\epsilon_l^2) + \epsilon_l^2\,(1-\epsilon_c)^2 \\
\epsilon^{W_{csud}}_{\text{4j2btag}} &= 3\,\epsilon_c\,\epsilon_j\,(1-\epsilon_j)^2 + 3\,\epsilon_l^2\,(1-\epsilon_c)\,(1-\epsilon_j) \\
\epsilon^{W_{udud}}_{\text{4j2btag}} &= 4\,\epsilon_l^2\,(1-\epsilon_j)^2.
\end{aligned} \tag{5.23}$$

The numerical values of $\epsilon^{W_{cscs}}_{\text{4j2btag}}$, $\epsilon^{W_{cdud}}_{\text{4j2btag}}$, $\epsilon^{W_{udud}}_{\text{4j2btag}}$ are 0.006, 0.002 and 0.0004 respectively, giving $B^{\text{4fermion}}_{\text{4j2btag}} \approx 2$. The factor 4 or 3 represents the variation combination again. In

W_{cscs}, there are four combination of $cscs$ to be tagged as exactly 2 b quark jets (one fake b quark from c quark and one fake b quark from s or the light quark). In W_{csud}, there are 3 combinations to be tagged as exactly 2 b quark jets. s, u, and d are light quarks, so there are three possibilities that they could combine with c quark to be tagged as 2 b quark jets. The other terms are similar situation as these two examples.

OPAL had around 100 4-jet events that originated from 2-fermion events. Around 15 of these would be $b\bar{b}$ events, due to $\frac{\sigma(e^+e^-\to b\bar{b})}{\sigma(e^+e^-\to u\bar{u},c\bar{c},s\bar{s},b\bar{b})}$ being roughly 0.15 at $\sqrt{s} = 200$ GeV. We then estimate the 2-fermion background to the 4-jet signal with two tagged b quarks to the following value:

$$B^{\text{2fermion}}_{\text{4j2btag}} = 15\,\epsilon_b^2. \tag{5.24}$$

This is around 7 events. The contribution to the 2-fermion background from $c\bar{c}$ events would be around $15\epsilon_c^2$ and is much smaller than one event. The total background B_{4j2btag} to the signal with 4-jets and 2 tagged b quarks (S_{4j2btag}) is:

$$B_{\text{4j2btag}} = B^{\text{4fermion}}_{\text{4j2btag}} + B^{\text{2fermion}}_{\text{4j2btag}} \tag{5.25}$$

Since the $B^{\text{4fermion}}_{\text{4j2btag}}$ is around 2 events, then the dominant background is from the 2-fermion events.

5.4.2.7 Background to 4-jets channel with exactly one $b-$tagged jet

The 4-fermion background to the 4-jets signal with one tagged b-jet is given by:

$$B^{\text{4fermion}}_{\text{4j1btag}} = 1000 \times (0.25 \times \epsilon^{W_{cscs}}_{\text{4j1btag}} + 0.5 \times \epsilon^{W_{csud}}_{\text{4j1btag}} + 0.25 \times \epsilon^{W_{udud}}_{\text{4j1btag}}) \tag{5.26}$$

The explicit expressions for $\epsilon^{W_{cscs}}_{\text{4j1btag}}$, $\epsilon^{W_{csud}}_{\text{4j1btag}}$, and $\epsilon^{W_{udud}}_{\text{4j1btag}}$ are below:

$$\begin{aligned}
\epsilon^{W_{cscs}}_{\text{4j1btag}} &= 2\,(1-\epsilon_c)^2\,\epsilon_j\,(1-\epsilon_j) + 2\,\epsilon_c\,(1-\epsilon_c)\,(1-\epsilon_j)^2 \\
\epsilon^{W_{csud}}_{\text{4j1btag}} &= 3\,\epsilon_j\,(1-\epsilon_c)\,(1-\epsilon_j)^2 + \epsilon_c\,(1-\epsilon_j)^3 \\
\epsilon^{W_{udud}}_{\text{4j1btag}} &= 4\,\epsilon_j\,(1-\epsilon_j)^3
\end{aligned} \tag{5.27}$$

The numerical values of $\epsilon^{W_{cscs}}_{\text{4j1btag}}$, $\epsilon^{W_{csud}}_{\text{4j1btag}}$, and $\epsilon^{W_{udud}}_{\text{4j1btag}}$ are 0.13, 0.08, 0.04 respectively.

We then estimate the 2-fermion background (from $b\bar{b}$ production) to the 4-jets signal with one tagged b quark to be:

$$B^{\text{2fermion}}_{\text{4j1btag}} = 30\,\epsilon_b\,(1-\epsilon_b). \tag{5.28}$$

This is about 6 events, but is much less than the 4-fermion background, which is of the order of 90 events. We neglect the contribution to the 2-fermion background from $c\bar{c}$ events, which would be $30\,\epsilon_c\,(1-\epsilon_c)$ and equal to around 1.7 events. Similar to before, one has:

$$B_{\text{4j1btag}} = B^{\text{4fermion}}_{\text{4j1btag}} + B^{\text{2fermion}}_{\text{4j1btag}} \tag{5.29}$$

5.4.2.8 Background to 2-jets channel plus $\tau\nu_\tau$ with exact one $b-$ tagged jet

The background to the 2-jet plus $\tau\nu_\tau$ channel with exactly one b-tagged jet is dominantly from 4-fermion production, and is given by:

$$B^{\text{4fermion}}_{2j\tau 1btag} = 316 \times \frac{1}{2} \times (\epsilon^{W_{cs\tau\nu_\tau}}_{2j\tau 1btag} + \epsilon^{W_{ud\tau\nu_\tau}}_{2j\tau 1btag}). \tag{5.30}$$

The explicit expressions for $\epsilon^{W_{cs\tau\nu_\tau}}_{2j\tau 1btag}$ and $\epsilon^{W_{ud\tau\nu_\tau}}_{2j\tau 1btag}$ are as follows:

$$\epsilon^{W_{cs\tau\nu_\tau}}_{2j\tau 1btag} = \epsilon_c\,(1-\epsilon_j) + \epsilon_j\,(1-\epsilon_c) \tag{5.31}$$

$$\epsilon^{W_{ud\tau\nu_\tau}}_{2j\tau 1btag} = 2\,\epsilon_j\,(1-\epsilon_j) \tag{5.32}$$

Thus, the numerical values of $\epsilon^{W_{cs\tau\nu_\tau}}_{2j\tau 1btag}$ and $\epsilon^{W_{ud\tau\nu_\tau}}_{2j\tau 1btag}$ are 0.07, 0.02 respectively. The factor 2 in front of the term $\epsilon_j\,(1-\epsilon_j)$ means that two combinations for this expression since u or d quark could be tagged as fake b quark separately.

5.4.3 LEP2 results numerical analysis and future electron-positron collider numerical analysis

We now present the numerical results of the statistical significances for $H^\pm \to cb$ at LEP2 and CEPC/FCC-ee colliders. Since we focus on the case of a light charged Higgs state, we use the notation $H_2^\pm$. We firstly show the parameter space of mixing parameters under 4-jets channel with exactly two $b-$tags, exactly one $b-$tag, no $b-$tag, and 2-jets channel with exactly one $b-$-tag, and no $b-$tag significances ($S\sqrt{B}$) with variety of charged Higgs masses.

Since there is a sizeable parameter space for a large BR($H_2^\pm \to cb$) in the type - Y (Flipped) 3HDM our analysis is carried out in this model only. Throughout Chapter 4, the dependence of BR of ($H_2^\pm \to cb$) on the parameter space of four parameters ($\tan\beta$, $\tan\gamma$, θ, δ was discussed). In this section, the statistical significance of a signal in the channel $H_2^\pm \to cb$ will be quantified.

In Fig. (4.5) the contour of BR($H_2^\pm \to cb$) is displayed in the plane [$\tan\gamma$, $\tan\beta$] with the mass of $H_2^\pm = 80$ GeV. The value of θ is $-\frac{\pi}{2.1}$ and the value of δ has been set to 0. For

this particular choice of parameters, this a sizeable parameters space of BR($H_2^\pm \to cb$) larger than 60%, with a maximum to 80%, as can be seen in the plot. In Fig. (4.6), the contours of BR($H_2^\pm \to cs$) and BR($H_2^\pm \to \tau\nu_\tau$) in the plane [$\tan\gamma, \tan\beta$] with the same choices of the other two parameters (θ and δ) are displayed. The statistical significances will be presented in the same plane.

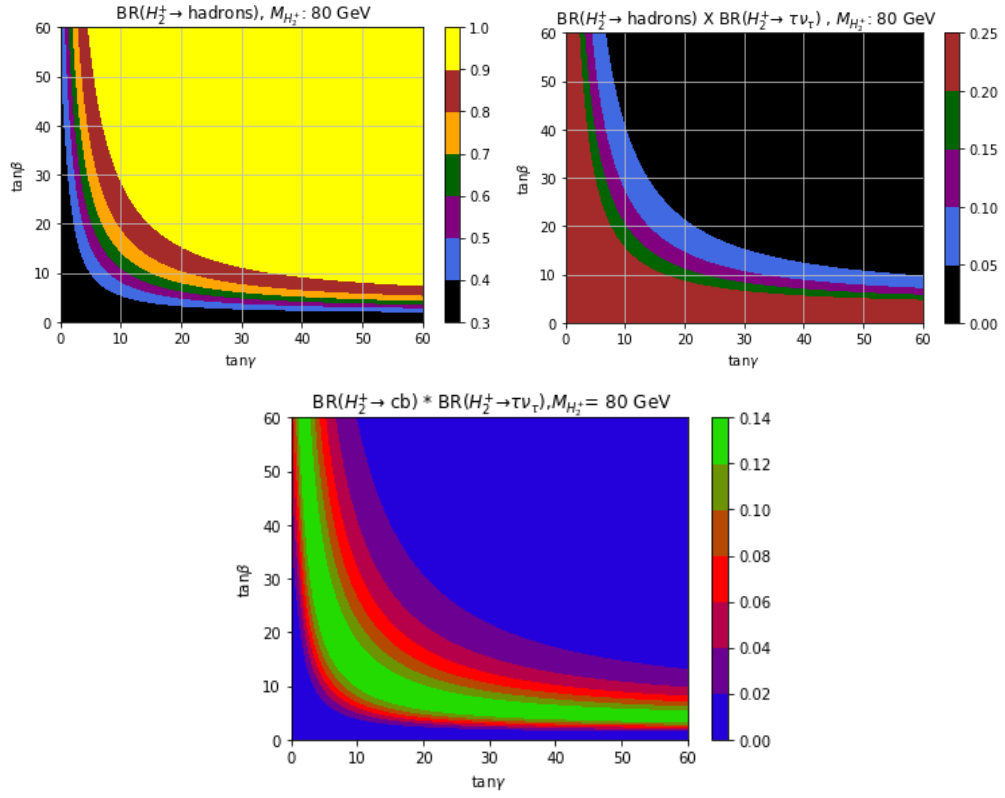

FIGURE 5.9: The type - Y (Flipped) 3HDM contour plots under mixing parameter plane [$\tan\gamma, \tan\beta$] with the mass of $H_2^\pm = 80$ GeV which is same as Fig. (4.5). Top left panel: BR($H_2^\pm \to$ Hadrons). Top right panel: BR($H_2^\pm \to$ Hadrons) $\times$ BR($H_2^\pm \to \tau\nu_\tau$).Bottom panel: BR($H_2^\pm \to cb$) $\times$ BR($H_2^\pm \to \tau\nu_\tau$).

The top panel of Fig. (5.9) shows the sum of hadrons arsing from charged Higgs decay. In this scenario, 'hadrons' refers to ($H_2^\pm \to (cb + cs)$). In the top right panel of Fig. (5.9), the contour of BR($H_2^\pm \to (cb + cs)$) $\times$ BR($H_2^\pm \to \tau\nu_\tau$) is shown. Also, the product BR($H_2^\pm \to cb$) $\times$ BR($H_2^\pm \to \tau\nu_\tau$) is shown in the bottom panel of Fig. (5.9). The maximum of BR($H_2^\pm \to cb$) $\times$ BR($H_2^\pm \to \tau\nu_\tau$) appears in the centre of green band close to 14%. This band area arise for both small and large values of $\tan\gamma$ and $\tan\beta$.

In Fig. (5.10) to (5.13), the statistical significances ($\frac{S}{\sqrt{B}}$) are shown in the five channels (three with b-tagging and two without b-tagging) at a single experiment at LEP2 in the parameter plane [$\tan\gamma, \tan\beta$] with $M_{H_2^\pm} = 80$ and 89 GeV. In the first two Figures, Fig. (5.10) and Fig. (5.11), the significances ($S/\sqrt{B}$) of 4-jets and 2-jets with the $M_{H_2^\pm} =$ 80 GeV respectively are shown. The top left panel of Fig. (5.10) represents the significance ($S_{\text{4j2btag}}/\sqrt{B_{\text{4jet2btag}}}$) in the 4-jets channel. The top right panel of Fig. (5.10) represents the the significance ($S_{\text{4j1btag}}/\sqrt{B_{\text{4jet1btag}}}$) in the 4-jets channel and the bottom panel

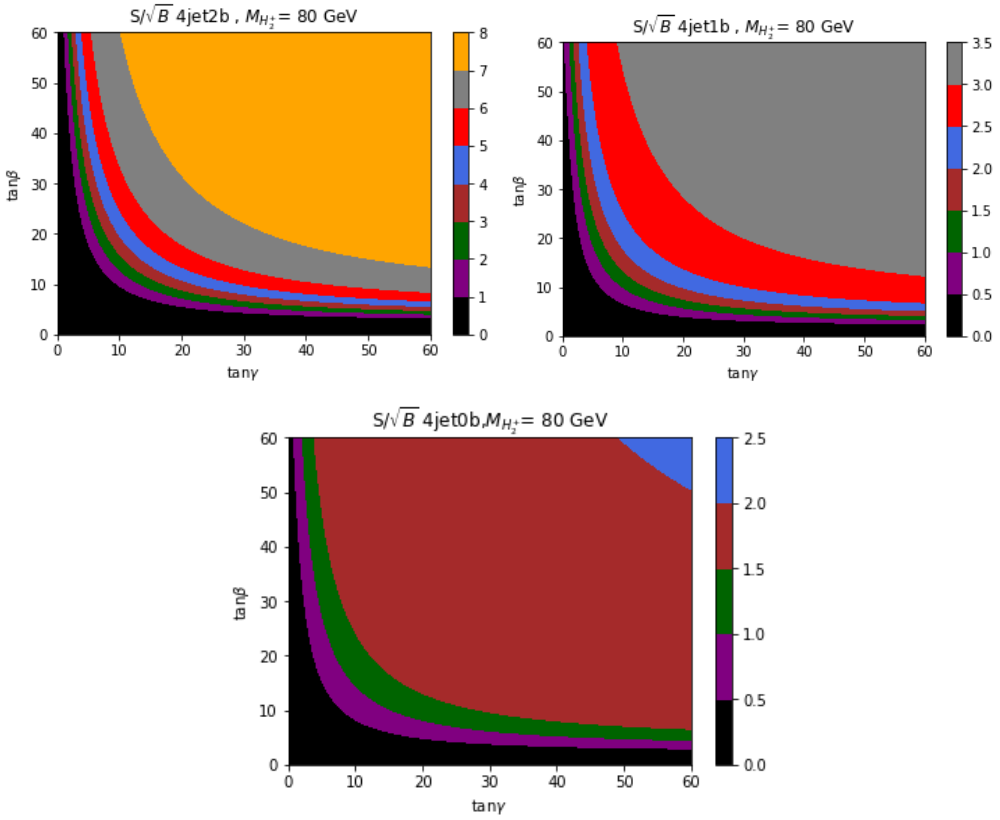

FIGURE 5.10: The type - Y (Flipped) 3HDM contour plots under mixing parameter plane $[\tan\gamma, \tan\beta]$ with the mass of $H_2^{\pm} = 80$ GeV which is same as Fig. (4.5). Top left panel: Significance $(S/\sqrt{B})$ of a single LEP2 experiment in the 4-jets channel with $2b-$tags. Top right panel: Significance $(S/\sqrt{B})$ of a single LEP2 experiment in the 4-jets channel with $1b-$tag. Bottom panel: Significance $(S/\sqrt{B})$ of a single LEP2 experiment in the 4-jets channel without $b-$tag.

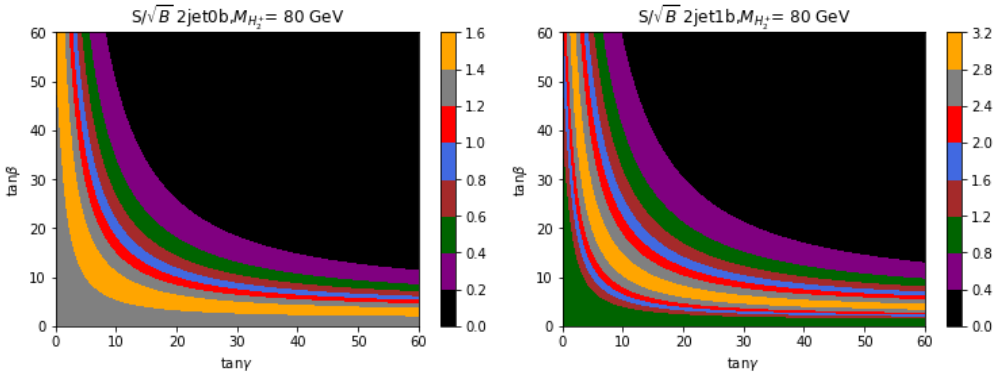

FIGURE 5.11: The type - Y (Flipped) 3HDM contour plots under mixing parameter plane $[\tan\gamma, \tan\beta]$ with the mass of $H_2^{\pm} = 80$ GeV which is same as Fig. (4.5). Left panel: Significance $(S/\sqrt{B})$ of a single LEP2 experiment in the 2-jets channel without $b-$tag. Right panel: Significance $(S/\sqrt{B})$ of a single LEP2 experiment in the 2-jets channel with $1b-$tag.

is the significance $(S_{4\text{jnobtag}}/\sqrt{B_{4\text{jetnobtag}}})$ in 4-jets channel. In the case of no $b-$tagging the maximum of $S/\sqrt{B}$ is less than 2.5 in this case, and is roughly consistent with the

OPAL search rule out limit for $M_{H_2^\pm} < 80$ GeV with BR$(H_2^\pm \to \text{Hadrons}) \approx 100\%$. For the case with two $b-$tags it is evident that $S_{\text{4j2btag}}/\sqrt{B_{\text{4jet2btag}}}$ can be enhanced significantly with respect to the case with no $b-$tag. A large area of the $[\tan\gamma, \tan\beta]$ has $S/\sqrt{B} > 3$, with $S/\sqrt{B} \approx 8$ being possible. Note that these significances are for a single LEP2 experiment, and thus a 3σ signal at all four experiments might approach the 5σ threshold for a confident discovery if the four group searches are combined. The case with only one $b-$tag has values of $S_{\text{4j1btag}}/\sqrt{B_{\text{4jet1btag}}}$ that are slightly larger than the case of $S_{\text{4jnobtag}}/\sqrt{B_{\text{4jetnobtag}}}$, as expected. The background of the one $b-$tag channel is smaller than that with no $b-$tag, but the siginificances do not improve much.

In the search with two jets, Fig. (5.11), in the left panel $S_{\text{2j0btag}}/\sqrt{B_{\text{2jet0btag}}}$ the largest possible $S/\sqrt{B}$ is around 1.6. This maximum value of $S/\sqrt{B}$ is roughly consistent with the OPAL limits that rule out $M_{H_2^\pm} < 80$ GeV in the 2-jets channel. For the case of one $b-$tag case, which is the right panel of Fig. (5.11), it can be seen that $S_{\text{2j1btag}}/\sqrt{B_{\text{2jet1btag}}}$ has increased but the its value is small compared with the 4-jet search with two $b-$tags case. The largest value of $S/\sqrt{B}$ is 3.2 in the bottom panel of Fig. (5.9), and this occurs when BR$(H_2^\pm \to cb) \times$ BR$(H_2^\pm \to \tau\nu_\tau)$ takes its largest values in the $[\tan\gamma, \tan\beta]$ plane.

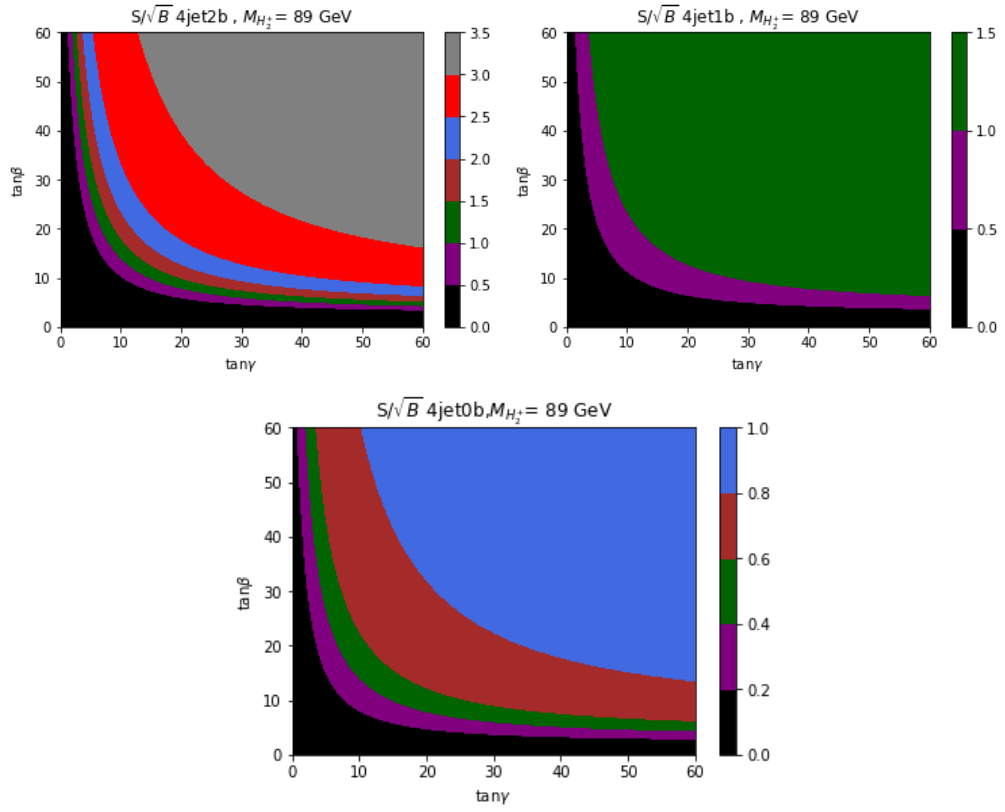

FIGURE 5.12: The type - Y (Flipped) 3HDM contour plots under mixing parameter plane $[\tan\gamma, \tan\beta]$ with the mass of $H_2^\pm = 89$ GeV which is same as Fig. (4.5). Top left panel: Significance $(S/\sqrt{B})$ of a single LEP2 experiment in the 4-jets channel with $2b-$tags. Top right panel: Significance $(S/\sqrt{B})$ of a single LEP2 experiment in the 4-jets channel with $1b-$tag. Bottom panel: Significance $(S/\sqrt{B})$ of a single LEP2 experiment in the 4-jets channel without $b-$tag.

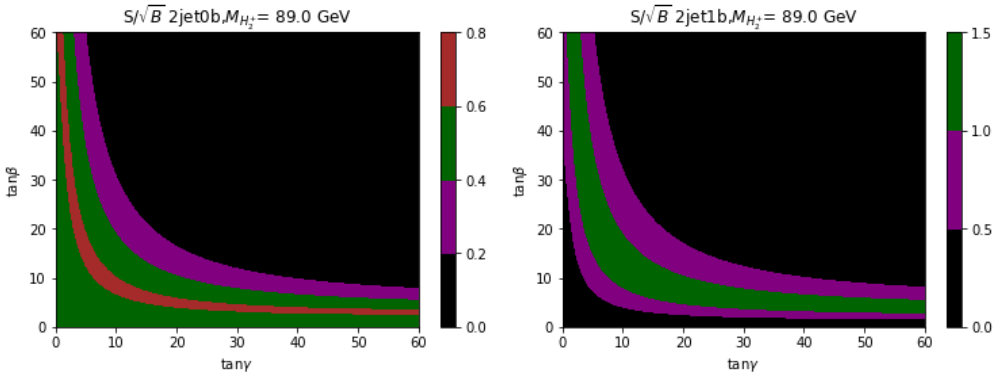

FIGURE 5.13: The type - Y (Flipped) 3HDM contour plots under mixing parameter plane $[\tan\gamma, \tan\beta]$ with the mass of $H_2^{\pm} = 89$ GeV which is same as Fig. (4.5). Left panel: Significance $(S/\sqrt{B})$ of a single LEP2 experiment in the 2-jets channel without $b-$tag.
Right panel: Significance $(S/\sqrt{B})$ of a single LEP2 experiment in the 2-jets channel with $1b-$tag.

Fig. (5.12) and (5.13) are the same as Fig. (5.10) and (5.10) but with $M_{H_2^{\pm}} = 89$ GeV rather than 80 GeV. The maximum values of $S/\sqrt{B}$ in the 4-jets channel with two $b-$tags and in the 2-jets channel with one $b-$tag drop by roughly a factor of 2. The reason is due to the reduced production rate of charged Higgs boson pairs in e^+e^- collider. The cross-section of $e^+e^- \to H^+H^-$ decreases as the charged Higgs boson mass increases, as can be seen from Eq. (5.1). As mentioned earlier, a 3σ signal at each LEP2 experiment might become close to a 5σ signal if data from all four experiment groups are combined. Hence a discovery for $M_{H_2^{\pm}} = 89$ GeV is possible in the optimistic scenario of BR($H_2^{\pm} \to cb$) close to 80%.

In Fig. (5.14), we present the values of $S/\sqrt{B}$ for a range of values of $M_{H_2^{\pm}}$ in the 4-jets channel with BR($H_2^{\pm} \to cb$) = 0.8 (i.e its maximal value) and BR($H_2^{\pm} \to cs$) = 0.2. The top left panel is the 4-jets channel with two $b-$tags, the top right panel is the 4-jets channel with one $b-$tag, and the bottom panel is the 4-jets channel without a $b-$tag. The dependence is linear, and a 5σ signal at a single at LEP2 experiment is possible in the 4-jets channel with 2 $b-$tags up to around the $M_{H_2^{\pm}} = 84$ GeV. Since the production of charged Higgs from electron-positron correlated with charged Higgs mass and centre of mass energy, the feature of significances drops linearly is from the dependence of cross-section of charged Higgs against $\frac{4M^2_{H_2^{\pm}}}{s}$ relationship which is mentioned in Eq. (5.1).

In Fig. (5.15), the dependence of the $S/\sqrt{B}$ for a range of values of $M_{H_2^{\pm}}$ in the 2-jets channel is shown. The left panel is the 2-jets channel without a $b-$tag while the right panel is 2-jets channel with one $b-$tag. In each plot fixed the BRs are fixed to take the values BR($H_2^{\pm} \to cs$) = 0.1, BR($H_2^{\pm} \to cb$) = 0.4, and BR($H_2^{\pm} \to \tau\nu_\tau$) = 0.5. (i.e. the most optimistic scenario for discovery in this channel). A roughly linear dependence on $M_{H_2^{\pm}}$ can be seen in both panels.

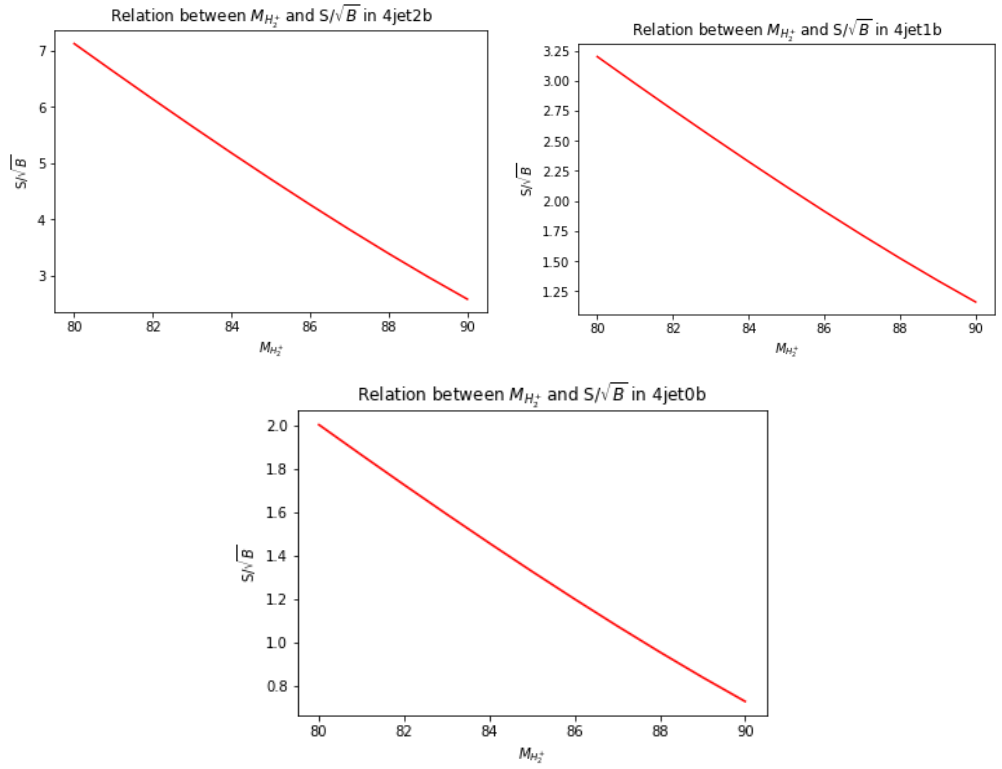

FIGURE 5.14: The relationship between $S/\sqrt{B}$ and $M_{H_2^\pm}$ with with BR$(H_2^\pm \to cb) = 0.8$ (approximate maximal), BR$(H_2^\pm \to cs) = 0.2$ at a single LEP2 experiment.
Top left panel: 4-jets channel with two $b-$tags. Top right panel: 4-jets channel with one $b-$tag. Bottom panel: 4-jets channel without $b-$tag.

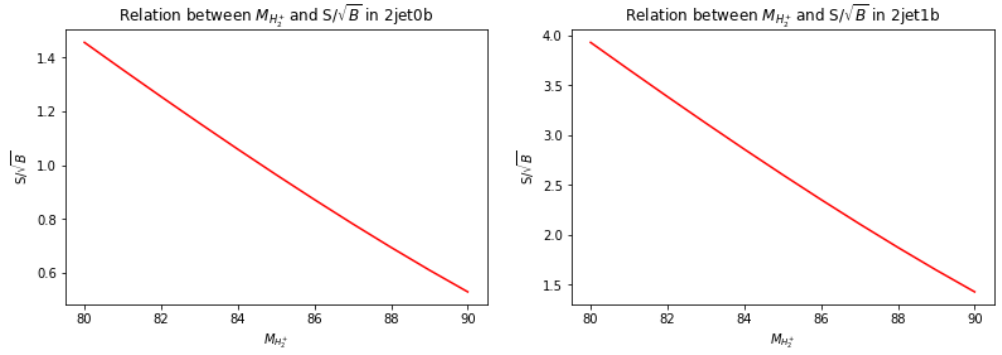

FIGURE 5.15: The relationship between $S/\sqrt{B}$ and $M_{H_2^\pm}$ with with BR$(H_2^\pm \to$ Hadrons$) = 0.5$ and BR$(H_2^\pm \to \tau\nu_\tau) = 0.5$ at a single LEP2 experiment.
Left panel: 2-jets channel without $b-$tag.
Right panel: 2-jets channel with one $b-$tag.

Individual numbers of for signal events (S) and background events (B) of Figs. (5.14-5.15) are listed in the Tab. (5.4) and (5.5)[4]. In Tab. (5.4), the number of signal events (S), the background number (B) and significances ($S/\sqrt{B}$) are presented with the choice

[4]Notice here, the numerical values of signals and significances are slightly different than the [arXiv: 1908.00826] due to the fact a factor 2 was missing in the last formula $\epsilon^{cbcs}_{\text{4j2btag}}$ of Eq. (5.12). However, the paper [18] already corrected that expression.

$M_{H_2^\pm}$	80 GeV	85 GeV	89 GeV	80 GeV	85 GeV	89 GeV	
	S	S	S	$\frac{S}{\sqrt{B}}$	$\frac{S}{\sqrt{B}}$	$\frac{S}{\sqrt{B}}$	B
4j0b	67.015	44.367	28.027	2.004	1.327	0.838	1117.8
4j1b	30.602	20.260	12.799	3.200	2.119	1.338	91.445
4j2b	22.470	14.876	9.398	7.128	4.719	2.981	9.938

TABLE 5.4: Number of signal events (S), number of background events (B), and the corresponding significances ($\frac{S}{\sqrt{B}}$) in all 4-jets channels at a single experiment LEP2. Results are shown for $M_{H_2^\pm} = 80, 85, 90$ GeV, with BR($H_2^\pm \to cb$) = 0.8, BR($H_2^\pm \to cs$) = 0.2.

of $M_{H_2^\pm} = 80, 85, 89$ GeV in the 4-jets channels (with two $b-$tags, one $b-$tag, and no $b-$tag). In the case of $M_{H_2^\pm} = 89$ GeV in the 4-jets channel with two $b-$tags, the number of signal events is still sizeable ($\approx$ 9). In Tab. (5.5), each individual number of $S, B, S/\sqrt{B}$ is presented in 2-jet channels for two scenarios (one $b-$tag and no $b-$tag) with the above values of $M_{H_2^\pm}$.

$M_{H_2^\pm}$	80 GeV	85 GeV	89 GeV	80 GeV	85 GeV	89 GeV	
	S	S	S	$\frac{S}{\sqrt{B}}$	$\frac{S}{\sqrt{B}}$	$\frac{S}{\sqrt{B}}$	B
2j0b	25.927	17.164	10.843	1.456	0.964	0.609	1117.8
2j1b	14.735	9.755	6.162	3.933	2.604	1.645	91.445

TABLE 5.5: Number of signal events (S), number of background events (B), and the corresponding significances ($\frac{S}{\sqrt{B}}$) in all 2-jets channels at a single experiment LEP2. Results are shown for $M_{H_2^\pm} = 80, 85, 90$ GeV, with BR($H_2^\pm \to cb$) = 0.4, BR($H_2^\pm \to cs$) = 0.1 and BR($H_2^\pm \to \tau\nu_\tau$) = 0.5.

$M_{H_2^\pm}$	88 GeV	89 GeV	90 GeV	88 GeV	89 GeV	90 GeV	
	S	S	S	$\frac{S}{\sqrt{B}}$	$\frac{S}{\sqrt{B}}$	$\frac{S}{\sqrt{B}}$	B
4j0b	13.484	11.842	10.266	0.403	0.354	0.307	1117.8
4j1b	6.239	5.479	4.749	0.652	0.573	0.497	91.445
4j2b	4.249	3.732	3.236	1.348	1.184	1.026	9.938
2j0b	11.236	9.867	8.554	0.631	0.554	0.481	316.9
2j1b	6.200	5.444	4.720	1.655	1.453	1.260	14.039

TABLE 5.6: Number of signal events (S), number of background events (B), and the corresponding significances ($\frac{S}{\sqrt{B}}$) in all five channels at a single experiment LEP2. Results are shown for $M_{H_2^\pm} = 80, 89, 90$ GeV, with BR($H_2^\pm \to cb$) = 0.5, BR($H_2^\pm \to cs$) = 0.15, and BR($H_2^\pm \to \tau\nu_\tau$) = 0.35.

In Fig. (5.16), we present the values of $S\sqrt{B}$ in the plane [$M_{H_2^\pm}$, BR($H_2^\pm \to cb$)]. In the left panel, we show the 4-jets channel with two $b-$tags, taking BR($H_2^\pm \to$ Hadrons) = 1 (BR($H_2^\pm \to cb$) + BR($H_2^\pm \to cs$) = 1). The right panel is for 2-jets channel with one $b-$tag, and with BR($H_2^\pm \to \tau\nu_\tau$) = 0.5 and BR($H_2^\pm \to cb$) + BR($H_2^\pm \to cs$) = 0.5. In the 4-jets channel the BR($H_2^\pm \to cb$) has to larger than 0.35 in order to have $S\sqrt{B}$ larger

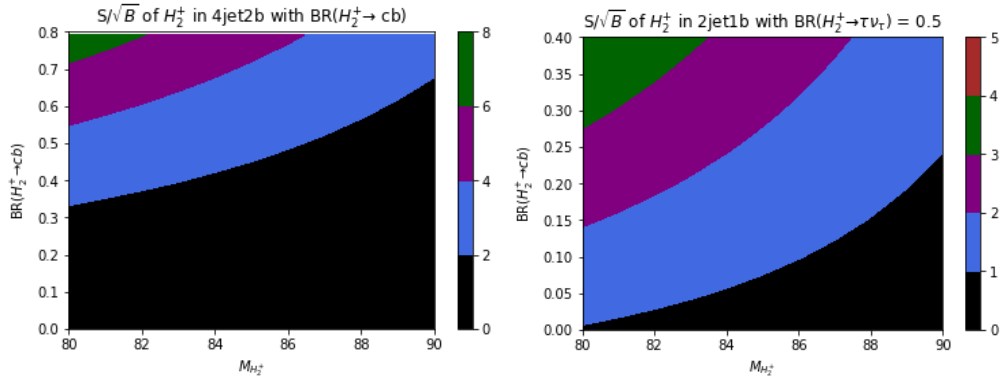

FIGURE 5.16: The values of $S/\sqrt{B}$ in plane of $[M_{H_2^\pm}, \text{BR}(H_2^\pm \to cb)]$ at a single LEP2 experiment. Left panel: 4-jets channel with two $b-$tags with $\text{BR}(H_2^\pm \to \text{Hadrons}) = 1$. Right panel: 2-jets channel with one $b-$tag. $\text{BR}(H_2^\pm \to \tau\nu_\tau) = 0.5$ and $\text{BR}(H_2^\pm \to cb) + \text{BR}(H_2^\pm \to cs) = 0.5$.

than 2 for $M_{H_2^\pm} = 80$ GeV. In the 2-jets channel, obatining $S\sqrt{B}$ larger than 2 requires $\text{BR}(H_2^\pm \to cb)$ to be larger than 0.15.

We expect the dominant background to the 4-jets $2b$ channel to come from the 2-fermion background since the mass distribution of two of the 4-jets from 2-fermion background has a flat distribution which can be seen in the OPAL search [111]. On the other hand, the signal mainly lies in the region of m_{jj} between 80 and 89 GeV. Using the plots in the OPAL search, we estimate that an invariant mass cut could reduce the 2-fermion background and maintain a signal in the mass region between 80 and 89 GeV. In Fig. (5.17), the invariant mass cut effect on $S\sqrt{B}$ is plotted for both $4j2b$ (left panel) and $4j1b$ (right panel) cases. The parameter ϵ_{mass} varies from 1 (no invariant mass cut) to a maximum value of cut 0.1. From a figure in Ref. [111], a realistic range of ϵ_{mass} is estimated to be between 0.4 and 0.5. In these two plots, for simplicity we assumed that the invariant mass cut has no effect on the number of signal events (in realisty there would be a slight reduction of signal events when using this cut). The left panel shows that the value of $S/\sqrt{B}$ can increase significantly if an invariant mass cut is used.

Finally, we present a comment on the slight excess of events (greater than 2σ significance) which was collected with the combined analysis of the four LEP2 experiment groups, and shown in Fig. (5.3) from Ref. [5]. In that figure, the excess occurs around a charged Higgs mass of 89 GeV, with the BR to hadrons being approximately 65% and and BR to $\tau\nu_\tau \approx 35\%$. Previous works stated that this excess could possibly be due to a charged Higgs boson in 3HDM [17; 97]. If the excess is genuine, and arises from a large BR of a charged Higgs boson to cb, then $b-$tagging would increase the significance. In Tab. (5.6), we took $\text{BR}(H_2^\pm \to cb) = 0.5$, $\text{BR}(H_2^\pm \to cs) = 0.15$, and $\text{BR}(H_2^\pm \to \tau\nu_\tau) = 0.35$ in order to obtain a rough $\text{BR}(H_2^\pm \to \text{Hadrons}) = 65\%$ and $\text{BR}(H_2^\pm \to \tau\nu_\tau) = 35\%$. The cases of $4j0b$ and $2j0b$ with $M_{H_2^\pm} = 89$ GeV in the table show a significance of 0.354 and 0.573 for a single LEP2 experiment. Thus, a combination of the four experiment

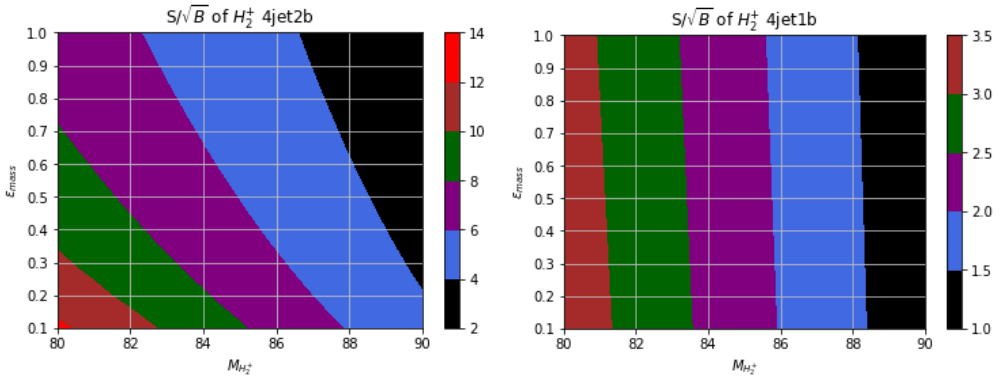

FIGURE 5.17: The contour values of $S/\sqrt{B}$ in plane of $[M_{H_2^\pm}, \epsilon_{\text{mass}}]$ at a single LEP2 experiment with BR($H_2^\pm \to cb$) = 0.8 and BR($H_2^\pm \to cs$) = 0.2. Left panel: 4-jets channel with two $b-$tags. Right panel: 4-jets channel with one $b-$tag.

measurements could possibly be expected to give a 2σ excess, especially if an upward fluctuation occured. With the addition of $b-$tagging case, the channels $4j2b$ and $2j1b$ have significances of 1.184 and 1.453 respectively, which are roughly a factor of four and factor of three larger than the case no with no b-tagging. Crucially, the number of signal events in these two search channels is still larger than 3 events. Thus, these two channels could provide a statistically larger signal after $b-$tagging if the excess is genuine and the charged Higgs boson has a large BR to cb. Such an excess could also possibly show up in LHC searches for the decay of a top quark to a charged Higgs boson and b quark since the charged Higgs mass region between 80 and 90 has been covered for a charged Higgs decay into $\tau\nu_\tau$. However, there is currently no sensitivity at the LHC in that mass region for a charged Higgs decays to hadrons. It is important to note that the LHC search strategy actually involves the Yukawa couplings, in contrast to the search a LEP. Hence a light charged Higgs boson of mass around 90 GeV could be present in the decays of the top quark and escape detection if the Yukawa couplings are relative small (especially $|X_2|$ and $|Y_2|$). Such a light $H_2^\pm$ would not escape detection at an e^+e^- collider.

5.4.4 Prospects for detecting of $H_2^\pm \to cb$ at CEPC/FCC-ee

Future e^+e^- colliders would provide more precise measurement of the discovered 125 GeV neutral Higgs boson. In addition such colliders can also search for charged Higgs bosons. Two proposed circular e^+e^- colliders with a centre-of-mass energy ($\sqrt{s}$) around 240 GeV are CEPC in China [134] and FCC-ee [135]. Two proposed linear e^+e^- colliders are the ILC in Japan [136] and CLIC at CERN [137][5]. The latter machines would

[5]The linear collider has its own benefit based on the construction is much easier than circular one (Cicular collider requires large magnets to confine the electron and positron beams). However, the circular collider can have more collisions since the circle shape of synchrotron would lead particles go ground more times.

provide a centre-of-mass energy larger than 240 GeV. Circular e^+e^- colliders would produce a charged Higgs boson pair each with a mass up to 120 GeV. The integrated luminosity with 240 GeV energy is expected to be of the order of a few ab^{-1}, which is roughly a thousand times larger than the total integrated luminosity taken at a single LEP2 experiment (0.6 fb^{-1}). In the case of the 3HDM, only type-Y (Flipped) and -Z (Democratic) 3HDM can possibly have a BR($H_2^\pm \to cb$) larger than 1% while in type-I,-II, and -X (lepton-specific) 3HDM this branching ratio of the order of 1% at most. In this section, we investigate whether a small value of BR($H_2^\pm \to cb$) could be observed at future e^+e^- colliders. For the background, we use the values from LEP2 (for which $\sqrt{s} = 200$ GeV) for simplicity in order to make a first estimate of the potential of future circular colliders to measure $H_2^\pm$ [132]. The jet detection rates of the search would already cover the photon fake which help us out to rescale to the future e^+e^- collider analysis. We expect that the efficiency ϵ_c could be improved and so in our numerical analysis we considered values of ϵ_c between $0.01 \to 0.06$ while taking ϵ_b and ϵ_j to be the same as at LEP2 in Tab. (5.3).

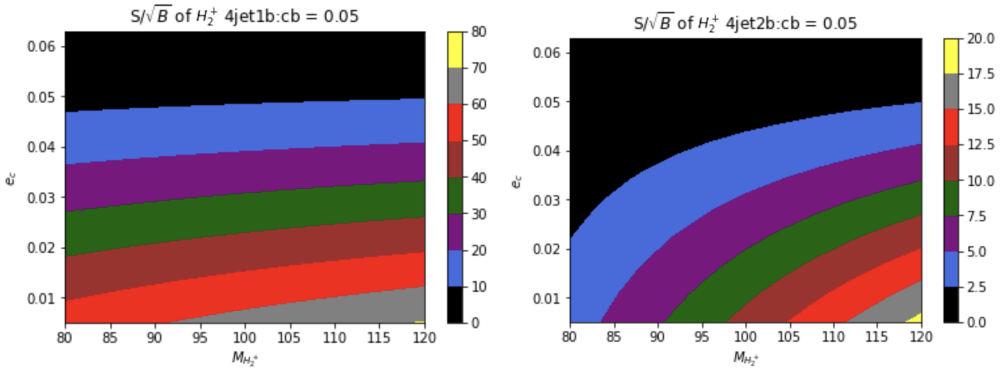

FIGURE 5.18: The values of $S/\sqrt{B}$ in plane of $[M_{H_2^\pm}, \epsilon_c]$ at $\sqrt{s} = 240$ GeV (CEPC/FCC-ee). BR($H_2^\pm \to cb$) = 0.05 and BR($H_2^\pm \to cs$) = 0.95 (Fully hadronic decays). Left panel: 4-jets channel with one $b-$tag. Right panel: 4-jets channel with two $b-$tags.

In Fig. (5.18), the significance ($S/\sqrt{B}$) of the 4-jets channel in the plane $[M_{H_2^\pm}, \epsilon_c]$ is plotted with BR($H_2^\pm \to cb$) = 5% (which is only possible for type - Y (Flipped) and democratic 3HDM) and BR($H_2^\pm \to cs$) = 95% (i.e. fully hadronic decay). The left panel is the 4-jets channel with one $b-$tag and the right panel is the 4-jets channel with two $b-$tags. In the 4-jets channel with one $b-$tag case, it can be seen that very large values of significance can be achieved in the mass region from 80 to 90 GeV (e.g. $S/\sqrt{B} \approx 30$ for $\epsilon_c \approx 0.03$ and $M_{H_2^\pm} = 90$ GeV). On the right-hand side, the values of $S/\sqrt{B}$ are much lower than left-hand side due to the fact that lower BR($H_2^\pm \to cb$) leads to a reduced number of signal events because the BR to cb is squared (in contrast to the case with one tagged b quark). A value of BR($H_2^\pm \to cb$) close to 1% is possible in all five types of the 3HDM. In Fig. (5.18) we plot $S/\sqrt{B}$ with BR($H_2^\pm \to cb$) = 0.01 and BR($H_2^\pm \to cs$) = 0.5 and BR($H_2^\pm \to \tau\nu_\tau$) = 0.49 in Fig. (5.19). The top left panel shows the 4-jets channel with one $b-$tag and the top right panel presents the 4-jets channel with two $b-$tags. The bottom panel shows the 2-jets channel with one $b-$tag. In the 4-jet with a single $b-$tag

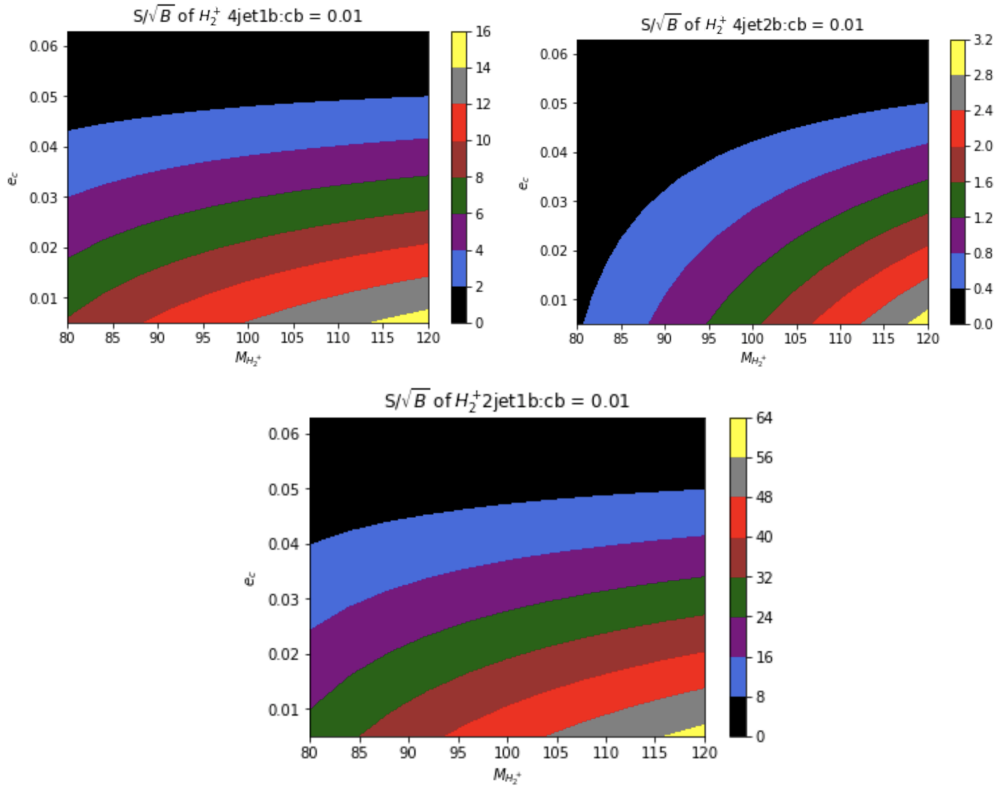

FIGURE 5.19: The values of $S/\sqrt{B}$ in plane of $[M_{H_2^\pm}, \epsilon_c]$ at $\sqrt{s} = 240$ GeV (CEPC/FCC-ee). BR($H_2^\pm \to cb$) = 0.01 and BR($H_2^\pm \to cs$) = 0.50. Top left panel: 4-jets channel with one $b-$tag. Top right panel: 4-jets channel with two $b-$tags. Bottom panel: 2-jets channel with one $b-$tag.

and 2-jet channels a clear signal is possible and a precise measurement of the BR to cb could be achieved. In these two scenarios, the signals do not satisfy $S << B$, which is a requirement for $S/\sqrt{B}$ to accurately represent the significance. If a more accurate formula for estimating the significance [138] is used for the two figures Fig. (5.18) and Fig. (5.19) , then the significance will be reduced compared to that given in two figures.

5.5 Conclusion

In this chapter, the phenomenology of a charged Higgs boson in the 3HDM was investigated at LEP and at the LHC. First, we explained the production mechanisms and summarised the searches at both colliders and drew attention to the excess of 2σ events in the mass region between 80 and 90 GeV in the LEP search. In the LHC analysis we showed the parameter space of $\tan\beta, \tan\gamma, \theta, \delta$ that is ruled out by current searches, and we showed the parameter space that will be probed in current and future runs of the LHC. We then used the OPAL LEP2 results for the background events and quantified the increase in sensitivity that can be obtained by applying one or two b-tags to the existing search strategy, assuming that $H_2^\pm \to cb$ has a large BR (which is only possible in the 3HDMs of type-Y and type-Z 3HDM). For the numerical analysis the signatures are separated into two channels: 4-jet channel and 2-jet (with $\tau\nu_\tau$) channel. By using a $b-$quark tag, we separated these two channels into five search strategies (4-jet channel without $b-$tag, 4-jet channel with one $b-$tag, 4-jet channel with two $b-$tags, 2-jet channel without $b-$tag, and 2-jets channel with one $b-$tag). We showed that a considerable gain in sensitivity could be obtained by adding a $b-$tag requirement, with a possible explanation of the slight excess around a charged Higgs mass of 89 GeV.

The detection prospects at proposed electron-positron colliders (such as CEPC and FCC-ee) were investigated and it was shown that even for a small BR($H_2^\pm \to cb$), there would be still be enough events for detection in this channel, would allow information to be obtained on underlying Yukawa structure. An important point is that the pair production of $H_2^\pm$ at an e^+e^- collider of charged Higgs depends only on the mass of the charged Higgs mass, while at hadron colliders the Yukawa couplings are enter the formula for the production cross sections. In this sense the two colliders are complementary in the search for a charged Higgs boson. If the Yukawa couplings are very small, the charged Higgs boson would possibly escape the detection at LHC or future proton-proton collider, but could be discovered at a future e^+e^- collider.

Chapter 6

CP violation constraints for Yukawa couplings

6.1 Overview

In this chapter, we will discuss two separate CP-violation observables and study the contribution from a charged Higgs bosons of CP-violation in the 3HDM. These observables we study are i) various CP-asymmetry observables in $\bar{B} \to X_s\gamma$ ($\mathcal{A}_{X_{s(d)}\gamma}$,$\Delta\mathcal{A}_{X_s\gamma}$, and $\mathcal{A}_{\text{CP}}(\bar{B} \to X_{s+d}\gamma)$, to be defined later) and ii) neutron/electron electric-dipole-moment (EDM)). This chapter covers both work from [15] and [16].

In this section the experimental measurements of the inclusive decays $B \to X_s\gamma$ and $B \to X_{s+d}\gamma$ (charged conjugated processes are implied) are described, followed by a discussion of direct CP asymmetries in these decays. The symbol B signifies B^+ or B^0 (which contain an anti-b quark and a b quark, respectively), while $\overline{B}$ signifies B^- or $\overline{B^0}$ (which contain a b quark and an anti-b quark, respectively). The symbol X_s means any hadronic final state that originates from a strange quark hadronising (e.g., states with at least one kaon), X_d means any hadronic final state that originates from a down quark hadronising (e.g., states with at least one pion) while X_{s+d} means any hadronic final state that is X_s or X_d.

Since the research focuses on the decay of $\bar{B} \to X_s\gamma$, we will illustrate how the BR of this decay is computed in the 3HDM, explaining the calculational framework. The current experimental measurements of BR($\bar{B} \to X_s\gamma$), and the limits on its CP-asymmetry are presented, as well as the expected sensitivity of the ongoing BELLE-II experiment to these observables. We then study the effect of the charged Higgs bosons $H_2^\pm$ and $H_3^\pm$ on both the BR and the CP-asymmetry in the context of the 3HDM. A measurement of a non-zero CP-asymmetry in $\bar{B} \to X_s\gamma$ would provide a signal of physics beyond the SM, and the magnitude of the CP asymmetry in the 3HDM is studied in detail.

Lastly, two EDMs (electron and neutron-EDMs), which are CP-violating observables, are investigated in the 3HDM.

6.2 Numerical evaluation of $\bar{B} \to X_s\gamma$ in 3HDM

In Ref. [99], it was shown that the experiment bound on $\bar{B} \to X_s\gamma$ limits the Yukawa couplings of Re(XY^*) and Im(XY^*). Both papers [17; 18] used the rough bound of BR$(\bar{B} \to X_s\gamma)$, with the bounds being $-1.1 \leq \text{Re}(XY^*) \leq 0.7$ and $-0.1 \leq \text{Im}(XY^*) \leq 0.1$ with charged Higgs mass of 100 GeV. In this section, we study in detail the prediction for BR$(\bar{B} \to X_s\gamma)$ at next-to-leading order (NLO) in QCD.

The effective Hamiltonian for $\bar{B} \to X_s\gamma$ with $|\Delta B| = |\Delta S| = 1$ is given by [139]:

$$H_{\text{eff}} = -\frac{4G_f}{\sqrt{2}} V_{ts}^* V_{tb} \sum_i^8 C_i(\mu) O_i(\mu) \tag{6.1}$$

$$\begin{aligned}
O_1 &= (\bar{s}_L \gamma_\mu T^a c_L)(\bar{c}_L \gamma^\mu T_a b_L), \\
O_2 &= \bar{s}_L \gamma_\mu c_L \bar{c}_L \gamma^\mu b_L \\
O_3 &= (\bar{s}_L \gamma_\mu b_L) \sum_q (\bar{q} \gamma^\mu q) \\
O_4 &= (\bar{s}_L \gamma_\mu T^a b_L) \sum_q (\bar{q} \gamma^\mu T_a q) \\
O_5 &= (\bar{s}_L \gamma_\mu \gamma_\nu \gamma_\rho b_L) \sum_q (\bar{q} \gamma^\mu \gamma^\mu \gamma^\nu \gamma^\rho q) \\
O_6 &= (\bar{s}_L \gamma_\mu \gamma_\nu \gamma_\rho T^a b_L) \sum_q (\bar{q} \gamma^\mu \gamma^\mu \gamma^\nu \gamma^\rho T_a q) \\
O_7 &= \frac{e m_b}{16\pi^2} \bar{s}_L \sigma_{\mu\nu} F^{\mu\nu} b_R \\
O_8 &= \frac{g_s m_b}{16\pi^2} \bar{s}_L \sigma_{\mu\nu} G_a^{\mu\nu} t_a b_R
\end{aligned} \tag{6.2}$$

Here T^a are SU(3) generators with $a = 1, 2, ..8$; e and g_s are the electromagnetic and strong couplings; $O_{1,2}$ are the current-current operators and $O_{3,..6}$ are the QCD penguin operators. The new operators are $O_{7,8}$ which are the transitions $b \to s\gamma$ and $b \to s\gamma g$ respectively. They are called penguin magnetic operators.

Following Eqs. (6.1,6.2), the procedure of the perturbation calculation consists of three steps [139; 140].

- Calculate each Wilson coefficient $C_i(\mu)$ at $\mu = \mu_W$ scale based on the particular choice of α_s, where the μ_W is the scale order of M_W or m_t.
- Calculate the anomalous dimension operators and obtain the solution of the renormalisation group equations of $C_i(\mu_W)$.

- The relevant scale for the calculation of $\bar{B} \to X_s\gamma$ is μ_b, which is the order of m_b. The Wilson coefficients are evaluated at this scale μ_b, and $C_i(\mu_b)$ is obtained from $C_i(\mu_W)$ by using an evolution matrix U which contains the anomalous dimension operators.

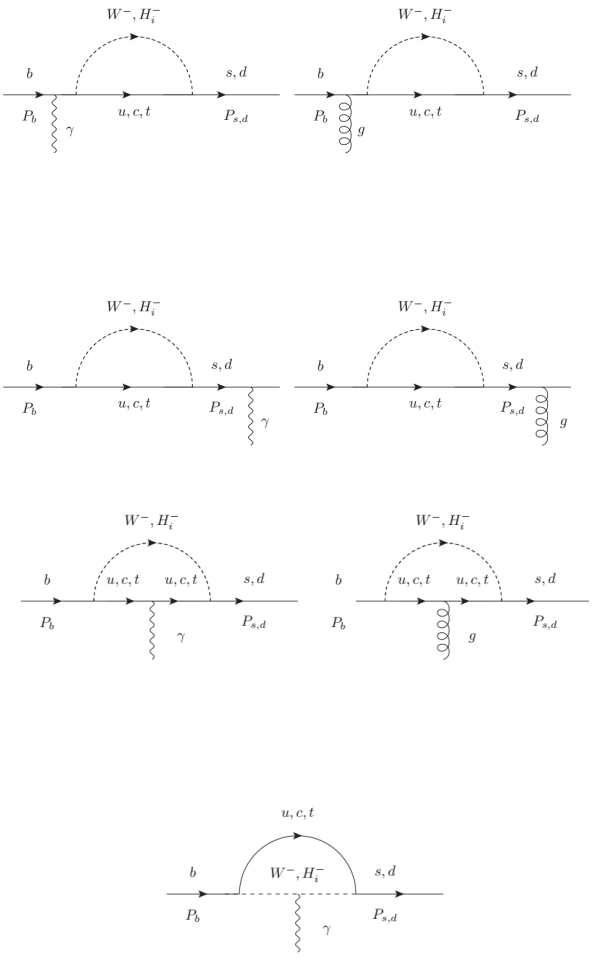

FIGURE 6.1: Feynman diagrams for charged Higgs $H_i^\pm$ and gauge boson $W^\pm$ which contribute to $\bar{B} \to X_s\gamma$ at the one-loop level.

The typical Feynman diagrams are shown in Fig. (6.1). The charged Higgs contributions at the one-loop level are inside the loop while in the SM only the W boson contributes. The top six figures in Fig. (6.1) are similar, with the only difference coming from the possibility of releasing a gluon or photon. The photon/gluon is either emitted from the initial state, in the loop, or from the final-state s or d quarks. In the bottom figure a photon is emitted from the gauge boson W and charged Higgs boson $H_i^\pm$.

Next, the calculation involving the charged Higgs is evaluated below. We first used Ref. [13] for the Leading-Order (LO) and Next Leading-Order (NLO) Wilson coefficients in the 2HDM, and adapted them for use in the 3HDM. As first mentioned in

Ref. [141], the contribution to $\bar{B} \to X_s\gamma$ in a 2HDM and in a 3HDM are similar but two charged Higgs states will contribute in the 3HDM case. The contribution of two types of charged Higgs states $H^{\pm}_{2,3}$ both contribute to the final BR($\bar{B} \to X_s\gamma$) which gives a constraint on the Yukawa couplings and masses of both $H^{\pm}_2$ and $H^{\pm}_3$.

The LO Wilson coefficients from Ref. [141] at the matching scale $\mu_W = M_W$ are as follows:

$$
\begin{aligned}
C_2^{0,\text{eff}}(\mu_W) &= 1, && (6.3)\\
C_i^{0,\text{eff}}(\mu_W) &= 0 \quad (i = 1,3,4,5,6), && (6.4)\\
C_7^{0,\text{eff}}(\mu_W) &= C^0_{7,SM} + |Y_2|^2 C^0_{7,Y_2Y_2} + |Y_3|^2 C^0_{7,Y_3Y_3} \\
&\quad + (X_2Y_2^*) C^0_{7,X_2Y_2} + (X_3Y_3^*) C^0_{7,X_3Y_3}, && (6.5)\\
C_8^{0,\text{eff}}(\mu_W) &= C^0_{8,SM} + |Y_2|^2 C^0_{8,Y_2Y_2} + |Y_3|^2 C^0_{8,Y_3Y_3}, \\
&\quad + (X_2Y_2^*) C^0_{8,X_2Y_2} + (X_3Y_3^*) C^0_{8,X_3Y_3}\,. && (6.6)
\end{aligned}
$$

Terms with $X_1Y_1^*$, $X_2Y_2^*$, $|X_1|^2$ and $|X_2|^2$ are absent because $m_s = 0$ (as is usually taken) in the effective Hamiltonian. The NLO Wilson coefficients at the matching scale are as follows:

$$
\begin{aligned}
C_1^{1,\text{eff}}(\mu_W) &= 15 + 6\,\ln\frac{\mu_W^2}{M_W^2}, && (6.7)\\
C_4^{1,\text{eff}}(\mu_W) &= E_0 + \frac{2}{3}\,\ln\frac{\mu_W^2}{M_W^2} + |Y_2|^2 E_{H_2} + |Y_3|^2 E_{H_3} && (6.8)\\
C_i^{1,\text{eff}}(\mu_W) &= 0 \quad (i = 2,3,5,6) && (6.9)\\
C_7^{1,\text{eff}}(\mu_W) &= C^{1,\text{eff}}_{7,SM}(\mu_W) + |Y_2|^2 C^{1,\text{eff}}_{7,Y_2Y_2}(\mu_W) + |Y_3|^2 C^{1,\text{eff}}_{7,Y_3Y_3}(\mu_W) \\
&\quad + (X_2Y_2^*) C^{1,\text{eff}}_{7,X_2Y_2}(\mu_W) + (X_3Y_3^*) C^{1,\text{eff}}_{7,X_3Y_3}(\mu_W) && (6.10)\\
C_8^{1,\text{eff}}(\mu_W) &= C^{1,\text{eff}}_{8,SM}(\mu_W) + |Y_2|^2 C^{1,\text{eff}}_{8,Y_2Y_2}(\mu_W) + |Y_3|^2 C^{1,\text{eff}}_{8,Y_3Y_3}(\mu_W) \\
&\quad + (X_2Y_2^*) C^{1,\text{eff}}_{8,X_2Y_2}(\mu_W) + (X_3Y_3^*) C^{1,\text{eff}}_{8,X_3Y_3}(\mu_W)\,. && (6.11)
\end{aligned}
$$

The explicit forms for all functions are given in [13] and are written in Appendix B. Renormalisation group running is then used to evaluate the Wilson coefficients at the lower scale, $\mu = m_b$.

The partial width of $\bar{B} \to X_s\gamma$ has four distinct parts:

i) short-distance contribution from the $b \to s\gamma$ partonic process (to a given order in perturbation theory);

ii) short-distance contribution from the $b \to s\gamma g$ partonic process;

iii) and iv) non-perturbative corrections that scale as $1/m_b^2$ and $1/m_c^2$, respectively.

The partial width of $\bar{B} \to X_s\gamma$ is as follows:

$$\begin{aligned}\Gamma(\bar{B} \to X_s\gamma) &= \frac{G_F^2}{32\pi^4}|V_{ts}^* V_{tb}|^2 \alpha_{em} m_b^5 \\ &\times \left\{ |\bar{D}|^2 + A + \frac{\delta_\gamma^{NP}}{m_b^2}|\mathrm{C}_7^{0,\mathrm{eff}}(\mu_b)|^2 \right. \\ &+ \left. \frac{\delta_c^{NP}}{m_c^2}\mathrm{Re}\left[[\mathrm{C}_7^{0,\mathrm{eff}}(\mu_b)]^* \times \left(\mathrm{C}_2^{0,\mathrm{eff}}(\mu_b) - \frac{1}{6}\mathrm{C}_1^{0,\mathrm{eff}}(\mu_b) \right) \right] \right\}.\end{aligned} \tag{6.12}$$

The short-distance contribution is contained in $|\bar{D}|^2$, with $\bar{D}$ given by

$$\bar{D} = \mathrm{C}_7^{0,\mathrm{eff}}(\mu_b) + \frac{\alpha_s(\mu_b)}{4\pi}[\mathrm{C}_7^{1,\mathrm{eff}}(\mu_b) + V(\mu_b)]\,. \tag{6.13}$$

The LO Wilson coefficient $C_7^{0,\mathrm{eff}}(\mu_b)$ is a linear combination of $C_7^{0,\mathrm{eff}}(\mu_W)$, $C_8^{0,\mathrm{eff}}(\mu_W)$ and $C_2^{0,\mathrm{eff}}(\mu_W)$, while $C_7^{1,\mathrm{eff}}(\mu_b)$ is a linear combination of these three LO coefficients as well as the NLO coefficients $C_1^{1,\mathrm{eff}}(\mu_W)$, $C_4^{1,\mathrm{eff}}(\mu_W)$, $C_7^{1,\mathrm{eff}}(\mu_W)$ and $C_8^{1,\mathrm{eff}}(\mu_W)$.

The parameter $V(\mu_b)$ is a summation over all the LO Wilson coefficients. The formula is defined as :

$$V(\mu_b) = \sum_{i=1}^{8} \mathrm{C}_i^{0,\mathrm{eff}}(\mu_b)\left[r_i + \frac{1}{2}\gamma_{ji}^{0,\mathrm{eff}} \ln\frac{m_b^2}{\mu_b^2} \right] - \frac{16}{3}\mathrm{C}_7^{0,\mathrm{eff}}(\mu_b) \tag{6.14}$$

The virtual correction functions r_i can be seen in Appendix B.7. The contribution from $b \to s\gamma g$ is contained in A and the remaining two terms are the non-perturbative contributions. In $|\bar{D}|^2$ there are terms of order α_s^2 but, to only keep terms to the NLO order for a consistent calculation (to α_s), the following form is used in [13]:

$$|\bar{D}|^2 = |C_7^{0,\mathrm{eff}}(\mu_b)|^2\{1 + 2\mathrm{Re}(\Delta\bar{D})\}\,, \tag{6.15}$$

$$\Delta\bar{D} = \frac{\bar{D} - C_7^{0,\mathrm{eff}}(\mu_b)}{C_7^{0,\mathrm{eff}}(\mu_b)} = \frac{\alpha_s(\mu_b)}{4\pi}\frac{C_7^{1,\mathrm{eff}}(\mu_b) + V(\mu_b)}{C_7^{0,\mathrm{eff}}(\mu_b)}\,. \tag{6.16}$$

The m_b^5 dependence is removed by using the measured value of the BR of semi-leptonic decay of $\bar{B}$, $\mathrm{BR}_{SL} \approx 0.1$, and its partial width, Γ_{SL} (which also depends on m_b^5), so that $\mathrm{BR}(\bar{B} \to X_s\gamma)$ can be written as follows:

$$\mathrm{BR}(\bar{B} \to X_s\gamma) = \frac{\Gamma(\bar{B} \to X_s\gamma)}{\Gamma_{SL}}\mathrm{BR}_{SL}\,. \tag{6.17}$$

6.3 Direct CP asymmetries in $\overline{B} \to X_s\gamma$ and $\overline{B} \to X_{s+d}\gamma$

In this section the experimental measurements of the inclusive decays $\overline{B} \to X_s\gamma$ and $\overline{B} \to X_{s+d}\gamma$ (charged conjugated processes are implied) are described, followed by a discussion of direct CP asymmetries in these decays. The symbol B signifies B^+ or B^0 (which contain anti-b quarks), while $\overline{B}$ signifies B^- or $\overline{B^0}$ (which contain b quarks). The symbol X_s denotes any hadronic final state that originates from a strange quark hadronising (e.g. states with at least one kaon), X_d means any hadronic final state that originates from a down quark hadronising (e.g. states with at least one pion), and X_{s+d} denotes any hadronic final state that is X_s or X_d.

6.3.1 Experimental measurements of $\overline{B} \to X_s\gamma$ and $\overline{B} \to X_{s+d}\gamma$

There are two ways to measure the BR of the inclusive decays $\overline{B} \to X_{s/d}\gamma$:
i) The fully inclusive method;
ii) The sum-of-exclusives method (also known as "semi-inclusive").

In the fully inclusive approach only a photon from the signal $\overline{B}$ (or B) meson in the $B\overline{B}$ event, which decays via $b \to s/d\gamma$, is selected. Consequently, this method cannot distinguish between hadronic states X_s and X_d, and what is measured is actually the sum of $\overline{B} \to X_s\gamma$ and $\overline{B} \to X_d\gamma$. From the other $\overline{B}$ (or B) meson ("tag B meson") either a lepton (e or μ) can be selected or full reconstruction (either hadronic or semi-leptonic) can be carried out. The former method has a higher signal efficiency, but the latter method has greater background suppression. Measurements of $\overline{B} \to X_{s+d}\gamma$ using the fully inclusive method with leptonic tagging have been carried out by the CLEO collaboration [142], the BABAR collaboration [143] and the BELLE collaboration [144]. A measurement of $\overline{B} \to X_{s+d}\gamma$ using the fully inclusive method with full (hadronic) reconstruction of the tag $\overline{B}$ meson has so far only been carried out by the BABAR collaboration [145]. At the current integrated luminosities (0.5 to 1 ab^{-1}) the errors associated with measurements that involve full reconstruction are significantly larger than the errors from measurements with leptonic tagging. However, with the larger integrated luminosity at BELLE II (50 ab^{-1}) it is expected that both approaches will provide roughly similar errors. To obtain a measurement of $\overline{B} \to X_s\gamma$ alone, the contribution of $\overline{B} \to X_d\gamma$ (which is smaller by roughly $|V_{td}/V_{ts}|^2 \approx 1/20$ in the SM, which has also been confirmed experimentally) is subtracted.

In the sum-of-exclusives approach the selection criteria are sensitive to as many exclusive decays as possible in the hadronic final states X_s and X_d of the signal $\overline{B}$, as well as requiring a photon from $b \to s/d\gamma$. In contrast to the fully inclusive approach, no selection is made on the other B meson in the $B\overline{B}$ event. The sum-of-exclusives method is sensitive to whether the decay $b \to s\gamma$ or $b \to d\gamma$ occurred and so this approach measures $\overline{B} \to X_s\gamma$ or $\overline{B} \to X_d\gamma$. It has different systematic uncertainties to that of the fully

inclusive approach. Measurements of $\overline{B} \to X_s\gamma$ have been carried out by the BABAR collaboration [146] and the BELLE collaboration [147]. Currently, 38 exclusive decays in $\overline{B} \to X_s\gamma$ (about 70% of the total BR) and 7 exclusive decays in $\overline{B} \to X_d\gamma$ [148] are included. At current integrated luminosities the error in the measurement of $\overline{B} \to X_s\gamma$ is about twice that of the fully inclusive approach, whereas at BELLE II integrated luminosities the latter is still expected to give the more precise measurement.

Measurements in both the above approaches are made with a lower cut-off on the photon energy E_γ in the range 1.7 GeV to 2.0 GeV, and then an extrapolation is made to $E_\gamma > 1.6$ GeV using theoretical models. The current world average for the above six measurements of $\overline{B} \to X_s\gamma$ is [149]:

$$\mathcal{B}^{\text{exp}}_{s\gamma} = (3.32 \pm 0.15) \times 10^{-4} \quad \text{with} \quad E_\gamma > 1.6\,\text{GeV}\,. \tag{6.18}$$

The error is currently 4.5%, and is expected to be reduced to around 2.6% with the final integrated luminosity at the BELLE II experiment [150].

The theoretical prediction including corrections to order α_s^2 (i.e. Next-to-Next-to leading order, NNLO) is [151]:

$$\mathcal{B}^{\text{SM}}_{s\gamma} = (3.40 \pm 0.17) \times 10^{-4} \quad \text{with} \quad E_\gamma > 1.6\,\text{GeV}\,.$$

There is excellent agreement between the world average and the NNLO prediction in the SM. Consequently, $\mathcal{B}^{\text{exp}}_{s\gamma}$ allows stringent lower limits to be derived on the mass of new particles, most notably the mass of the charged scalar ($M_{H^\pm} > 480$ GeV [152], as mentioned earlier) in the 2HDM (Type II).

6.3.2 Direct CP asymmetries of $\overline{B} \to X_s\gamma$ and $\overline{B} \to X_{s+d}\gamma$

Although it is clear that measurements of BR($\overline{B} \to X_s\gamma$) alone will not provide evidence for new physics with BELLE II data, the direct CP asymmetry in this decay might [153]. Direct CP asymmetries in $\overline{B} \to X_s\gamma$ and $\overline{B} \to X_d\gamma$ are defined as follows:

$$\mathcal{A}_{X_{s(d)}\gamma} = \frac{\Gamma(\overline{B} \to X_{s(d)}\gamma) - \Gamma(B \to X_{\overline{s}(\overline{d})}\gamma)}{\Gamma(\overline{B} \to X_{s(d)}\gamma) + \Gamma(B \to X_{\overline{s}(\overline{d})}\gamma)}\,. \tag{6.19}$$

If B is B^+ (and so $\overline{B} = B^-$) in the definition of $\mathcal{A}_{X_{s(d)}\gamma}$ then the CP asymmetry is for the charged B mesons, is labelled as $\mathcal{A}^\pm_{X_s\gamma}$ or $\mathcal{A}^\pm_{X_d\gamma}$, and can be individually probed in a search that reconstructs X_s or X_d (sum-of-exclusives method). If B is B^0 the CP asymmetry is for the neutral B mesons, is labelled as $\mathcal{A}^0_{X_s\gamma}$ or $\mathcal{A}^0_{X_d\gamma}$, and can also be individually probed. A general formula for the short-distance contribution (from "direct photons") to $\mathcal{A}_{X_{s(d)}\gamma}$ in terms of Wilson coefficients was derived in Ref. [153]. Prior to the publication of Ref. [153] a few works [154; 155; 13] had calculated $\mathcal{A}_{X_s\gamma}$ in the SM

and in specific extensions of the it that include a charged Higgs boson. The formula for $\mathcal{A}_{X_{s(d)}\gamma}$ in Ref. [153] was the first complete calculation of the asymmetry in terms of all the contributing Wilson coefficients, and was extended twelve years later to include the long-distance contributions (from "resolved photons") in Ref. [156]. In approximate form $\mathcal{A}_{X_{s(d)}\gamma}$ is as follows:

$$\begin{aligned}\mathcal{A}_{X_{s(d)}\gamma} &\approx \pi\Bigg\{\left[\left(\frac{40}{81}-\frac{40}{9}\frac{\Lambda_c}{m_b}\right)\frac{\alpha_s}{\pi}+\frac{\tilde{\Lambda}^c_{27}}{m_b}\right]\mathrm{Im}\frac{C_2}{C_{7\gamma}}\\ &- \left(\frac{4\alpha_s}{9\pi}-4\pi\alpha_s e_{\rm spec}\frac{\tilde{\Lambda}_{78}}{m_b}\right)\mathrm{Im}\frac{C_{8g}}{C_{7\gamma}}\\ &- \left(\frac{\tilde{\Lambda}^u_{17}-\tilde{\Lambda}^c_{27}}{m_b}+\frac{40}{9}\frac{\Lambda_c}{m_b}\frac{\alpha_s}{\pi}\right)\mathrm{Im}\left(\epsilon_{s(d)}\frac{C_2}{C_{7\gamma}}\right)\Bigg\}. \qquad (6.20)\end{aligned}$$

The above four asymmetries are obtained from Eq. (6.20) with the choices for $e_{\rm spec}$ (the charge of the spectator quark) and $\epsilon_{s(d)}$ given in Tab. (6.1). The parameters $\tilde{\Lambda}^u_{27}, \tilde{\Lambda}^c_{27}, \tilde{\Lambda}_{78}$

$\mathcal{A}_{X_{s(d)}\gamma}$	$e_{\rm spec}$	$\epsilon_{s(d)}$
$\mathcal{A}^0_{X_s\gamma}$	$-\frac{1}{3}$	ϵ_s
$\mathcal{A}^\pm_{X_s\gamma}$	$\frac{2}{3}$	ϵ_s
$\mathcal{A}^0_{X_d\gamma}$	$-\frac{1}{3}$	ϵ_d
$\mathcal{A}^\pm_{X_d\gamma}$	$\frac{2}{3}$	ϵ_d

TABLE 6.1: The choices of $e_{\rm spec}$ and $\epsilon_{s(d)}$ in the generic formula for $\mathcal{A}_{X_{s(d)}\gamma}$ that give rise to the four asymmetries.

are hadronic parameters that determine the magnitude of the long-distance contribution. Their allowed ranges were updated in Ref. [157] to be as follows:

$$\begin{aligned}-660\ \text{MeV} < \tilde{\Lambda}^u_{27} < +660\ \text{MeV}\,,\\ -7\ \text{MeV} < \tilde{\Lambda}^c_{27} < +10\ \text{MeV}\,,\\ 17\ \text{MeV} < \tilde{\Lambda}_{78} < 190\ \text{MeV}\,. \qquad (6.21)\end{aligned}$$

The short-distance contributions to $\mathcal{A}_{X_{s(d)}\gamma}$ are the terms that are independent of Λ_{ij}, and $\mathcal{A}^0_{X_{s(d)}\gamma} = \mathcal{A}^\pm_{X_{s(d)}\gamma}$ if long-distance terms are neglected. Other parameters are as follows: $\Lambda_c = 0.38$ GeV, $\epsilon_s = (V_{ub}V^*_{us})/(V_{tb}V^*_{ts}) = \lambda^2(i\bar{\eta}-\bar{\rho})/[1-\lambda^2(1-\bar{\rho}+i\bar{\eta})]$ (in terms of Wolfenstein parameters), $\epsilon_d = (V_{ub}V^*_{ud})/(V_{tb}V^*_{td}) = (\bar{\rho}-i\bar{\eta})/(1-\bar{\rho}+i\bar{\eta})$. The C_i's are Wilson coefficients of relevant operators that are listed in Ref. [153]. In the SM the Wilson coefficients are real and the only term in $\mathcal{A}_{X_{s(d)}\gamma}$ that is non-zero is the term with $\epsilon_{s(d)}$. Due to ϵ_s being of order λ^2 while ϵ_d is of order 1, for the imaginary parts one has $\mathrm{Im}(\epsilon_d)/\mathrm{Im}(\epsilon_s) \approx -22$. For the short-distance contribution only (i.e. neglecting the term with $(\Lambda^u_{27}-\Lambda^c_{27})/m_b$ in Eq. (6.20)) one has $\mathcal{A}_{X_s\gamma} \approx 0.5\%$ and $\mathcal{A}_{X_d\gamma} \approx 10\%$. The small value of $\mathcal{A}_{X_s\gamma}$ in the SM suggests that this observable could probe models of physics beyond the SM that contain Wilson coefficients with an imaginary part.

After the publication of Ref. [153], several works calculated $\mathcal{A}_{X_s\gamma}$ (for the short-distance contribution only) in the context of specific models of physics beyond the SM [158], usually in supersymmetric extensions of it. Values of $\mathcal{A}_{X_s\gamma}$ of up to $\pm 16\%$ were shown to be possible in specific models, while complying with stringent constraints from electric dipole moments (EDMs). Including the long-distance contributions, it was shown in Ref. [156] that the the SM prediction using Eq. (6.20) is enlarged to the range $-0.6\% < \mathcal{A}_{X_s\gamma} < 2.8\%$, and (using updated estimates of the Λ_{ij} parameters) is further increased to $-1.9\% < \mathcal{A}_{X_s\gamma} < 3.3\%$ in Ref. [157]. This revised SM prediction has decreased the effectiveness of $\mathcal{A}_{X_s\gamma}$ as a probe of physics beyond the SM. Consequently, in Ref. [156] the difference of CP asymmetries for the charged and neutral B mesons $\Delta\mathcal{A}_{X_s\gamma} = \mathcal{A}^{\pm}_{X_s\gamma} - \mathcal{A}^{0}_{X_s\gamma}$ was proposed, which is given by:

$$\Delta\mathcal{A}_{X_s\gamma} \approx 4\pi^2\alpha_s \frac{\tilde{\Lambda}_{78}}{m_b} \mathrm{Im}\frac{C_{8g}}{C_{7\gamma}}\,. \tag{6.22}$$

This formula is obtained from Eq. (6.20) in which only the terms with e_{spec} do not cancel out. The SM prediction is $\Delta\mathcal{A}_{X_s\gamma} = 0$ (due to the the Wilson coefficients being real) and hence this observable is potentially a more effective probe of new physics than $\mathcal{A}_{X_s\gamma}$. Note that $\Delta\mathcal{A}_{X_s\gamma}$ depends on the product of a long-distance term ($\tilde{\Lambda}_{78}$, whose value is only known to within an order of magnitude) and two short-distance terms (C_8 and C_7).

An alternative observable is the untagged (fully inclusive) asymmetry ,$\mathcal{A}_{CP}(\overline{B} \to X_{s+d}\gamma)$, given by

$$A_{X_{s+d}\gamma} = \frac{(A^0_{X_s\gamma} + r_{0\pm}A^{\pm}_{X_s\gamma}) + R_{ds}(A^0_{X_d\gamma} + r_{0\pm}A^{\pm}_{X_d\gamma})}{(1 + r_{0\pm})(1 + R_{ds})}\,. \tag{6.23}$$

Here R_{ds} is the ratio $\mathrm{BR}(\overline{B} \to d\gamma)/\mathrm{BR}(\overline{B} \to s\gamma) \approx |V_{td}/V_{ts}|^2$. The parameter $r_{0\pm}$ is defined as the following ratio:

$$r_{0\pm} \equiv \frac{N^+_{X_s} + N^-_{X_s}}{N^0_{X_s} + N^0_{X_s}}, \tag{6.24}$$

where $N^+_{X_s}$ is the number of B^+ mesons that decay to $X_s\gamma$ etc. Experimentally, $r_{0\pm} \approx 1.03$ [150] and in our numerical analysis we take $r_{0\pm} = 1$. In the fully inclusive measurement of $\mathrm{BR}(b \to s/d\gamma)$ the asymmetry $\mathcal{A}_{CP}(\overline{B} \to X_{s+d}\gamma)$ is measured by counting the difference in the number of positively and negatively charged leptons from the tagged (not signal) B meson. The SM prediction of $\mathcal{A}_{CP}(\overline{B} \to X_{s+d}\gamma)$ is essentially 0 [159; 153] (up to tiny m_s^2/m_b^2 corrections), even with the long-distance contribution included. Hence this observable is a cleaner test of new physics than $\mathcal{A}_{X_s\gamma}$. The first studies of the magnitude of the untagged asymmetry in the context of physics beyond the SM were in Ref. [160], and the importance of this observable was emphasised in

Ref. [161]. In this work we will consider the above three direct CP asymmetries in the context of 3HDMs: i) $\mathcal{A}_{X_s\gamma}$, ii) $\mathcal{A}_{CP}(\overline{B} \to X_{s+d}\gamma)$, iii) $\Delta\mathcal{A}_{X_s\gamma}$.

Measurements of all three asymmetries have been carried out, and the most recent BELLE and BABAR measurements are summarised in Tab. (6.2). In Tab. (6.2) the CP asymmetry $\mathcal{A}^{\text{tot}}_{X_s\gamma}$ would have the same magnitude as the average $\overline{\mathcal{A}} = (\mathcal{A}^0_{X_s\gamma} + \mathcal{A}^{\pm}_{X_s\gamma})/2$ if the production cross-sections of B^+B^- and $B^0\overline{B^0}$ were the same. The BELLE measurement [162] of $\overline{\mathcal{A}} = (0.91 \pm 1.21 \pm 0.13)\%$ differs only slightly from the BELLE measurement of $\mathcal{A}^{\text{tot}}_{X_s\gamma}$ in Tab. (6.2). The world averages are taken from Ref. [163]. The given averages for $\mathcal{A}^{\text{tot}}_{X_s\gamma}$ and $\Delta\mathcal{A}_{X_s\gamma}$ are obtained from the two displayed measurements in Tab. (6.2), while the average for $\mathcal{A}_{CP}(\overline{B} \to X_{s+d}\gamma)$ also includes two earlier BABAR measurements and the CLEO measurement $(-7.9 \pm 10.8 \pm 2.2)\%$ [164].

	BELLE	BABAR
$\mathcal{A}^{\text{tot}}_{X_s\gamma}$	$(1.44 \pm 1.28 \pm 0.11)\%$ [162]	$(1.73 \pm 1.93 \pm 1.02)\%$ [165]
$\mathcal{A}_{\text{CP}}(\bar{B} \to X_{s+d}\gamma)$	$(2.2 \pm 3.9 \pm 0.9)\%$[166]	$(5.7 \pm 6.0 \pm 1.8)\%$ [143]
$\Delta\mathcal{A}_{X_s\gamma}$	$(3.69 \pm 2.65 \pm 0.76)\%$[162]	$(5.0 \pm 3.9 \pm 1.5)\%$[165]

	World average
$\mathcal{A}^{\text{tot}}_{X_s\gamma}$	$1.5\% \pm 1.1\%$ [163]
$\mathcal{A}_{\text{CP}}(\bar{B} \to X_{s+d}\gamma)$	$1.0\% \pm 3.1\%$ [163]
$\Delta\mathcal{A}_{X_s\gamma}$	$4.1\% \pm 2.3\%$ [163]

TABLE 6.2: Measurements (given as a percentage) of $\mathcal{A}^{\text{tot}}_{X_s\gamma}$, $\mathcal{A}_{\text{CP}}(\bar{B} \to X_{s+d}\gamma)$ and $\Delta\mathcal{A}_{X_s\gamma}$ at BELLE, BABAR and the world average.

At BELLE II all three asymmetries will be measured with greater precision [150]. At present around 74 fb^{-1} of integrated luminosity have been accumulated, which is about one tenth of the integrated luminosity at the BELLE experiment, and about one sixth that at the BABAR experiment. By the end of the year 2021 about 1 ab^{-1} is expected, and thus measurements of $b \to s\gamma$ at BELLE II will then match (or better) in precision those at BELLE and BABAR. For an integrated luminosity of 50 ab^{-1} (which is expected to be obtained by the end of the BELLE II experiment in around the year 2030), the estimated precision for $\mathcal{A}^{\text{tot}}_{X_s\gamma}$ is 0.19%, for $\mathcal{A}_{CP}(\overline{B} \to X_{s+d}\gamma)$ is 0.48% (leptonic tag) and 0.7% (hadronic tag), and for $\Delta\mathcal{A}_{X_s\gamma}$ is 0.3% (sum-of-exclusives) and 1.3% (fully inclusive with hadronic tag, and so it measures a sum of $b \to s\gamma$ and $b \to d\gamma$). These numbers are summarised in Tab. 6.3, together with the SM predictions. Due to the SM prediction of $\mathcal{A}_{CP}(\overline{B} \to X_{s+d}\gamma)$ being essentially zero, a central value of 2.5% with 0.5% error would constitute a 5σ signal of physics beyond the SM. For $\Delta\mathcal{A}^{\text{tot}}_{X_s\gamma}$, whose prediction in the SM is also essentially zero, a central value of 1.5% with 0.3% error would constitute a 5σ signal. Note that the current 2σ allowed range of $\mathcal{A}^{\text{tot}}_{X_s\gamma}$ is $-0.7\% < \mathcal{A}^{\text{tot}}_{X_s\gamma} < 3.7\%$ ($-1.8\% < \mathcal{A}^{\text{tot}}_{X_s\gamma} < 4.8\%$ at 3σ). Comparing this range with the SM prediction of $-1.9\% < \mathcal{A}^{\text{tot}}_{X_s\gamma} < 3.3\%$ shows that it is less likely that the observable $\mathcal{A}^{\text{tot}}_{X_s\gamma}$ alone could provide a clear signal of physics beyond the SM, e.g. a future central value of above 4.3% (which is outside the current 2σ range) with the expected of error

0.19% would be required to give a 5σ discrepancy from the upper SM prediction of 3.3%.

	SM Prediction	Leptonic tag	Hadronic tag	Sum of exclusives
$\mathcal{A}^{\text{tot}}_{X_s\gamma}$	$-1.9\% < \mathcal{A}_{X_s\gamma} < 3.3\%$	x	x	0.19%
$\mathcal{A}_{CP}(\overline{B} \to X_{s+d}\gamma)$	0	0.48%	0.70%	x
$\Delta\mathcal{A}_{X_s\gamma}$	0	x	1.3%	0.3%

TABLE 6.3: SM predictions of $\mathcal{A}^{\text{tot}}_{X_s\gamma}$, $\mathcal{A}_{CP}(\overline{B} \to X_{s+d}\gamma)$ and $\Delta\mathcal{A}_{X_s\gamma}$, and expected experimental errors in their measurements at BELLE II with 50 ab^{-1}.

6.4 Results from constraint on $\bar{B} \to X_s\gamma$ and CP-asymmetries observables

In this section, we present the results of BR($\bar{B} \to X_s\gamma$) and the CP-asymmetries in the 3HDM with two charged Higgs states $H_2^\pm$ and $H_3^\pm$. The four mixing parameters that determine the charged Higgs Yukawa couplings (X_i, Y_i, and Z_i) are again varied in the same range as Eqs. (4.43). In all five 3HDMs, which can be seen back from Tab. (4.2), type-II, Y (Flipped), and type-Z (Democratic) 3HDMs have similar Yukawa structures and so have identical predictions for BR($\bar{B} \to X_s\gamma$) and the three CP-asymmetry observables. Two models (type-I and lepton-specific) will not be covered because the asymmetries of these two models cannot give rise to CP asymmetries which are significantly larger than in the SM. The reason for this is that the contribution of $X_2Y_2^*$ and $X_3Y_3^*$ have real values. Thus, there is no imaginary part and so the CP asymmetry observables will not be affected by the charged Higgs sector. In this section, our results will mainly focus on the Type-Y (Flipped) 3HDM for simplicity. For the allowed range of BR($\bar{B} \to X_s\gamma$), we use the experimental result of Eq. (6.18), which gives a 3σ allowed range between $(2.87 \leq \bar{B} \to X_s\gamma \leq 3.77) \times 10^{-4}$.

First of all, we show the region of the $[M_{H_2^\pm}, M_{H_3^\pm}]$ plane that satisfies the above 3σ interval for BR($\bar{B} \to X_s\gamma$). In our earlier works and earlier in this thesis we used the rough limit of $b \to s\gamma$ with a charged Higgs mass at 100 GeV in Refs. [17; 18]. Within the type-Y (Flipped) model we used the limit of Re $(X_2Y_2^*)$ between -0.7 and 1.1 and neglected the contribution of $X_3Y_3^*$, Y_2^2 and Y_3^2 (i.e. we neglected the contribution of charged Higgs state $H_3^\pm$). In Fig. (6.2), two plots are shown. The left panel fixes $\theta = -\frac{\pi}{4}$, $\tan\beta = 10$, and $\tan\gamma = 1$. The CP-violation phase in the left panel is $\delta = 0$ while in the right panel we use $\delta = \frac{\pi}{2}$. Results are shown in the plane $[M_{H_2^\pm}, M_{H_3^\pm}]$ for both plots, with the range between 80 GeV and 1000 GeV (1 TeV). For our numerical analysis, we took the scale μ_b to be the pole mass of the bottom quark m_b. By comparing difference the left and right panel of Fig. (6.2), it can be seen that more parameter space is allowed with a larger value of δ.

Fig. (6.3) shows the allowed parameter space of with θ changed to $-\frac{\pi}{2.1}$. These two plots show that the region in the plane $[M_{H_2^\pm}, M_{H_3^\pm}]$ that satisfies the constraint from BR($\bar{B} \to X_\gamma$) can changes significantly when δ and θ is changed. Notably, the scenario of $M_{H_2^\pm}, M_{H_3^\pm} \leq m_t$ is possible for $\delta = \frac{\pi}{2}$.

In Fig. (6.4), the allowed parameter space of $\bar{B} \to X_s\gamma$ is presented in the plane of $[\tan\gamma, \tan\beta]$ with θ chosen to be $-\frac{\pi}{3}$. Two charged Higgs masses are fixed to 85 GeV ($H_2^\pm$) and 800 GeV ($H_3^\pm$). The left panel of Fig. (6.4) has $\delta = 0$ while the right panel has $\delta = \frac{\pi}{2}$. The parameter space is much smaller than in Ref. [17] in which the constraint from $\bar{B} \to X_s\gamma$ only included the contribution from Re$X_2Y_2^*$.

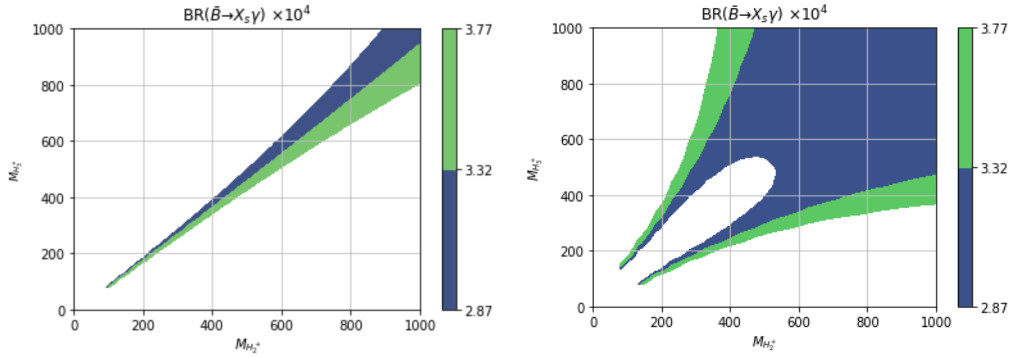

FIGURE 6.2: BR($\bar{B} \to X_s\gamma$) in the mass region plane of [$M_{H_2^\pm}$, $M_{H_3^\pm}$]. The mixing parameters are fixed for $\theta = -\frac{\pi}{4}$, $\tan\beta = 10$, $\tan\gamma = 1$. The left panel: $\delta = 0$. The right panel: $\delta = \frac{\pi}{2}$. The two color bands (green and blue) are allowed for 3σ of experiment result as Eq. (6.18).

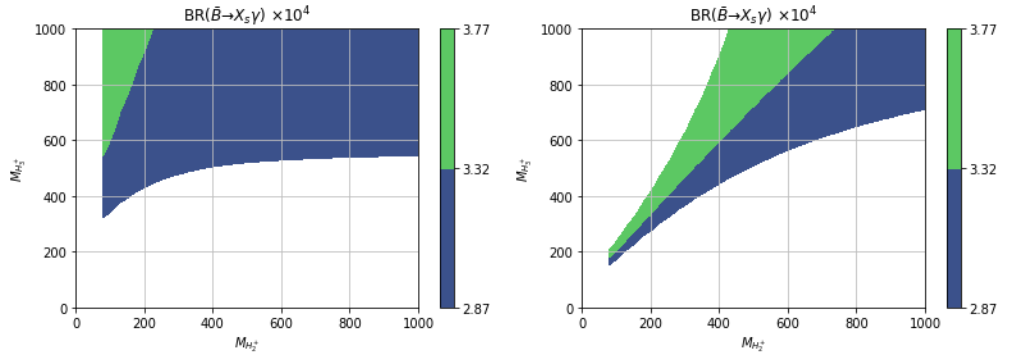

FIGURE 6.3: BR($\bar{B} \to X_s\gamma$) in the mass region plane of [$M_{H_2^\pm}$, $M_{H_3^\pm}$]. The mixing parameters are fixed for $\theta = -\frac{\pi}{2.1}$, $\tan\beta = 10$, $\tan\gamma = 1$. The left panel: $\delta = 0$. The right panel: $\delta = \frac{\pi}{2}$. The two color bands (green and blue) are allowed for 3σ of experiment result as Eq. (6.18).

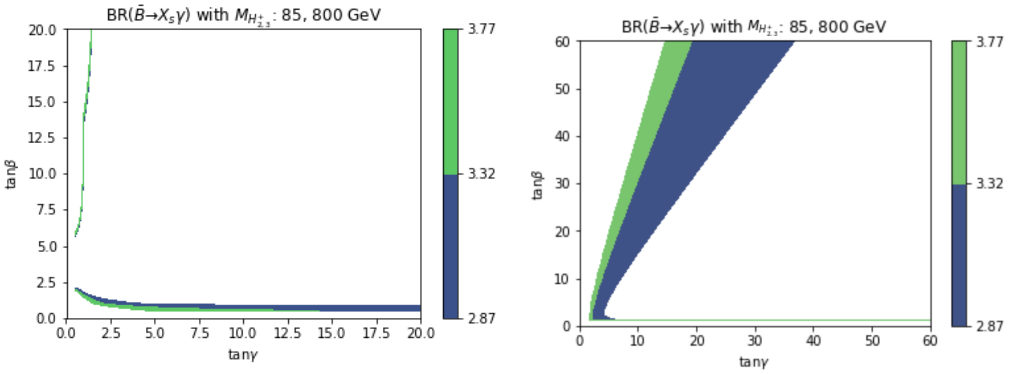

FIGURE 6.4: BR($\bar{B} \to X_s\gamma$) in the mixing parameter plane of [$\tan\gamma$, $\tan\beta$] with two charged Higgs states $M_{H^\pm_{2,3}} = 85$ and 800 GeV respectively. The mixing parameters of θ is equal to $-\frac{\pi}{3}$. The left panel: $\delta = 0$. The right panel: $\delta = \frac{\pi}{2}$. The two color bands (green and blue) are allowed for 3σ of experiment result as Eq. (6.18).

In Fig. (6.5), we show two plots in the same plane as Fig. (6.4), but with a different choice of charged Higgs masses, $M_{H_2^\pm} = 130$ GeV, and $M_{H_3^\pm} = 400$ GeV. The left panel takes

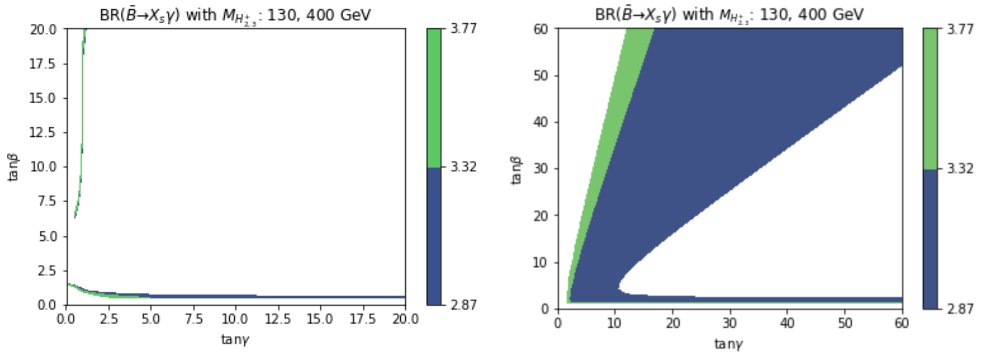

FIGURE 6.5: BR($\bar{B} \to X_s\gamma$) in the mixing parameter plane of [$\tan\gamma$, $\tan\beta$] with two charged Higgs states $M_{H^\pm_{2,3}} = 130$ and 400 GeV respectively. The mixing parameters of θ is equal to $-\frac{\pi}{3}$. The left panel: $\delta = \frac{\pi}{4}$. The right panel: $\delta = \frac{\pi}{2}$. The two color bands (green and blue) are allowed for 3σ of experiment result as Eq. (6.18).

$\delta = \frac{\pi}{4}$ and the right panel takes $\delta = \frac{\pi}{2}$. One can see that only a very small parameter space in the left panel space respects the constraint, while a larger parameters space is permitted for the $\frac{\pi}{2}$ case in the right panel. In our results for BR($H_2^\pm \to cb$) which we showed before, the value of δ does not have any effect in the plane of [$\tan\gamma, \tan\beta$]. In other words, the CP-violating phase δ cannot be probed in the decay of the charged Higgs boson. The scenario of type- Y (Flipped) 3HDM with a large BR($H_2^\pm \to cb$) is compatible with the $\bar{B} \to X_s\gamma$ constraint, especially if a non-zero phase δ is present (which allows more parameter space in the plane [$\tan\gamma, \tan\beta$] to respect the $\bar{B} \to X_s\gamma$ constraint, while having negligible effect on BR($H_2^\pm \to cb$) as mentioned above).

Now we show the CP-asymmetries results. Firstly, we specify the values of the parameters that will be used in our numerical analysis. For $\mathcal{A}_{X_s\gamma}$, we use the average of charged and neutral asymmetry result $((\mathcal{A}^\pm_{X_s\gamma} + \mathcal{A}^0_{X_s\gamma})/2)$, which uses the value of e_{spec} to be $\frac{1}{6}$. For the Wilson coefficients $C_2, C_{7\gamma}, C_{8g}$, we only used LO terms because the evaluation of the asymmetry results at the order of $(\mathcal{O}(\alpha^2))$ requires not only LO and NLO Wilson coefficients $C_2, C_{7\gamma}, C_{8g}$, but also the NNLO contributions. The long distance (or "hadronic parameters") are as follows: $\tilde{\Lambda}^u_{27} = 0.66$ GeV, $\tilde{\Lambda}^c_{27} = 0.01$ GeV, and $\tilde{\Lambda}_{78} = 0.19$ GeV.

Figs. (6.6) shows the three CP-asymmetry observables ($\mathcal{A}_{X_s\gamma}, \Delta(\mathcal{A}_{X_s\gamma})$ and $\mathcal{A}_{\rm CP}(\bar{B} \to X_{s+d}\gamma)$) which are plotted in the plane [$\tan\gamma, \tan\beta$] with fixed charged Higgs masses $M_{H_2^\pm} = 170$ GeV, and $M_{H_3^\pm} = 180$ GeV. The other two mixing parameters are fixed as $\theta = -\frac{\pi}{4}, \delta = 2.64$. The top left panel of Fig. (6.6) is for $\mathcal{A}_{X_s\gamma}$ and the top right panel is for $\Delta\mathcal{A}_{X_s\gamma}$. The bottom panel is for $\mathcal{A}_{\rm CP}(\bar{B} \to X_{s+d}\gamma)$. All values are in percentage. Three red lines inside each figure are the 3σ bounds allowed by BR($\bar{B} \to X_s\gamma$), from left to right are the upper to lower bound respectively. In the case of $\mathcal{A}_{X_s\gamma}$ plot, the magnitude of 0.5% to 1.5%, which is within the current experimental limits. In the plot $\Delta\mathcal{A}_{X_s\gamma}$ plot, the CP violating observable can reach -1.5% or above in the dark blue area between the values $\tan\gamma$ from 1 to 1.50. The is possible for 5σ signal at BELLE II with

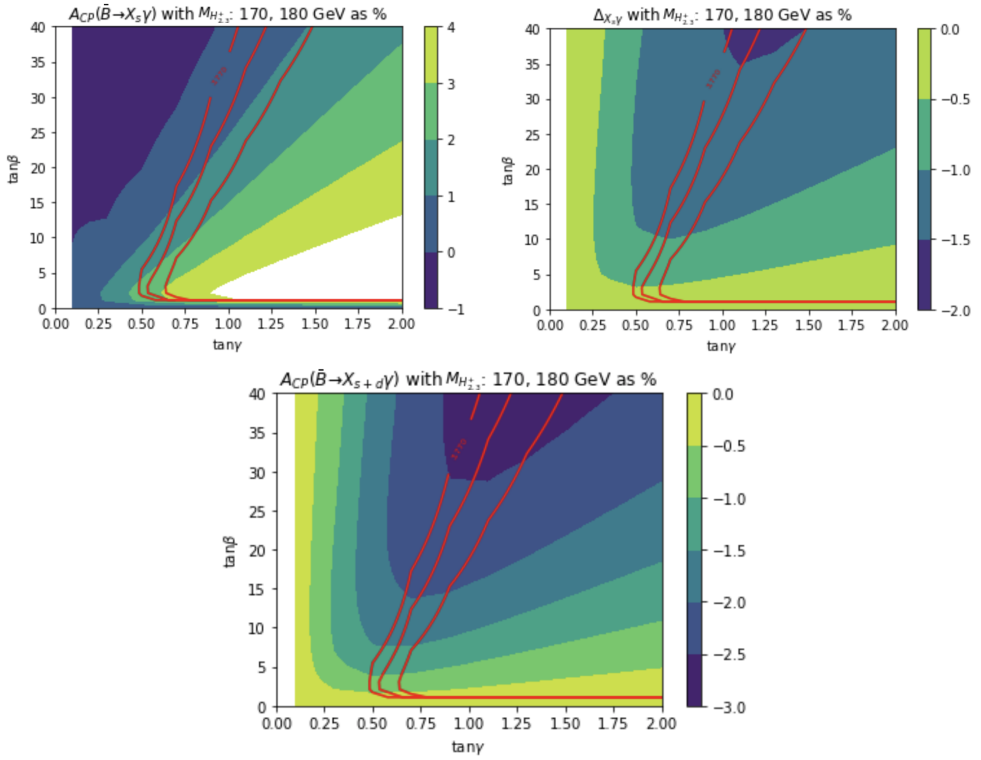

FIGURE 6.6: CP asymmetries (as a percentage) contour plots under mixing parameter plane $[\tan\gamma, \tan\beta]$ with the mass of $M_{H_2^\pm} = 170$ GeV, $M_{H_3^\pm} = 180$ GeV. Parameter $\theta = -\frac{\pi}{4}$, and $\delta = 2.64$. The three red lines from (left to right) are the allowed 3σ (upper to lower) bound of BR($\bar{B} \to X_s\gamma$) constraint. Top left panel: $\mathcal{A}_{X_s\gamma}$. Top right panel: $\Delta\mathcal{A}_{X_s\gamma}$. Bottom panel: $\mathcal{A}_{\rm CP}(\bar{B} \to X_{s+d}\gamma)$.

50 fb^{-1}. However, the effect of hadronic parameter would influence the uncertainty which we will discuss later. The bottom panel of $\mathcal{A}_{\rm CP}(\bar{B} \to X_{s+d}\gamma)$ shows the allowed region which in the dark blue area could achieve more negative values than -3%. Such values would therefore be a potential 5σ signal. The $\Delta\mathcal{A}_{X_s\gamma}$ case has a strong correlation with the hadronic parameter of $\tilde{\Lambda}_{78}$ and can also give sizeable asymmetries. Larger asymmetries are possible in the 3HDM than in the Aligned 2HDM [167; 168]. The reason is because the 3HDM has two charged scalars which leads to possible cancellations among the separate contributions, thus respecting BR($\bar{B} \to X_s\gamma$) and allowing large asymmetries. The white region in each figure is excluded for all three CP-asymmetries as they are outside the current 3σ experimental bounds on these CP-asymmetry observables.

The last figure of this section are CP-asymmetry plots in the plane $[\theta, \delta]$ using the same charged Higgs masses, $M_{H_2^\pm} = 170$ GeV, $M_{H_3^\pm} = 180$ GeV. These are Fig. (6.7) in which $\tan\beta$ =35 and $\delta = 2.64$. The top left panel is $\mathcal{A}_{X_s\gamma}$ and the top right panel is $\Delta\mathcal{A}_{X_s\gamma}$. The bottom panel of Fig. (6.7) is $\mathcal{A}_{\rm CP}(B \to X_{s+d}\gamma)$. Instead of red lines as the previous figures, the BR($\bar{B} \to X_s\gamma$) constraint is now shown as a red ellipse. Inside the circle is the allowed 3σ bound with the outer line being the lower bound. This restricts the allowed parameter space to be roughly $-1.1 < \theta < -0.5$ and $2.6 < \delta < 3.7$. The white

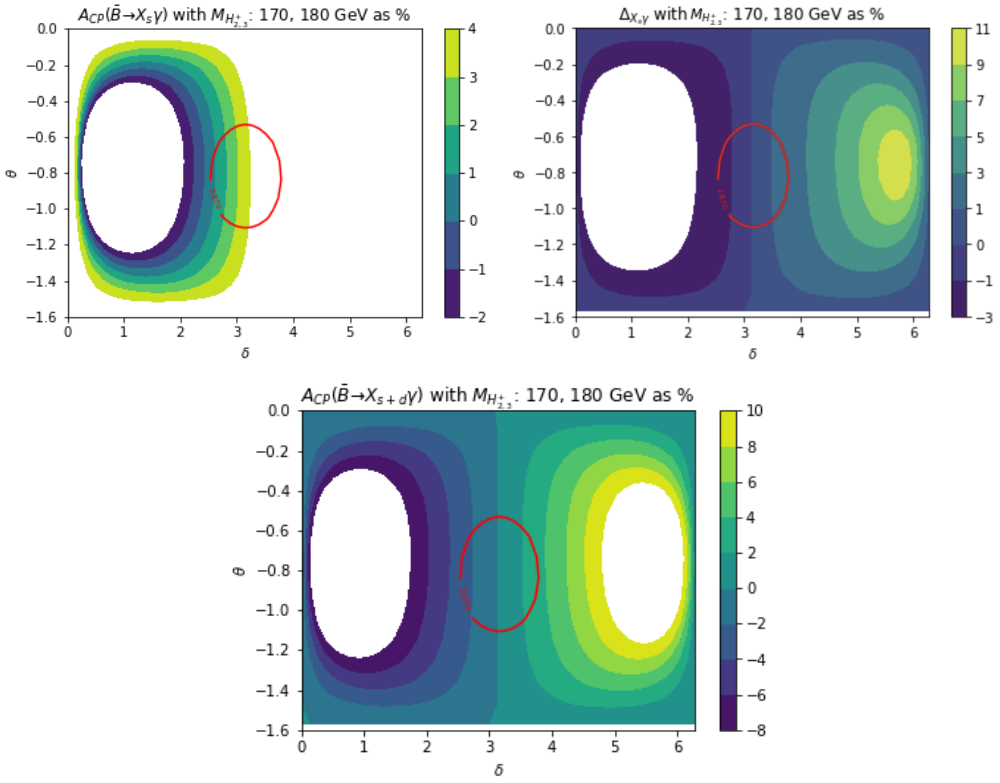

FIGURE 6.7: CP asymmetries (as a percentage) contour plots under mixing parameter plane $[\theta, \delta]$ with the mass of $M_{H_2^\pm} = 170$ GeV, $M_{H_3^\pm} = 180$ GeV. Parameter $\tan\beta = 35$, and $\tan\gamma = 1.32$. Inside the red circle is allowed for 3σ bound of $\text{BR}(\bar{B} \to X_s\gamma)$ constraint. Top left panel: $\mathcal{A}_{X_s\gamma}$. Top right panel: $\Delta\mathcal{A}_{X_s\gamma}$. Bottom panel: $\mathcal{A}_{\text{CP}}(\bar{B} \to X_{s+d}\gamma)$.

regions in the three plots are again excluded because they lie outside of the 3σ allowed ranges of the CP-asymmetry measurements in Tab. (6.2). Values of $\Delta\mathcal{A}_{X_s\gamma} \approx -1.5\%$ and $\mathcal{A}_{\text{CP}}(\bar{B} \to X_{s+d}\gamma) \approx -2.5\%$ can be achieved.

μ_b	$\text{BR}(\bar{B} \to X_s\gamma)$ $(\times 10^{-4})$	$\mathcal{A}_{\text{CP}}(\bar{B} \to X_s\gamma)\%$	$\Delta A_{X_s\gamma}$ %	$\mathcal{A}_{\text{CP}}(\bar{B} \to X_{s+d}\gamma)$ %
$\mu_b = m_b/2$	2.912	-3.170	-0.111	-0.974
$\mu_b = m_b$	2.968	-3.636	-0.134	-1.058
$\mu_b = 2m_b$	2.801	-4.137	-0.613	-1.153

TABLE 6.4: $\text{BR}(\bar{B} \to X_s\gamma)$, $\mathcal{A}_{\text{CP}}(\bar{B} \to X_s\gamma)$, $\Delta A_{X_s\gamma}$ and $\mathcal{A}_{\text{CP}}(B \to X_{s+d}\gamma)$ for three different values of the scale μ_b and using LO expression of $C_{7,8}$. Other parameters are fixed as follows: $M_{H_2^\pm} = 170$ GeV, $M_{H_3^\pm} = 180$ GeV, $\theta = -\frac{\pi}{4}$, $\tan\beta = 32$, $\tan\gamma = 1$, $\delta = 2.64$, $m_b = 4.71$ GeV, $\tilde{\Lambda}_{27}^u = -0.66$ GeV, $\tilde{\Lambda}_{27}^c = -0.007$ GeV and $\tilde{\Lambda}_{78} = 0.017$ GeV.

The theoretical uncertainty of our predictions arises from varying the scale μ_b and the hadronic parameters, $\tilde{\Lambda}_{27}^u, \tilde{\Lambda}_{27}^c, \tilde{\Lambda}_{78}$. To study the theoretical uncertainty we present three tables with the charged Higgs masses fixed as $M_{H_2^\pm} = 170$ GeV, $M_{H_3^\pm} = 180$ GeV. We also take $\theta = -\frac{\pi}{4}, \delta = 2.64$ as in Fig. (6.6); $\tan\beta = 35, \tan\gamma = 1.32$ as in Fig. (6.7) in Tab. (6.4,6.5,6.6). Each table picked the value of μ_b as $m_b/2, m_b, 2m_b$. In Tab. (6.4), the lowest value of m_b has set to be 4.71 GeV. Tab. (6.4) has $m_b = 4.77$ GeV

μ_b	BR($\bar{B} \to X_s\gamma$) ($\times 10^{-4}$)	$\mathcal{A}_{\rm CP}(\bar{B} \to X_s\gamma)$%	$\Delta A_{X_s\gamma}$ %	$\mathcal{A}_{\rm CP}(\bar{B} \to X_{s+d}\gamma)$ %
$\mu_b = m_b/2$	2.888	-1.220	-0.562	-1.755
$\mu_b = m_b$	2.931	-1.663	-0.673	-2.151
$\mu_b = 2m_b$	2.761	-2.212	-0.820	-2.670

TABLE 6.5: BR($\bar{B} \to X_s\gamma$), $\mathcal{A}_{\rm CP}(\bar{B} \to X_s\gamma)$, $\Delta A_{X_s\gamma}$ and $\mathcal{A}_{\rm CP}(\bar{B} \to X_{s+d}\gamma)$ for three different values of the scale μ_b and using LO expression of $C_{7,8}$. Other parameters are fixed as follows: $M_{H_2^\pm} = 170$ GeV, $M_{H_3^\pm} = 180$ GeV, $\theta = -\frac{\pi}{4}$, $\tan\beta = 32$, $\tan\gamma = 1$, $\delta = 2.64$, $m_b = 4.77$ GeV, $\tilde{\Lambda}_{27}^u = 0$ GeV, $\tilde{\Lambda}_{27}^c = 0.0085$ GeV and $\tilde{\Lambda}_{78} = 0.0865$ GeV.

μ_b	BR($\bar{B} \to X_s\gamma$) ($\times 10^{-4}$)	$\mathcal{A}_{\rm CP}(\bar{B} \to X_s\gamma)$%	$\Delta A_{X_s\gamma}$ %	$\mathcal{A}_{\rm CP}(\bar{B} \to X_{s+d}\gamma)$ %
$\mu_b = m_b/2$	2.865	1.145	-1.223	-2.123
$\mu_b = m_b$	2.896	0.914	-1.466	-2.641
$\mu_b = 2m_b$	2.724	0.581	-1.785	-3.323

TABLE 6.6: BR($\bar{B} \to X_s\gamma$), $\mathcal{A}_{\rm CP}(\bar{B} \to X_s\gamma)$, $\Delta A_{X_s\gamma}$ and $\mathcal{A}_{\rm CP}(\bar{B} \to X_{s+d}\gamma)$ for three different values of the scale μ_b and using LO expression of $C_{7,8}$. Other parameters are fixed as follows: $M_{H_2^\pm} = 170$ GeV, $M_{H_3^\pm} = 180$ GeV, $\theta = -\frac{\pi}{4}$, $\tan\beta = 32$, $\tan\gamma = 1$, $\delta = 2.64$, $m_b = 4.83$ GeV, $\tilde{\Lambda}_{27}^u = 0.66$ GeV, $\tilde{\Lambda}_{27}^c = 0.010$ GeV and $\tilde{\Lambda}_{78} = 0.19$ GeV.

and Tab. (6.6) has $m_b = 4.83$ GeV. The pole mass of the bottom quark has a central value 4.77 ± 0.66 GeV. The scale dependence is included for BR($\bar{B} \to X_s\gamma$) and the CP-asymmetry observables. One can see that scale μ_b has a strong effect on $\Delta A_{X_s\gamma}$ and $\mathcal{A}_{\rm CP}(\bar{B} \to X_{s+d}\gamma)$, for which a larger scale makes their values more negative. On the other hand, the hadronic parameters affect the value of $\mathcal{A}_{\rm CP}(\bar{B} \to X_s\gamma)$ and can even flip the sign, which can be seen in Tab. (6.4) and Tab. (6.6). $\Delta A_{X_s\gamma}$ is also sensitive to the hadronic parameter $\tilde{\Lambda}_{78}$ while the effect on $\mathcal{A}_{\rm CP}(\bar{B} \to X_{s+d}\gamma)$ is less. The minimum and maximum of values of the table are given below:

$$\begin{aligned}
2.724 < &\quad \bar{B} \to X_s\gamma &&< 2.968 \ \ (\times 10^{-4}) \\
-4.137\% < &\quad \mathcal{A}_{\rm CP}(\bar{B} \to X_s\gamma) &&< 0.581\% \\
-1.785 < &\quad \Delta A_{X_s\gamma} &&< -0.111\% \\
-3.323\% < &\quad \mathcal{A}_{\rm CP}(\bar{B} \to X_{s+d}\gamma) &&< -0.974\%
\end{aligned} \tag{6.25}$$

However, we did not check a full scan, and so it is possible that larger asymmetries could be possible.[1].

[1] In this case, an improvement of this research could be covered for a full scanning of the parameters to test the CP-asymmetry results.

6.5 Electric Dipole Moment (EDM) constraint for charged Higgs

In this section, we investigate other experimental constraints on the charged Higgs Yukawa couplings, which are due to the electric dipole moments (EDMs) of neutron and electron. These two observables constrain the imaginary components of the charged Higgs Yukawa couplings. First of all, the current experimental bound from the neutron-EDM (nEDM) will be covered. Within the model analysis, the calculation is performed with all relevant operators. Several contributions will be mentioned and formulas will be given. Based on the scheme of the Aligned 2HDM, the analysis will be extrapolated to the 3HDM. In the specific case of the type-Z (Democratic) 3HDM, the allowed mixing parameters with the nEDM will be singled out. Similarly, the electron-EDM (eEDM) will also be covered. Through the combination of the $\bar{B} \to X_s\gamma$ and two EDM constraints, this section will show the final allowed CP-violating parameter space for the Yukawa couplings of the two charged Higgs bosons of the 3HDMs. The whole material here is taken from Ref. [15].

6.5.1 Collider and perturbative constraints for two charged Higgs

For the allowed parameter space of EDM constraint discussion, several additional constraints are included. These are done by our colleagues in Ref. [15]. We used the CalcHEP [169] to simulate the production of charged Higgs from proton-proton collision and calculate the decay of charged Higgs with fermion modes. The first one is the collider constraint. In Figs. 6.8–6.9, we show the branching ratios (BRs) of $H_2^\pm$ (first and second row panels) and $H_3^\pm$ (third and fourth row panels) as a function of $\tan\beta$, in the 3HDM type-I, -II, -X (Lepton-Specific), -Y (Flipped) and the type-Z (Democratic) model. In Fig. (6.8) we take $M_{H_2^\pm} = 100$ GeV and $M_{H_3^\pm} = 150$ GeV, while in Fig. (6.9) we take $M_{H_2^\pm} = 200$ GeV and $M_{H_3^\pm} = 250$ GeV, with $\theta = -\pi/4$ and $\delta = 0$ in both. The solid and dotted curves show the case for $\tan\beta = 2$ and 5, respectively. We can see that a light charged Higgs boson (with $M_{H_i^\pm} < m_t$) predominantly decays to $\tau\nu$, although cs is more dominant for some types in specific $\tan\beta$ regions. Furthermore, the decay into cb becomes relevant for higher $\tan\beta$ in the type-Y and type-Z (Democratic) models. For a heavy charged Higgs boson (with $M_{H_i^\pm} > m_t$), the vastly dominant decay is into tb except for type-X at large $\tan\beta$, where $\tau\nu$ dominates instead. Instead, for the type-Z (Democratic) model, $\tau\nu$ dominates for large values of $\tan\gamma$. (Notice that, here, the 3HDM parameter values are chosen so we can directly compare with Figs. 1 and 2 of [97], where the parametrization of $\tan\beta$ and $\tan\gamma$ is, however, chosen differently from our work.[2])

Charged Higgs boson production in hadronic collisions can be described by the subprocesses $gg, q\bar{q} \to t\bar{b}H^-$ + c.c. for both light ($M_{H_i^\pm} < m_t$) and heavy ($M_{H_i^\pm} > m_t$)

[2]Furthermore, we use here the labeling $H_{2,3}^\pm$ in place of $H_{1,2}^\pm$ in Ref. [97], respectively.

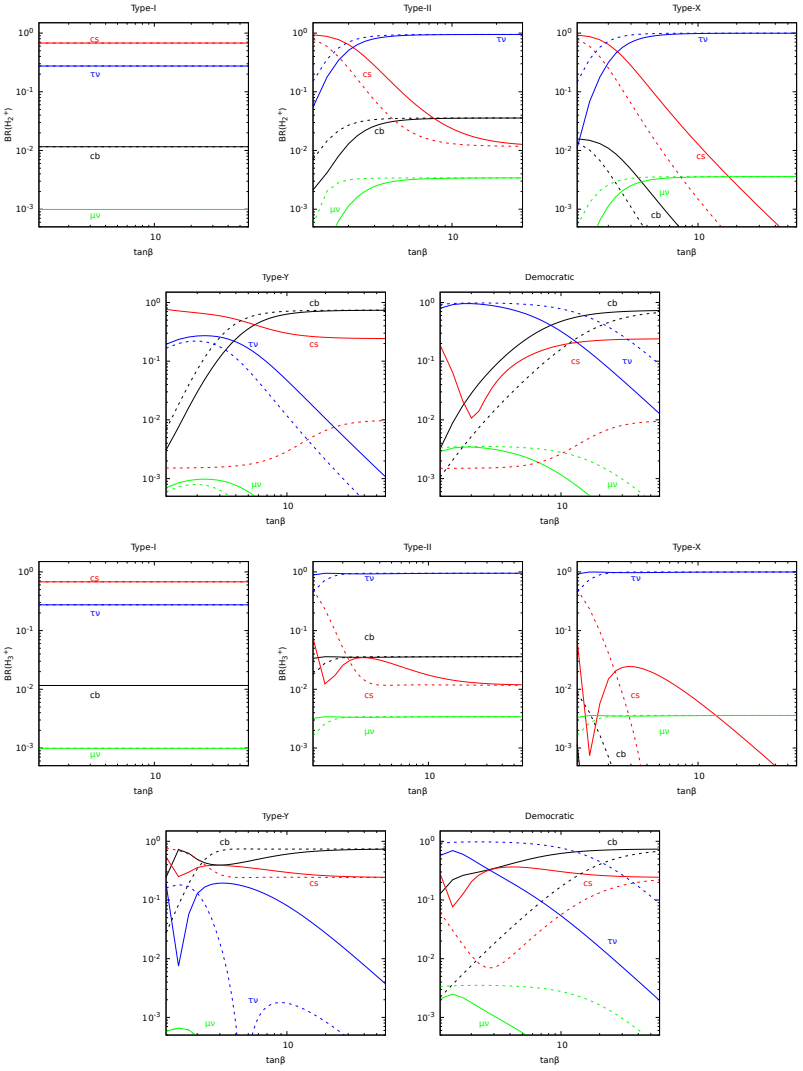

FIGURE 6.8: BRs of $H_2^\pm$ (first and second row panels) and $H_3^\pm$ (third and fourth row panels) as a function of $\tan\beta$ in, from upper row left to right, the type-I, -II, -X (Lepton-specific), lower row type-Y (Flipped), and type-Z (Democratic) 3HDMs. We take $M_{H_2^\pm} = 100$ GeV, $M_{H_3^\pm} = 150$ GeV, $\theta = -\pi/4$ and $\delta = 0$. The value of $\tan\gamma$ is 2 (5) for the solid (dotted) curves.

states [170; 171], as in the former case the dominant channel is $gg, q\bar{q} \to t\bar{t} \to t\bar{b}H^- +$ c.c. (i.e., t-quark pair production and decay) while in the latter case, it is $bg \to tH^-$ + c.c. (i.e., Higgs-strahlung off b-quarks).[3] Since the Higgs-strahlung cross section is much smaller than the one for top-antitop quark production, a light charged Higgs boson is severely constrained while direct searches for a heavy one leave it largely unconstrained. However, when $M_{H_i^\pm} \approx M_{W^\pm} \approx 80$ GeV, the $t \to bW^\pm$ background overwhelms the $t \to bH^\pm$ signal, so that, even at the current Large Hadron Collider (LHC), this mass region is still allowed for a charged Higgs state in a 3HDM, no matter its decay mode [17; 18]. Of relevance to our analysis are the constraints coming from $H^\pm \to \tau\nu$ [8], cb [9] and cs [10] searches at the LHC (with the first channel generally

[3]Recall that b-(anti)quarks are produced inside protons from a gluon splitting.

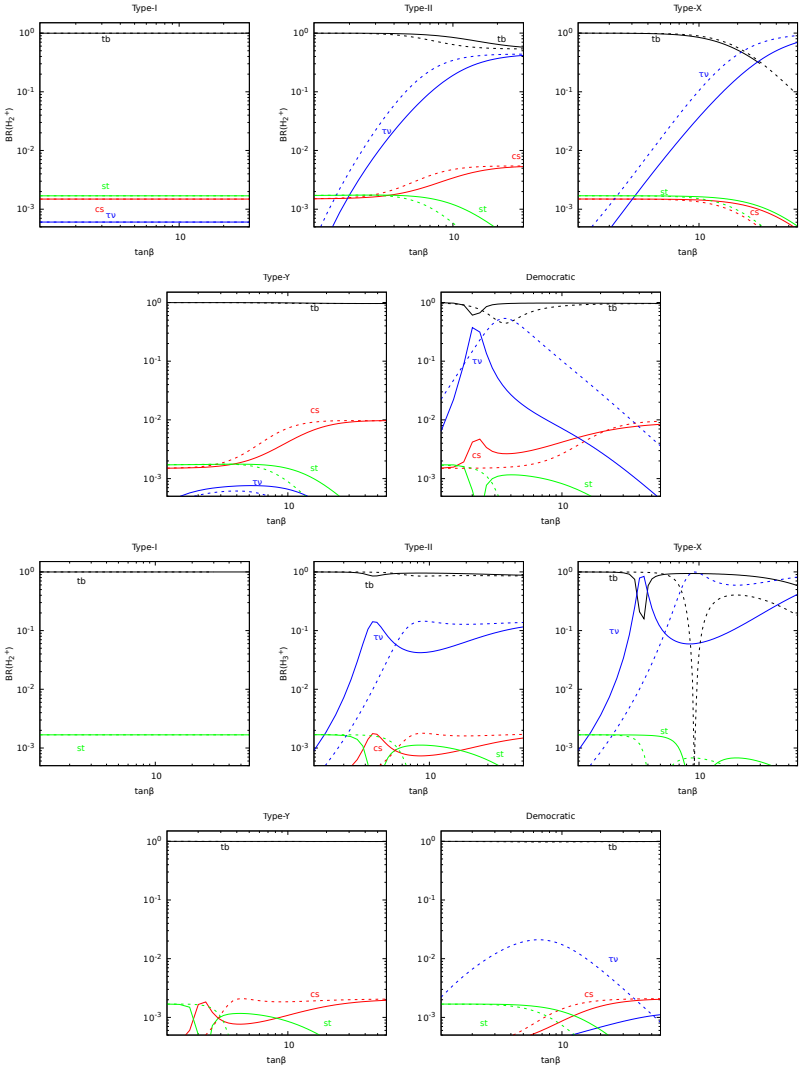

FIGURE 6.9: As in Fig. (6.8) but for $M_{H_2^\pm} = 200$ GeV and $M_{H_3^\pm} = 250$ GeV.

being more constraining than the second and third ones), which have been performed by both ATLAS and CMS.

In Fig. (6.10), we fix the values of $M_{H_2^\pm} = 80$ GeV, $M_{H_3^\pm} = 170$ (200) GeV in the upper (lower) panels and $\tan\beta = 20$.[4] We tested the region $-0.6 < \theta < 0$, $0.4 < \tan\gamma < 2.6$ against CMS searches for $H^\pm \to \tau\nu$ [8]. In the case of $H_2^\pm$, it is preferable to take values of θ closer to zero, which is in tension with the cross section for $H_3^\pm$, which prefers $\theta \lesssim -0.4$. However, we can quench this tension if we choose $\tan\gamma \lesssim 2$, as the BR of both charged Higgs states to $\tau\nu$ are smaller (see Fig. (6.8)). We can also notice that lower values for $M_{H_3^\pm}$ increase the cross section of $H_3^\pm \to \tau\nu$, thus making it harder to agree with collider limits. For example, this is very manifest for the case of $M_{H_3^\pm} = 150$ GeV, shown in Fig. (6.11), a scenario that is excluded by $H_3^\pm \to \tau\nu$ results. For this value of

[4]Comparing the upper and lower left panels of Fig. (6.10) shows that the cross section times BR of $H_2^\pm$ is essentially unaffected by the mass of the heavier $H_3^\pm$, once it is at least comparable to the top quark mass.

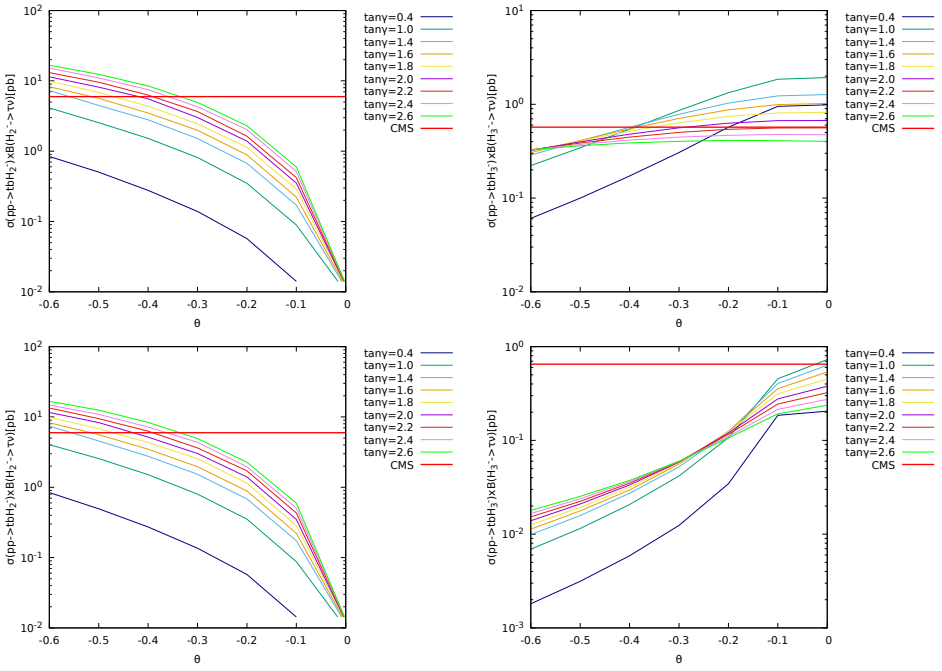

FIGURE 6.10: Production cross section times BR to $\tau\nu$ of $H_2^\pm$ (left panels) and $H_3^\pm$ (right panels) as a function of θ, for $\tan\beta = 20$, $\delta = 0$, $M_{H_2^\pm} = 80$ GeV, and $M_{H_3^\pm} = 170$ GeV (upper) and 200 GeV (lower). The coloured curves show various values of $\tan\gamma$. Regions above the red line are excluded by CMS [8].

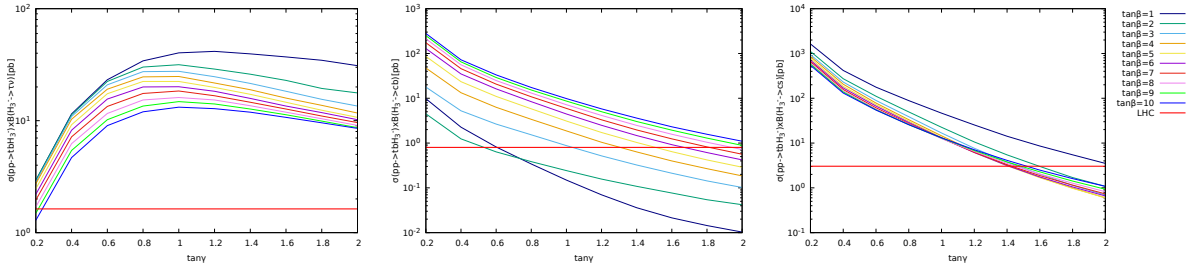

FIGURE 6.11: Production cross sections times BR for a 150 GeV heavier charged Higgs $H_3^\pm$ decaying to $\tau\nu$ (left), cb (middle) and cs (right) as a function of $\tan\gamma$ and varying $\tan\beta$, for $M_{H_2^\pm} = 80$ GeV, $\theta = -0.5$, and $\delta = 0.92\pi$. The red lines are the upper limits from LHC searches in Refs. [8] (CMS), [9] (CMS), and [10] (ATLAS), respectively. Notice that the $H_3^\pm \to \tau\nu$ limits strongly exclude almost all of this scenario. The $H_2^\pm$ signal on the other hand is well below the collider limits.

$M_{H_3^\pm}$, we should also compare to the collider limits for $H_3^\pm \to cb$ and cs. However, these are less constraining than the case of $\tau\nu$. In the case when $m_t < M_{H_2^\pm} < M_{H_3^\pm}$, the BR of $H_2^\pm$ to $\tau\nu$ only dominates over the BR to tb for small values of $\tan\beta$, as can be seen in Fig. (6.9). Later in this work, when we consider the masses of the charged Higgs bosons to be larger than the top-quark one, we take $\tan\beta > 10$, and then this region readily satisfies collider limits. Overall, notice that there is no significant interference between $H_2^\pm$ and $H_3^\pm$, unless their mass difference is comparable to either of their widths, which is never the case for the benchmark points that we will study.

Another one is the top decay width. The charged Higgs mass below top quark is constrained indirectly from the width of top. Our colleagues used the most precise measurement of Γ_t width which is $\Gamma_t = 1.9 \pm 0.5$ GeV [3; 172] to limit the parameter of mixing parameter $\tan\beta$ and $\tan\gamma$. In Fig. (6.12) from the Ref. [15], lower values of $\tan\beta$ are preferred to prevent blow up the top decay width from all three figures can be seen especially below 40 are satisfied. For the parameter $\tan\gamma$, lower value smaller than 1 should be prevented from Γ_t out of the range. The choices of two charged Higgs masses are benefit for future both $\bar{B} \to X_s\gamma$ and EDM parameter space discussion.

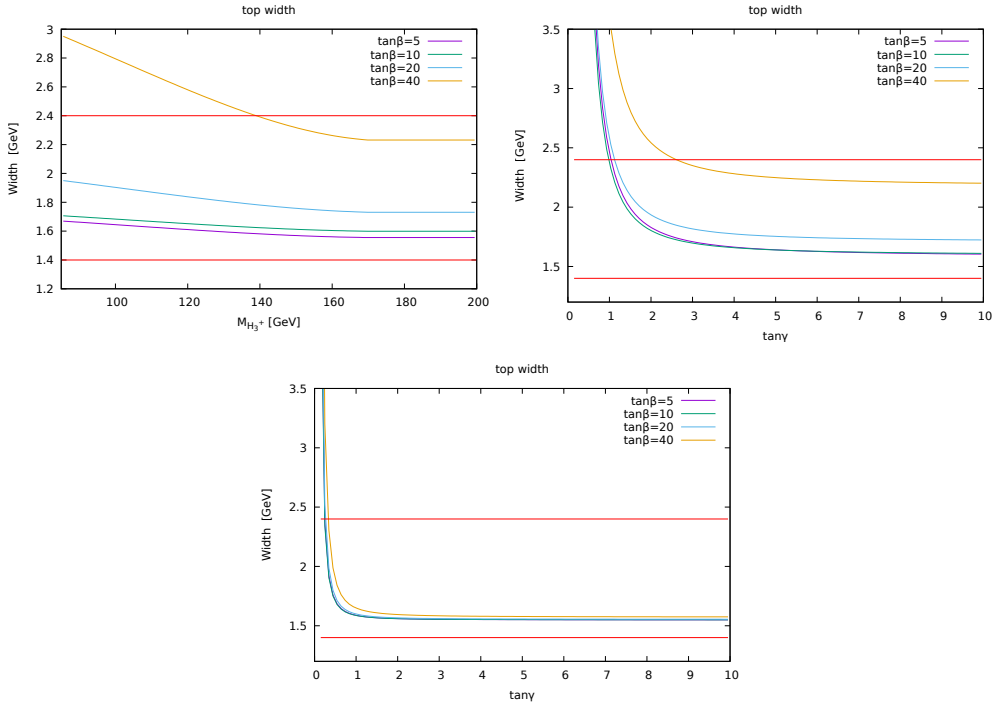

FIGURE 6.12: Constraint from the top decay width (Γ_t) against variety of $\tan\beta$. Top left Panel: The prediction of top decay width Γ_t as a function of $M_{H_3^\pm}$ in the type-Z (Democratic) 3HDM for value of $\theta = -\frac{\pi}{4}$. $M_{H_2^\pm}$ has set to 85 GeV with $\tan\gamma = 4, \delta = 0.85\pi$. Top right panel: [$\tan\gamma$, Γ_t] with charged Higgs masses, $M_{H_2^\pm} = 85$ GeV, $M_{H_3^\pm} = 500$ GeV and same value of δ as left panel. Bottom panel: [$\tan\gamma$, Γ_t] with charged Higgs masses, $M_{H_2^\pm} = 160$ GeV, $M_{H_3^\pm} = 170$ GeV and $\delta = 0.9\pi$. The allowed range of $1.4 < \Gamma_t < 2.4$ are inside two horizontal lines.

The last one is the perturbativity constraint. For a Lagrangian to be sufficiently perturbative, the mixing parameters of $\tan\beta$ and $\tan\gamma$ are constrained (i.e. The validity of the coupling for $t\,b\,H^\pm_{2,3}$ be perturbative.). In order to prevent the width of charged Higgs so widely which will be difficult for detection, our collaborators adopted the charged Higgs decay within the type-I and type-II 2HDM in the sense that the decay width of heavier charged Higgs ($M_{H^\pm_{2,3}} > m_t$) to top and bottom quarks no larger than half of the charged Higgs mass. Taking the limit from type-I 2HDM and type-II 2HDM in

Ref. [173], we obtain an upper and a lower bound for $\tan\beta$ as below:

$$\begin{aligned}\Gamma(H^+ \to t\bar{b}) &\simeq \frac{3G_F m_t^2}{4\sqrt{2}\pi \tan^2\beta} M_{H^\pm} < \frac{1}{2} M_{H^\pm}, \qquad \text{or} \qquad \tan\beta \gtrsim 0.34, \\ \Gamma(H^+ \to t\bar{b}) &\simeq \frac{3G_F m_b^2 \tan^2\beta}{4\sqrt{2}\pi} M_{H^\pm} < \frac{1}{2} M_{H^\pm}, \qquad \text{or} \qquad \tan\beta \lesssim 125. \end{aligned} \tag{6.26}$$

we interpreted the constraints as upper bounds on the Yukawa couplings themselves, so that, applied to the 2HDM equivalent of Eq. (4.29), these bounds on $\tan\beta$ are equivalent to imposing $g^t \lesssim 3.07$ and $g^b \lesssim 2.90$.

For uniformity we impose $g^f \lesssim 3$ and derive constraints on $v_1 = v\cos\beta\sin\gamma$, $v_2 = v\sin\beta\sin\gamma$ and $v_3 = v\cos\gamma$ in the type-Z (Democratic) 3HDM using the m_t and m_b values quoted above (plus $m_\tau = 1.78$ GeV). We find

$$\sin\beta\sin\gamma \gtrsim 0.33, \qquad \cos\beta\sin\gamma \gtrsim 0.0077, \qquad \tan\gamma \lesssim 290. \tag{6.27}$$

The first two constraints of Eq. (6.27) yield an absolute lower bound on $\tan\gamma$,

$$\tan\gamma \gtrsim 0.35. \tag{6.28}$$

So, for the lower bound of $\tan\gamma$ from this constraint, the region below value of 0.35 has to be excluded. Later in this section, we will show plots for $\tan\gamma = 1$ and 2. For $\tan\gamma = 1$, the perturbativity analysis above requires $0.53 \lesssim \tan\beta \lesssim 92$ and the allowed $\tan\beta$ range expands as $\tan\gamma$ increases.

Now, two CP-violation observables eEDM and nEDM, which are the main focus of the paper [15], will be carried in next two subsections. Both of them have been calculated through A2HDM [174] regime and extrapolate to the 3HDM. Whole work of these two observables are computed by myself in Python. The first observable in next subsection will be the eEDM.

6.5.2 Electron Electric Dipole Moment (eEDM)

The experimental sensitivity to the eEDM has improved by more than an order of magnitude in recent years, with a current upper bound from the ACME collaboration of [175]:

$$|d_e| \leq 1.1 \times 10^{-29}\, e\,\text{cm}. \tag{6.29}$$

The charged Higgs bosons in the 3HDM give rise to contributions to the eEDM via the CP violation in their couplings to fermion pairs. The one-loop contribution involving a charged Higgs loop is subdominant due to suppression by the tiny electron Yukawa

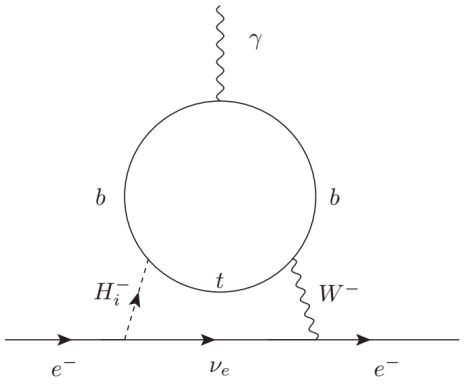

FIGURE 6.13: One of the Barr-Zee type diagrams that give the dominant charged Higgs boson contribution to the eEDM in the 3HDM.

coupling. The dominant contribution comes from the two-loop Barr-Zee type diagrams as shown in Fig. (6.13, first calculated in Ref. [176] in the 2HDM (see also Ref. [174]).

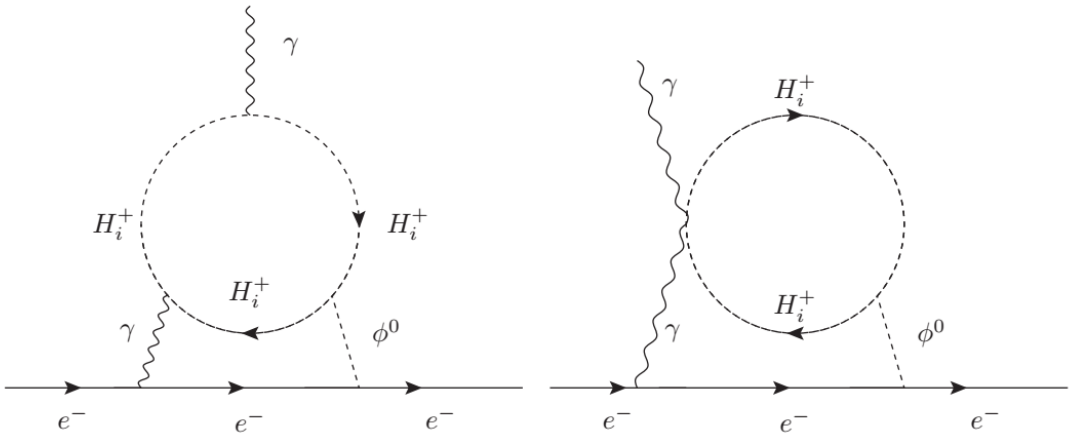

FIGURE 6.14: Two of the Barr-Zee type diagrams for the eEDM involving a charged Higgs boson in the loop. These do not contribute in the 3HDM when CP violation is turned off in the neutral Higgs sector, as we assume in our analysis.

The charged Higgs sector also appears in the Barr-Zee type diagrams of Fig. (6.14), where ϕ^0 is any of the neutral scalars in the model. It was pointed out in Ref. [177], in the context of the Aligned 2HDM, that these diagrams can contribute significantly and lead to interesting cancellations with the diagrams of Fig. (6.13). In the 3HDM scenario that we consider here, where CP violation is present in the charged Higgs sector but not in the neutral Higgs sector (which we have integrated out), these diagrams do not contribute to the eEDM because the $\phi^0\, e^+\, e^-$ and $\phi^0\, H_i^+\, H_i^-$ couplings contain no CP

phase.[5] The couplings $\phi^0 H_2^+ H_3^-$ do contain non-trivial CP phases, but these couplings do not appear in the diagrams of Fig. (6.14) because the photon coupling to the charged Higgs boson is diagonal.

Under our assumption that the neutral Higgs sector is CP-conserving and that CP violation appears only in the charged Higgs sector, the dominant Barr-Zee type contribution of the charged Higgs to the eEDM in the 2HDM [174; 176] can be generalized to the 3HDM as follows:

$$\begin{aligned}\frac{d_e(M_{H_2^\pm}, M_{H_3^\pm})_{BZ}}{2} &= -m_e \frac{12 G_F^2 M_W^2}{(4\pi)^4} |V_{tb}|^2 \\ &\times \left[\mathrm{Im}(-Y_2^* Z_2) \left(q_t F_t(z_{H_2^\pm}, z_W) + q_b F_b(z_{H_2^\pm}, z_W) \right) \right. \\ &+ \left. \mathrm{Im}(-Y_3^* Z_3) \left(q_t F_t(z_{H_3^\pm}, z_W) + q_b F_b(z_{H_3^\pm}, z_W) \right) \right] \end{aligned} \tag{6.30}$$

where $q_t = 2/3$ and $q_b = -1/3$ are quark electric charges, $z_a = M_a^2/m_t^2$ and from [174; 176]:

$$\begin{aligned} F_q(z_{H_i^\pm}, z_W) &= \frac{T_q(z_{H_i^\pm}) - T_q(z_W)}{z_{H_i^\pm} - z_W}, \\ T_t(z) &= \frac{1-3z}{z^2}\frac{\pi^2}{6} + \left(\frac{1}{z} - \frac{5}{2}\right)\log z - \frac{1}{z} - \left(2 - \frac{1}{z}\right)\left(1 - \frac{1}{z}\right)\mathrm{Li}_2(1-z), \\ T_b(z) &= \frac{2z-1}{z^2}\frac{\pi^2}{6} + \left(\frac{3}{2} - \frac{1}{z}\right)\log z + \frac{1}{z} - \frac{1}{z}\left(2 - \frac{1}{z}\right)\mathrm{Li}_2(1-z). \end{aligned} \tag{6.31}$$

Note that the original calculation of Ref. [176] was done setting $m_b = 0$ so that only the contribution involving the top-quark Yukawa couplings $m_t Y_i/v$ appears. Keeping the non-zero bottom mass would introduce additional contributions proportional to $m_b X_i/v$, which could become important at large values of $\tan\beta$. Finally, all other eEDM contributions at the loop level that are purely fermionic or induced by gauge bosons [178; 179] remain identical to those in the SM and are negligible compared to the current experimental bound.

6.5.3 Neutron Electric Dipole Moment (nEDM)

The current measurement of the nEDM at the Paul Scherrer Institute with ultra-cold neutrons (UCN) provided an upper limit as follows [180]:

$$|d_n| \leq 1.8 \times 10^{-26}\, e\,\mathrm{cm}\ (90\%\ \mathrm{CL}). \tag{6.32}$$

[5] It can be seen that, in the absence of neutral (pseudo)scalar sector CP violation, the latter coupling cannot contain a CP-violating phase because this term is Hermitian by itself and hence must have a real coefficient in the Lagrangian.

The exchange of charged Higgs boson contribute the observable of CP-violation through variety effective operators. In Ref. [174], Jung and Pich pointed out three types of effective operators through which the charged Higgs boson contributes to the nEDM in the 2HDM. These are four-fermion operators involving the up- and down-type quarks which are induced by CP-violating Higgs exchange, the Weinberg operator (the CP-violating three-gluon operator) which is neither suppressed by quark masses nor CKM matrix elements, and the Barr-Zee type two-loop diagrams contributing to the EDMs and chromo-electric dipole moments (CEDMs) of the up- and down-type quarks. The light quark masses suppress the contributions of the four fermion operators and the up- and down-type quark (C)EDMs.

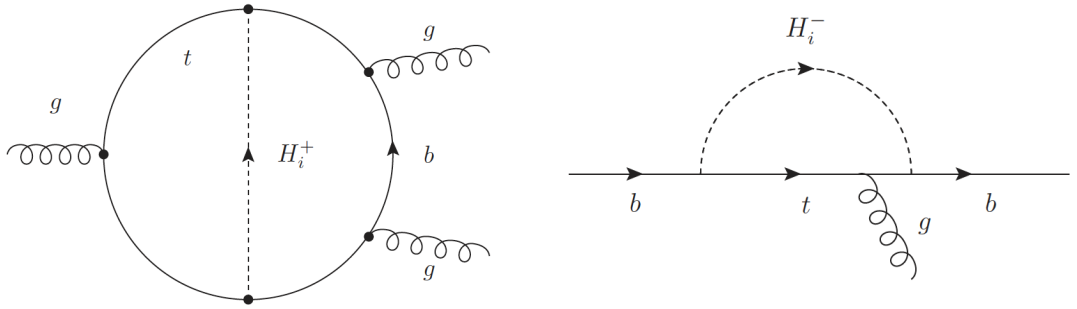

FIGURE 6.15: Left panel: Two-loop charged Higgs boson contribution to the Weinberg operator. Right panel: One-loop charged Higgs boson contribution to the bottom quark CEDM.

This leaves the Weinberg operator, the charged Higgs contribution to which is shown in the left panel of Fig. (6.15). Following Ref. [174], we compute this using an effective field theory approach [181], which amounts to computing only the one-loop short-distance piece at the high scale $\mu_{tH} = m_t$, which is the bottom quark CEDM shown in the right panel of Fig. (6.15).

The contribution of the Weinberg operator to the nEDM is given by [174]:

$$|d_n(C_W)/e| = \left[1.0^{+1.0}_{-0.5}\right] \times 20\,\text{MeV}\, C_W(\mu_h), \tag{6.33}$$

where the sign is unknown, and the theoretical uncertainty on the magnitude is a factor of two. In our numerical results, we follow Ref. [174] and use the central theoretical value. The Wilson coefficient C_W evaluated at the hadronic scale $\mu_h \sim 1$ GeV is expressed as

$$C_W(\mu_h) = \eta_{c-h}^{\kappa_W}\eta_{b-c}^{\kappa_W}\left(\eta_{t-b}^{\kappa_W}C_W(\mu_{tH}) + \eta_{t-b}^{\kappa_C}\frac{g_s^3(\mu_b)}{8\pi^2 m_b}\frac{d_b^C(\mu_{tH})}{2}\right), \tag{6.34}$$

where $C_W(\mu_{tH}) = 0$ because there is no short-distance contribution to the Weinberg operator involving the charged Higgs boson at the scale m_t. $d_b^C(\mu_{tH})$ is the short-distance contribution to the bottom quark CEDM, given below. The running of these

short-distance contributions down to the scale $\mu_b = m_b$ is accomplished by the factors of $\eta_{t-b} = \alpha_s(\mu_{tH})/\alpha_s(\mu_b)$ raised to the appropriate power $\kappa_i = \gamma_i/(2\beta_0)$, where $\gamma_W = N_C + 2n_f$ and $\gamma_C = 10C_F - 4N_C$ are the LO anomalous dimensions of the Weinberg and b-quark CEDM operator, respectively, and $\beta_0 = (11N_C - 2n_f)/3$ is the one-loop beta function of QCD. Here, $N_C = 3$, $C_F = 4/3$, and n_f is the number of active quark flavors involved in the QCD running at the relevant scale (e.g., between the top and bottom masses, $n_f = 5$). At the scale μ_b, the bottom quark is integrated out and the operators matched, then the remaining Weinberg operator is run down to the hadronic scale μ_h in two steps (integrating out the charm quark at $\mu_c = m_c$), giving rise to two more factors, $\eta_{b-c}^{\kappa_W}$ and $\eta_{c-h}^{\kappa_W}$, in which the running of α_s and the exponent are evaluated with the appropriate value of n_f. At LO, $\alpha_s(\mu)$ is given by:

$$\alpha_s(\mu) = \frac{\alpha_s(M_Z)}{v(\mu)}, \tag{6.35}$$

with

$$v(\mu) = 1 - \beta_0 \frac{\alpha_s(M_Z)}{2\pi} \log\left(\frac{M_Z}{\mu}\right). \tag{6.36}$$

Finally, the high-scale one-loop charged Higgs boson contribution to the bottom quark CEDM in the right panel of Fig. (6.15 has been calculated in the 2HDM in Ref. [174] (see also references therein). By adapting this to the 3HDM, one obtains

$$\begin{aligned}\frac{d_b^C(\mu_{tH})}{2} &= -\frac{G_F}{\sqrt{2}}\frac{1}{16\pi^2}|V_{tb}|^2 m_b(\mu_{tH})\left[\mathrm{Im}(-X_2Y_2^*)x_{tH_2}\left(\frac{\log(x_{tH_2})}{(x_{tH_2}-1)^3} + \frac{(x_{tH_2}-3)}{2(x_{tH_2}-1)^2}\right)\right. \\ &+ \left.\mathrm{Im}(-X_3Y_3^*)x_{tH_3}\left(\frac{\log(x_{tH_3})}{(x_{tH_3}-1)^3} + \frac{(x_{tH_3}-3)}{2(x_{tH_3}-1)^2}\right)\right].\end{aligned} \tag{6.37}$$

where $x_{tH_i} = m_t^2/M_{H_i^\pm}^2$. Again, purely fermionic and gauge contributions [174] remain identical to those in the SM and are negligible compared to the current experimental bound.

6.5.4 The Glashow–Iliopoulos–Maiani (GIM) like mechanism for EDMs

For CP-violation observables such as EDMs, the CP-violation phase in the charged Higgs mixing matrix is responsible to explain the characteristics. One interesting CP-violation feature comes from the exact CP-violation cancellation by taking two physical charged Higgs mass degenerate in mass. Following this scenario, the EDM is avoided as the contribution of such CP-violation distinct. This is somehow similar to the GIM mechanism [182] in which the mixing parameters of θ and δ become non-physical.

Any internal charged Higgs propagator that begins and ends on a fermion line brings with it one factor of X_i^*, Y_i^* or Z_i^* and one factor of X_i, Y_i or Z_i. The combinations $X_iX_i^*$, $Y_iY_i^*$, and $Z_iZ_i^*$ are purely real and cannot contribute to CP-odd observables, leaving

only the combinations $X_i Y_i^*$, $X_i Z_i^*$ and $Y_i Z_i^*$ (or their complex conjugates) which can have an imaginary part. Consider, for example, $X_i Y_i^*$, which is given in the type-Z (Democratic) 3HDM in terms of the unitary rotation matrix in Eq. (4.19) by

$$X_i Y_i^* = -\frac{U_{1i}^\dagger U_{i2}}{U_{11}^\dagger U_{12}}, \tag{6.38}$$

where $i = 2$ or 3. The denominator is real by construction since $U_{1j} = v_j/v$. Computation of CP-odd observables in this context always involves a sum over the two charged Higgs bosons that can appear in the contributing diagrams, yielding

$$\sum_{i=2}^{3} \mathrm{Im}(X_i Y_i^*) f(M_{H_i^\pm}) = -\frac{1}{U_{11}^\dagger U_{12}} \left[\mathrm{Im}(U_{12}^\dagger U_{22}) f(M_{H_2^\pm}) + \mathrm{Im}(U_{13}^\dagger U_{32}) f(M_{H_3^\pm}) \right], \tag{6.39}$$

where $f(M_{H_i^\pm})$ represents the dependence of the diagram on the charged Higgs boson mass. We can trivially add zero in the form of $\mathrm{Im}(U_{11}^\dagger U_{12}) f(m)$ inside the square brackets. Then, in the limit $M_{H_2^\pm} = M_{H_3^\pm} \equiv m$, Eq. (6.39) becomes

$$\sum_{i=2}^{3} \mathrm{Im}(X_i Y_i^*) f(m) = -\frac{1}{U_{11}^\dagger U_{12}} \mathrm{Im} \left[\sum_{i=1}^{3} U_{1i}^\dagger U_{i2} \right] f(m) = -\frac{1}{U_{11}^\dagger U_{12}} \mathrm{Im}(\delta_{12}) f(m) = 0, \tag{6.40}$$

where δ_{12} is the $(1,2)$ element of the Kronecker delta. This also shows that $\mathrm{Im}(X_2 Y_2^*) = -\mathrm{Im}(X_3 Y_3^*)$, due to the unitarity of the charged Higgs mixing matrix, and similarly for the imaginary parts of $X_i Z_i^*$ and $Y_i Z_i^*$. The form of Eq. (6.39) also implies that, for small non-zero mass splitting $\Delta M_{H^\pm} \ll M_{H^\pm}$, CP-violating amplitudes must be linear in $\Delta M_{H^\pm}/M_{H^\pm}$, where $\Delta M_{H^\pm} \equiv M_{H_3^\pm} - M_{H_2^\pm}$ and $M_{H^\pm} \equiv (M_{H_3^\pm} + M_{H_2^\pm})/2$.

In this part, the reason we focus on the type-Z (Democratic) 3HDM because CP violation in the charged Higgs sector gives rise to interesting contributions to the EDMs of both the electron and neutron. In the other types of 3HDM, the effects of charged Higgs CP violation are more limited because, in these models, at least two of X_i, Y_i, and Z_i become identical (see Tab. (4.2)). In particular, the dominant charged Higgs contribution to the eEDM, proportional to $\mathrm{Im}(-Y_i^* Z_i)$, is zero in the type-I and type-Y (Flipped) 3HDMs because in those models $Y_i = Z_i$. Similarly, the dominant charged Higgs contribution to the nEDM, proportional to $\mathrm{Im}(-X_i Y_i^*)$, is zero in the type-I and type-X (Lepton-specific) 3HDMs because in those models $X_i = Y_i$. In the type-II 3HDM, $X_i = Z_i$, so that this model also leads to CP-violating charged Higgs boson contributions to both the electron and neutron EDMs.

6.5.5 Results of both $\bar{B} \to X_s\gamma$ and EDMs

We now present our results for the type-Z (Democratic) 3HDM as a function of the relevant coupling parameters (θ, $\tan\beta$, $\tan\gamma$, and δ) and masses ($M_{H_2^\pm}$ and $M_{H_3^\pm}$) against

the eEDM and nEDM constraints. We will also impose the constraints from direct searches for charged Higgs bosons, as well as from the measurement of BR($\bar{B} \to X_s\gamma$), which provides the most stringent indirect constraint on the charged Higgs masses.

To start with, it is instructive to compare the 3HDM results with those available in the literature for the analogous case in a 2HDM, which we do by presenting the nEDM and eEDM constraints against the Yukawa coupling combinations $\mathrm{Im}(X_i Y_i^*)$ and $\mathrm{Im}(Y_i^* Z_i)$ ($i = 2$). In Fig. (6.16), we show the Aligned 2HDM results in the plane of the charged Higgs mass and the imaginary part of the relevant combination of Yukawa coupling factors, to be compared to Figs. 3, 4, and 5 of Ref. [174],[6] updated using the latest nEDM and eEDM experimental limits as given in Eqs. (6.32) and (6.29), respectively. The shaded areas in Fig. (6.16) represent the viable parameter regions in both cases. The newest bounds from both nEDM and eEDM induce a strong suppression on the allowed parameter space corresponding to the imaginary contributions of the couplings $X_2 Y_2^*$ and $Y_2^* Z_2$. In Figs. (6.17) and (6.18), we show the 3HDM cases as a function of $M_{H_2^\pm}$ with $M_{H_3^\pm} = 85$ and 300 GeV, respectively. We can then see that the parameter space is generally enlarged in the type-Z (Democratic) 3HDM with respect to the Aligned 2HDM, particularly in the $M_{H_2^\pm} = M_{H_3^\pm}$ limit, clearly illustrating the aforementioned cancellation mechanism between the two charged Higgs states of the 3HDM. It is worth noticing here that, while in the exact mass degeneracy case there is virtually no constraint applicable to the type-Z (Democratic) 3HDM from either nEDM or eEDM, even when the $M_{H_2^\pm} = M_{H_3^\pm}$ condition is lifted, there are substantial differences in the values allowed for the Yukawa couplings between the two scenarios at both small and large values of the lightest charged Higgs boson mass.

Next, we consider the effect of the coupling parameters θ, $\tan\beta$, $\tan\gamma$, and δ for various scenarios for the charged Higgs masses $M_{H_2^\pm}$ and $M_{H_3^\pm}$ within the type-Z (Democratic) 3HDM. We consider two classes of mass scenarios: the first in which either or both $H_i^\pm$ masses are lighter than m_t (in Sec. 6.5.6) and the second in which they are both heavier than m_t (in Sec. 6.5.7). Explicit expressions for the parameter combinations $\mathrm{Im}(-X_2 Y_2^*)$ and $\mathrm{Im}(-Y_3^* Z_3)$ that enter the calculations of the EDMs are given in Appendix C; in particular we note that these quantities are proportional to $\sin\delta$ and to the product $\sin\theta\cos\theta$, so that the CP-violating effects are largest when $\delta = \pi/2$ or $3\pi/2$ and $\theta = -\pi/4$.

[6] Herein, there is no subscript 2 for the couplings and masses of the 2HDM, as only one charged Higgs state is present in the model.

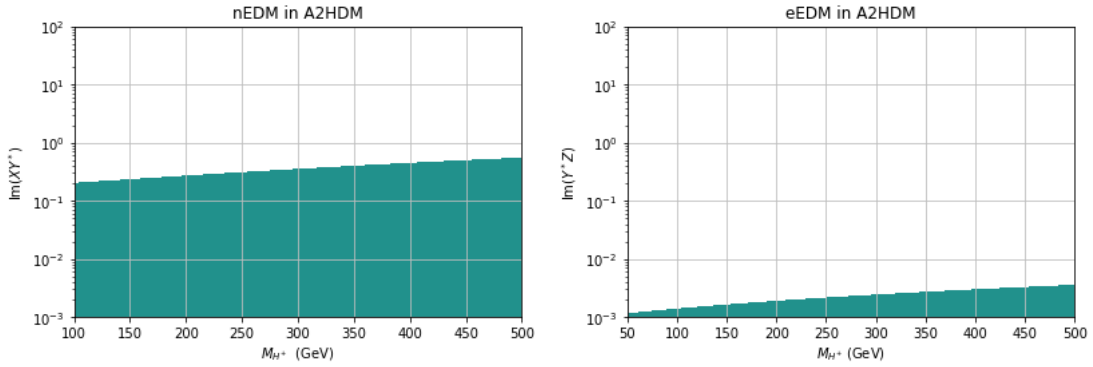

FIGURE 6.16: Constraint from the nEDM (left) and the eEDM (right) on $|\mathrm{Im}(XY^*)|$ and $|\mathrm{Im}(Y^*Z)|$, respectively, in the Aligned 2HDM as a function of the charged Higgs mass. The shaded region is allowed.

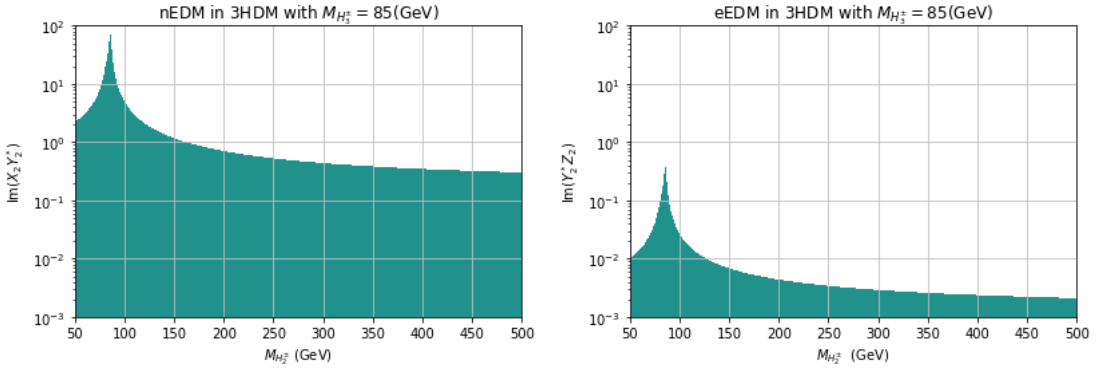

FIGURE 6.17: Constraint from the nEDM (left) and the eEDM (right) on $|\mathrm{Im}(X_2Y_2^*)|$ and $|\mathrm{Im}(Y_2^*Z_2)|$ in the 3HDM as a function of the mass of $H_2^\pm$. $M_{H_3^\pm}$ is fixed to be 85 GeV. The structure of the model forces $\mathrm{Im}(X_3Y_3^*) = -\mathrm{Im}(X_2Y_2^*)$ and $\mathrm{Im}(Y_3^*Z_3) = -\mathrm{Im}(Y_2^*Z_2)$.

6.5.6 Light charged Higgses

6.5.6.1 The $M_{H_2^\pm} < m_t < M_{H_3^\pm}$ case

In Fig. (6.19), we show the constraints from $\bar{B} \to X_s\gamma$, eEDM and nEDM on the $[\delta, \theta]$ plane, for $M_{H_2^\pm} = 80$ GeV, $M_{H_3^\pm} = 200$ GeV, and small values of $\tan\beta$ and $\tan\gamma$ so as to be compliant with collider limits, as seen previously. (Notice that the $\bar{B} \to X_s\gamma$ constraint is satisfied within the green and grey shaded areas while the two EDM constraints are satisfied outside the corresponding closed curves. Details of our calculation of $\bar{B} \to X_s\gamma$ are already taken from) From these plots, we learn that we need δ to be very close to $\delta = n\pi$ to satisfy all three constraints at once. That is, we are forced to find solutions very close to the CP-conserving limit; furthermore, the constraint from $\bar{B} \to X_s\gamma$ furthermore tends to favour $\delta \simeq \pi$.

In Fig. (6.20), we show the effect of varying $\tan\gamma$ and increasing the mass of the heavier charged Higgs state while keeping $M_{H_2^\pm} = 80$ GeV and fixing $\tan\beta = 20$. As can

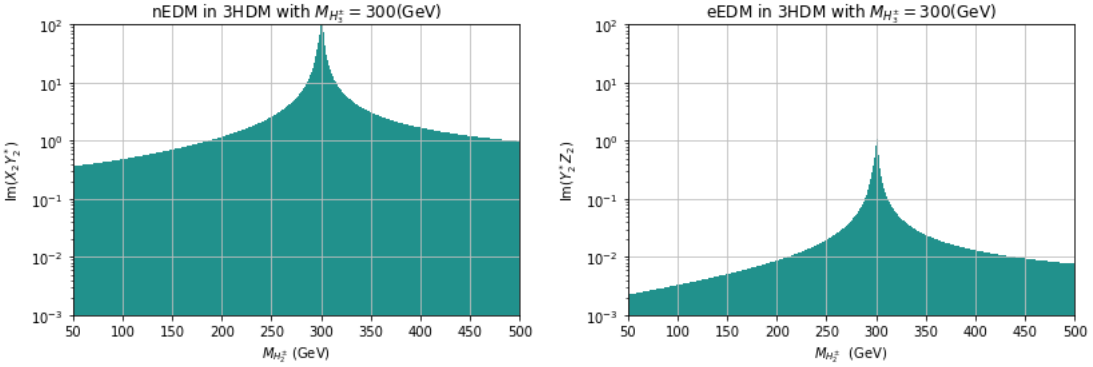

FIGURE 6.18: Same as in Fig. (6.17) but for $M_{H_3^\pm} = 300$ GeV.

be seen, increasing $M_{H_3^\pm}$ from 200 to 500 GeV makes it more difficult to find regions that can survive all constraints, in line with the requirements of the aforementioned cancellation mechanism. Comparing with Fig. (6.19) we also see that larger values of $\tan\beta$ lead to tighter constraints from the nEDM while larger values of $\tan\gamma$ lead to tighter constraints from the eEDM.

In Fig. (6.21), we show the same constraints on the $[\tan\gamma, \tan\beta]$ plane instead, for two values of δ very close to $\delta = \pi$. We have also added here the constraints from the top-quark width and perturbativity of the $H_i^+ b\bar{t}$ vertex. For all the parameter region, the collider limits are satisfied. We can see that, for $\tan\gamma > 1.5$ and $\tan\beta > 8$, we can satisfy all other constraints, but the value of δ should roughly be at least $\delta = 0.975\pi$ to 0.985π for, e.g., $\theta = -0.3$. The allowed region is in the range of black dashed and blue line area. For an allowed parameter space, the CP-violation phase (δ) has to be close to π. These two plots show that if the value of δ is closer to π, more area of the constraints are allowed.

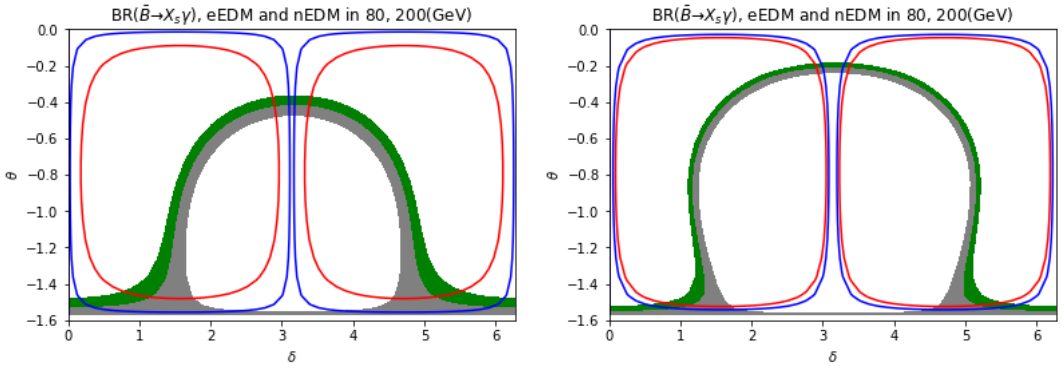

FIGURE 6.19: The allowed regions from $\bar{B} \to X_s\gamma$ (within the green and grey shaded areas), eEDM (outside the blue curves), and nEDM (outside the red curves) in the $[\delta, \theta]$ plane, with $M_{H_2^\pm} = 80$ GeV, $M_{H_3^\pm} = 200$ GeV, $\tan\gamma = 1$, and $\tan\beta = 5$ (left) or 10 (right).

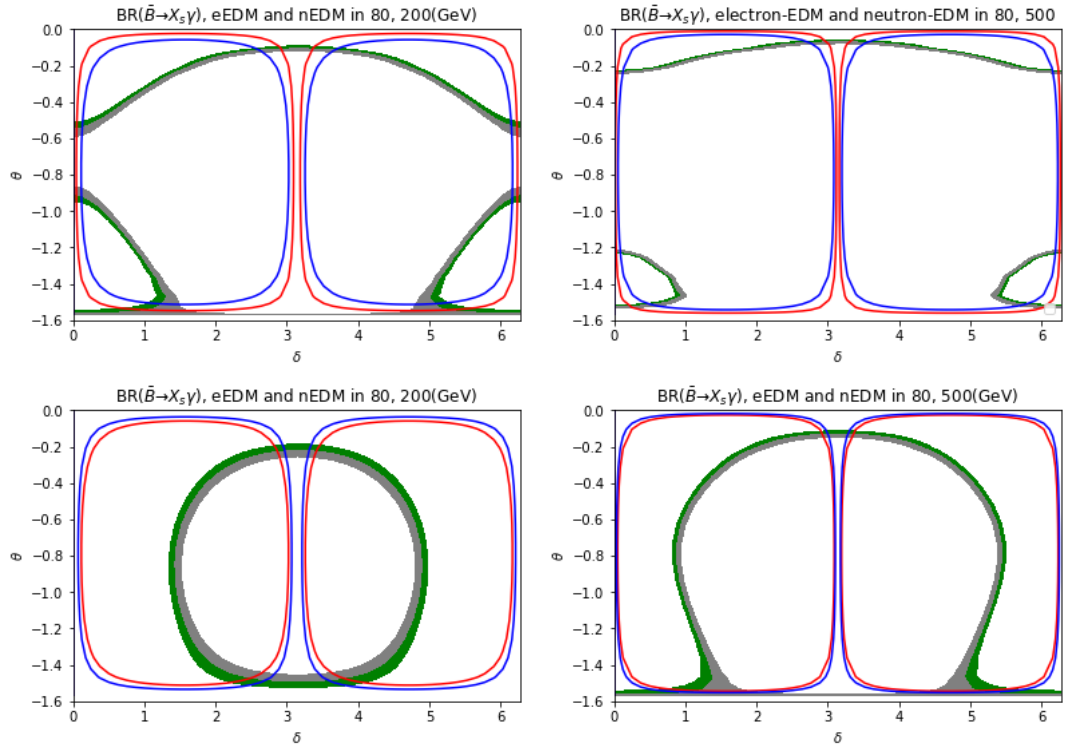

FIGURE 6.20: The allowed regions from $\bar{B} \to X_s\gamma$ (within the green and grey shaded areas), eEDM (outside the blue curves), and nEDM (outside the red curves) in the $[\delta, \theta]$ plane, with $M_{H_2^\pm} = 80$ GeV and $\tan\beta = 20$. $M_{H_3^\pm} = 200$ GeV in the left panels and 500 GeV in the right panels. Here, $\tan\gamma = 1$ in the upper panels and 2 in the lower panels.

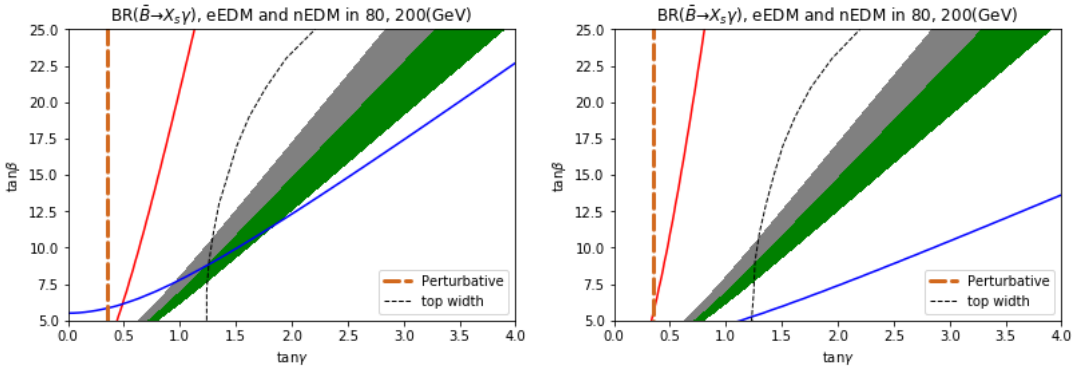

FIGURE 6.21: The allowed regions from $\bar{B} \to X_s\gamma$ (within the green and grey shaded areas), eEDM (above the blue line) and nEDM (to the right of the red line) in the $[\tan\gamma, \tan\beta]$ plane, with $M_{H_2^\pm} = 80$ GeV, $M_{H_3^\pm} = 200$ GeV, $\theta = -0.3$, and $\delta = 0.975\pi$ (left) or 0.985π (right). We also show constraints from the top-quark width (black dotted line) and perturbativity (orange dashed line), wherein the region to the right of the respective curves is allowed.

6.5.6.2 The $M_{H_2^\pm} < M_{H_3^\pm} < m_t$ case

Similarly to the previous case, also here we need low values of $\tan\beta$ to satisfy the top-quark width measurements. However, this is in tension with the region of parameter

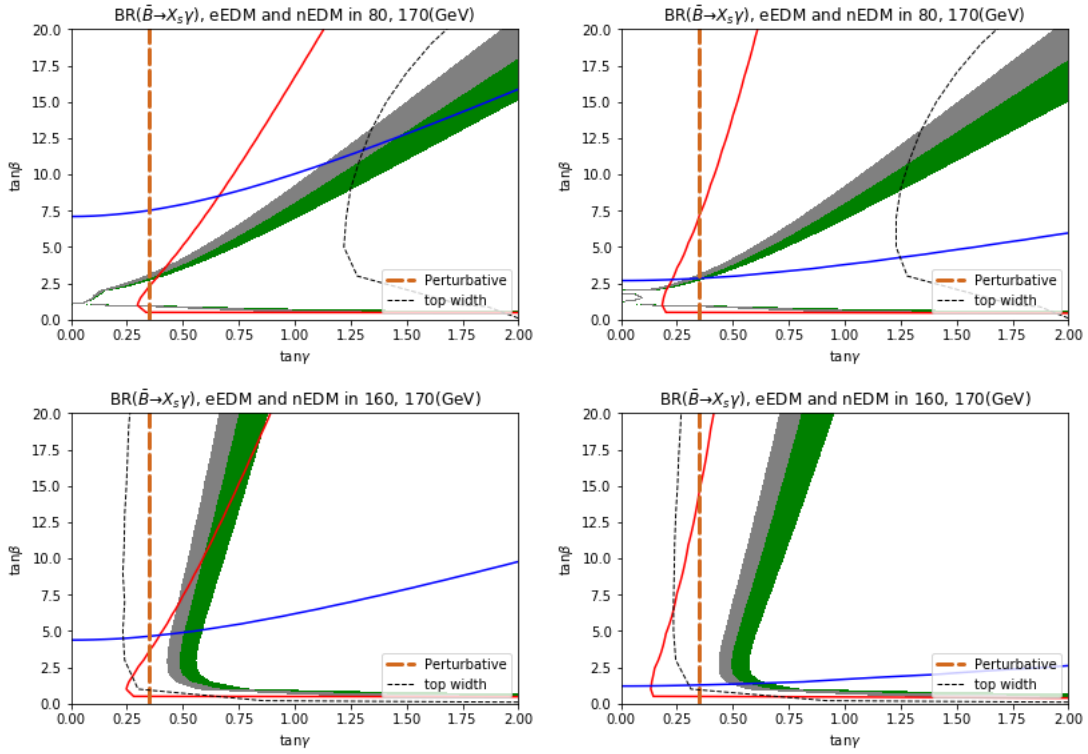

FIGURE 6.22: The allowed regions from $\bar{B} \to X_s\gamma$ (within the green and grey shaded areas), eEDM (above the blue line), and nEDM (to the right of the red line) in the $[\tan\gamma, \tan\beta]$ plane, with $M_{H_3^\pm} = 170$ GeV. In the upper panels $M_{H_2^\pm} = 80$ GeV, $\theta = -0.3$, and $\delta = 0.96\pi$ (left) or 0.985π (right). In the lower panels $M_{H_2^\pm} = 160$ GeV, $\theta = -0.5$, and $\delta = 0.8\pi$ (left) or 0.95π (right). We also show constraints from the top-quark width (black dotted line) and perturbativity (orange dashed line), wherein the region to the right of the respective curves is allowed.

space that satisfies simultaneously the constraints from $\bar{B} \to X_s\gamma$, eEDM, and nEDM, despite which, as can be seen in Fig. (6.23), we could have a somewhat wider interval of δ around π for large values of $\tan\beta$ and $\tan\gamma$. There also seems to be a broader band satisfying the $\bar{B} \to X_s\gamma$ constraint for lower values of $M_{H_3^\pm}$, while keeping $M_{H_2^\pm} = 80$ GeV. This, again, is in tension with the aforementioned experimental constraints. However, in this case, it is the collider limit on $H^\pm \to \tau\nu$ that becomes too restrictive on the $H_3^\pm$ properties as we decrease its mass. But we can prevent this from happening if we keep $M_{H_3^\pm} = 170$ GeV and increase instead the mass of $M_{H_2^\pm}$, which is what we do in Fig. (6.22). In the upper panel of this figure, we show the case $M_{H_2^\pm} = 80$ GeV and $M_{H_3^\pm} = 170$ GeV. In this case, the top-quark width measurement is very constraining, and very low values of $\tan\gamma$ are ruled out. In the lower panel of this figure, we show the case $M_{H_2^\pm} = 160$ GeV and $M_{H_3^\pm} = 170$ GeV. Here, the top-quark width measurement is not that constraining, and very low values of $\tan\gamma$ are allowed. With the two charged Higgs masses closer to being degenerate, a larger range of the CP-violating phase δ also becomes allowed.

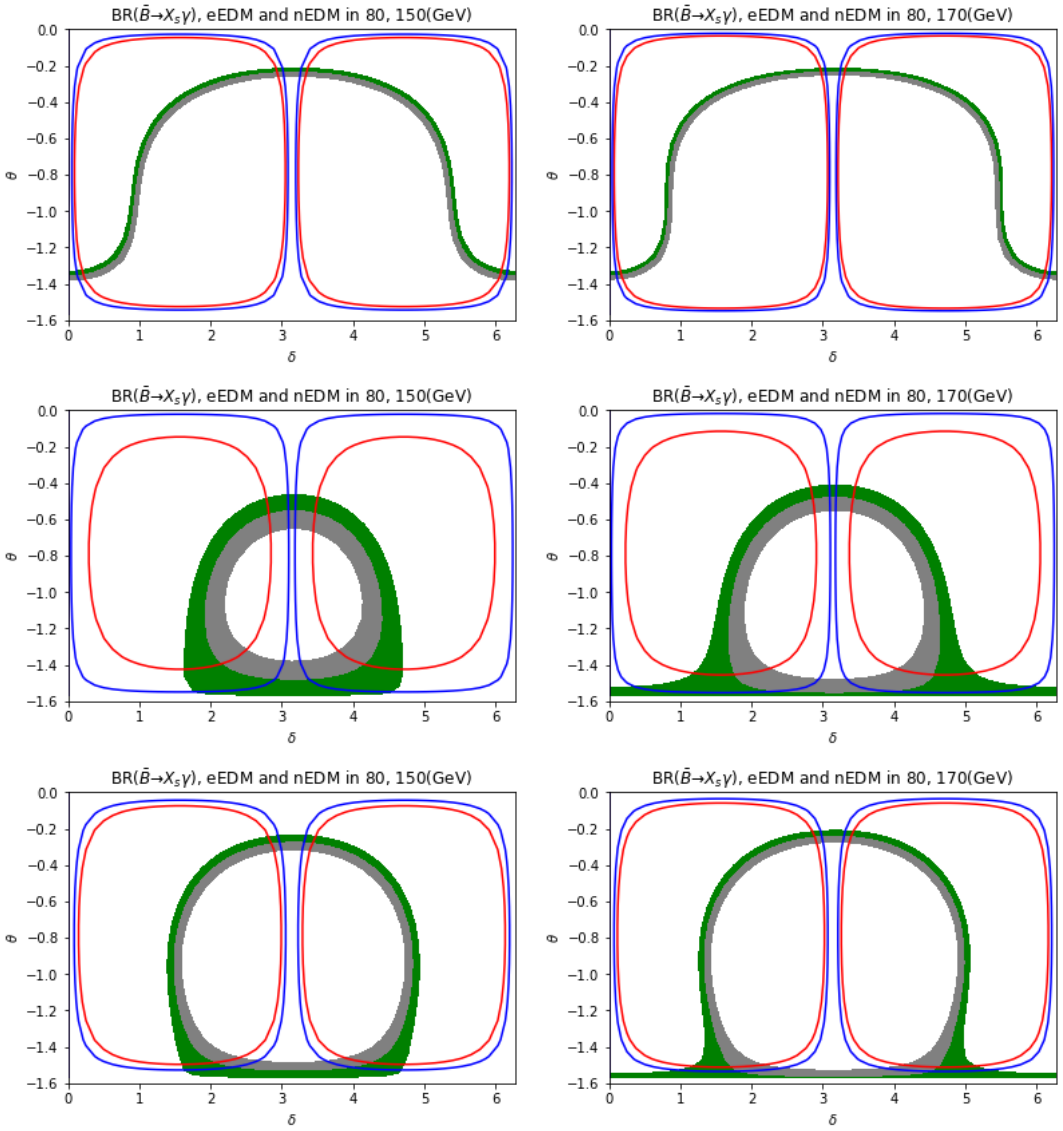

FIGURE 6.23: The allowed regions from $\bar{B} \to X_s\gamma$ (within the green and grey shaded areas), eEDM (outside the blue curves), and nEDM (outside the red curves) in the $[\delta, \theta]$ plane, with $M_{H_2^\pm} = 80$ GeV and $M_{H_3^\pm} = 150$ (left) or 170 (right) GeV. From top to bottom, $(\tan\beta, \tan\gamma) = (5, 0.5)$; $(5, 1)$; and $(10, 1)$.

6.5.7 Heavy charged Higgses

In the case that both the $H_2^\pm$ and $H_3^\pm$ masses are heavier than the top-quark mass, collider searches no longer significantly limit the parameter space, so we present the $\bar{B} \to X_s\gamma$, eEDM and nEDM constraints on the $[M_{H_2^\pm}, M_{H_3^\pm}]$ plane with different choices for the mixing parameters ($\tan\beta$, $\tan\gamma$, θ, and δ). We choose the parameters $\theta = -0.476\pi$ $(-\pi/4)$, $\tan\beta = 20$ (40) and $\tan\gamma = 1$ (2) to plot from Fig. (6.24) to Fig. (6.29). Specifically, Figs. (6.24)–(6.26) are plotted for three different δ values for the same $\theta = -0.476\pi$, where $\delta = 0.5\pi$ (maximum CP-violating scenario), 0.85π, and 0.9π (two choices closer to the CP-conserving limit). In Fig. (6.24), the two bottom panels clearly

show that the most constraining limit comes from the nEDM when $\tan\beta = 40$. For the choice of $\tan\beta = 20$ and $\tan\gamma = 2$, the top right panel shows instead that the eEDM constraint is the one limiting most of the parameter space. In Figs. (6.25 and 6.26), a large expanse of parameter space is allowed by both the eEDM and nEDM constraints. In fact, here, EDM constraints no longer strictly limit the parameter space so that $\bar{B} \to X_s\gamma$ becomes the essential constraint, especially as δ gets close to π. The typical funnel shape of the allowed region along the mass diagonal for the EDM constraints illustrates again the impact of the GIM-like cancellation mechanism driven by the charged Higgs mass degeneracy, the more so the smaller their absolute values. Such a cancellation is not present in the $\bar{B} \to X_s\gamma$ constraint, since this observable receives both real and imaginary contributions from $X_iY_i^*$ terms, with the real components of $X_2Y_2^*$ and $X_3Y_3^*$ not being strongly correlated as their imaginary parts are; the corresponding shape thus departs from the funnel one and depends more on a judicious choice of θ for given values of $\tan\beta$ and $\tan\gamma$.

In the case of $\theta = -\pi/4$, three similar figures, Figs. (6.27, 6.28, and 6.29), are presented for $\delta = 0.5\pi$, 0.85π and 0.9π, respectively. For this θ value, it is intriguing to note that even the exact degeneracy case between $H_2^\pm$ and $H_3^\pm$ fails the $\bar{B} \to X_s\gamma$ constraint for the smallest δ choice. In contrast, for the other δ values, the main effect is a significant restriction of the parameter space allowed by $\bar{B} \to X_s\gamma$ along the $M_{H_2^\pm} = M_{H_3^\pm}$ diagonal while, conversely, the EDM constraints are less invasive. This is a generalized feature quite irrespectively of the value of $\tan\beta$, so long as $\tan\gamma$ remains small.

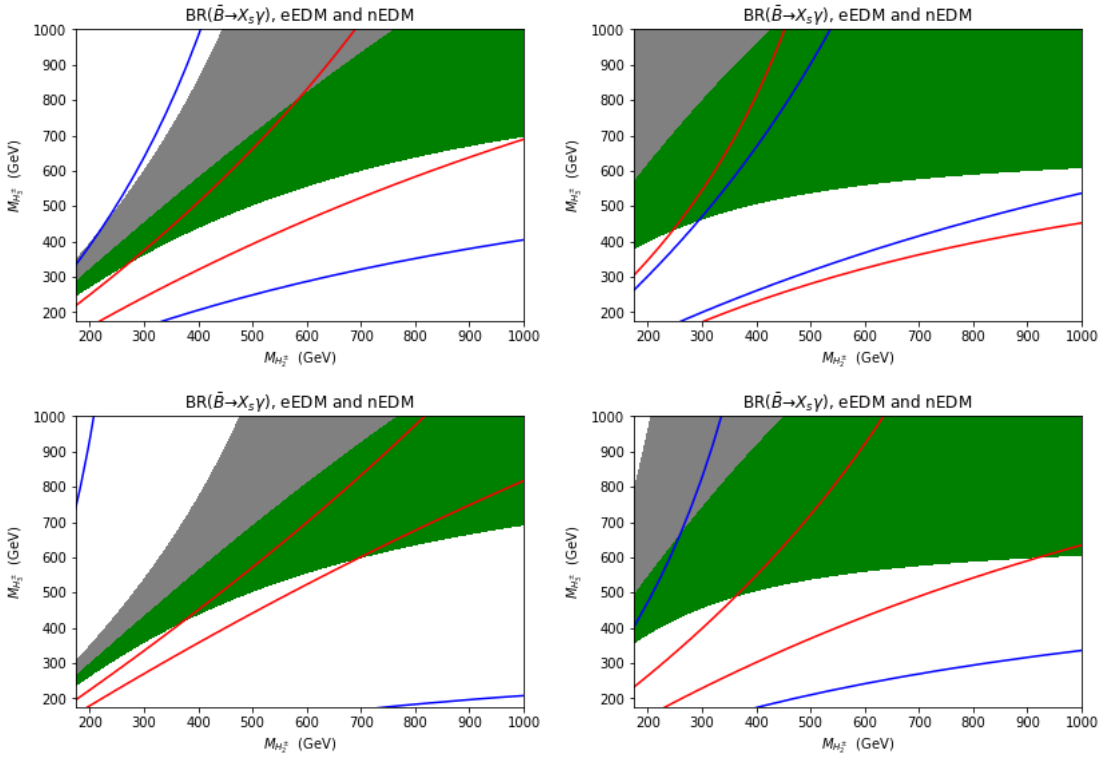

FIGURE 6.24: The allowed regions from $\bar{B} \to X_s\gamma$ (within the green and grey shaded areas), eEDM (between the blue lines), and nEDM (between the red lines) in the $[M_{H_2^\pm}, M_{H_3^\pm}]$ plane, for $\theta = -0.476\pi$ and $\delta = 0.5\pi$ (i.e., maximal CP violation), with $\tan\beta = 20$ (upper panels) or 40 (lower panels) and $\tan\gamma = 1$ (left panels) or 2 (right panels).

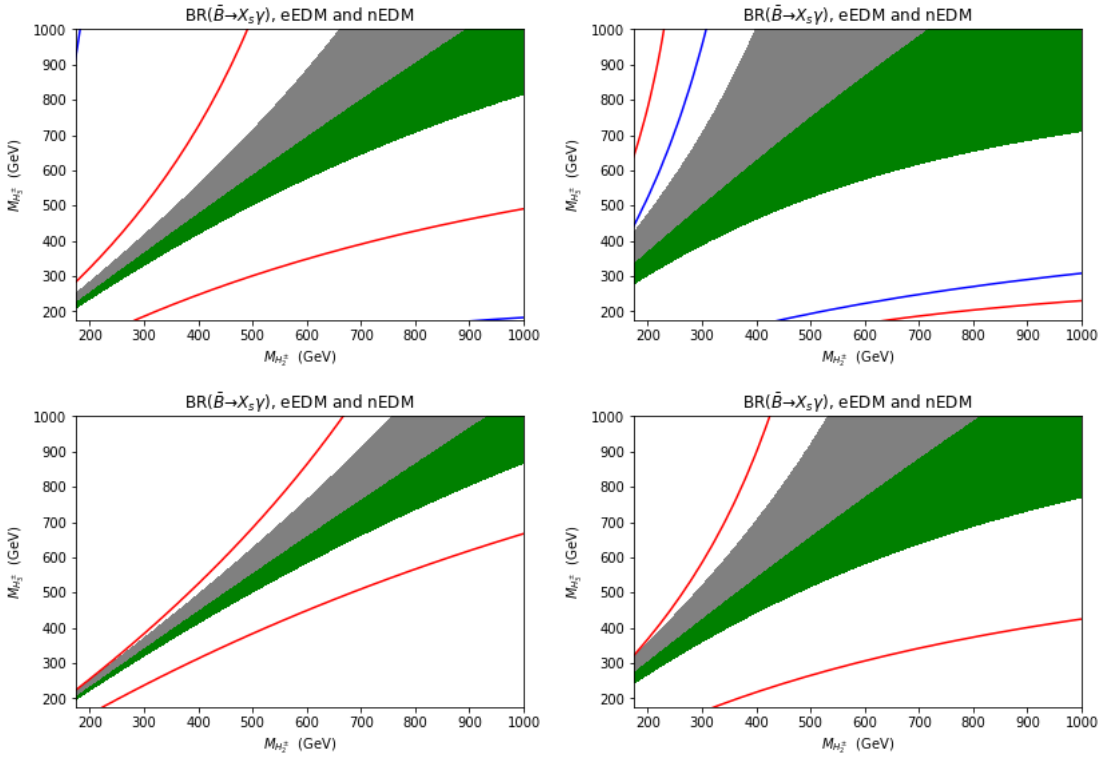

FIGURE 6.25: Same as Fig. (6.24) but with $\delta = 0.85\pi$.

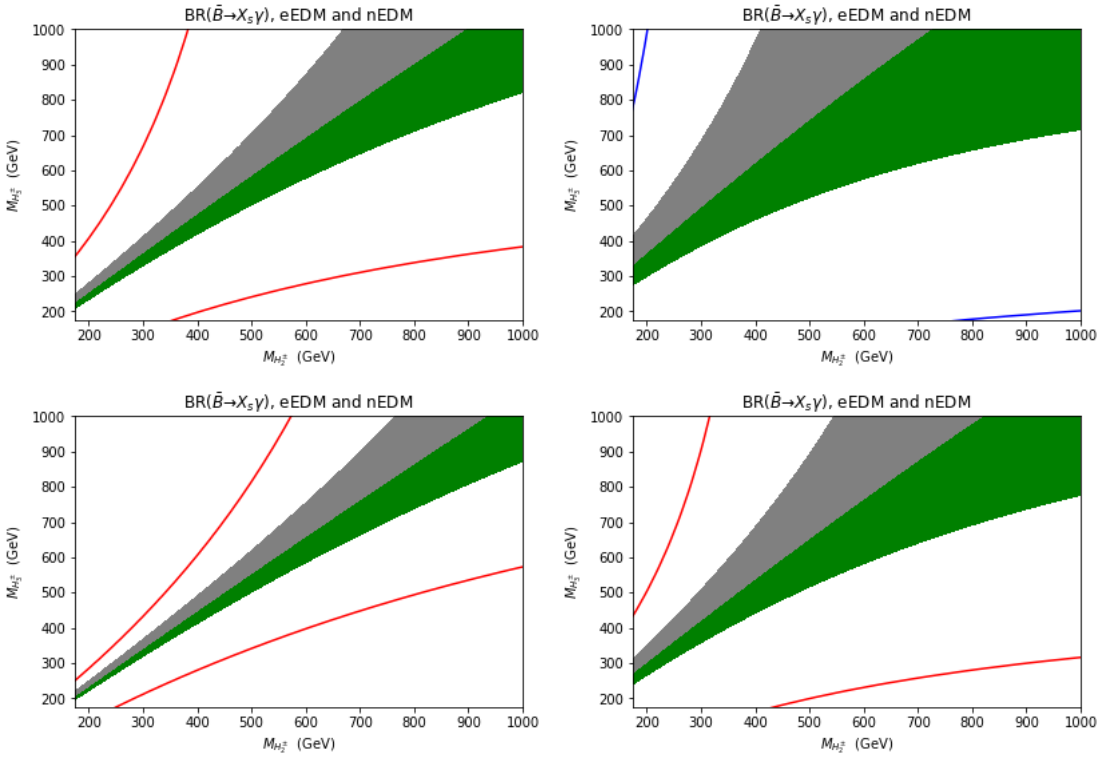

FIGURE 6.26: Same as Fig. (6.24) but with $\delta = 0.9\pi$.

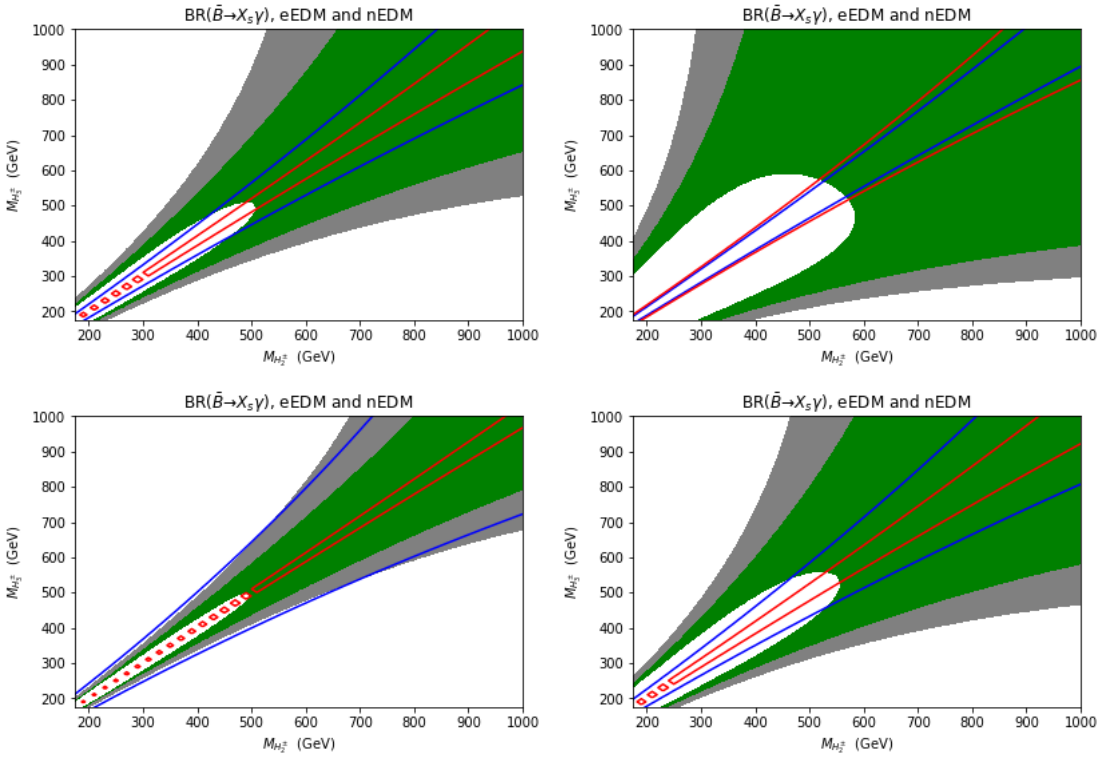

FIGURE 6.27: Same as Fig. (6.24) but with $\theta = -\pi/4$.

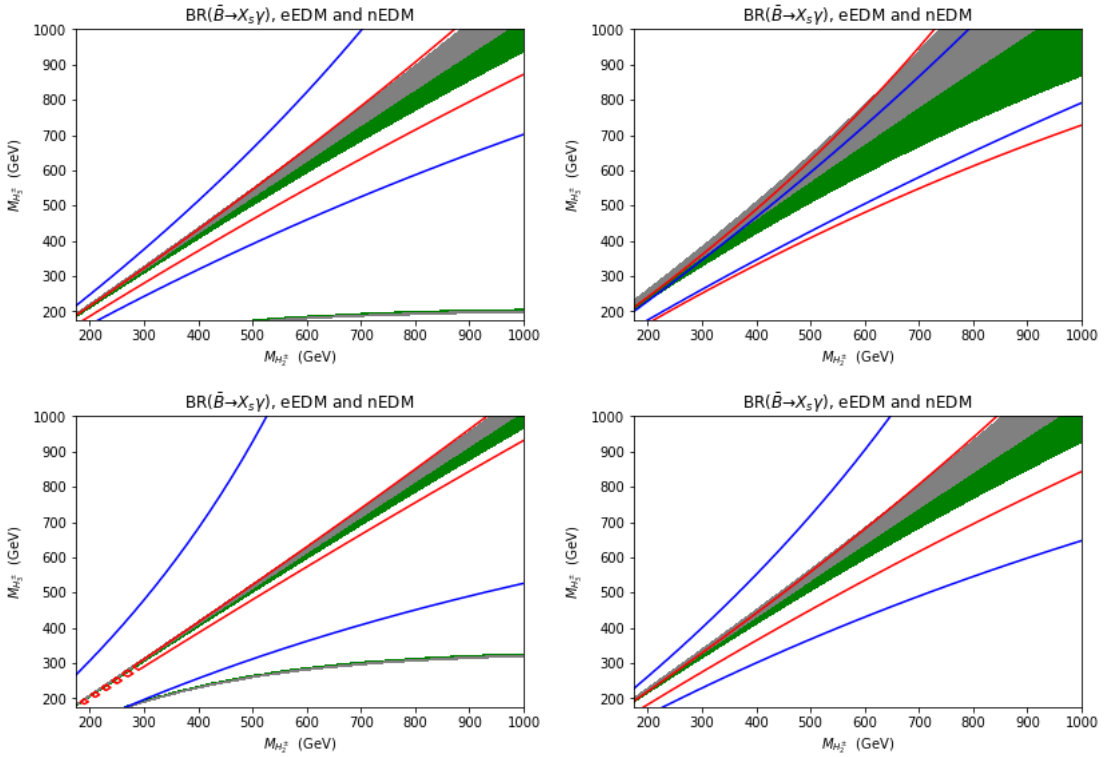

FIGURE 6.28: Same as Fig. (6.25) but with $\theta = -\pi/4$.

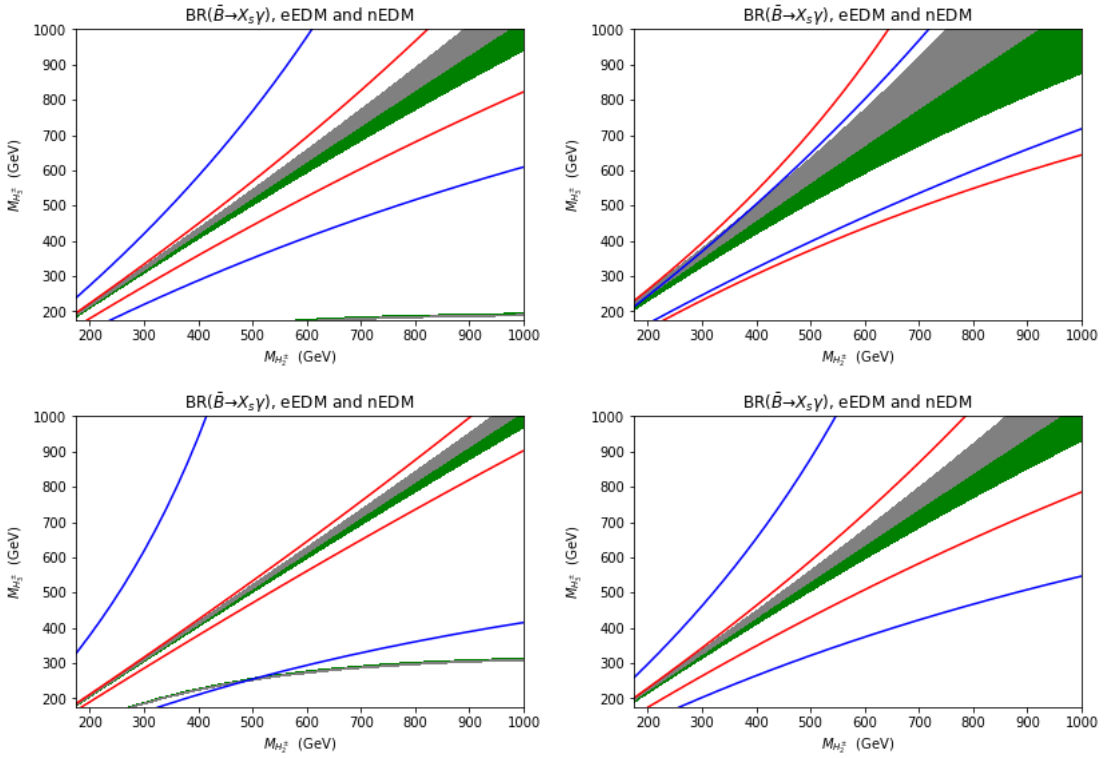

FIGURE 6.29: Same as Fig. (6.26) but with $\theta = -\pi/4$.

6.6 Conclusion

In this chapter, we investigated the CP-violation anomalies of charged Higgs bosons in 3HDM. The motivation comes from the constraining of Yukawa couplings from charged Higgs sector. Only 2HDM has covered for the detailed study of Yukawa couplings limitation [13]. In our analysis, we calculated the both two charged Higgs contribution ($H_2^\pm, H_3^\pm$) correspond to the Yukawa couplings of the two states (X_2, Y_2, Z_2, X_3, Y_3, Z_3) which limit from both BR($\bar{B} \to X_s\gamma$) and EDMs constraints. For BR($\bar{B} \to X_s\gamma$) constraint, the process took the effective Hamiltonian of $\bar{B} \to X_s\gamma$ and calculated the BSM (or 3HDM charged Higgs) Wilson coefficients contribution under a matching scale $\mu \approx M_w$ and evaluated to a lower scale $\mu \approx m_b$ by the anomalous dimensional operators with different scales. The whole process took both LO and NLO contributions which then obtain the final result based on two perturbative processes $b \to s\gamma$ and $b \to s\gamma\, g$ and two non perturbative or long distance correction with m_b and m_c two masses. We then discussed the experimental $\bar{B} \to X_s\gamma$ from BELLE and BABAR experiments. The experiment and theoretical prediction for BR($\bar{B} \to X_s\gamma$) are under a good agreement, so the BSM physics will need to be compatible for this constraint.

For the decay of $\bar{B} \to X_s\gamma$, there are some CP-asymmetry observables which could be test for new physics. They are direct CP-asymmetry as $\mathcal{A}_{X_{s(d)}\gamma}$, the difference of CP-asymmetry $\Delta\mathcal{A}_{X_{s(d)}\gamma}$, and the untagged (inclusive) asymmetry $\mathcal{A}_{\rm CP}(\bar{B} \to X_{s+d}\gamma)$. These asymmetry observables have potential large uncertainty from BELLE and BABAR experiments. The untagged asymmetry can be the tool for new physics test. The reason is the SM prediction of it is zero due to the unitarity of CKM matrix. Thus, a large value which out of the centre would provide a hint for new physics discovery. We then show the available parameter space of Yukawa couplings which could obtain such clear signal for light and heavy charged Higgs states.

Finally, the constraint of EDMs we covered for both neutron and electron EDMs which limit the combination of X_i and Y_i and the combination of Y_i and Z_i. In specific type-Z (Democratic) 3HDM, we investigated the contribution of two EDMs based on the Weinberg operator, bottom quark chromo-EDM operator and two loop charged Higgs Barr-Zee operators to compare with recent eEDM [175] and nEDM [180] experiment measurements. We showed the several charged Higgs scenarios ($M_{H_2^\pm} < m_t < M_{H_3^\pm}$, $M_{H_2^\pm} < M_{H_3^\pm} < m_t$, and $m_t < M_{H_2^\pm} < M_{H_3^\pm}$). For the mixing of light charged Higgs and heavy charged Higgs states, the CP-violation phase prefers to have solution close to π. For the both heavy charged Higgs states case, we found an interesting cancellation mechanism for EDM CP-violation which is similar as GIM mechanism. The cancellation becomes exact if the two charged Higgs states degenerate in mass which makes the mixing angle θ and δ to be non-physical.

Chapter 7

Conclusions

In this thesis, to start with, we have introduced the SM structure which embeds the Higgs mechanism of EW symmetry breaking and mass generation. Then, the need for new physics is motivated in terms of a lot of unsolved problems within the SM. From the point of view of Higgs sector, we are motivated to study the BSM scenarios called 2HDM and 3HDM, because of their rich scalar structures. In the context of the 3HDM, which is especially tackled in this thesis, we have concentrated upon the investigation of the charged Higgs particle states in presence of effects due to CP-violation emerging solely in the charged Higgs sector.

We have demonstrated that, in the 3HDM with two additional Higgs doublets, the physical charged Higgs bosons can be made compatible with results from their collider searches. Within two possible scenarios of a softly broken Z_2 symmetry, we have discussed the phenomenology of the lightest light charged Higgs boson production and decay when its mass is smaller than that of the top quark. The charm and bottom quarks decay channel can produce significant contributions to the observation of such a charged Higgs state, so that the intervening parameter space, mapped in terms of the charged Higgs boson Yukawa couplings to the cb quark pair, the independent parameters in the active Higgs doublet VEVs ($\tan\beta$ and $\tan\gamma$), the mixing angle between the two physical charged Higgs states (θ for $H_2^\pm, H_3^\pm$) and the CP-violation phase in charged Higgs sector (δ), was then studied. We have firstly investigated the correlation between the light charged Higgs mass $M_{H_2^\pm}$ and the Yukawa couplings X_2, Y_2 and Z_2. Following the discussion of recent LEP2 and LHC search sensitivities to light charged Higgs bosons, we have performed a statistical analysis based on LEP2 data and commented on the 2σ significances found in light charged Higgs boson searches. Such significances could be explained through the 3HDM if they are genuine. We have used a new $b-$tagging strategy and evaluated the significances in two different charged Higgs boson search channels, i.e., 2-jet ($e^+e^- \to H^+H^- \to \text{hadrons}\,(jj) + \tau\nu_\tau$) and 4-jet ($e^+e^- \to H^+H^- \to \text{hadrons}\,(jj) + \text{hadrons}\,(jj)$) final states. For each hadronic scenario, we have presented the improvement in significances based on a variety of

flavour tagging approaches within the type-Y (Flipped) 3HDM. In addition, we have discussed the prospects of charged Higgs boson searches at future electron-positron colliders based on the numerical extrapolations from LEP2 results (e.g., at CEPC and FCC-ee). If a small BR of a light charged Higgs boson into a cb final state (i.e. $< 1\%$) is possible, there exists a clear possibility of its detection at a higher center-of-mass energy leptonic collider.

We have then discussed the phenomenological constraints on the two charged Higgs boson states of the 3HDM ($H_2^\pm, H_3^\pm$) based on three observables, $\bar{B} \to X_s\gamma$ and the EDMs of the neutron and electron, all of which limit both real and imaginary contributions entering the charged Higgs boson Yukawa couplings. Since the SM theoretical prediction of the NNLO BR($\bar{B} \to X_s\gamma$) and the experimental measurement match very well, it certainly does not provide any hint for new physics, hence we have interpreted the ensuing results as constraints placed on our BSM scenario. Then, several CP-violating asymmetry observables based on the new contributions from such charged Higgs bosons have been investigated by using an effective Hamiltonian. The first one is called direct CP-asymmetry ($\mathcal{A}_{X_{s(d)}\gamma}$) and it is the ratio of the difference between $\bar{B} \to X_{s/d}\gamma$ and $B \to X_{s/d}\gamma$ over their sum. The second observable is the difference of CP-asymmetry ($\Delta\mathcal{A}_{X_{s(d)}\gamma}$), i.e., the difference between the charged B meson decay rate to $X_{s/d}\gamma$ and that of the neutral B meson decay to $X_{s/d}\gamma$. The last one is the untagged-asymmetry, also called the inclusive asymmetry ($\mathcal{A}_{\rm CP}(\bar{B} \to X_{s+d}\gamma)$), which is correlated to both $\Gamma(\bar{B} \to X_s\gamma)$ and $\Gamma(\bar{B} \to X_d\gamma)$. Three benchmarks points have been introduced and have shown that the untagged-asymmetry observable $\mathcal{A}_{\rm CP}(\bar{B} \to X_{s+d}\gamma)$ is the most sensitive one to new physics as it is essentially zero (with a small theoretical error) in the SM. If a measurement of $2.5\% \pm 0.5\%$ of the untagged-asymmetry could be attained, the potential new physics advocated here will be waiting for a discovery as such a construct could yield a 5σ excess. Specifically, it was shown that the Flipped 3HDM could well accommodate a clear signal, which thus motivates our BSM scenario also in the context of B factories.

We have then moved on to study the constraints on the imaginary Yukawa coupling contributions which enter BR($\bar{B} \to X_s\gamma$) and the nEDM and eEDM, again, with the CP-violation source stemming solely from the charged Higgs boson sector. We have computed these three observables in the 3HDM for the first time, which has allowed us to study the viable parameter space described in terms of $\tan\beta, \tan\gamma, \theta$ and the CP-violation phase (δ) for both charged Higgs states ($H_2^\pm, H_3^\pm$) in the case of both light mass states (either two masses lighter than m_t or one lighter than m_t ($H_2^\pm$) and the other heavier ($H_3^\pm$)) as well as the scenario with all heavy mass states ($H_2^\pm$ and $H_3^\pm$ both heavier than m_t). Several parameter space plots have been presented showing the strong sensitivity of these observables to all such mass combinations. Lastly, we have found an interesting GIM-like mechanism for the cancellation of even very large imaginary parts

of the charged Higgs boson Yukawas. Indeed, such CP-violating parameters would cancel exactly if the two physical charged Higgs masses were degenerate.

Appendix A

Input Parameters for the Numerical Analysis

$m_c/m_b = 0.29$	$m_b - m_c = 3.39$ GeV	$m_t = 173$ GeV	$G_F = 1.1663787 \times 10^{-5}$ GeV^{-2}
$\alpha_{em} = 1/\ 130.3$	$M_Z = 91.1875$ GeV	$M_{W^\pm} = 80.33$ GeV	$\alpha(M_Z) = 0.119$
$\lambda = 0.22650$	$A = 0.790$	$\bar{\rho} = 0.141$	$\bar{\eta} = 0.357$
$BR_{SL} = 0.1049$			

TABLE A.1: Input values for the SM parameters. The central value of $\bar{B} \to X_s\gamma$ used here is obtained from these input parameters. We refer to [13] for the choice of pole fermion masses. Here m_b and m_c are the pole mass of the b and c quarks respectively. The Wolfenstein parameters of the CKM matrix are taken from Ref. [14].

Appendix B

The Formulas for Wilson coefficients in $\bar{B} \to X_s\gamma$

In this appendix, it includes all necessary Wilson coefficient formulas for BR($\bar{B} \to X_s\gamma$) and they are taken from the Ref. [13].

B.1 Wilson Coefficients at scale μ_W

In SM case, the LO function is:

$$\begin{aligned} C^0_{7,\mathrm{SM}} &= \frac{x}{24}\left[\frac{-8x^3+3x^2+12x-7+(18x^2-12x)\ln x}{(x-1)^4}\right] \\ C^0_{8,\mathrm{SM}} &= \frac{x}{8}\left[\frac{-x^3+6x^2-3x-2-6x\ln x}{(x-1)^4}\right] \end{aligned} \tag{B.1}$$

In the $\overline{\text{MS}}$ scheme, NLO functions are:

$$
\begin{aligned}
E_0 &= \frac{x(x^2+11x-18)}{12(x-1)^3} + \frac{x^2(4x^2-16x+15)}{6(x-1)^4}\ln x - \frac{2}{3}\ln x - \frac{2}{3} \\
W_{7,\text{SM}} &= \frac{-16x^4-122x^3+80x^2-8x}{9(x-1)^4}\text{Li}_2(1-\frac{1}{x}) + \frac{(6x^4+46x^3-28x^2)(\ln^2 x)}{3(x-1)^5} \\
&+ \frac{(-102x^5-588x^4-2262x^3+3244x^2-1364x+208)\ln x}{81(x-1)^5} \\
&+ \frac{(1646x^4+12205x^3-10740x^2+2509x-436)}{486(x-1)^4} \\
W_{8,\text{SM}} &= \frac{(-4x^4+40x^3+41x^2+x)}{6(x-1)^4}\text{Li}_2(1-\frac{1}{x}) + \frac{-17x^3-31x^2}{2(x-1)^5}\ln^2 x \\
&+ \frac{(-210x^5+1086x^4+4893x^3+2857x^2-1994x+280)}{216(x-1)^5}\ln x \\
&+ \frac{(737x^4-14102x^3-28209x^2+610x-508)}{1296(x-1)^4} \\
M_{7,\text{SM}} &= \frac{82x^5+301x^4+703x^3-2197x^2+1319x-208-(162x^4+1242x^3-756x^2)\ln x}{81(x-1)^5} \\
M_{8,\text{SM}} &= \frac{77x^5-475x^4-1111x^3+607x^2+1042x-140+(918x^3+1674x^2)\ln x}{108(x-1)^5} \\
T_{7,\text{SM}} &= \frac{x}{3}\left[\frac{47x^3-63x^2+9x+7-(18x^3+30x^2-24x)\ln x}{(x-1)^5}\right] \\
T_{8,\text{SM}} &= 2x\left[\frac{-x^3-9x^2+9x+1+(6x^2+6x)\ln x}{(x-1)^5}\right]
\end{aligned}
\tag{B.2}
$$

For charged Higgs case, $|Y|^2$. LO charged Higgs contribution with the mass ratio $y = \frac{m_t^2}{M_{H^\pm}^2}$.

$$
\begin{aligned}
C_{7,\text{YY}}^0 &= \frac{1}{3}C_{7,\text{SM}}^0(x \to y) \\
C_{8,\text{YY}}^0 &= \frac{1}{3}C_{8,\text{SM}}^0(x \to y)
\end{aligned}
\tag{B.3}
$$

At the NLO,

$$\begin{aligned}
E_H &= \frac{1}{36}y\left[\frac{7y^3-36y^2+45y-16+(18y-12)\ln y}{(y-1)^4}\right] \\
W_{7,\mathrm{YY}} &= \frac{2}{9}y\left[\frac{8y^3-37y^2+18y}{(y-1)^4}\mathrm{Li}_2\left(1-\frac{1}{y}\right)+\frac{3y^3+23y^2-14y}{(y-1)^5}\ln^2 y\right. \\
&+ \frac{21y^4-192y^3-174y^2+251y-50}{9(y-1)^5}\ln y \\
&+ \left.\frac{-1202y^3+7569y^2-5436y+797}{108(y-1)^4}\right]-\frac{4}{9}E_H \\
W_{8,\mathrm{YY}} &= \frac{1}{6}y\left[\frac{(13y^3-17y^2+30y}{(y-1)^4}\mathrm{Li}_2\left(1-\frac{1}{y}\right)-\frac{17y^2+31y}{(y-1)^5}\ln^2 y\right. \\
&+ \frac{42y^4+318y^3+1353y^2+817y-226}{36(y-1)^5)}\ln y \\
&+ \left.\frac{-4451y^3+7650y^2-18153y+1130}{108(y-1)^4}\right]-\frac{1}{6}E_H \\
M_{7,\mathrm{YY}} &= \frac{1}{27}y\left[\frac{-14y^4+149y^3-153y^2-13y+31-(18y^3+138y^2-84y)\ln y}{(y-1)^5}\right] \\
M_{8,\mathrm{YY}} &= \frac{1}{36}y\left[\frac{-7y^4+25y^3-279y^2+223y+38-(102y^2+186y)\ln y}{(y-1)^5}\right] \\
T_{7,\mathrm{YY}} &= \frac{1}{3}T_{7,\mathrm{SM}}(x\to y) \\
T_{8,\mathrm{YY}} &= \frac{1}{3}T_{8,\mathrm{SM}}(x\to y)
\end{aligned} \tag{B.4}$$

For charged Higgs case, (XY^*). LO charged Higgs contribution with the mass ratio $y=\frac{m_t^2}{M_{H^\pm}^2}$.

$$\begin{aligned}
C_{7,\mathrm{XY}}^0 &= \frac{1}{12}y\left[\frac{-5y^2+8y-3+(6y-4)\ln y}{(y-1)^3}\right] \\
C_{8,\mathrm{XY}}^0 &= \frac{1}{4}y\left[\frac{-y^2+4y-3-2\ln y}{(y-1)^3}\right]
\end{aligned} \tag{B.5}$$

And at NLO,

$$\begin{aligned}
W_{7,XY} &= \frac{4}{3}y\left[\frac{8y^2-28y+12}{3(y-1)^3}\mathrm{Li}_2\left(1-\frac{1}{y}\right)+\frac{3y^2+14y-8}{3(y-1)^4}\ln^2 y\right.\\
&+ \left.\frac{4y^3-24y^2+2y+6}{3(y-1)^4}\ln y+\frac{-2y^2+13y-7}{(y-1)^3}\right]\\
W_{8,XY} &= \frac{1}{3}y\left[\frac{17y^2-25y+36}{2(y-1)^3}\mathrm{Li}_2\left(1-\frac{1}{y}\right)-\frac{17y+19}{(y-1)^4}\ln^2 y\right.\\
&+ \left.\frac{14y^3-12y^2+187y+3}{4(y-1)^4}\ln y-\frac{3(29y^2-44y+143)}{8(y-1)^3}\right]\\
M_{7,XY} &= \frac{2}{9}y\left[\frac{-8y^3+55y^2-68y+21-(6y^2+28y-16)\ln y}{(y-1)^4}\right]\\
M_{8,XY} &= \frac{1}{6}y\left[\frac{-7y^3+23y^2-97y+81+(34y+38)\ln y}{(y-1)^4}\right]\\
T_{7,XY} &= \frac{2}{3}y\left[\frac{13y^2-20y+7-(6y^2+4y-4)\ln y}{(y-1)^4}\right]\\
T_{8,XY} &= 2y\left[\frac{-y^2-4y+5+(4y+2)\ln y}{(y-1)^4}\right] \qquad \text{(B.6)}
\end{aligned}$$

B.2 Effective Wilson Coefficients from scale μ_W to μ_b

LO term, $C_{7,SM}^{0,\mathrm{eff}}(\mu_b)$:

$$\begin{aligned}
C_{7,SM}^{0,\mathrm{eff}}(\mu_b) &= \eta^{\frac{16}{23}}C_{7,SM}^{0,\mathrm{eff}}(\mu_W)+\frac{8}{3}(\eta^{\frac{14}{23}}-\eta^{\frac{16}{23}})C_{8,SM}^{0,\mathrm{eff}}(\mu_W)\\
&+ \sum_{i=1}^{8}h_i\eta^{a_i}C_2^{0,eff}(\mu_W) \qquad \text{(B.7)}
\end{aligned}$$

$C_2^{0,\mathrm{eff}}(\mu_W)=1$ and $\eta=\alpha_s(\mu_W)/\alpha_s(\mu_b)$.

NLO term, $C_{7,SM}^{1,\mathrm{eff}}(\mu_b)$:

$$\begin{aligned}
C_{7,SM}^{1,\mathrm{eff}}(\mu_b) &= \eta^{39/23}C_{7,SM}^{1,\mathrm{eff}}(\mu_W)+\frac{8}{3}(\eta^{37/23}-\eta^{39/23})C_{8,SM}^{1,\mathrm{eff}}(\mu_W)\\
&+ \left(\frac{297664}{14283}\eta^{16/23}-\frac{7164416}{357075}\eta^{14/23}+\frac{256868}{14283}\eta^{37/23}-\frac{6698884}{357075}\eta^{39/23}\right)C_{8,SM}^{0,\mathrm{eff}}(\mu_W)\\
&+ \frac{37208}{4761}(\eta^{39/23}-\eta^{16/23})C_{7,SM}^{0,\mathrm{eff}}(\mu_W) \qquad \text{(B.8)}
\end{aligned}$$

LO $C_{7,XY}^{0,\mathrm{eff}}(\mu_b)$:

$$C_{7,XY}^{0,\mathrm{eff}}(\mu_b)=\eta^{\frac{16}{23}}C_{7,XY}^{0,\mathrm{eff}}(\mu_W)+\frac{8}{3}(\eta^{\frac{14}{23}}-\eta^{\frac{16}{23}})C_{8,XY}^{0,\mathrm{eff}}(\mu_W) \qquad \text{(B.9)}$$

NLO $C_{7,XY}^{1,\text{eff}}(\mu_b)$:

$$\begin{aligned} C_{7,XY}^{1,\text{eff}}(\mu_b) &= \eta^{39/23} C_{7,XY}^{1,\text{eff}}(\mu_W) + \frac{8}{3}\,(\eta^{37/23} - \eta^{39/23}) C_{8,XY}^{1,\text{eff}}(\mu_W) \\ &+ \left(\frac{297664}{14283}\eta^{16/23} - \frac{7164416}{357075}\eta^{14/23} + \frac{256868}{14283}\eta^{37/23} - \frac{6698884}{357075}\eta^{39/23}\right) C_{8,XY}^{0,\text{eff}}(\mu_W) \\ &+ \frac{37208}{4761}(\eta^{39/23} - \eta^{16/23}) C_{7,XY}^{0,\text{eff}}(\mu_W) \end{aligned} \tag{B.10}$$

LO $C_{7,YY}^{0,\text{eff}}(\mu_b)$:

$$C_{7,YY}^{0,\text{eff}}(\mu_b) = \eta^{\frac{16}{23}} C_{7,YY}^{0,\text{eff}}(\mu_W) + \frac{8}{3}(\eta^{\frac{14}{23}} - \eta^{\frac{16}{23}}) C_{8,YY}^{0,\text{eff}}(\mu_W) \tag{B.11}$$

NLO $C_{7,YY}^{1,\text{eff}}(\mu_b)$:

$$\begin{aligned} C_{7,YY}^{1,\text{eff}}(\mu_b) &= \eta^{39/23} C_{7,YY}^{1,\text{eff}}(\mu_W) + \frac{8}{3}\,(\eta^{37/23} - \eta^{39/23}) C_{8,YY}^{1,\text{eff}}(\mu_W) \\ &+ \left(\frac{297664}{14283}\eta^{16/23} - \frac{7164416}{357075}\eta^{14/23} + \frac{256868}{14283}\eta^{37/23} - \frac{6698884}{357075}\eta^{39/23}\right) C_{8,YY}^{0,\text{eff}}(\mu_W) \\ &+ \frac{37208}{4761}(\eta^{39/23} - \eta^{16/23}) C_{7,YY}^{0,\text{eff}}(\mu_W) \end{aligned} \tag{B.12}$$

B.3 NLO Wilson coefficients at the matching scale : $\mathbf{C}_i^{eff}(\mu_W)$

LO Wilson coefficients at the matching scale.

$$C_2^{0,\text{eff}}(\mu_W) = 1, \tag{B.13}$$

$$C_i^{0,\text{eff}}(\mu_W) = 0 \quad (i = 1,3,4,5,6) \tag{B.14}$$

$$C_7^{0,\text{eff}}(\mu_W) = C_{7,SM}^0 + |Y_2|^2 C_{7,Y_2Y_2}^0 + |Y_3|^2 C_{7,Y_3Y_3}^0 \tag{B.15}$$
$$+(X_2Y_2^*)C_{7,X_2Y_2}^0 + (X_3Y_3^*)C_{7,X_3Y_3}^0$$

$$C_8^{0,\text{eff}}(\mu_W) = C_{8,SM}^0 + |Y_2|^2 C_{8,Y_2Y_2}^0 + |Y_3|^2 C_{8,Y_3Y_3}^0 \tag{B.16}$$
$$+(X_2Y_2^*)C_{8,X_2Y_2}^0 + (X_3Y_3^*)C_{8,X_3Y_3}^0$$

NLO Wilson coefficients at the matching scale.

$$C_1^{1,\text{eff}}(\mu_W) = 15 + 6\ \ln\frac{\mu_W^2}{M_W^2}, \tag{B.17}$$

$$C_4^{1,\text{eff}}(\mu_W) = E_0 + \frac{2}{3}\ \ln\frac{\mu_W^2}{M_W^2} + |Y_2|^2 E_{H_2} + |Y_3|^2 E_{H_3} \tag{B.18}$$

$$C_i^{1,\text{eff}}(\mu_W) = 0 \quad (i = 2,3,5,6) \tag{B.19}$$

$$C_7^{1,\text{eff}}(\mu_W) = C_{7,SM}^{1,\text{eff}}(\mu_W) + |Y_2|^2 C_{7,Y_2Y_2}^{1,\text{eff}}(\mu_W) + \tag{B.20}$$
$$|Y_3|^2 C_{7,Y_3Y_3}^{1,\text{eff}}(\mu_W) + (X_2Y_2^*)C_{7,X_2Y_2}^{1,\text{eff}}(\mu_W) + (X_3Y_3^*)C_{7,X_3Y_3}^{1,\text{eff}}(\mu_W)$$

$$C_8^{1,\text{eff}}(\mu_W) = C_{8,SM}^{1,\text{eff}}(\mu_W) + |Y_2|^2 C_{8,Y_2Y_2}^{1,\text{eff}}(\mu_W) + \tag{B.21}$$
$$|Y_3|^2 C_{8,Y_3Y_3}^{1,\text{eff}}(\mu_W) + (X_2Y_2^*)C_{8,X_2Y_2}^{1,\text{eff}}(\mu_W) + (X_3Y_3^*)C_{8,X_3Y_3}^{1,\text{eff}}(\mu_W)$$

For $i = 7,8$, the three terms $C_{i,SM}^{1,\text{eff}}$, $C_{i,YY}^{1,\text{eff}}$ and $C_{i,XY}^{1,\text{eff}}$ are defined by:

$$C_{i,SM}^{1,\text{eff}}(\mu_W) = W_{i,SM} + M_{i,SM}\ln\frac{\mu_W^2}{M_W^2} + T_{i,SM}(\ \ln\frac{m_t^2}{\mu_W^2} - \frac{4}{3}) \tag{B.22}$$

$$C_{i,Y_jY_j}^{1,\text{eff}}(\mu_W) = W_{i,Y_jY_j} + M_{i,Y_jY_j}\ln\frac{\mu_W^2}{M_H^2} + T_{i,Y_jY_j}(\ \ln\frac{m_t^2}{\mu_W^2} - \frac{4}{3}) \tag{B.23}$$

$$C_{i,X_jY_j}^{1,\text{eff}}(\mu_W) = W_{i,X_jY_j} + M_{i,X_jY_j}\ln\frac{\mu_W^2}{M_H^2} + T_{i,X_jY_j}(\ \ln\frac{m_t^2}{\mu_W^2} - \frac{4}{3}) \tag{B.24}$$

where $j = 2,3$ for two charged Higgs.

B.4 NLO Wilson coefficients at the low-scale : $C_i^{eff}(\mu_b)$

The evolution from the matching scale μ_w drops down to the low-energy scale μ_b by RGE:

$$\mu\frac{\mathrm{d}}{\mathrm{d}\mu}C_i^{\mathrm{eff}}(\mu) = C_j^{\mathrm{eff}}(\mu)\gamma_{ji}^{\mathrm{eff}}(\mu) \tag{B.25}$$

LO term:

$$C_1^{0,\mathrm{eff}}(\mu_b) = (\eta^{6/23} - \eta^{-12/23})C_2^{0,\mathrm{eff}}(\mu_W) \tag{B.26}$$

$$C_2^{0,\mathrm{eff}}(\mu_b) = \left(\frac{2}{3}\eta^{6/23} + \frac{1}{3}\eta^{-12/23}\right)C_2^{0,\mathrm{eff}}(\mu_W) \tag{B.27}$$

$$C_7^{0,\mathrm{eff}}(\mu_b) = \eta^{16/23}C_7^{0,\mathrm{eff}}(\mu_W) + \frac{8}{3}\,(\eta^{14/23} - \eta^{16/23})C_8^{0,\mathrm{eff}}(\mu_W) + \sum_{i=1}^{8} h_i\eta^{a_i}C_2^{0,eff}(\mu_W) \tag{B.28}$$

$$C_8^{0,\mathrm{eff}}(\mu_b) = \eta^{14/23}C_8^{0,\mathrm{eff}}(\mu_W) + \sum_{i=1}^{5} h_i^{'}\eta^{a_i^{'}}C_2^{0,\mathrm{eff}}(\mu_W) \tag{B.29}$$

NLO term:

$$\begin{aligned} C_7^{1,\mathrm{eff}}(\mu_b) &= \eta^{39/23}C_7^{1,\mathrm{eff}}(\mu_W) + \frac{8}{3}\,(\eta^{37/23} - \eta^{39/23})C_8^{1,\mathrm{eff}}(\mu_W) \\ &+\left(\frac{297664}{14283}\eta^{16/23} - \frac{7164416}{357075}\eta^{14/23} + \frac{256868}{14283}\eta^{37/23} - \frac{6698884}{357075}\eta^{39/23}\right)C_8^{0,\mathrm{eff}}(\mu_W) \\ &+\frac{37208}{4761}(\eta^{39/23} - \eta^{16/23})C_7^{0,\mathrm{eff}}(\mu_W) \\ &+\sum_{i=1}^{8}[e_i\eta C_4^{1,\mathrm{eff}}(\mu_W) + (f_i + k_i\eta)C_2^{0,\mathrm{eff}}(\mu_W) + l_i\eta C_1^{1,\mathrm{eff}}(\mu_W)]\eta^{a_i} \end{aligned} \tag{B.30}$$

The symbol η is defined as $\eta = \frac{\alpha_s(\mu_W)}{\alpha_s(\mu_b)}$; The vectors a_i, h_i, a_i', h_i' are defined in B.6.

B.5 Anomalous Dimension Matrix for $\mu_W \to \mu_b$

Pertubatively, the anomalous dimension matrix which evolves from scale μ_W to μ_b is :

$$\gamma_{ji}^{\mathrm{eff}} = \frac{\alpha_s(\mu)}{4\pi}\gamma_{ji}^{0,\mathrm{eff}} + \frac{\alpha_s^2(\mu)}{(4\pi)^2}\gamma_{ji}^{1,\mathrm{eff}} + \mathcal{O}(\alpha_s^3(\mu)) \tag{B.31}$$

The matrix $\gamma_{ji}^{0,\text{eff}}$ is given by:

$$\gamma_{ji}^{0,\text{eff}} = \begin{bmatrix} -4 & \frac{8}{3} & 0 & -\frac{2}{9} & 0 & 0 & \frac{208}{403} & \frac{173}{162} \\ 12 & 0 & 0 & \frac{4}{3} & 0 & 0 & \frac{416}{81} & \frac{70}{27} \\ 0 & 0 & 0 & -\frac{52}{3} & 0 & 2 & -\frac{176}{81} & \frac{14}{27} \\ 0 & 0 & -\frac{40}{9} & -\frac{100}{9} & \frac{4}{9} & \frac{5}{6} & -\frac{152}{243} & -\frac{587}{162} \\ 0 & 0 & 0 & -\frac{256}{3} & 0 & 20 & -\frac{6272}{81} & -\frac{6596}{27} \\ 0 & 0 & -\frac{256}{9} & \frac{56}{9} & \frac{40}{9} & -\frac{2}{3} & -\frac{4624}{243} & -\frac{4772}{81} \\ 0 & 0 & 0 & 0 & 0 & 0 & \frac{32}{3} & 0 \\ 0 & 0 & 0 & 0 & 0 & 0 & -\frac{32}{9} & \frac{28}{3} \end{bmatrix} \tag{B.32}$$

and in the $\overline{MS}$ scheme with fully anticommuting γ_5, $\gamma_{ji}^{1,\text{eff}}$ is defined by [183] :

$$\gamma_{ji}^{1,\text{eff}} = \begin{bmatrix} -\frac{355}{9} & -\frac{502}{27} & -\frac{1412}{243} & \frac{134}{243} & -\frac{35}{162} & 0 & -\frac{818}{243} & \frac{3779}{324} \\ -\frac{35}{3} & -\frac{28}{3} & -\frac{416}{81} & \frac{1280}{81} & \frac{56}{81} & \frac{35}{27} & \frac{508}{81} & \frac{1841}{108} \\ 0 & 0 & -\frac{4468}{81} & -\frac{31469}{81} & \frac{400}{81} & \frac{3373}{108} & \frac{22348}{243} & \frac{10178}{81} \\ 0 & 0 & -\frac{8158}{243} & -\frac{59399}{243} & \frac{269}{486} & \frac{12899}{648} & -\frac{17584}{243} & -\frac{17241}{648} \\ 0 & 0 & -\frac{251680}{81} & -\frac{128648}{81} & \frac{23836}{81} & \frac{6106}{27} & \frac{1183696}{729} & \frac{2901296}{243} \\ 0 & 0 & \frac{58640}{243} & -\frac{26348}{243} & -\frac{14324}{243} & -\frac{2551}{162} & \frac{2480344}{2187} & -\frac{3296257}{729} \\ 0 & 0 & 0 & 0 & 0 & 0 & \frac{4688}{27} & 0 \\ 0 & 0 & 0 & 0 & 0 & 0 & -\frac{2192}{81} & \frac{4063}{27} \end{bmatrix} \tag{B.33}$$

B.6 Running numbers

Vectors a_i, h_i, a_i', h_i' needed for the μ_b effective Wilson coefficients $C_7^{0,\text{eff}}(\mu_b)$ and $C_8^{0,\text{eff}}(\mu_b)$ are:

$$\begin{aligned} a_i &= \left\{\frac{14}{23}, \frac{16}{23}, \frac{6}{23}, -\frac{12}{23}, 0.4086, -0.4230, -0.8994, 0.1456\right\} \\ h_i &= \left\{\frac{626126}{272277}, -\frac{56281}{51730}, -\frac{3}{7}, -\frac{1}{14}, -0.6494, -0.0380, -0.0186, -0.0057\right\} \\ a_i' &= \left\{\frac{14}{23}, 0.4086, -0.4230, -0.8994, 0.1456\right\} \\ h_i' &= \left\{\frac{313063}{363036}, -0.9135, 0.0873, -0.0571, 0.0209\right\} \end{aligned} \tag{B.34}$$

For $C_7^{1,\text{eff}}(\mu_b)$,

$$
\begin{aligned}
e_i &= \left\{4661194/816831, -8516/2217, 0.0, 0.0, -1.9043, -0.1008, 0.1216, 0.0183\right\} \\
f_i &= \left\{-17.3023, 8.5027, 4.5508, 0.7519, 2.0040, 0.7476, -0.5385, 0.0914\right\} \\
k_i &= \left\{9.9372, -7.4878, 1.2688, -0.2925, -2.2923, -0.1461, 0.1239, 0.0812\right\} \\
l_i &= \left\{0.5784, -0.3921, -0.1429, 0.0476, -0.1275, 0.0317, 0.0078, -0.0031\right\} \qquad \text{(B.35)}
\end{aligned}
$$

B.7 Virtual Correction Functions r_i

The functions r_i which inside the eq. (6.14) are:

$$
\begin{aligned}
r_1 &= -\frac{1}{6}r_2 \\
r_2 &= \frac{2}{243}\{-833 + 144\pi^2 z^{3/2} \\
&+ [1728 - 180\pi^2 - 1296\zeta(3) + (1296 - 324\pi^2)L + 108L^2 + 36L^3]z \\
&+ (648 + 72\pi^2 + (432 - 216\pi^2)L + 36L^3)z^2 \\
&+ (-54 - 84\pi^2 + 1092L - 756L^2)z^3\} \\
&+ \frac{16\pi i}{81}\{-5 + [45 - 3\pi^2 + 9L + 9L^2]z + (-3\pi^2 + 9L^2)z^2 + (28 - 12L)z^3)\} \\
&+ \mathcal{O}(z^4) \\
r_7 &= \frac{32}{9} - \frac{8}{9}\pi^2 \\
r_8 &= -\frac{4}{27}(-33 + 2\pi^2 - 6i\pi) \qquad \text{(B.36)}
\end{aligned}
$$

where $z = \frac{m_c^2}{m_b^2}$ and $L = ln(z)$. $r_{3,4,5,6}$ are zero since the $C_{3,4,5,6}^{0,\text{eff}}(\mu_b) = 0$.

B.8 Semi-leptonic decay width Γ_{SL}

$$
\begin{aligned}
\Gamma_{\text{SL}} &= \frac{G_f^2}{192\pi^3}|V_{cb}|^2 m_b^5 g(z)\left(1 - \frac{2\alpha_s(\bar{\mu}_b)}{3\pi}f(z) + \frac{\delta_{\text{SL}}^{\text{NP}}}{m_b^2}\right);\ z = \frac{m_c^2}{m_b^2} \qquad \text{(B.37)} \\
g(z) &= 1 - 8z + 8z^3 - z^4 - 12z^2 \ln z, \qquad \text{(B.38)} \\
f(z) &= (\pi^2 - \frac{31}{4})(1 - \sqrt{z})^3 + \frac{3}{2} \qquad \text{(B.39)}
\end{aligned}
$$

B.9 Non-perturbative corrections for Eq. (6.12)

$$\delta_\gamma^{\rm NP} = \frac{\lambda_1}{2} - \frac{9\lambda_2}{2} \tag{B.40}$$

$$\delta_c^{\rm NP} = -\frac{\lambda_2}{9} \tag{B.41}$$

$$\delta_{\rm SL}^{\rm NP} = \frac{\lambda_1}{2} + \frac{3\lambda_2}{2}[1 - 4\frac{(1-z)^4}{g(z)}] \tag{B.42}$$

$$\lambda_1 = -0.5{\rm GeV}^2,\ \lambda_2 = -0.12{\rm GeV}^2 \tag{B.43}$$

Appendix C

Charged Higgs Yukawa couplings

In this section we collect the combinations of the Yukawa coupling coefficients X_i, Y_i, and Z_i ($i = 2, 3$) that appear in the various calculations in our analysis, and give their expressions as a function of the four mixing parameters (θ, $\tan\gamma$, $\tan\beta$ and δ) in the Flipped and Democratic 3HDM. For Democratic 3HDM, we will show specific combination of of couplings which contribute to $\bar{B} \to X_s + \gamma$ and EDMs[1]. We use the shorthand notation s_θ, c_θ, t_θ for $\sin\theta$, $\cos\theta$, and $\tan\theta$, respectively, and analogously for the other angles.

Firstly, the Flipped 3HDM expression of X_2, Y_2, Z_2, X_3, Y_3, Z_3 can be taken from Tab. (4.2), and they are:

$$X_2 = \frac{U_{12}^\dagger}{U_{11}^\dagger} = \frac{-c_\theta s_\beta (c_\delta + i s_\delta) - s_\theta c_\gamma c_\beta}{c_\beta s_\gamma}, \tag{C.1}$$

$$Y_2 = -\frac{U_{22}^\dagger}{U_{21}^\dagger} = \frac{-c_\theta c_\beta (c_\delta + i s_\delta) + s_\theta c_\gamma s_\beta}{s_\beta s_\gamma}, \tag{C.2}$$

$$Z_2 = \frac{U_{22}^\dagger}{U_{21}^\dagger} = \frac{c_\theta c_\beta (c_\delta + i s_\delta) - s_\theta c_\gamma s_\beta}{s_\beta s_\gamma}, \tag{C.3}$$

$$X_3 = \frac{U_{13}^\dagger}{U_{11}^\dagger} = \frac{s_\theta s_\beta (c_\delta + i s_\delta) - c_\theta c_\gamma c_\beta}{c_\beta s_\gamma}, \tag{C.4}$$

$$Y_3 = -\frac{U_{23}^\dagger}{U_{21}^\dagger} = \frac{s_\theta c_\beta (c_\delta + i s_\delta) + c_\theta c_\gamma s_\beta}{s_\beta s_\gamma}, \tag{C.5}$$

$$Z_3 = \frac{U_{23}^\dagger}{U_{21}^\dagger} = \frac{-s_\theta c_\beta (c_\delta + i s_\delta) - c_\theta c_\gamma s_\beta}{s_\beta s_\gamma} \tag{C.6}$$

[1]Since the Yukawa combination contribution of $\bar{B} \to X_s\gamma$ is same for both Flipped and Democratic 3HDM, only Democratic 3HDM will be covered for convenience.

For Democratic 3HDM, the expression taken from Eqs. (4.19, 4.25 and 4.26), the Yukawa coupling coefficients in our parameterization are:

$$X_2 = \frac{U^\dagger_{12}}{U^\dagger_{11}} = \frac{-c_\theta s_\beta (c_\delta + i s_\delta) - s_\theta c_\gamma c_\beta}{c_\beta s_\gamma}, \tag{C.7}$$

$$Y_2 = -\frac{U^\dagger_{22}}{U^\dagger_{21}} = \frac{-c_\theta c_\beta (c_\delta + i s_\delta) + s_\theta c_\gamma s_\beta}{s_\beta s_\gamma}, \tag{C.8}$$

$$Z_2 = \frac{U^\dagger_{32}}{U^\dagger_{31}} = \frac{s_\theta s_\gamma}{c_\gamma}, \tag{C.9}$$

$$X_3 = \frac{U^\dagger_{13}}{U^\dagger_{11}} = \frac{s_\theta s_\beta (c_\delta + i s_\delta) - c_\theta c_\gamma c_\beta}{c_\beta s_\gamma}, \tag{C.10}$$

$$Y_3 = -\frac{U^\dagger_{23}}{U^\dagger_{21}} = \frac{s_\theta c_\beta (c_\delta + i s_\delta) + c_\theta c_\gamma s_\beta}{s_\beta s_\gamma}, \tag{C.11}$$

$$Z_3 = \frac{U^\dagger_{33}}{U^\dagger_{31}} = \frac{c_\theta s_\gamma}{c_\gamma}. \tag{C.12}$$

The combinations that appear in the EDM calculations are:

$$\mathrm{Im}(-X_2 Y_2^*) = \frac{s_\theta c_\theta s_\delta}{s_\beta c_\beta s_\gamma t_\gamma} = -\mathrm{Im}(-X_3 Y_3^*), \tag{C.13}$$

$$\mathrm{Im}(-Y_2^* Z_2) = -\frac{s_\theta c_\theta s_\delta}{t_\beta c_\gamma} = -\mathrm{Im}(-Y_3^* Z_3). \tag{C.14}$$

The following contribute to the calculation of BR($\bar{B} \to X_s \gamma$). The real components of $X_i Y_i^*$ ($i = 2, 3$) are as follows:

$$\mathrm{Re}(X_2 Y_2^*) = \frac{c_\theta^2}{s_\gamma^2} + \frac{c_\delta c_\theta s_\theta}{t_\beta t_\gamma s_\gamma} - \frac{c_\delta t_\beta c_\theta s_\theta}{t_\gamma s_\gamma} - \frac{s_\theta^2}{t_\gamma^2}, \tag{C.15}$$

$$\mathrm{Re}(X_3 Y_3^*) = \frac{s_\theta^2}{s_\gamma^2} + \frac{c_\delta t_\beta c_\theta s_\theta}{t_\gamma s_\gamma} - \frac{c_\delta c_\theta s_\theta}{t_\beta t_\gamma s_\gamma} - \frac{c_\theta^2}{t_\gamma^2}. \tag{C.16}$$

Finally for $|Y_2^2|$ and $|Y_3^2|$ we have:

$$|Y_2^2| = \frac{c_\delta^2 c_\theta^2}{t_\beta^2 s_\gamma^2} - \frac{s_\delta^2 c_\theta^2}{t_\beta^2 s_\gamma^2} - \frac{2 c_\delta c_\theta s_\theta}{t_\beta t_\gamma s_\gamma} + \frac{s_\theta^2}{t_\gamma^2}, \tag{C.17}$$

$$|Y_3^2| = \frac{c_\delta^2 s_\theta^2}{t_\beta^2 s_\gamma^2} - \frac{s_\delta^2 s_\theta^2}{t_\beta^2 s_\gamma^2} + \frac{2 c_\delta c_\theta s_\theta}{t_\beta t_\gamma s_\gamma} + \frac{c_\theta^2}{t_\gamma^2}. \tag{C.18}$$

References

[1] Abdelhak Djouadi. The Anatomy of electro-weak symmetry breaking. I: The Higgs boson in the standard model. *Phys. Rept.*, 457:1–216, 2008.

[2] Deckard. The higgs mechanism, Sep 2016.

[3] P. A. Zyla et al. Review of Particle Physics. *PTEP*, 2020(8):083C01, 2020.

[4] D. Brandt, H. Burkhardt, M. Lamont, S. Myers, and J. Wenninger. Accelerator physics at LEP. *Rept. Prog. Phys.*, 63:939–1000, 2000.

[5] G. Abbiendi et al. Search for Charged Higgs bosons: Combined Results Using LEP Data. *Eur. Phys. J. C*, 73:2463, 2013.

[6] Georges Aad et al. Search for charged Higgs bosons decaying into a top quark and a bottom quark at $\sqrt{s}$=13 TeV with the ATLAS detector. 2 2021.

[7] Georges Aad et al. Search for charged Higgs bosons decaying via $H^+ \to \tau\nu$ in top quark pair events using pp collision data at $\sqrt{s} = 7$ TeV with the ATLAS detector. *JHEP*, 06:039, 2012.

[8] Albert M Sirunyan et al. Search for charged Higgs bosons in the $\mathrm{H}^{\pm} \to \tau^{\pm}\nu_{\tau}$ decay channel in proton-proton collisions at $\sqrt{s} = 13$ TeV. *JHEP*, 07:142, 2019.

[9] Albert M Sirunyan et al. Search for a charged Higgs boson decaying to charm and bottom quarks in proton-proton collisions at $\sqrt{s} = 8$ TeV. *JHEP*, 11:115, 2018.

[10] Georges Aad et al. Search for a light charged Higgs boson in the decay channel $H^+ \to c\bar{s}$ in $t\bar{t}$ events using pp collisions at $\sqrt{s}$ = 7 TeV with the ATLAS detector. *Eur. Phys. J. C*, 73(6):2465, 2013.

[11] R. Assmann, M. Lamont, and S. Myers. A brief history of the LEP collider. *Nucl. Phys. B Proc. Suppl.*, 109:17–31, 2002.

[12] Serguei Chatrchyan et al. Search for a light charged Higgs boson in top quark decays in pp collisions at $\sqrt{s} = 7$ TeV. *JHEP*, 07:143, 2012.

[13] Francesca Borzumati and Christoph Greub. 2HDMs predictions for $\bar{B} \to X_s\gamma$ in NLO QCD. *Phys. Rev. D*, 58:074004, 1998.

[14] Particle Data Group, P A Zyla, et al. Review of Particle Physics. *Progress of Theoretical and Experimental Physics*, 2020(8), 08 2020. 083C01.

[15] Heather E. Logan, Stefano Moretti, Diana Rojas-Ciofalo, and Muyuan Song. CP violation from charged Higgs bosons in the three Higgs doublet model. 12 2020.

[16] A. G. Akeroyd, Stefano Moretti, Tetsuo Shindou, and Muyuan Song. CP asymmetries of $\overline{B} \to X_s/X_d\gamma$ in models with three Higgs doublets. *Phys. Rev. D*, 103(1):015035, 2021.

[17] A. G. Akeroyd, Stefano Moretti, and Muyuan Song. Light charged Higgs boson with dominant decay to quarks and its search at the LHC and future colliders. *Phys. Rev. D*, 98(11):115024, 2018.

[18] A. G. Akeroyd, Stefano Moretti, and Muyuan Song. Light charged Higgs boson with dominant decay to a charm quark and a bottom quark and its search at LEP2 and future e^+e^- colliders. *Phys. Rev. D*, 101(3):035021, 2020.

[19] Antonella Del Rosso. Higgs: the beginning of the exploration. Étude du Higgs : ce n'est que le début. (BUL-NA-2012-357. 47/2012):3, Nov 2012.

[20] Andrey Katz and Maxim Perelstein. Higgs Couplings and Electroweak Phase Transition. *JHEP*, 07:108, 2014.

[21] E. Accomando et al. Workshop on CP Studies and Non-Standard Higgs Physics. 7 2006.

[22] G.C. Branco, P.M. Ferreira, L. Lavoura, M.N. Rebelo, Marc Sher, and Joao P. Silva. Theory and phenomenology of two-Higgs-doublet models. *Phys. Rept.*, 516:1–102, 2012.

[23] T. D. Lee. A Theory of Spontaneous T Violation. *Phys. Rev. D*, 8:1226–1239, 1973.

[24] Steven Weinberg. A model of leptons. *Phys. Rev. Lett.*, 19:1264–1266, Nov 1967.

[25] Sheldon L. Glashow. Partial-symmetries of weak interactions. *Nuclear Physics*, 22(4):579–588, 1961.

[26] Salam Abdus. *Weak and electromagnetic interactions*, pages 244–254.

[27] Cliff Burgess and Guy Moore. *The Standard Model: A Primer*. Cambridge University Press, 2006.

[28] S. F. Novaes. Standard model: An Introduction. In *10th Jorge Andre Swieca Summer School: Particle and Fields*, 1 1999.

[29] François Englert and Robert Brout. Broken symmetry and the mass of gauge vector mesons. *Physical Review Letters*, 13(9):321, 1964.

[30] Peter Ware Higgs. Broken symmetries, massless particles and gauge fields. *Phys. Lett.*, 12:132–133, 1964.

[31] Peter W Higgs. Broken symmetries and the masses of gauge bosons. *Physical Review Letters*, 13(16):508, 1964.

[32] Rodolfo A. Diaz and R. Martinez. The Custodial symmetry. *Rev. Mex. Fis.*, 47:489–492, 2001.

[33] Stephen P. Martin. A Supersymmetry primer. *Adv. Ser. Direct. High Energy Phys.*, 21:1–153, 2010.

[34] Nathaniel Craig. Implications of SUSY Searches for Physics Beyond the Standard Model. In *27th Rencontres de Blois on Particle Physics and Cosmology*, 12 2015.

[35] J. Wess and B. Zumino. Supergauge Transformations in Four-Dimensions. *Nucl. Phys. B*, 70:39–50, 1974.

[36] S. L. Glashow. Partial Symmetries of Weak Interactions. *Nucl. Phys.*, 22:579–588, 1961.

[37] Abdus Salam and John Clive Ward. Electromagnetic and weak interactions. *Phys. Lett.*, 13:168–171, 1964.

[38] Steven Weinberg. A Model of Leptons. *Phys. Rev. Lett.*, 19:1264–1266, 1967.

[39] A. Pich. The Standard model of electroweak interactions. In *22nd International Meeting on Fundamental Physics: The Standard Model and Beyond*, 2 1994.

[40] A. Pich. The Standard model of electroweak interactions. In *2004 European School of High-Energy Physics*, 2 2005.

[41] A. D. Sakharov. Violation of CP Invariance, C asymmetry, and baryon asymmetry of the universe. *Pisma Zh. Eksp. Teor. Fiz.*, 5:32–35, 1967.

[42] A. D. Sakharov. Baryonic Asymmetry of the Universe. *Sov. Phys. JETP*, 49:594–599, 1979.

[43] Laurent Canetti, Marco Drewes, and Mikhail Shaposhnikov. Matter and Antimatter in the Universe. *New J. Phys.*, 14:095012, 2012.

[44] Gustavo Castelo-Branco and David Emmanuel-Costa. Flavour Physics and CP Violation in the Standard Model and Beyond. *Springer Proc. Phys.*, 161:145–186, 2015.

[45] Ling-Lie Chau and Wai-Yee Keung. Comments on the Parametrization of the Kobayashi-Maskawa Matrix. *Phys. Rev. Lett.*, 53:1802, 1984.

[46] J. H. Christenson, J. W. Cronin, V. L. Fitch, and R. Turlay. Evidence for the 2π Decay of the K_2^0 Meson. *Phys. Rev. Lett.*, 13:138–140, 1964.

[47] A. Alavi-Harati et al. Observation of direct CP violation in $K_{S,L} \to \pi\pi$ decays. *Phys. Rev. Lett.*, 83:22–27, 1999.

[48] Bernard Aubert et al. Observation of CP violation in the B^0 meson system. *Phys. Rev. Lett.*, 87:091801, 2001.

[49] R. Aaij et al. Evidence for CP violation in time-integrated $D^0 \to h^-h^+$ decay rates. *Phys. Rev. Lett.*, 108:111602, 2012.

[50] Ziro Maki, Masami Nakagawa, and Shoichi Sakata. Remarks on the unified model of elementary particles. *Prog. Theor. Phys.*, 28:870–880, 1962.

[51] M. Fukugita and T. Yanagida. Baryogenesis Without Grand Unification. *Phys. Lett. B*, 174:45–47, 1986.

[52] K. Abe et al. Constraint on the matter–antimatter symmetry-violating phase in neutrino oscillations. *Nature*, 580(7803):339–344, 2020. [Erratum: Nature 583, E16 (2020)].

[53] M. B. Gavela, P. Hernandez, J. Orloff, and O. Pene. Standard model CP violation and baryon asymmetry. *Mod. Phys. Lett. A*, 9:795–810, 1994.

[54] HW Hamber. *The Feynman path integral approach*. Springer, Berlin-Heidelberg, 2009.

[55] Y Fukuda, T Hayakawa, E Ichihara, K Inoue, K Ishihara, Hirokazu Ishino, Y Itow, T Kajita, J Kameda, S Kasuga, et al. Evidence for oscillation of atmospheric neutrinos. *Physical Review Letters*, 81(8):1562, 1998.

[56] G. B. Gelmini and M. Roncadelli. Left-Handed Neutrino Mass Scale and Spontaneously Broken Lepton Number. *Phys. Lett. B*, 99:411–415, 1981.

[57] Manuel Drees. Dark Matter Theory. *PoS*, ICHEP2018:730, 2019.

[58] See e.g. the Review on Dark Matter in the Particle Data Book. M. Tanabashi et al. Review of particle physics. *Physical Review D*, 98(3), 8 2018.

[59] J. H. Christenson, J. W. Cronin, V. L. Fitch, and R. Turlay. Evidence for the 2π decay of the k_2^0 meson. *Phys. Rev. Lett.*, 13:138–140, Jul 1964.

[60] Neil Turok and John Zadrozny. Dynamical generation of baryons at the electroweak transition. *Phys. Rev. Lett.*, 65:2331–2334, 1990.

[61] Utpal Sarkar. *Particle and Astroparticle physics*, pages 429–460. CRC Press, 2007.

[62] E. Sather. The Mystery of the matter asymmetry. *SLAC Beam Line*, 26N1:31–37, 1996.

[63] H.E. Haber and G.L. Kane. The search for supersymmetry: Probing physics beyond the standard model. *Physics Reports*, 117(2):75 – 263, 1985.

[64] Gustavo C. Branco, Dipankar Das, Miguel Levy, and Palash B. Pal. Crossed two Higgs-doublet models: reduction of Yukawa parameters in the low-scale limit of left-right symmetry and other avatars. *Phys. Rev. D*, 102(3):035007, 2020.

[65] Amine Ahriche, Gaber Faisel, Shu-Yu Ho, Salah Nasri, and Jusak Tandean. Effects of two inert scalar doublets on Higgs boson interactions and the electroweak phase transition. *Phys. Rev. D*, 92(3):035020, 2015.

[66] Shinya Kanemura, Yasuhiro Okada, and Eibun Senaha. Electroweak baryogenesis and quantum corrections to the triple Higgs boson coupling. *Phys. Lett. B*, 606:361–366, 2005.

[67] Diana Rojas-Ciofalo, Adriana Cordero, Jaime Hernández-Sánchez, Venus Keus, Stefano Moretti, and Dorota Sokolowska. Dark Matter Signals at the LHC from a 3HDM. *PoS*, LHCP2019:013, 2019.

[68] A. Aranda, D. Hernández-Otero, J. Hernández-Sanchez, V. Keus, S. Moretti, D. Rojas-Ciofalo, and T. Shindou. Z_3 symmetric inert (2+1)-Higgs-doublet model. *Phys. Rev. D*, 103(1):015023, 2021.

[69] A. Cordero, J. Hernandez-Sanchez, V. Keus, S. F. King, S. Moretti, D. Rojas, and D. Sokolowska. Dark Matter Signals at the LHC from a 3HDM. *JHEP*, 05:030, 2018.

[70] Wei-Shu Hou, Tanmoy Modak, and Tilman Plehn. A Final Word on FCNC-Baryogenesis from Heavy Higgs Bosons. 12 2020.

[71] Paul Langacker. Grand Unified Theories and Proton Decay. *Phys. Rept.*, 72:185, 1981.

[72] John F Gunion, Gordon L Kane, Sally Dawson, and Howard E Haber. The higgs hunter's guide. *Front. Phys.*, 80(BNL-41644):1–404, 1989.

[73] Yuval Grossman. Phenomenology of models with more than two Higgs doublets. *Nucl. Phys. B*, 426:355–384, 1994.

[74] Antonio Pich and Paula Tuzon. Yukawa Alignment in the Two-Higgs-Doublet Model. *Phys. Rev. D*, 80:091702, 2009.

[75] Sheldon L Glashow and Steven Weinberg. Natural conservation laws for neutral currents. *Physical Review D*, 15(7):1958, 1977.

[76] John F. Gunion and Howard E. Haber. The CP conserving two Higgs doublet model: The Approach to the decoupling limit. *Phys. Rev. D*, 67:075019, 2003.

[77] Jérémy Bernon, John F. Gunion, Howard E. Haber, Yun Jiang, and Sabine Kraml. Scrutinizing the alignment limit in two-Higgs-doublet models: m_h=125 GeV. *Phys. Rev. D*, 92(7):075004, 2015.

[78] Jérémy Bernon, John F. Gunion, Howard E. Haber, Yun Jiang, and Sabine Kraml. Scrutinizing the alignment limit in two-Higgs-doublet models. II. m_H=125 GeV. *Phys. Rev. D*, 93(3):035027, 2016.

[79] A combination of measurements of Higgs boson production and decay using up to 139 fb^{-1} of proton–proton collision data at $\sqrt{s} = 13$ TeV collected with the ATLAS experiment. 8 2020.

[80] Dipankar Das and Ipsita Saha. Alignment limit in three Higgs-doublet models. *Phys. Rev. D*, 100(3):035021, 2019.

[81] A. Arhrib, R. Benbrik, M. Krab, B. Manaut, S. Moretti, Yan Wang, and Qi-Shu Yan. New Discovery Modes for a Light Charged Higgs Boson at the LHC. 6 2021.

[82] Venus Keus, Stephen F. King, and Stefano Moretti. Three-Higgs-doublet models: symmetries, potentials and Higgs boson masses. *JHEP*, 01:052, 2014.

[83] I. P. Ivanov and E. Vdovin. Classification of finite reparametrization symmetry groups in the three-Higgs-doublet model. *Eur. Phys. J. C*, 73(2):2309, 2013.

[84] I. P. Ivanov and C. C. Nishi. Symmetry breaking patterns in 3HDM. *JHEP*, 01:021, 2015.

[85] Dipankar Das and Ujjal Kumar Dey. Analysis of an extended scalar sector with S_3 symmetry. *Phys. Rev. D*, 89(9):095025, 2014. [Erratum: Phys.Rev.D 91, 039905 (2015)].

[86] Venus Keus, Stephen F. King, and Stefano Moretti. Phenomenology of the inert $(2+1)$ and $(4+2)$ higgs doublet models. *Phys. Rev. D*, 90:075015, Oct 2014.

[87] M. Maniatis and O. Nachtmann. Stability and symmetry breaking in the general three-Higgs-doublet model. *JHEP*, 02:058, 2015. [Erratum: JHEP 10, 149 (2015)].

[88] Maria Krawczyk and Dorota Sokolowska. The Charged Higgs boson mass in the 2HDM: Decoupling and CP violation. *eConf*, C0705302:HIG09, 2007.

[89] John F. Gunion and Howard E. Haber. Conditions for CP-violation in the general two-Higgs-doublet model. *Phys. Rev. D*, 72:095002, 2005.

[90] Graham Cree and Heather E. Logan. Yukawa alignment from natural flavor conservation. *Phys. Rev. D*, 84:055021, 2011.

[91] Nicola Cabibbo. Unitary symmetry and leptonic decays. *Physical Review Letters*, 10(12):531, 1963.

[92] Makoto Kobayashi et al. M. kobayashi and t. maskawa, prog. theor. phys. 49, 652 (1973). *Prog. Theor. Phys.*, 49:652, 1973.

[93] Carl H Albright, J Smith, and S-HH Tye. Signatures for charged-higgs-boson production in e^+e^- collisions. *Physical Review D*, 21(3):711, 1980.

[94] Lay Nam Chang and Jihn E. Kim. Possible Signature of Charged Higgs Particles in High-energy e^+e^- Annihilation. *Phys. Lett. B*, 81:233–237, 1979.

[95] AG Akeroyd and William James Stirling. Light charged higgs scalars at high-energy e^+e^- colliders. Technical report, SCAN-9411463, 1994.

[96] A.G. Akeroyd, S. Moretti, and J. Hernandez-Sanchez. Light charged Higgs bosons decaying to charm and bottom quarks in models with two or more Higgs doublets. *Phys. Rev. D*, 85:115002, 2012.

[97] A.G. Akeroyd, S. Moretti, K. Yagyu, and E. Yildirim. Light charged Higgs boson scenario in 3-Higgs doublet models. *Int. J. Mod. Phys. A*, 32(23n24):1750145, 2017.

[98] J. Hernandez-Sanchez, S. Moretti, R. Noriega-Papaqui, and A. Rosado. Off-diagonal terms in Yukawa textures of the Type-III 2-Higgs doublet model and light charged Higgs boson phenomenology. *JHEP*, 07:044, 2013.

[99] Michael Trott and Mark B. Wise. On Theories of Enhanced CP Violation in $B_{s,d}$ Meson Mixing. *JHEP*, 11:157, 2010.

[100] Guido Van Rossum and Fred L. Drake. *Python 3 Reference Manual*. CreateSpace, Scotts Valley, CA, 2009.

[101] J. D. Hunter. Matplotlib: A 2d graphics environment. *Computing in Science & Engineering*, 9(3):90–95, 2007.

[102] Pierre Raybaut. Spyder-documentation. *Available online at: pythonhosted. org*, 2009.

[103] Wolfram Research, Inc. Mathematica, Version 12.3.1. Champaign, IL, 2021.

[104] Martin Jung, Antonio Pich, and Paula Tuzon. Charged-Higgs phenomenology in the Aligned two-Higgs-doublet model. *JHEP*, 11:003, 2010.

[105] A.G. Akeroyd and W.James Stirling. Light charged Higgs scalars at high-energy e^+e^- colliders. *Nucl. Phys. B*, 447:3–17, 1995.

[106] Search for charged Higgs bosons with the $H^\pm \to \tau^\pm \nu_\tau$ decay channel in the fully hadronic final state at $\sqrt{s} = 13$ TeV. Technical Report CMS-PAS-HIG-16-031, CERN, Geneva, 2016.

[107] CERN. *Physics at LEP2: CERN, Geneva, Switzerland 2 - 3 Nov 1995. Workshop on Physics at LEP2*, Geneva, 1996. CERN. Composed by 3 sessions.

[108] A. Heister et al. Search for charged Higgs bosons in e^+e^- collisions at energies up to $\sqrt{s}$ = 209-GeV. *Phys. Lett. B*, 543:1–13, 2002.

[109] J. Abdallah et al. Search for charged Higgs bosons at LEP in general two Higgs doublet models. *Eur. Phys. J. C*, 34:399–418, 2004.

[110] P. Achard et al. Search for charged Higgs bosons at LEP. *Phys. Lett. B*, 575:208–220, 2003.

[111] G. Abbiendi et al. Search for Charged Higgs Bosons in e^+e^- Collisions at $\sqrt{s} = 189 - 209$ GeV. *Eur. Phys. J. C*, 72:2076, 2012.

[112] Georges Aad et al. Search for charged Higgs bosons through the violation of lepton universality in $t\bar{t}$ events using pp collision data at $\sqrt{s} = 7$ TeV with the ATLAS experiment. *JHEP*, 03:076, 2013.

[113] Vardan Khachatryan et al. Search for a light charged Higgs boson decaying to $c\bar{s}$ in pp collisions at $\sqrt{s} = 8$ TeV. *JHEP*, 12:178, 2015.

[114] Vardan Khachatryan et al. Search for a charged Higgs boson in pp collisions at $\sqrt{s} = 8$ TeV. *JHEP*, 11:018, 2015.

[115] Morad Aaboud et al. Search for charged Higgs bosons decaying via $H^\pm \to \tau^\pm \nu_\tau$ in the τ+jets and τ+lepton final states with 36 fb^{-1} of pp collision data recorded at $\sqrt{s} = 13$ TeV with the ATLAS experiment. *JHEP*, 09:139, 2018.

[116] Georges Aad et al. Search for charged Higgs bosons decaying via $H^\pm \to \tau^\pm \nu$ in fully hadronic final states using pp collision data at $\sqrt{s} = 8$ TeV with the ATLAS detector. *JHEP*, 03:088, 2015.

[117] Geoffrey T J Arnison et al. Experimental observation of isolated large transverse energy electrons with associated missing energy at $\sqrt{s} = 540GeV$. *Phys. Lett. B*, 122(CERN-EP-83-13):103–116. 31 p, Jan 1983.

[118] C. Rubbia. The Discovery of the W and Z bosons. *Phys. Rept.*, 239:241–284, 1994.

[119] D. Decamp et al. ALEPH: A detector for electron-positron annnihilations at LEP. *Nucl. Instrum. Meth. A*, 294:121–178, 1990. [Erratum: Nucl.Instrum.Meth.A 303, 393 (1991)].

[120] Eva Halkiadakis. Introduction to the LHC Experiments. In *Theoretical Advanced Study Institute in Elementary Particle Physics: Physics of the Large and the Small*, 4 2010.

[121] James Pinfold. MoEDAL becomes the LHC's magnificent seventh. *CERN Cour.*, 50(4):19–20, 2010.

[122] Akitaka Ariga et al. FASER's physics reach for long-lived particles. *Phys. Rev. D*, 99(9):095011, 2019.

[123] Akitaka Ariga et al. FASER: ForwArd Search ExpeRiment at the LHC. 1 2019.

[124] Jonathan L. Feng, Iftah Galon, Felix Kling, and Sebastian Trojanowski. ForwArd Search ExpeRiment at the LHC. *Phys. Rev. D*, 97(3):035001, 2018.

[125] Georges Aad et al. Observation of a new particle in the search for the Standard Model Higgs boson with the ATLAS detector at the LHC. *Phys. Lett. B*, 716:1–29, 2012.

[126] Serguei Chatrchyan et al. Observation of a New Boson at a Mass of 125 GeV with the CMS Experiment at the LHC. *Phys. Lett. B*, 716:30–61, 2012.

[127] G. Aad et al. The ATLAS Experiment at the CERN Large Hadron Collider. *JINST*, 3:S08003, 2008.

[128] S. Chatrchyan et al. The CMS Experiment at the CERN LHC. *JINST*, 3:S08004, 2008.

[129] Particle Data Group and et al. Review of Particle Physics. *Progress of Theoretical and Experimental Physics*, 2020(8), 08 2020. 083C01.

[130] T. Aaltonen et al. Search for charged Higgs bosons in decays of top quarks in p anti-p collisions at $\sqrt{s}$ = 1.96 TeV. *Phys. Rev. Lett.*, 103:101803, 2009.

[131] V. M. Abazov et al. Search for Charged Higgs Bosons in Top Quark Decays. *Phys. Lett. B*, 682:278–286, 2009.

[132] G. Abbiendi et al. Search for Charged Higgs Bosons in e^+e^- Collisions at $\sqrt{s} = 189 - 209$ GeV. *Eur. Phys. J. C*, 72:2076, 2012.

[133] G. Abbiendi et al. Measurement of R(b) in e+ e- collisions at 182-GeV to 209-GeV. *Phys. Lett. B*, 609:212–225, 2005.

[134] Mingyi Dong et al. CEPC Conceptual Design Report: Volume 2 - Physics & Detector. 11 2018.

[135] A. Abada et al. FCC Physics Opportunities: Future Circular Collider Conceptual Design Report Volume 1. *Eur. Phys. J. C*, 79(6):474, 2019.

[136] The International Linear Collider Technical Design Report - Volume 1: Executive Summary. 6 2013.

[137] T. K. Charles et al. The Compact Linear Collider (CLIC) - 2018 Summary Report. 2/2018, 12 2018.

[138] Glen Cowan, Kyle Cranmer, Eilam Gross, and Ofer Vitells. Asymptotic formulae for likelihood-based tests of new physics. *Eur. Phys. J. C*, 71:1554, 2011. [Erratum: Eur.Phys.J.C 73, 2501 (2013)].

[139] Gerhard Buchalla, Andrzej J. Buras, and Markus E. Lautenbacher. Weak decays beyond leading logarithms. *Rev. Mod. Phys.*, 68:1125–1144, 1996.

[140] Tobias Hurth. Inclusive rare B decays. In *5th International Symposium on Radiative Corrections: Applications of Quantum Field Theory to Phenomenology*, 4 2001.

[141] JoAnne L. Hewett. Top ten models constrained by $b \to s\gamma$. In *21st Annual SLAC Summer Institute on Particle Physics: Spin Structure in High-energy Processes (School: 26 Jul - 3 Aug, Topical Conference: 4-6 Aug) (SSI 93)*, pages 463–475, 5 1994.

[142] S. Chen et al. Branching fraction and photon energy spectrum for $b \to s\gamma$. *Phys. Rev. Lett.*, 87:251807, 2001.

[143] J. P. Lees et al. Measurement of BR($B \to X_s\gamma$), the $B \to X_s\gamma$ photon energy spectrum, and the direct CP asymmetry in $B \to X_{s+d}\gamma$ decays. *Phys. Rev. D*, 86:112008, 2012.

[144] A. Abdesselam et al. Measurement of the inclusive $B \to X_{s+d}\gamma$ branching fraction, photon energy spectrum and HQE parameters. In *38th International Conference on High Energy Physics*, 8 2016.

[145] Bernard Aubert et al. Measurement of the $B \to X_s\gamma$ branching fraction and photon energy spectrum using the recoil method. *Phys. Rev. D*, 77:051103, 2008.

[146] J. P. Lees et al. Exclusive Measurements of $b \to s\gamma$ Transition Rate and Photon Energy Spectrum. *Phys. Rev. D*, 86:052012, 2012.

[147] T. Saito et al. Measurement of the $\bar{B} \to X_s\gamma$ Branching Fraction with a Sum of Exclusive Decays. *Phys. Rev. D*, 91(5):052004, 2015.

[148] P. del Amo Sanchez et al. Study of $B \to X\gamma$ Decays and Determination of $|V_{td}/V_{ts}|$. *Phys. Rev. D*, 82:051101, 2010.

[149] Yasmine Sara Amhis et al. Averages of b-hadron, c-hadron, and τ-lepton properties as of 2018. 9 2019.

[150] W. Altmannshofer et al. The Belle II Physics Book. *PTEP*, 2019(12):123C01, 2019. [Erratum: PTEP 2020, 029201 (2020)].

[151] M. Misiak, Abdur Rehman, and Matthias Steinhauser. Towards $\overline{B} \to X_s\gamma$ at the NNLO in QCD without interpolation in m_c. *JHEP*, 06:175, 2020.

[152] M. Misiak et al. Updated NNLO QCD predictions for the weak radiative B-meson decays. *Phys. Rev. Lett.*, 114(22):221801, 2015.

[153] Alexander L. Kagan and Matthias Neubert. Direct CP violation in $B \to X_s\gamma$ decays as a signature of new physics. *Phys. Rev. D*, 58:094012, 1998.

[154] L. Wolfenstein and Y. L. Wu. CP violation in the decay b —> s gamma in the two Higgs doublet model. *Phys. Rev. Lett.*, 73:2809–2812, 1994.

[155] G. M. Asatrian and A. Ioannisian. CP violation in the decay $b \to s\gamma$ in the left-right symmetric model. *Phys. Rev. D*, 54:5642–5646, 1996.

[156] Michael Benzke, Seung J. Lee, Matthias Neubert, and Gil Paz. Long-Distance Dominance of the CP Asymmetry in $B \to X_{s,d} + \gamma$ Decays. *Phys. Rev. Lett.*, 106:141801, 2011.

[157] Ayesh Gunawardana and Gil Paz. Reevaluating uncertainties in $\overline{B} \to X_s\gamma$ decay. *JHEP*, 11:141, 2019.

[158] Chun-Khiang Chua, Xiao-Gang He, and Wei-Shu Hou. CP violating $b \to s\gamma$ decay in supersymmetric models. *Phys. Rev. D*, 60:014003, 1999.

[159] Joao M. Soares. CP violation in radiative b decays. *Nucl. Phys. B*, 367:575–590, 1991.

[160] A. G. Akeroyd, Y. Y. Keum, and S. Recksiegel. Effect of supersymmetric phases on the direct CP asymmetry of $B \to X_d\gamma$. *Phys. Lett. B*, 507:252–259, 2001.

[161] Tobias Hurth, Enrico Lunghi, and Werner Porod. Untagged $\bar{B} \to X_{s+d}\gamma$ CP asymmetry as a probe for new physics. *Nucl. Phys. B*, 704:56–74, 2005.

[162] S. Watanuki et al. Measurements of isospin asymmetry and difference of direct *CP* asymmetries in inclusive $B \to X_s\gamma$ decays. *Phys. Rev. D*, 99(3):032012, 2019.

[163] M. Tanabashi et al. Review of particle physics. *Phys. Rev. D*, 98:030001, Aug 2018.

[164] T. E. Coan et al. Bounds on the CP asymmetry in $b \to s\gamma$ decays. *Phys. Rev. Lett.*, 86:5661–5665, 2001.

[165] J. P. Lees et al. Measurements of direct CP asymmetries in $B \to X_s\gamma$ decays using sum of exclusive decays. *Phys. Rev. D*, 90(9):092001, 2014.

[166] L. Pesántez et al. Measurement of the direct *CP* asymmetry in $\bar{B} \to X_{s+d}\gamma$ decays with a lepton tag. *Phys. Rev. Lett.*, 114(15):151601, 2015.

[167] Martin Jung, Antonio Pich, and Paula Tuzon. The B -> Xs gamma Rate and CP Asymmetry within the Aligned Two-Higgs-Doublet Model. *Phys. Rev. D*, 83:074011, 2011.

[168] Martin Jung, Xin-Qiang Li, and Antonio Pich. Exclusive radiative B-meson decays within the aligned two-Higgs-doublet model. *JHEP*, 10:063, 2012.

[169] Alexander Belyaev, Neil D. Christensen, and Alexander Pukhov. CalcHEP 3.4 for collider physics within and beyond the Standard Model. *Comput. Phys. Commun.*, 184:1729–1769, 2013.

[170] Monoranjan Guchait and Stefano Moretti. Improving the discovery potential of charged Higgs bosons at Tevatron run II. *JHEP*, 01:001, 2002.

[171] K. A. Assamagan, M. Guchait, and S. Moretti. Charged Higgs bosons in the transition region $M(H^{\pm}) \sim m(t)$ at the LHC. In *3rd Les Houches Workshop on Physics at TeV Colliders*, 2 2004.

[172] Tomas Dado. Direct top-quark decay width measurement at $\sqrt{s}$ = 13 TeV with the ATLAS experiment. *PoS*, LeptonPhoton2019:089, 2019.

[173] Vernon D. Barger, J. L. Hewett, and R. J. N. Phillips. New Constraints on the Charged Higgs Sector in Two Higgs Doublet Models. *Phys. Rev. D*, 41:3421–3441, 1990.

[174] Martin Jung and Antonio Pich. Electric Dipole Moments in Two-Higgs-Doublet Models. *JHEP*, 04:076, 2014.

[175] V. Andreev et al. Improved limit on the electric dipole moment of the electron. *Nature*, 562(7727):355–360, 2018.

[176] David Bowser-Chao, Darwin Chang, and Wai-Yee Keung. Electron electric dipole moment from CP violation in the charged Higgs sector. *Phys. Rev. Lett.*, 79:1988–1991, 1997.

[177] Shinya Kanemura, Mitsunori Kubota, and Kei Yagyu. Aligned CP-violating Higgs sector canceling the electric dipole moment. *JHEP*, 08:026, 2020.

[178] D. Chang, W. Y. Keung, and T. C. Yuan. Two-loop bosonic contribution to the electron electric dipole moment. *Phys. Rev. D*, 43:R14–R16, Jan 1991.

[179] M. E. Pospelov and I. B. Khriplovich. Electric dipole moment of the W boson and the electron in the Kobayashi-Maskawa model. *Sov. J. Nucl. Phys.*, 53:638–640, 1991.

[180] C. Abel et al. Measurement of the permanent electric dipole moment of the neutron. *Phys. Rev. Lett.*, 124(8):081803, 2020.

[181] Eric Braaten, Chong Sheng Li, and Tzu Chiang Yuan. Evolution of weinberg's gluonic cp-violation operator. *Phys. Rev. Lett.*, 64:1709–1712, Apr 1990.

[182] S. L. Glashow, J. Iliopoulos, and L. Maiani. Weak Interactions with Lepton-Hadron Symmetry. *Phys. Rev. D*, 2:1285–1292, 1970.

[183] Konstantin G. Chetyrkin, Mikolaj Misiak, and Manfred Munz. Weak radiative B meson decay beyond leading logarithms. *Phys. Lett. B*, 400:206–219, 1997. [Erratum: Phys.Lett.B 425, 414 (1998)].